Studies on Moving Boundary Problems in Rarefied Gas Dynamics

Tetsuro Tsuji

2013

Preface

A gas is called rarefied gas when the mean free path of gas molecules is not negligibly small compared with the typical length of a problem under concern. The Knudsen number, the ratio between the mean free path and the typical length, is a parameter that represents the degree of gaseous rarefaction. Gas flows in micro-scale devices or in vacuum equipments are typical examples of rarefied gas flows. In both cases, the Knudsen number is not negligible, because the typical length is small in the former case and the mean free path is large in the latter case. The state of a rarefied gas deviates from the local equilibrium state, since a gas molecule undergoes few inter-molecular collisions with other molecules during the characteristic time scale of the problem. Hence, the behavior of the rarefied gas cannot be described by the ordinary gas dynamics, which is known to be valid only when the gas is close to the local equilibrium. Instead, rarefied gas dynamics (or molecular gas dynamics) based on kinetic theory of gases is the fundamental framework to treat it.

The basic equation in rarefied gas dynamics is the Boltzmann equation (or its model equation), which describes the behavior of the velocity distribution function of gas molecules. The velocity distribution function contains the mesoscopic (a scale in between macro and micro) information of the gas, and thus the rarefied gas dynamics is capable of describing the gas in non-equilibrium. The macroscopic quantities such as density, flow velocity, temperature etc. are expressed by the suitable moments of the velocity distribution function. In the literature, various steady problems for a rarefied gas have been studied extensively. When a gas is highly rarefied so that the collision between gas molecules can be neglected (a free-molecular gas), the Boltzmann equation is reduced to the free transport equation, which is more tractable at first glance. In fact, the steady behavior of the free-molecular gas is well understood because of the simplicity of the equation. However, detailed studies on the time-dependent behavior of the rarefied gas, as well as the free-molecular gas, have rarely been treated so far, especially when a physical boundary is present.

Recently, time-dependent problems of a rarefied gas with a physical boundary draw much attention due to their practical importance as well as theoretical (or mathematical) significance in rarefied gas dynamics. In particular, the case when the physical boundary is moving, varying its velocity depending on time, is a challenging subject. During the last decade, some progress has been made on the mathematical structure of the solution of time-dependent problems with a stationary or moving boundary. On the other hand, numerical studies, which are essential for engineering applications and useful to understand the mechanism underlying them, are still far from being matured. The present thesis aims to investigate in detail some fundamental time-dependent problems of the rarefied gas with a stationary or moving boundary by the accurate numerical analysis, and clarify the basic features of the problems such as the macroscopic profiles, the momentum (or energy) flux across the boundary, the long-time behavior of the solution, and the singularities in the velocity distribution function. As seen in the title of the thesis, our attention is mainly paid to moving boundary problems, however, the stationary boundary problem is also treated in Chapter 2.

The thesis is organized as follows. In Chapters 1, 2, and 3, time-dependent problems of a

free-molecular gas are considered. More specifically, moving boundary problems are treated in Chapters 1 and 3, and a stationary boundary problem in Chapter 2. Unlike steady problems, time-dependent problems of a free-molecular gas are not simple as they look. In fact, under certain situations, which will be seen in Chapter 4, the free-molecular gas is more delicate than the model Boltzmann equation. The difficulty arises from the *long-memory* due to the collisionless property of the free-molecular gas. In Chapter 3, in addition, a collision model between gas molecules and a background is introduced in order to investigate the effect of molecular collisions on the moving boundary problem. In Chapter 4, moving boundary problems of a rarefied gas, described by the Bhatnagar-Gross-Krook (BGK) model of the Boltzmann equation, are studied in detail at the level of the velocity distribution function. Throughout the thesis, the gas-surface interaction, i.e. a reflection law of a gas molecule impinging on the boundary, is described by diffuse reflection. To be more specific, a gas molecule that hits a boundary surface is assumed to be reflected according to the Maxwellian distribution characterized by the velocity and temperature of the boundary, with the density adjusted in such a way that there is no net mass flux across the boundary.

In Chapter 1, the rectilinear motion of a plate in its perpendicular direction in a free-molecular gas under a constant external force is studied numerically. The external force acts only on the plate in its perpendicular direction. This is a moving boundary problem of a free-molecular gas. As time goes on, the plate motion approaches a terminal motion, at which the drag exerted by the gas balances with the external force. It is shown by the accurate numerical analysis that the rate of approach is algebraic in time, and it is attributed to the long-memory created by the unsteady plate motion.

In Chapter 2, a stationary boundary is considered exceptionally. A free-molecular gas is contained in a vessel with a uniform constant temperature. Since the gas molecules undergo diffuse reflection on the vessel wall, the velocity distribution function is driven to the equilibrium distribution characterized by the vessel temperature as time goes on. This approach to the equilibrium is investigated numerically, and it is shown that the rate of approach is algebraic in time. The long-memory in this problem, the cause of the algebraic approach, manifests itself as the localization of the velocity distribution function, which is treated carefully in the numerical analysis.

In Chapter 3, a simple model of a linear pendulum in a free-molecular gas is considered. To be more specific, a plate is subject to an external restoring force obeying the Hooke's law in its perpendicular direction. The plate oscillates around its equilibrium position, attenuating its amplitude as time goes on due to the drag force exerted by the gas. This is a variation of the problem in Chapter 1, and thus a moving boundary problem. Decay rate of the pendulum motion is shown to be algebraic in time by the accurate numerical analysis. In this case, unlike the problem in Chapter 1, the motion of the boundary is more complicated. Hence, the long-memory results in a lot of discontinuities in the velocity distribution function, which need a careful treatment in the numerical analysis. Moreover, the special Lorentz gas, a model gas that interacts with a given background, is introduced to destroy the long-memory to investigate its effect on the decay rate.

Finally, in Chapter 4, the detailed investigation of the velocity distribution function in moving boundary problems in rarefied gas dynamics is carried out. This chapter consists of two parts. In the first part, based on the knowledge established so far in Chapters 1, 2, and 3, the singularities in the velocity distribution function induced by the unsteady motion of the boundary are clarified, and the accurate numerical method that captures them is developed. The method is applied to two moving boundary problems: the nonlinear acoustic wave in a rarefied gas generated by an oscillating boundary and a linear pendulum in a rarefied gas. In the second part, as the application of the above numerical method to a typical problem in micro engineering, the oscillatory flow in a micro gap consisting of a perpendicularly oscillating plate and a stationary plate is studied.

I feel grateful to my adviser, Professor Kazuo Aoki, for his patient guidance. I learned many important things on research activities from his kind advices, which will definitely contribute my future career as a researcher. I would like to express my gratitude also to Associate Professor Sigeru Takata, who gave me a lot of useful comments and encouragement, and Assistant Professor Shingo Kosuge for his support.

Professor Tetsuo Sawaragi gave me three chances to visit foreign research institutes through the JSPS Institutional Program for Young Researcher Overseas Visits. It was a valuable experience to have discussions with many distinguished researchers all over the world. In particular, I had some fruitful discussions with Professor Mario Pulvirenti, Professor Carlo Marchioro, and Assistant Professor Guido Cavallaro in Università di Roma "La Sapienza"; Professor Francis Filbet and Doctor Thomas Rey in Université de Lyon. A portion of my publications consists of the collaborative works with Professor Carlo Marchioro, Assistant Professor Guido Cavallaro in Università di Roma "La Sapienza"; with Professor François Golse in École Polytechnique.

My research activity was very stimulating and enjoyable thanks to nice colleagues in the Aoki laboratory and the department. Let me limit myself to the statement of some of the colleagues, otherwise the list would be too long. I appreciate Doctor Hitoshi Funagane, Ko Kugimoto, Hiroki Umetsu, Takuya Okamura, Doctor Shinya Okino, Kengo Deguchi, Masashi Kishimoto, Masahiro Abe, and Masanari Hattori for making my PhD period fulfilling.

I also would like to express my gratitude to my girl friend Tomoko Maeda for her warm relationship and cheer. Last but not the least, I would like to thank my parents Yoshinori Tsuji and Reiko Tsuji for their support throughout my life and giving me a chance to chase my dream. Also, my grand mother Michiko Saito took care of me for more than nine years. It is not too much to say that I would not have finished the thesis without her cordial support.

The present thesis was partly supported by Grant-in-Aid for JSPS Fellows (No. 24·2418).

Contents

Chapter 1

Approach to steady motion of a plate moving in a free-molecular gas under a constant external force

Abstract A thin plate accelerated or decelerated in a free-molecular gas at rest by a constant external force is considered. The force is in the direction perpendicular to the plate. In this situation, the plate velocity approaches its final constant velocity as time goes on. It is shown numerically that, under the diffuse-reflection boundary condition, the difference between the plate velocity and its final value decreases in proportion to an inverse power of time. This agrees with the previous theoretical result obtained under the assumption that the initial plate velocity is sufficiently close to the final one.

1 Introduction

In kinetic theory of gases, the two limiting cases, the continuum limit of vanishing Knudsen number (the mean free path of gas molecules divided by the characteristic length of the system) and the free-molecular limit of infinitely large Knudsen number, have been studied extensively. The former limit clarifies the relation between kinetic theory and fluid dynamics [1, 2, 3, 4, 5, 6]. In the latter limit (free-molecular gas or Knudsen gas), the fact that the collision term of the Boltzmann equation can be neglected simplifies the analysis dramatically, and the basic properties and phenomena appear to have been understood completely [2, 3, 6, 7]. However, most of the existing works are devoted to steady flows of a gas or steady motions of a body, and little is known about problems containing unsteady motion of a body (motion with acceleration, deceleration, or rotation of a non-symmetric body). The difficulty in this case arises from the fact that, because of the absence of intermolecular collisions, the gas molecules impinging on the body may have a long memory and be affected by the trajectory of the body in the far past, i.e., there exists the effect of long memory. Indeed, this fact was mentioned already in Sec. H,9 in [7]. However, to the best of the authors' knowledge, there is no systematic study of the effect. The present study, as well as the preceding studies [8, 9, 10, 11], aims at clarifying the memory effect in the problems with an unsteady body motion by considering a simple problem of a body moving in a free-molecular gas with acceleration or deceleration. This is a numerical study complementing the previous mathematical works [8, 9, 10, 11].

Let us consider a motion of a body in a uniform fluid (not a free-molecular gas) at rest caused by a constant external force. We assume that the body starts its motion with an initial velocity parallel to the external force and moves in the direction parallel to the external force without rotation because of a constraint or the symmetry of the body. A drag by the fluid acts on the body, and its velocity approaches a constant value (final velocity) for which the drag counterbalances the external force. If we assume that the drag is proportional to the speed of the body, its velocity approaches the final velocity exponentially fast. That is, if we let τ the time variable, $v_w(\tau)$ the velocity of the body in the direction of the external force, and $v_{w\infty}$ (> 0) its final value, then for sufficiently large τ,

$$|v_{w\infty} - v_w(\tau)| \approx C_1 e^{-C_2\tau} \tag{1.1}$$

holds, where C_1 and C_2 are positive constants.

However, if the fluid is a free-molecular gas in an equilibrium state at rest, the manner of approach to the final velocity is quite different from Eq. (1.1) [8, 9, 10, 11]. Let us assume that the body is a circular disk (with or without thickness) of dimension d ($d = 1, 2, 3$) and moves in the gas in the direction perpendicular to the disk. More specifically, the body is a real circular disk for $d = 3$, an infinite plate with a finite width for $d = 2$, and an infinite plate for $d = 1$ (see Fig. 1.1; in [8, 9, 11] the gas molecules are assumed to move on the plane for $d = 2$ and on the line for $d = 1$, but there is no essential difference). In this case, the approach to the final velocity is slow and is proportional to an inverse power of time. That is, for sufficiently large τ,

$$|v_{w\infty} - v_w(\tau)| \approx C_1' \tau^{-n} \tag{1.2}$$

holds, where C_1' is a positive constant, and n is an integer, which depends on the dimension d of the disk and the model of gas-surface interaction. In [8, 9], it was proven that $n = d + 2$ when the gas molecules undergo specular reflection (or elastic collision) on the surface of the disk. The proof was extended to the case of a general convex body, and it was shown that the same is true in this case [10]. Subsequently, it was shown in [11] that $n = d + 1$ when the gas molecules undergo diffuse reflection (or reflection with complete accommodation). Moreover, as proven in [9] for the specular reflection, if the initial velocity v_{w0} (in the direction of the external force) is greater than the final velocity ($0 \le v_{w\infty} < v_{w0}$), the disk velocity first decreases to a velocity smaller than the final one and then approaches it from below.

The law (1.2) is not exponential, and this may appear somewhat surprising. The reason for this behavior is attributed to the presence of recollisions between the gas molecules and the disk. In fact, when it is accelerated, the disk can catch up with a gas molecule already hit by the disk and hit it again. In other words, the disk can hit the same molecule successively, giving rise to a sequence of recollisions whose time intervals can be arbitrarily large. This creates a long tail memory, which is the cause of the power law (1.2). In particular, in the presence of recollisions, the assumption to take a drag force proportional to the velocity of the disk is no more valid even when the velocity is small. If we ignore recollisions, for example, assuming that the disk always hits new molecules at a given thermal equilibrium, the behavior becomes that of Eq. (1.1). It is reasonable to expect that the effect of recollisions can be destroyed if the background is not a free-molecular gas but a gas with intermolecular collisions. In this case we can say that our result remains valid, not as a strict asymptotic behavior, but as a transient behavior. From an experimental point of view, it is delicate to observe such an effect, and the authors are not aware of experiments in this direction. However, we should emphasize that the effect of recollision plays an important role when a body undergoes unsteady motion in a highly rarefied gas. It is also worth mentioning that it was already known that recollisions can produce a power law decay. In fact the velocity-velocity correlation of a tagged particle of a one-dimensional free gas decays as τ^{-3} (see [12]).

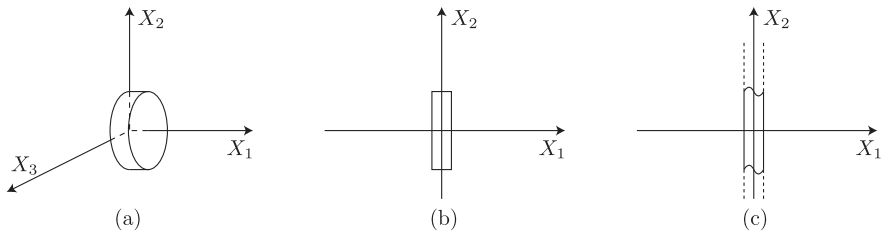

Fig. 1.1 A circular disk in a free-molecular gas. (a) Circular disk ($d = 3$), (b) infinite plate with a rectangular cross section ($d = 2$), (c) infinite plate with a finite thickness ($d = 1$).

The results in [8, 9, 10, 11] described above have been proven under the condition that the initial velocity of the disk is sufficiently close to the final velocity, i.e.,

$$|v_{w\infty} - v_{w0}|/(2kT_0/m_*)^{1/2} \ll 1, \tag{1.3}$$

where T_0 is a reference temperature (e.g., the temperature of the ambient gas), k is the Boltzmann constant, and m_* is the mass of a molecule. Since this restriction is imposed by mathematical technicalities rather than physical situations, one cannot know how small it should be. In addition, the slow approach to the final steady motion is caused by the memory effect, so that it is not obvious whether the same results hold or not for an arbitrary initial velocity that does not satisfy Eq. (1.3). In the present study, therefore, we investigate this problem numerically and try to give a numerical evidence for the case of diffuse reflection. The reason why we restrict ourselves to the case of the diffuse reflection, rather than the specular reflection, will be explained in Sec. 5.4.

The origin of the problem of a specularly reflecting disk treated in Refs. [8, 9] is explained from the point of view of particle dynamics in [8]. It should be remarked that the same problem has also been considered in connection with the so-called piston problem, which is a fundamental problem in statistical physics (see Refs. [13, 14] and the references therein). For other types of obstacle-background interaction, the reader is referred to [15, 16] (see also the references in [8, 9, 10, 11]).

2 Formulation of the problem

2.1 Problem, assumptions, and notations

In the present study, we consider a rectangular plate of dimension d without thickness instead of a circular disk for convenience of the numerical analysis. That is, the body is a real rectangular plate for $d = 3$, an infinite plate with a finite width for $d = 2$, and an infinite plate for $d = 1$ (Fig. 1.2). However, since the actual computation will be done mostly for $d = 1$ and 2, we formulate the problem for the two-dimensional problem ($d = 2$).

Let us consider an infinite expanse of an ideal gas in an equilibrium state at rest at temperature T_0 and density ρ_0. Suppose that an infinitely long plate with width L and without thickness, kept at temperature T_0, is fixed in the gas. Taking the X_1 axis perpendicular to the plate, the X_2 axis in the width direction, and the X_3 axis in the infinitely long spanwise direction, we assume that the plate is located at $X_1 = 0$, $-L/2 \le X_2 \le L/2$, and $-\infty < X_3 < \infty$ [Fig. 1.2(b)]. The plate is subject to a constant external force $\mathcal{F}$ (≥ 0) per unit mass in the direction of the positive X_1 axis. At $\tau = 0$, the plate is released and launched with an initial velocity v_{w0} in the X_1 direction. Then, it moves along the X_1 axis and approaches the final steady motion with a constant velocity (final velocity). We investigate the motion of the plate, with special interest in the rate of approach to the

final steady motion, under the following assumptions:

(i) The behavior of the gas is described by the Boltzmann equation [2, 3, 6].
(ii) The gas is so rarefied that the collisions between the gas molecules can be neglected (free-molecular gas or Knudsen gas) [2, 3, 6], and no external force acts on the gas molecules.
(iii) The gas molecules reflected on the plate are distributed according to the half-range Maxwellian distribution characterized by the temperature and velocity of the plate, and there is no net mass flux across the plate (diffuse reflection) [2, 3, 6].

Before presenting the basic equations, we summarize the notations used in the paper. We first introduce (and repeat) dimensional quantities: The X_i is the Cartesian coordinate system in space, τ is the time variable, ξ_i is the molecular velocity, $X_w(\tau)$ is the position (X_1 coordinate) of the plate at time τ, $v_w(\tau)$ is the corresponding velocity (in the X_1 direction) of the plate, v_{w0} is the initial value of $v_w(\tau)$ at $\tau = 0$, $v_{w\infty}$ is the final steady velocity of the plate [$v_{w\infty} = \lim_{\tau\to\infty} v_w(\tau)$], $\tilde{f}(X_i, \xi_i, \tau)$ is the velocity distribution function of the gas molecules, $\mathcal{F}$ is the external force acting on the plate per unit mass in the positive X_1 direction, $\mathcal{G}(\tau)$ is the drag acting on the plate per unit mass in the X_1 direction, and $\mathcal{M}$ is the mass of the plate per unit area. Then, we introduce the dimensionless counterparts x_i, t, ζ_i, x_w, u_w, u_{w0}, $u_{w\infty}$, f, F, G, and M by the following equations:

$$
\begin{array}{ll}
x_i = X_i/L, & t = \tau/\tau_0, \\
\zeta_i = \xi_i/(2kT_0/m_*)^{1/2}, & x_w(t) = X_w(\tau)/L, \\
u_w(t) = v_w(\tau)/(2kT_0/m_*)^{1/2}, & u_{w0} = v_{w0}/(2kT_0/m_*)^{1/2}, \\
u_{w\infty} = v_{w\infty}/(2kT_0/m_*)^{1/2}, & f(x_i, \zeta_i, t) = \tilde{f}(X_i, \xi_i, \tau)/\rho_0(2kT_0/m_*)^{-3/2}, \\
F = \mathcal{F}/L\tau_0^{-2}, & G(t) = \mathcal{G}(\tau)/L\tau_0^{-2}, \\
M = \mathcal{M}/\rho_0 L, &
\end{array}
\tag{1.4}
$$

where $\tau_0 = L(2kT_0/m_*)^{-1/2}$ is the reference time, k the Boltzmann constant, and m_* the mass of a gas molecule.

2.2 Basic equations

In the present spatially two-dimensional problem in which the physical quantities do not depend on x_3, we can eliminate the third component ζ_3 of the molecular velocity by considering the following marginal distribution function g:

$$
g(x_1, x_2, \zeta_1, \zeta_2, t) = \int_{-\infty}^{\infty} f(x_1, x_2, \zeta_i, t)\, d\zeta_3. \tag{1.5}
$$

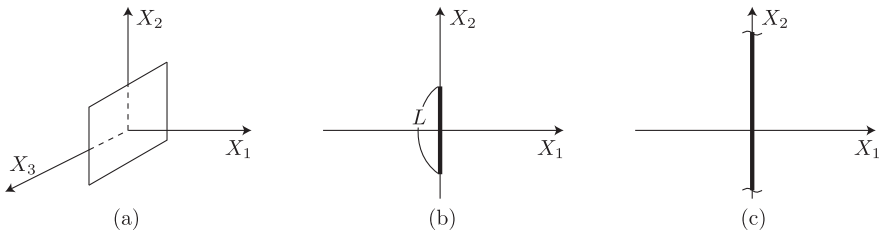

Fig. 1.2 A rectangular plate without thickness in a free-molecular gas. (a) Rectangular plate ($d = 3$), (b) infinite plate with a finite width ($d = 2$), (c) infinite plate ($d = 1$).

Then, the Boltzmann equation for a free-molecular gas reads

$$\frac{\partial g}{\partial t} + \zeta_1 \frac{\partial g}{\partial x_1} + \zeta_2 \frac{\partial g}{\partial x_2} = 0. \tag{1.6}$$

The corresponding initial condition is

$$g = g_0, \qquad g_0 = \pi^{-1} \exp(-\zeta_1^2 - \zeta_2^2), \qquad (t = 0), \tag{1.7}$$

and the boundary condition (diffuse reflection) on the plate is written as

$$g(x_1,\, x_2,\, \zeta_1,\, \zeta_2,\, t) = g_{w\pm}(x_2,\, \zeta_1,\, \zeta_2,\, t), \qquad \left[x_1 = x_{w\pm}(t),\ \ -\frac{1}{2} \le x_2 \le \frac{1}{2},\ \ \zeta_1 - u_w(t) \gtrless 0 \right], \tag{1.8a}$$

$$g_{w\pm}(x_2,\, \zeta_1,\, \zeta_2,\, t) = \pi^{-1} \rho_{w\pm}(x_2,\, t)\, \exp\Big(- [\zeta_1 - u_w(t)]^2 - \zeta_2^2 \Big), \tag{1.8b}$$

$$\rho_{w\pm}(x_2,\, t) = \mp 2\sqrt{\pi} \int_{-\infty}^{\infty} \int_{\zeta_1 - u_w(t) \lessgtr 0} [\zeta_1 - u_w(t)] \times g(x_{w\pm}(t),\, x_2,\, \zeta_1,\, \zeta_2,\, t)\, d\zeta_1 d\zeta_2. \tag{1.8c}$$

Here, $x_1 = x_{w\pm}(t)$ indicates $x_1 = x_w(t) \pm 0$, so that $\{\, (x_1, x_2) \,|\, x_1 = x_{w\pm},\ -1/2 \le x_2 \le 1/2 \}$ stands for the surface of the plate facing to the positive x_1 axis (plus sign) or that facing to the negative x_1 axis (minus sign). In Eq. (1.8) and in what follows, the upper (or lower) signs go together.

The equation of motion of the plate is given as

$$dx_w(t)/dt = u_w(t), \qquad du_w(t)/dt = F - G(t), \tag{1.9}$$

where the dimensionless drag $G(t)$ is expressed in terms of the velocity distribution function on the plate as follows:

$$G(t) = G_+(t) + G_-(t), \tag{1.10a}$$

$$G_\pm(t) = \pm \frac{1}{M} \int_{-1/2}^{1/2} \Big\{ \int_{-\infty}^{\infty} \int_{\zeta_1 - u_w(t) \lessgtr 0} [\zeta_1 - u_w(t)]^2 \times g(x_{w\pm},\, x_2,\, \zeta_1,\, \zeta_2,\, t)\, d\zeta_1 d\zeta_2 + \int_{-\infty}^{\infty} \int_{\zeta_1 - u_w(t) \gtrless 0} [\zeta_1 - u_w(t)]^2 \times g_{w\pm}(x_2,\, \zeta_1,\, \zeta_2,\, t)\, d\zeta_1 d\zeta_2 \Big\}\, dx_2. \tag{1.10b}$$

Here, $G_+(t)$ and $G_-(t)$ indicate, respectively, the drag acting on the surface at $x_{w+}(t)$ and $x_{w-}(t)$. The initial condition for Eq. (1.9) is

$$x_w(0) = 0, \qquad u_w(0) = u_{w0}. \tag{1.11}$$

We are going to solve numerically the coupled systems, Eqs. (1.6)–(1.8) and Eqs. (1.9)–(1.11).

In the spatially one-dimensional problem ($d = 1$), in which the plate is an infinitely wide plate in the x_2x_3 plane and the physical quantities depend only on x_1, we can also eliminate the second component ζ_2 of the molecular velocity by introducing the marginal distribution function

$$\overline{g}(x_1, \zeta_1, t) = \int_{-\infty}^{\infty} \int_{-\infty}^{\infty} f(x_1, \zeta_i, t) d\zeta_2 d\zeta_3. \tag{1.12}$$

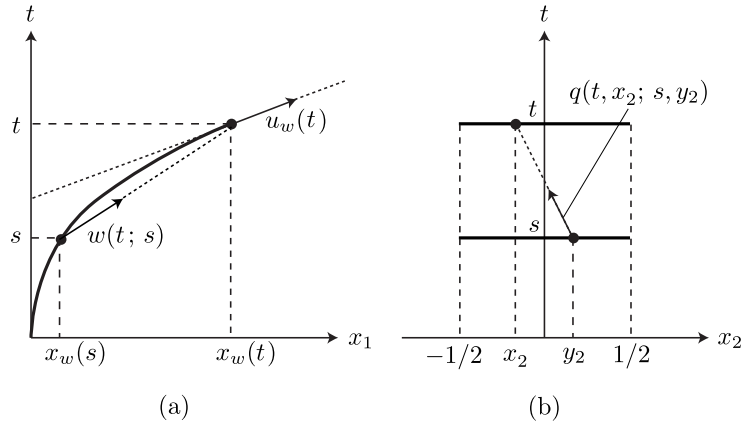

Fig. 1.3 Definitions of $w(t;\ s)$ and $q(t,\ x_2;\ s,\ y_2)$. (a) $w(t;\ s)$, (b) $q(t,\ x_2;\ s,\ y_2)$.

Therefore, the problem is much simpler. In this case, since there is no length scale related to the plate, we need to introduce an appropriate length scale (see Sec. 5.1). In the spatially three-dimensional problem ($d = 3$), we have to handle the full distribution function $f(x_i, \zeta_i, t)$, so that the problem is more involved.

3 Preliminaries

In this section, we transform Eqs. (1.6)–(1.8) into integral equations for ρ_{w+} and ρ_{w-}, which are more convenient for numerical analysis.

The Boltzmann equation (1.6) indicates that g is constant along the characteristic line $x_\ell - \zeta_\ell t = \text{const}$ ($\ell = 1,\ 2$), i.e., the projection of the molecular trajectory on the x_1x_2 plane. Let us consider the molecules impinging on the plate at time t, i.e., the molecules at $x_1 = x_{w+}$ (or $x_1 = x_{w-}$) and $-1/2 \le x_2 \le 1/2$ with $\zeta_1 - u_w(t) < 0$ [or $\zeta_1 - u_w(t) > 0$]. If we trace back the trajectories of such molecules reversing the time, we either (i) hit on the plate at a time in the past, or (ii) reach the initial distribution g_0 at $t = 0$ without hitting on the plate. The case (i) corresponds to the recollision mentioned in Sec. 1. Taking this fact into account, we will express the right-hand side of Eq. (1.8c) in terms of g_0 and $g_{w\pm}$ (i.e., $\rho_{w\pm}$) in the past.

Let us suppose that a molecule that left the plate at point $(x_1,\ x_2) = (x_w(s),\ y_2)$ at time s in the past impinges on the plate again at point $(x_w(t),\ x_2)$ at time t. Here, we do not specify the side of the plate. Then, the x_1 and x_2 components of the velocity of the molecule, denoted by $w(t;\ s)$ and $q(t,\ x_2;\ s,\ y_2)$ respectively, are given by

$$w(t;\ s) = \frac{x_w(t) - x_w(s)}{t - s}, \qquad q(t,\ x_2;\ s,\ y_2) = \frac{x_2 - y_2}{t - s}, \tag{1.13}$$

where $0 \le s < t,\ -1/2 \le y_2 \le 1/2$ (Fig. 1.3). By definition, $\lim_{s\to t} w(t;\ s) = dx_w(t)/dt = u_w(t)$.

Let us assume that the trajectory of the plate $x_w(t')$ and the quantity $\rho_{w\pm}(x_2,\ t')$ in the boundary

condition (1.8) are known for all $t' \in [0,\, t)$. The trajectory is depicted schematically in Fig. 1.4, where $x_1 = x_w(t')$ is shown by the solid curve in the $x_1 t$ plane. The trajectory in the figure is exaggerated in order that the description of the solution method is facilitated. The projection on the $x_1 t$ plane of the trajectory of a molecule is a straight line, and the faster the molecule, the milder the slope of the line. Let us consider the molecules impinging on the plate at point $(x_w(t),\, t)$, which is denoted by the symbol "A". An inclined straight line drawn downward from A indicates the trajectory of a molecule impinging on the plate at time t with a velocity (x_1 component) determined by the gradient of the line. More specifically, a line, such as line 5 in Fig. 1.4, located on the right-hand side of the tangential line at point A [line 3 in Fig. 1.4, the gradient of which corresponds to $u_w(t)$] stands for the trajectory of a molecule impinging on the right-hand face of the plate ($x_1 = x_{w+},\, -1/2 \le x_2 \le 1/2$), and a line, such as line 1 in the figure, located on the left-hand side of the tangential line stands for that of a molecule impinging on the left-hand face of the plate ($x_1 = x_{w-},\, -1/2 \le x_2 \le 1/2$).

We first consider the molecules impinging on the right-hand face of the plate. Let us consider the part of the trajectory of the plate (the solid curve in Fig. 1.4) located on the right-hand side of the tangential line at A. There are a finite number of segments of the trajectory that can be seen from point A without being hidden by the trajectory itself, which are numbered from below as 1, 2, ..., n_+ ($n_+ = 2$ in the case of Fig. 1.4). If there is no such segment, we set $n_+ = 0$. Let s_c^+ be the (dimensionless) time corresponding to the lower end of the cth segment, and $s_c^{+\prime}$ that corresponding to its upper end ($c = 1,\, 2,\, ...,\, n_+$). Then, the following relation holds when $n_+ \ge 1$.

$$w(t; s_c^+) = u_w(s_c^+), \quad (c = 1,\, 2,\, ...,\, n_+), \tag{1.14a}$$

$$w(t; s_c^+) < w(t; s_c^{+\prime}) = w(t; s_{c+1}^+), \quad (c = 1,\, 2,\, ...,\, n_+ - 1). \tag{1.14b}$$

Note that the relation (1.14a) does not hold if $s_1^+ = 0$ [i.e., $w(t; 0) \ne u_{w0}$].

We define the corresponding quantities also for the molecules impinging on the left-hand face of the plate. We consider the part of the trajectory of the plate, located on the left-hand side of the tangential line at A, and we number, as 1, 2, ..., n_- from below ($n_- = 2$ in the case of Fig. 1.4), the segments of the trajectory that can be seen from point A without being hidden by the trajectory itself. Let s_c^- be the time corresponding to the lower end of the cth segment, and $s_c^{-\prime}$ that corresponding to its upper end ($c = 1,\, 2,\, ..., n_-$). Then, the following relation holds when $n_- \ge 1$.

$$w(t; s_c^-) = u_w(s_c^-), \quad (c = 1,\, 2,\, ...,\, n_-), \tag{1.15a}$$

$$w(t; s_c^-) > w(t; s_c^{-\prime}) = w(t; s_{c+1}^-), \quad (c = 1,\, 2,\, ...,\, n_- - 1). \tag{1.15b}$$

Note that the relation (1.15a) does not hold if $s_1^- = 0$ [i.e., $w(t; 0) \ne u_{w0}$] (see Fig. 1.4).

With the help of s_c^+ and $s_c^{+\prime}$ defined above, the ρ_{w+} at point A, consisting of the contribution of the initial equilibrium distribution g_0 and that of g_{w+} in the boundary condition on the plate in the past, can be expressed as

$$\begin{aligned}\rho_{w+}(x_2,\, t) = -2\sqrt{\pi}\, \Big\{ & \int_{-\infty}^{\infty} \int_{-\infty}^{u_w(t)} [\zeta_1 - u_w(t)]\, g_0(\zeta_1,\, \zeta_2)\, d\zeta_1 d\zeta_2 \\ & + \sum_{c=1}^{n_+} \int_{w(t; s_c^+)}^{w(t; s_c^{+\prime})} \int_{q(t, x_2;\, s, -1/2)}^{q(t, x_2;\, s, 1/2)} [\zeta_1 - u_w(t)] \\ & \times [g_{w+}(y_2, \zeta_1, \zeta_2, s) - g_0(\zeta_1, \zeta_2)] d\zeta_2 d\zeta_1 \Big\},\end{aligned} \tag{1.16}$$

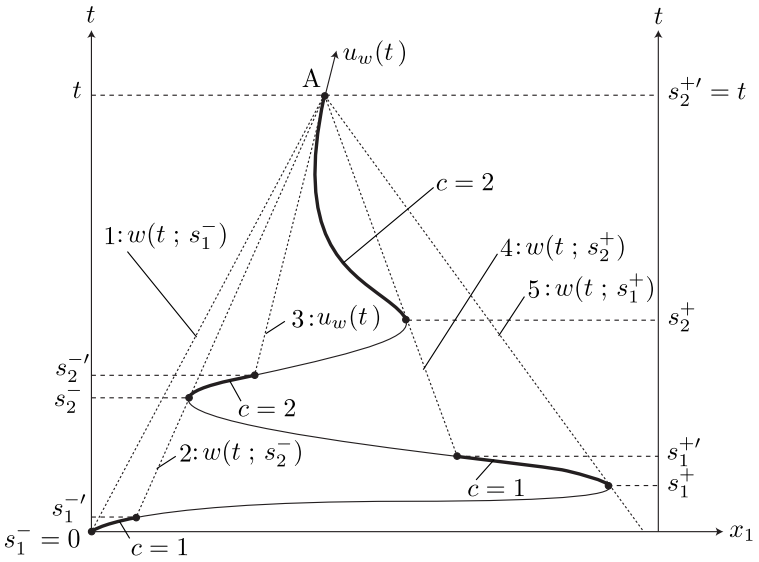

Fig. 1.4 Trajectory of the plate and definitions of the symbols.

where $\sum_{c=1}^{n_+} = 0$ if $n_+ = 0$. In Eq. (1.16), s means $s(\zeta_1, t)$ determined implicitly by the first equation of Eq. (1.13) with $w = \zeta_1$, and y_2 means $y_2(x_2, \zeta_1, \zeta_2, t)$ determined by the second equation of Eq. (1.13) with $q = \zeta_2$ and $s = s(\zeta_1, t)$, i.e.,

$$\frac{x_w(t) - x_w(s(\zeta_1,t))}{t - s(\zeta_1,t)} = \zeta_1, \qquad \frac{x_2 - y_2(x_2,\zeta_1,\zeta_2,t)}{t - s(\zeta_1,t)} = \zeta_2. \tag{1.17}$$

In Eq. (1.16), the first double integral on the right-hand side indicates the contribution if all the impinging molecules at time t come from the initial velocity distribution g_0. However, the impinging molecules whose velocity $(\zeta_1,\ \zeta_2)$ is contained in the ranges of integration in the terms under summation $\sum_{c=1}^{n_+}$ departed from the plate in the past, not from the initial distribution. We call such molecules recolliding molecules and their effect the effect of recollision. The correction caused by the recolliding molecules is made by the terms contained in the summation $\sum_{c=1}^{n_+}$.

Similarly, ρ_{w-} is expressed in the form

$$\begin{aligned}\rho_{w-}(x_2,\ t) = 2\sqrt{\pi}\Big\{ &\int_{-\infty}^{\infty}\int_{u_w(t)}^{\infty} [\zeta_1 - u_w(t)]\, g_0(\zeta_1,\ \zeta_2)\, d\zeta_1 d\zeta_2 \\ &+ \sum_{c=1}^{n_-} \int_{w(t;s_c^-)}^{w(t;s_c^-)} \int_{q(t,x_2;\,s,\,1/2)}^{q(t,x_2;\,s,\,-1/2)} [\zeta_1 - u_w(t)] \\ &\times [g_{w-}(y_2,\zeta_1,\zeta_2,s) - g_0(\zeta_1,\zeta_2)] d\zeta_2 d\zeta_1 \Big\},\end{aligned} \tag{1.18}$$

where $\sum_{c=1}^{n_-} = 0$ if $n_- = 0$, and s and y_2 mean $s(\zeta_1, t)$ and $y_2(x_2, \zeta_1, \zeta_2, t)$ determined by Eq. (1.17).

On the other hand, $G_+(t)$ and $G_-(t)$ in Eq. (1.10b) are recast as

$$G_+ = \frac{1}{M}\int_{-1/2}^{1/2} \Big\{ \int_{-\infty}^{\infty}\int_{-\infty}^{u_w(t)} [\zeta_1 - u_w(t)]^2 g_0(\zeta_1,\zeta_2) d\zeta_1 d\zeta_2$$

$$+\sum_{c=1}^{n_+}\int_{w(t;s_c^{+\prime})}^{w(t;s_c^+)}\int_{q(t,x_2;\,s,1/2)}^{q(t,x_2;\,s,-1/2)}[\zeta_1-u_w(t)]^2 \times[g_{w+}(y_2,\zeta_1,\zeta_2,s)-g_0(\zeta_1,\zeta_2)]d\zeta_2 d\zeta_1 +\int_{-\infty}^{\infty}\int_{u_w(t)}^{\infty}[\zeta_1-u_w(t)]^2 g_{w+}(x_2,\zeta_1,\zeta_2,t)d\zeta_1 d\zeta_2\Big\}dx_2, \tag{1.19}$$

$$G_- = -\frac{1}{M}\int_{-1/2}^{1/2}\Big\{\int_{-\infty}^{\infty}\int_{u_w(t)}^{\infty}[\zeta_1-u_w(t)]^2 g_0(\zeta_1,\zeta_2)d\zeta_1 d\zeta_2 +\sum_{c=1}^{n_-}\int_{w(t;s_c^{-\prime})}^{w(t;s_c^-)}\int_{q(t,x_2;\,s,1/2)}^{q(t,x_2;\,s,-1/2)}[\zeta_1-u_w(t)]^2 \times[g_{w-}(y_2,\zeta_1,\zeta_2,s)-g_0(\zeta_1,\zeta_2)]d\zeta_2 d\zeta_1 +\int_{-\infty}^{\infty}\int_{-\infty}^{u_w(t)}[\zeta_1-u_w(t)]^2 g_{w-}(x_2,\zeta_1,\zeta_2,t)d\zeta_1 d\zeta_2\Big\}dx_2, \tag{1.20}$$

where $\sum_{c=1}^{n_\pm}=0$ if $n_\pm=0$. The last integrals, containing $[\zeta_1-u_w(t)]^2 g_{w\pm}(x_2,\zeta_1,\zeta_2,t)$ on the right-hand sides of Eqs. (1.19) and (1.20), indicate the contribution of the molecules leaving the plate at time t, whereas the other terms the contribution of the impinging molecules. The latter contribution consists, as in Eqs. (1.16) and (1.18), of the contribution of the initial velocity distribution and that of the molecules reflected by the plate in the past (recolliding molecules).

Equations (1.16) and (1.18), with the explicit form of $g_{w\pm}(y_2,\zeta_1,\zeta_2,s)$ in Eq. (1.8b), are the integral equations for ρ_{w+} and ρ_{w-}, respectively, to be solved together with Eqs. (1.9), (1.10a) [with Eqs. (1.19) and (1.20)], and (1.11).

4 Numerical analysis

Let Δt be a small interval in t, $t_{(i)}=i\Delta t$ be the ith time step ($i=0,\ 1,\ 2,\ ...$), and $x_{w(i)}$, $u_{w(i)}$ and $G_{(i)}$ be defined by

$$x_{w(i)}=x_w(t_{(i)}),\qquad u_{w(i)}=u_w(t_{(i)}),\qquad G_{(i)}=G(t_{(i)}). \tag{1.21}$$

Then, we discretize Eq. (1.9) as follows:

$$x_{w(i+1)}=x_{w(i)}+u_{w(i)}\Delta t, \tag{1.22a}$$

$$u_{w(i+1)}=u_{w(i)}+(F-G_{(i+1)})\Delta t, \tag{1.22b}$$

where $x_{w(0)}=0$ and $u_{w(0)}=u_{w0}$.

Suppose that $x_{w(j)}$, $u_{w(j)}$, and $g_{w\pm}$ (or $\rho_{w\pm}$) at $t=t_{(j)}$ are known for $j=0,\ 1,\ 2,\ ...,\ i$. Then, $x_{w(i+1)}$ is obtained from Eq. (1.22a). In order to obtain $u_{w(i+i)}$ from Eq. (1.22b), we need to compute $G_{(i+1)}=G_+(t_{(i+1)})+G_-(t_{(i+1)})$. This can be done by the use of Eqs. (1.19) and (1.20) if we have $g_{w\pm}$ (or $\rho_{w\pm}$) at $t=t_{(i+1)}$. We obtain the latter quantity using the discretized version of Eqs. (1.16) and (1.18), as explained below.

Let us consider Eq. (1.16) at $t=t_{(i+1)}$ and $x_2=x_{2(l)}$, where $x_{2(l)}=l\Delta x_2$ ($l=-N,\ ...,\ 0,\ ...,\ N$; $\Delta x_2=1/2N$). Thus, $(x_{w\pm}(t_{(i+1)}),\ x_{2(l)})$ is a discrete point on the plate at $t=t_{(i+1)}$. We first replace $u_w(t)$ $(=u_{w(i+1)})$, which is unknown, on the right-hand side of Eq. (1.16) with $u_{w(i)}$ that is known. Then, the integrals containing g_0 can be reduced to expressions containing the error function, for which fast algorithms are available (see Sec. 5.4).

The integrals containing g_{w+} are evaluated numerically using the discrete data in the past, i.e., $x_{w(j)}$, $u_{w(j)}$, and $\rho_{w+}(x_{2(l)},\, t_{(j)})$ ($j = 0,\, 1,\, ...,\, i;\; l = -N,\, ...,\, 0,\, ...,\, N$). With the explicit form of g_{w+} [Eq. (1.8b)], the integral containing g_{w+} under the summation in Eq. (1.16), after the replacement $u_{w(i+1)} \to u_{w(i)}$, is written as

$$\frac{1}{\pi}\int_{w(t;s_c^+)}^{w(t;s_c^{+\prime})}\int_{q(t,x_2;\,s,1/2)}^{q(t,x_2;\,s,-1/2)}[\zeta_1 - u_{w(i)}] \times \rho_{w+}(y_2,s)\exp\Big(-[\zeta_1-u_w(s)]^2-\zeta_2^2\Big)d\zeta_2 d\zeta_1, \quad (\text{at}\;\; t=t_{(i+1)},\quad x_2 = x_{2(l)}\,), \tag{1.23}$$

where $s = s(\zeta_1, t)$ and $y_2 = y_2(x_2, \zeta_1, \zeta_2, t)$ defined by Eq. (1.17). Let us suppose that $t_{(j)}$ ($j = \alpha,\, \alpha+1,\, ...,\, \alpha'$) $\in [s_c^+,\, s_c^{+\prime}]$ and $s_c^{+\prime} < t_{(\alpha'+1)}$. Since the trajectory $x_w(t)$ is approximated by straight line segments [Eq. (1.22)], $t_{(\alpha)} = s_c^+$ holds. Thus, Eq. (1.23) can be expressed as follows.

$$\frac{1}{\pi}\Big(\sum_{j=\alpha}^{\alpha'-1}\int_{w(t;\,t_{(j)})}^{w(t;\,t_{(j+1)})} + \int_{w(t;\,t_{(\alpha')})}^{w(t;\,s_c^{+\prime})}\Big)R(x_2,\zeta_1,t)Q(\zeta_1,t)d\zeta_1, \quad (\text{at}\;\; t=t_{(i+1)},\quad x_2 = x_{2(l)}\,), \tag{1.24}$$

where

$$R(x_2,\zeta_1,t) = \sum_{m=-N}^{N-1}\int_{q(t,x_2;\,s(\zeta_1,t),-m\Delta x_2)}^{q(t,x_2;\,s(\zeta_1,t),-(m+1)\Delta x_2)} P(x_2,\zeta_1,\zeta_2,t)\,d\zeta_2, \tag{1.25a}$$

$$Q(\zeta_1,t) = [\zeta_1 - u_{w(i)}]\exp\big(-[\zeta_1-u_w(s(\zeta_1,t))]^2\big), \tag{1.25b}$$

$$P(x_2,\zeta_1,\zeta_2,t) = \rho_{w+}\big(y_2(x_2,\zeta_1,\zeta_2,t),\; s(\zeta_1,t)\big)\exp(-\zeta_2^2). \tag{1.25c}$$

We first approximate $R(x_2, \zeta_1, t)$ and $u_w(s(\zeta_1, t))$ in $Q(\zeta_1, t)$ by linear functions of ζ_1 in each range of integration in Eq. (1.24). Noting that $s(\zeta_1, t) = t_{(j)}$ and thus $u_w(s(\zeta_1, t)) = u_w(t_{(j)}) = u_{w(j)}$ for $\zeta_1 = w(t;\, t_{(j)})$, we let

$$R(x_2,\zeta_1,t) = R(x_2,w(t;\,t_{(j)}),t) + [R(x_2,w(t;\,t_{(j+1)}),t) - R(x_2,w(t;\,t_{(j)}),t)]\,\frac{\zeta_1 - w(t;\,t_{(j)})}{w(t;\,t_{(j+1)}) - w(t;\,t_{(j)})}, \tag{1.26a}$$

$$u_w(s(\zeta_1,t)) = u_{w(j)} + [u_{w(j+1)} - u_{w(j)}]\,\frac{\zeta_1 - w(t;\,t_{(j)})}{w(t;\,t_{(j+1)}) - w(t;\,t_{(j)})}, \tag{1.26b}$$

$$\text{for}\quad w(t;\,t_{(j)}) < \zeta_1 < w(t;\,t_{(j+1)}), \qquad (j = \alpha,\, \alpha+1,\, ...,\, \alpha'),$$

where

$$R(x_2,w(t;\,t_{(j)}),t) = \sum_{m=-N}^{N-1}\int_{q(t,x_2;\,t_{(j)},-m\Delta x_2)}^{q(t,x_2;\,t_{(j)},-(m+1)\Delta x_2)} P(x_2,w(t;\,t_{(j)}),\zeta_2,t)\,d\zeta_2, \tag{1.27a}$$

$$P(x_2,w(t;\,t_{(j)}),\zeta_2,t) = \rho_{w+}\big(y_2(x_2,w(t;\,t_{(j)}),\zeta_2,t),\; t_{(j)}\big)\exp(-\zeta_2^2). \tag{1.27b}$$

Then, we approximate $\rho_{w+}\big(y_2(x_2, w(t;\, t_{(j)}), \zeta_2, t),\; t_{(j)}\big)$ by a linear function of ζ_2 in each range of integration in Eq. (1.27a). That is, letting

$$\hat{q}_{(j,m)}(x_2,t) = q(t,x_2;\,t_{(j)},-m\Delta x_2), \tag{1.28a}$$

and noting that

$$y_2(x_2, w(t;\, t_{(j)}), \hat{q}_{(j,m)}(x_2, t), t) = -m\Delta x_2, \tag{1.29}$$

we put

$$\begin{aligned}\rho_{w+}\big(y_2(x_2, w(t;\, t_{(j)}), \zeta_2, t),\, t_{(j)}\big) &= \rho_{w+}\big(-m\Delta x_2, t_{(j)}\big) \\ &+ \big[\rho_{w+}\big(-(m+1)\Delta x_2, t_{(j)}\big) - \rho_{w+}\big(-m\Delta x_2, t_{(j)}\big)\big]\,\frac{\zeta_2 - \hat{q}_{(j,m)}}{\hat{q}_{(j,m+1)} - \hat{q}_{(j,m)}}, \\ &\text{for}\quad q(t, x_2;\, t_{(j)}, -m\Delta x_2) < \zeta_2 < q(t, x_2;\, t_{(j)}, -(m+1)\Delta x_2), \\ &\qquad (m = -N,\, ...,\, 0,\, ...,\, N-1).\end{aligned} \tag{1.30}$$

With these linear approximations in ζ_1 and ζ_2, the integral in Eq. (1.24) for each j can be expressed in terms of the error function. By summing up the results for j, we can compute Eq. (1.24) or (1.23). Thus, we can compute the integrals containing g_{w+} in Eq. (1.16) at $t = t_{(i+1)}$ and $x_2 = x_{2(l)}$.

Here, we should note the following. If the trajectory $x_1 = x_w(t')$ ($t' \in [0,\, t]$) is convex upward at t in the $x_1 t$ plane as in Fig. 1.4, then $t_{(\alpha')}$ for $c = n_+$ becomes $t_{(\alpha')}\,(= s_c^{+\prime}) = t_{(i+1)}$ (see Fig. (1.4), where $n_+ = 2$). Thus, the integral from $w(t;\, t_{(\alpha')})$ to $w(t;\, s_c^{+\prime})$ in Eq. (1.24) vanishes, and the upper limit of the integral for $j = \alpha' - 1$ in the same equation becomes $\lim_{\epsilon(>0)\to 0} w(t_{(i+1)};\, t_{(i+1)} - \epsilon)$. But in consistency with the linear approximation in Eq. (1.22a), we should assume $x_w(t_{(i+1)} - \epsilon) = x_{w(i)} + u_{w(i)}(\Delta t - \epsilon)$, so that it follows from Eqs. (1.13) and (1.22a) that $\lim_{\epsilon(>0)\to 0} w(t_{(i+1)};\, t_{(i+1)} - \epsilon) = u_{w(i)}$ [we should interpret that $\lim_{\epsilon(>0)\to 0} w(t_{(i+1)};\, t_{(i+1)} + \epsilon) = u_{w(i+1)}$]. On the other hand, the lower limit of the integral in Eq. (1.24) for $j = \alpha' - 1$ becomes $w(t_{(i+1)};\, t_{(i)})$, which reduces to $u_{w(i)}$ by the use of Eqs. (1.13) and (1.22a). Therefore, the integral for $j = \alpha' - 1$ in Eq. (1.24) vanishes. In this way, we get rid of $\rho_{w+}(\,\cdot\,, t_{(i+1)})$, which is unknown, from the numerical computation of the right-hand side of Eq. (1.16) at $t = t_{(i+1)}$ and $x_2 = x_{2(l)}$.

When the velocity of the plate u_w approaches the final velocity $u_{w\infty}$, the trajectory $x_1 = x_w(t)$ becomes almost a straight line. Suppose that it approaches the straight line from below in the $x_1 t$ plane. For $c = n_+$ and for large j, the $w(t_{(i+1)}; t_{(j)})$, appearing as the limits of the range of integrals in Eq. (1.24), becomes almost the same as the plate velocity $u_{w(i)}$. In this case, many integrals under the summation in Eq. (1.24) can be replaced by a single integral over a much wider integration range.

In this way, we obtain $\rho_{w+}(x_{2(l)}, t_{(i+1)})$. Similarly, by the use of Eq. (1.18), we can obtain $\rho_{w-}(x_{2(l)}, t_{(i+1)})$. With these quantities, $G_{\pm}(t_{(i+1)})$ are obtained by the discretized versions of Eqs. (1.19) and (1.20). In this process, the integrals under $\sum_{c=1}^{n_+}$ and $\sum_{c=1}^{n_-}$ in Eqs. (1.19) and (1.20) are computed in the same way as in the case of Eq. (1.16) that have been explained above. The only difference is that $[\zeta_1 - u_w(t)]$ in the integrand in Eq. (1.16) is replaced by $[\zeta_1 - u_w(t)]^2$ in Eqs. (1.19) and (1.20). The additional integration with respect to x_2 in Eqs. (1.19) and (1.20) is carried out by the Simpson rule.

Starting from $i = 0$, we can determine the sequence $\{x_{w(n)},\, u_{w(n)}\}$ ($n = 1,\, 2,\, ...$) by the use of Eq. (1.22), until a necessary time is reached. We regard this sequence as the numerical solution of our initial-boundary value problem given by Eqs. (1.6)–(1.11).

The reduction of the above solution procedure to the spatially one-dimensional problem ($d = 1$), as well as its extension to the three-dimensional problem ($d = 3$), is straightforward.

5 Results of numerical analysis

In the long time limit $t \to \infty$, the velocity of the plate $u_w(t)$ approaches the final velocity $u_{w\infty}$, for which the drag G acting on the plate counterbalances the external force F. In this situation, $\rho_{w\pm}$ is obtained from Eqs. (1.16) and (1.18) by setting $u_w(t) = u_{w\infty}$ and the summation terms (the terms under $\sum_{c=1}^{n_+}$ and $\sum_{c=1}^{n_-}$) to be zero. We can calculate the drag $G = G_+ + G_-$ from Eqs. (1.19) and (1.20) by using the above $\rho_{w\pm}$ and by setting $u_w(t) = u_{w\infty}$ and the summation terms to be zero. In this way, for given u_{w0} and M, the final velocity $u_{w\infty}$ is determined uniquely by F. In what follows, we take $u_{w\infty}$ rather than F as a parameter, so that the dimensionless parameters characterizing the problem are u_{w0}, $u_{w\infty}$, and M [see Eq. (1.4)]. In addition, we set $M = 1$ in this section, in consistency with Ref. [8, 9, 10, 11]. This might look unphysical because M should be quite large for a standard solid. However, for the one-dimensional problem, the result for a given M (and given u_{w0} and $u_{w\infty}$) can be obtained from that for $M = 1$ (and for the same u_{w0} and $u_{w\infty}$) just by changing the scales of t and x_1 by M (see Sec. 5.1). More specifically, u_w and ρ_w at $t = \bar{t}$ for $M = \overline{M}$ are given by u_w and ρ_w at $t = \overline{M}\,\bar{t}$ for $M = 1$. For the two- and three-dimensional problem, since the change of the scale by M also applies to x_2 and x_3, the result for $M = 1$ corresponds to that for $M \neq 1$ for a plate with a size shrunk by M. In the two-dimensional problem, for instance, u_w and ρ_w at $t = \bar{t}$ for $M = \overline{M}$ for the plate with width 1 are given by u_w and ρ_w at $t = \overline{M}\,\bar{t}$ for $M = 1$ for the plate with width $\overline{M}$. In any case, the assumption $M = 1$ does not harm any essential feature of the problem.

In what follows, we will present the results of numerical analysis for the cases of $d = 1$, 2, and 3 separately. In addition, some remarks on the numerical computation, including the discussions on the accuracy, will be given in Sec. 5.4. Our main concern is the time evolution of the velocity $u_w(t)$ of the plate, or more specifically, the decay rate of $u_{w\infty} - u_w(t)$, for long time $t \gg 1$. Moreover, one can infer from the analysis in [11] that the quantities $r_{w+}(t) = G_+(t) - G_{0+}(t)$ and/or $r_{w-}(t) = G_-(t) - G_{0-}(t)$ have similar long-time behavior as $u_{w\infty} - u_w(t)$. Here, $G_{0\pm}(t)$ is the drag acting on the left and right sides of the plate when the effect of recollision is neglected, i.e.,

$$G_{0\pm}(t) = \pm\frac{1}{M}\int_{-1/2}^{1/2}\Big\{\int_{-\infty}^{\infty}\int_{\zeta_1-u_w(t)\lesseqgtr 0}[\zeta_1 - u_w(t)]^2\, g_0(\zeta_1,\,\zeta_2)\, d\zeta_1 d\zeta_2 + \int_{-\infty}^{\infty}\int_{\zeta_1-u_w(t)\gtreqless 0}[\zeta_1 - u_w(t)]^2 \times \pi^{-1}\rho_{w0\pm}(t)\,\exp\big(-[\zeta_1 - u_w(t)]^2 - \zeta_2^2\big)\, d\zeta_1 d\zeta_2\Big\}\, dx_2, \tag{1.31a}$$

$$\rho_{w0\pm}(t) = \mp 2\sqrt{\pi}\int_{-\infty}^{\infty}\int_{\zeta_1-u_w(t)\lesseqgtr 0}[\zeta_1 - u_w(t)]\, g_0(\zeta_1,\,\zeta_2)\, d\zeta_1 d\zeta_2, \tag{1.31b}$$

with the correct solution $u_w(t)$ inserted. We will also show the behavior of these quantities. We also introduce the following auxiliary quantities:

$$\alpha_u = \frac{d\log|u_{w\infty} - u_w(t)|}{d\log t}, \qquad \alpha_{r\pm} = \frac{d\log|r_{w\pm}(t)|}{d\log t}, \tag{1.32}$$

where $\log(\,\cdot\,)$ is the common logarithm [$\log(\,\cdot\,) = \log_{10}(\,\cdot\,)$]. Corresponding to the long-time behavior (1.1) and (1.2), we have $\alpha_u \approx -Ct$ (C is a constant) and $\alpha_u \approx -n$, respectively.

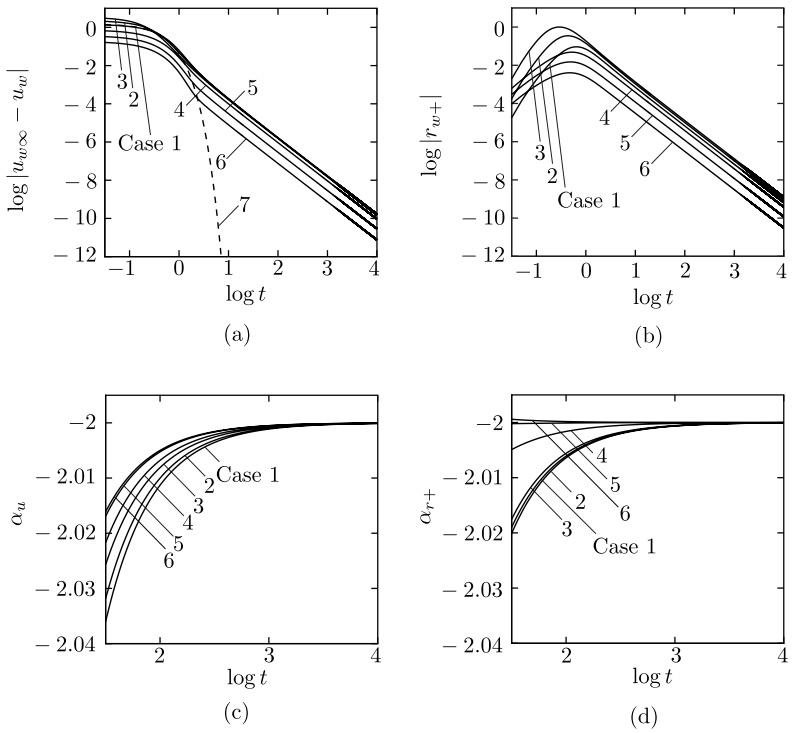

Fig. 1.5 Long-time behavior for $0 \leq u_{w0} < u_{w\infty}$ (one-dimensional problem). (a) $\log|u_{w\infty} - u_w|$ vs $\log t$, (b) $\log|r_{w+}|$ vs $\log t$, (c) α_u vs $\log t$, (d) α_{r+} vs $\log t$.

For large t, $|u_{w\infty} - u_w(t)|$ becomes very small and loses accuracy because of the cancellation error. Even if it keeps the accuracy of, say three figures, it becomes very difficult to obtain accurate values of the derivative α_u by a finite difference applied to local values of $\log|u_{w\infty} - u_w|$. To avoid this difficulty, we calculate α_u and $\alpha_{r\pm}$ in the following manner. Let $\eta = \log t$ and let us consider the interval $m \leq \eta < m + 1$ (m: integer). We divide this interval into 100 small sections with the grid points $\eta_j = m + 0.01j$ ($j = 0, 1, 2, ..., 99$). Then, we associate each grid point $\eta = \eta_j$ with an interval $I_j = [\eta_j - 0.005, \eta_j + 0.005]$. On the basis of the data points of $\log|u_{w\infty} - u_w(t)|$ (or $\log|r_{w\pm}(t)|$) contained in I_j, we obtain a linear function of η using the least square method and regard its gradient as α_u (or $\alpha_{r\pm}$) at $\eta = \eta_j$. Since the standard time step in the present computation is $\Delta t = 0.01$, there are many data points in each I_j for large t.

5.1 One-dimensional problem

We start with the one-dimensional (1D) problem ($d = 1$), where the plate is an infinitely wide plate in the x_2x_3 plane. In this case, the reference length L and the reference time τ_0 should be defined as arbitrary numbers satisfying the relation $\tau_0 = L(2kT_0/m_*)^{-1/2}$. Therefore, we can choose them in such a way that $M = 1$.

We first consider the case of $0 \leq u_{w0} < u_{w\infty}$. Figure 1.5 shows the results for various values of the parameters $(u_{w\infty},\ u_{w0})$: More specifically, $\log|u_{w\infty} - u_w(t)|$ vs $\log t$ is shown in Fig. 1.5(a), $\log|r_{w+}(t)|$ vs $\log t$ in Fig. 1.5(b), α_u vs $\log t$ in Fig. 1.5(c), and α_{r+} vs $\log t$ in Fig. 1.5(d) for the

Table 1.1 Values of $\alpha_u(t)$ at large times (one-dimensional problem).

		$-\alpha_u$					
t	$\log t$	Case 1	Case 2	Case 3	Case 4	Case 5	Case 6
31.62	1.5	2.036055	2.031885	2.025712	2.016124	2.016933	2.016124
100.00	2.0	2.011302	2.010035	2.008112	2.004999	2.005267	2.004999
316.23	2.5	2.003564	2.003168	2.002563	2.001571	2.001657	2.001571
1000.00	3.0	2.001126	2.001001	2.000810	2.000496	2.000523	2.000496
3162.28	3.5	2.000356	2.000316	2.000256	2.000157	2.000165	2.000157
10000.00	4.0	2.000113	2.000100	2.000081	2.000048	2.000052	2.000048

Table 1.2 Value of $\alpha_{r+}(t)$ at large times (one-dimensional problem).

		$-\alpha_{r+}$					
t	$\log t$	Case 1	Case 2	Case 3	Case 4	Case 5	Case 6
31.62	1.5	2.018999	2.020111	2.017545	2.004910	2.000202	1.999407
100.00	2.0	2.006094	2.006417	2.005585	2.001617	2.000090	1.999824
316.23	2.5	2.001935	2.002034	2.001769	2.000518	2.000031	1.999945
1000.00	3.0	2.000613	2.000644	2.000560	2.000164	2.000010	1.999983
3162.28	3.5	2.000194	2.000204	2.000177	2.000052	2.000003	1.999995
10000.00	4.0	2.000061	2.000064	2.000056	2.000016	2.000001	1.999998

following values of the parameters:

Case 1: $(u_{w\infty},\ u_{w0}) = (1.5,\ 0)$,
Case 2: $(u_{w\infty},\ u_{w0}) = (2.35815,\ 0)$,
Case 3: $(u_{w\infty},\ u_{w0}) = (3.55659,\ 0)$,
Case 4: $(u_{w\infty},\ u_{w0}) = (1.5,\ 0.75)$,
Case 5: $(u_{w\infty},\ u_{w0}) = (1.5,\ 1.125)$,
Case 6: $(u_{w\infty},\ u_{w0}) = (1.5,\ 1.3125)$,
Case 7: $(u_{w\infty},\ u_{w0}) = (1.5,\ 0)$ [no recollision].

Case 7 is the same as Case 1, but the effect of recollision is neglected. Some values of α_u and α_{r+} at large times for Case 1 to Case 6 are shown in Tables 1.1 and 1.2. It is seen from Figs. 1.5(a) and 1.5(b) that, in all cases except Case 7, $\log|u_{w\infty} - u_w(t)|$ and $\log|r_{w+}(t)|$ seem to become linearly decreasing functions of $\log t$ for t larger than 10. Figures 1.5(c) and 1.5(d), together with Tables 1.1 and 1.2, demonstrate that the gradients, α_u and α_{r+}, approach -2, which is consistent with Eq. (1.2) with $n = d+1$, obtained theoretically in [11] under the condition (1.3). On the other hand, in Case 7, the approach of $u_w(t)$ to $u_{w\infty}$ is much faster. If $\log|u_{w\infty} - u_w(t)|$ is plotted versus t rather than $\log t$, one can see that the approach is exponential as in Eq. (1.1). The computation shows that in all the cases, $u_{w\infty} - u_w(t)$ is always positive and decreases monotonically (i.e., the velocity of the plate increases monotonically to the final velocity). In other words, the trajectory $x_1 = x_w(t)$ is always convex upward in the $x_1 t$ plane, so that $n_+ = 1$ and $n_- = 0$. Incidentally, r_{w+} is always positive (except Case 7 for which $r_{w+} = 0$), and $r_{w-} = 0$.

We next show some results for the case of $0 \le u_{w\infty} < u_{w0}$. Figure 1.6 contains the results of

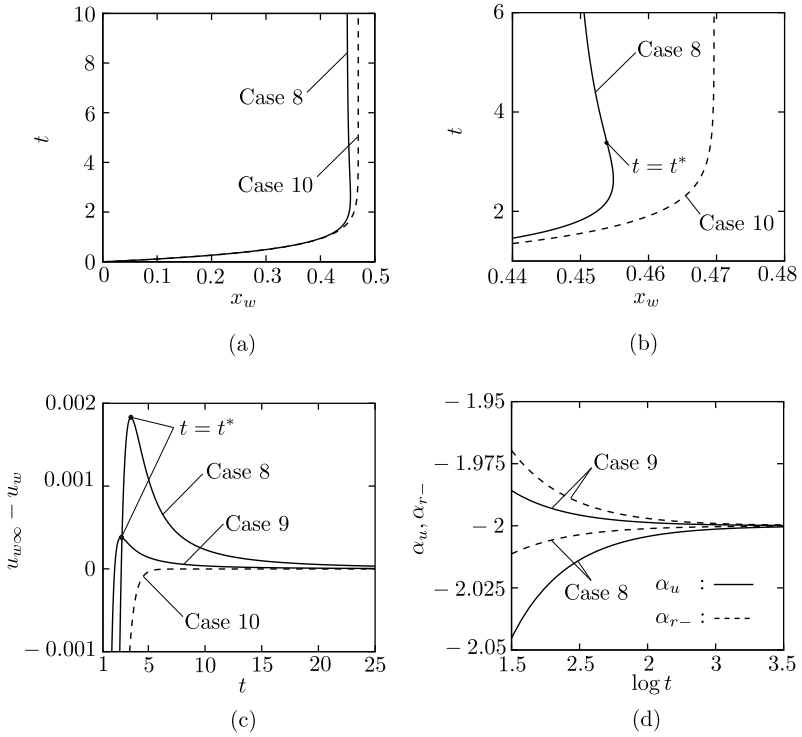

Fig. 1.6 Time evolution for $0 \leq u_{w0} < u_{w\infty}$ (one-dimensional problem). (a) trajectory $x_1 = x_w(t)$, (b) magnified figure of (a), (c) $u_{w\infty} - u_w(t)$ vs t, (d) α_u and α_{r-} vs $\log t$.

the following three cases:

Case 8: $(u_{w\infty},\ u_{w0}) = (0,\ 1)$,
Case 9: $(u_{w\infty},\ u_{w0}) = (1.5,\ 6)$,
Case 10: $(u_{w\infty},\ u_{w0}) = (0,\ 1)$ [no recollision].

Case 10 is the same as Case 8 except that the effect of recollision is neglected. Figure 1.6(a) shows the trajectory $x_1 = x_w(t)$ for Case 8 (solid line) and Case 10 (dashed line) in the $x_1 t$ plane (cf. Fig. 1.4). In these cases the plate stops in the limit $t \to \infty$, since there is no external force. As one can see from the figure, $x_w(t)$ in Case 8 does not increase monotonically as time goes on. That is, the plate once exceeds the final position $x_w(\infty)$ slightly and then comes back to it. In contrast, such an overshoot is not observed in Case 10. Figure 1.6(b) is a magnified figure of Fig. 1.6(a), and Fig. 1.6(c) shows $u_{w\infty} - u_w(t)$ vs t for the three cases. As seen from Fig. 1.6(c), the plate velocity $u_w(t)$, which is larger than $u_{w\infty}$ initially, once becomes slightly smaller than $u_{w\infty}$ and then approaches it from below. In Cases 8 and 9, the peak of $u_{w\infty} - u_w(t)$ ($u_{w\infty} = 0$ in Case 8) is attained, respectively, at $t = t^* = 3.4775$ and 2.6125, at which the curvature of the trajectory $x_1 = x_w(t)$ changes its sign [see Fig. 1.6(b)]. In contrast, the overshoot of $u_{w\infty} - u_w(t)$ is not observed in Case 10 where the effect of recollision is neglected. In Fig. 1.6(d), α_u and α_{r-} vs $\log t$ are shown for Cases 8 and 9. Both of them approach -2. In these cases, $n_+ = 0$ and $n_- = 1$ for $0 < t \leq t^*$, whereas $n_+ = 1$ and $n_- = 1$ for $t^* < t$. In Cases 8 and 9, $|r_{w+}|$ is negligibly small compared with $|r_{w-}|$. The overshoot of the position and the velocity difference $u_{w\infty} - u_w(t)$ have been predicted theoretically in [9] in the case of specular reflection under the condition (1.3).

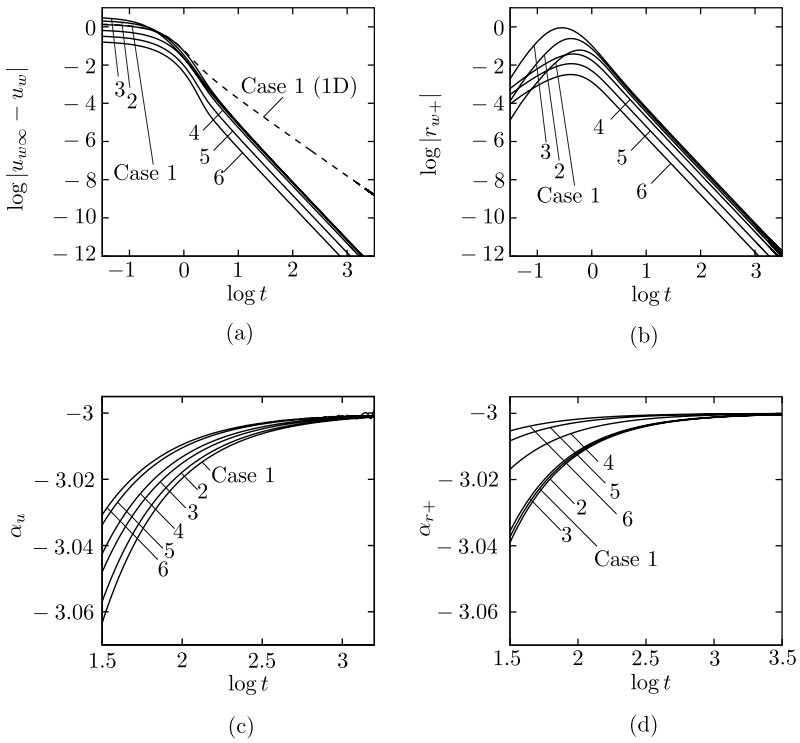

Fig. 1.7 Long-time behavior for $0 \le u_{w0} < u_{w\infty}$ (two-dimensional problem). (a) $\log|u_{w\infty} - u_w|$ vs $\log t$, (b) $\log|r_{w+}|$ vs $\log t$, (c) α_u vs $\log t$, (d) α_{r+} vs $\log t$.

5.2 Two-dimensional problem

Next we consider the two-dimensional (2D) problem ($d = 2$) that is described explicitly in Secs. 2–4. Figure 1.7 shows the results for Case 1, ..., Case 6 (see Sec. 5.1) in the present 2D problem. The figure corresponds to Fig. 1.5 for the 1D problem. Some values of α_u and α_{r+} at large times up to $t = 10^3$ for Case 1 to Case 6 are shown in Tables 1.3 and 1.4. In the figure, "Case 1 (1D)" indicates the result for Case 1 in the 1D problem. As seen from Figs. 1.7(a)–1.7(d) and Tables 1.3 and 1.4, both of $\log|u_{w\infty} - u_w(t)|$ and $\log|r_{w+}(t)|$ seem to become linearly decreasing functions, with gradient -3, of $\log t$ for large t. This is consistent with Eq. (1.2) with $n = d+1$, obtained theoretically under the condition (1.3) in [11]. The results of α_u in Fig. 1.7 (c), in particular those for Cases 5 and 6, show oscillation for $\log t$ larger than about 3 (i.e., $t \gtrsim 1000$). The reason for this phenomenon is the following. The decay of $|u_{w\infty} - u_w(t)|$ is faster in the 2D problem, and its value becomes smaller than 10^{-11} for t larger than 10^3. This is smaller than the same quantity in the 1D problem by three to four orders of magnitude, so that it suffers from cancellation errors at earlier times. Because of this factor, the accuracy of the derivative α_u seems to be lost for $t \gtrsim 1000$ though $|u_{w\infty} - u_w(t)|$ itself is still fairly accurate. The fact that we need to handle the additional x_2 variable in the 2D problem also increases the computational load. For α_{r+} in Fig. 1.7(d), the oscillation is not observed yet. As in the 1D problem, $u_{w\infty} - u_w(t)$ is positive and decreases monotonically, and we have $n_+ = 1$, $n_- = 0$, $r_{w+} > 0$, and $r_{w-} = 0$.

Table 1.3 Values of $\alpha_u(t)$ at large times (two-dimensional problem).

		$-\alpha_u$					
t	$\log t$	Case 1	Case 2	Case 3	Case 4	Case 5	Case 6
31.62	1.5	3.063329	3.056900	3.048011	3.042502	3.033773	3.030717
100.00	2.0	3.019708	3.017834	3.015121	3.013234	3.010493	3.009530
316.23	2.5	3.006203	3.005624	3.004769	3.004169	3.003297	3.003054
1000.00	3.0	3.001961	3.001778	3.001516	3.001286	3.000979	3.000809

Table 1.4 Values of $\alpha_{r+}(t)$ at large times (two-dimensional problem).

		$-\alpha_{r+}$					
t	$\log t$	Case 1	Case 2	Case 3	Case 4	Case 5	Case 6
31.62	1.5	3.037372	3.039033	3.035636	3.016899	3.008318	3.005314
100.00	2.0	3.011864	3.012389	3.011320	3.005424	3.002697	3.001738
316.23	2.5	3.003757	3.003922	3.003585	3.001723	3.000859	3.000555
1000.00	3.0	3.001188	3.001241	3.001134	3.000546	3.000272	3.000176

5.3 Three-dimensional problem

Finally we show some results for the three-dimensional (3D) problem ($d = 3$), where the plate (without thickness) is a rectangle with sides L and H, located initially at $X_1 = 0$, $-L/2 \le X_2 \le L/2$, and $-H/2 \le X_3 \le H/2$ (or $x_1 = 0$, $-1/2 \le x_2 \le 1/2$, and $-H/2L \le x_3 \le H/2L$). Figure 1.8 shows some preliminary results, based on rather coarse grids in x_2 and x_3 (see Sec. 5.4), for Case 1 in Sec. 5.1 for different aspect ratios: $H/L = 1$, 2, 4, 8, and 16. As in Figs. 1.5 and 1.7, the panels (a), (b), (c), and (d) show $\log|u_{w\infty} - u_w(t)|$, $\log|r_w(t)|$, α_u, and α_{r+} vs $\log t$, respectively. The 2D problem ($H/L \to \infty$) is also shown by the dashed line in Figs. 1.8(a) and 1.8(b). It is seen from the figure that α_u and α_{r+} have a tendency to approach -4, which is consistent with the theoretical result, Eq. (1.2) with $n = d+1$, obtained in [11] under the condition (1.3). However, to see it more clearly, we have to obtain a more accurate numerical solution until much larger t, which requires a very heavy computation. Therefore, we carry out such computation only for $H/L = 1$. Figure 1.9 shows α_u and α_{r+} vs $\log t$ obtained by this computation, and Table 1.5 gives the corresponding numerical values at long times. It is seen from Fig. 1.9 and Table 1.5 that α_u and α_{r+} tends to approach -4. In Fig. 1.9(a), an oscillation, similar to that in Fig. 1.7(c), is observed before $\log t = 2.5$ ($t = 316$). As in the 1D and 2D problems, $u_{w\infty} - u_w(t)$ is always positive and decreases monotonically, and we have $n_+ = 1$, $n_- = 0$, $r_{w+} > 0$, and $r_{w-} = 0$ for all the cases in Figs. 1.8 and 1.9

5.4 Remarks on numerical computation

In the present computation, we have restricted ourselves to the case of the diffuse reflection, rather than the specular reflection. The first reason is that the case of the specular reflection is more

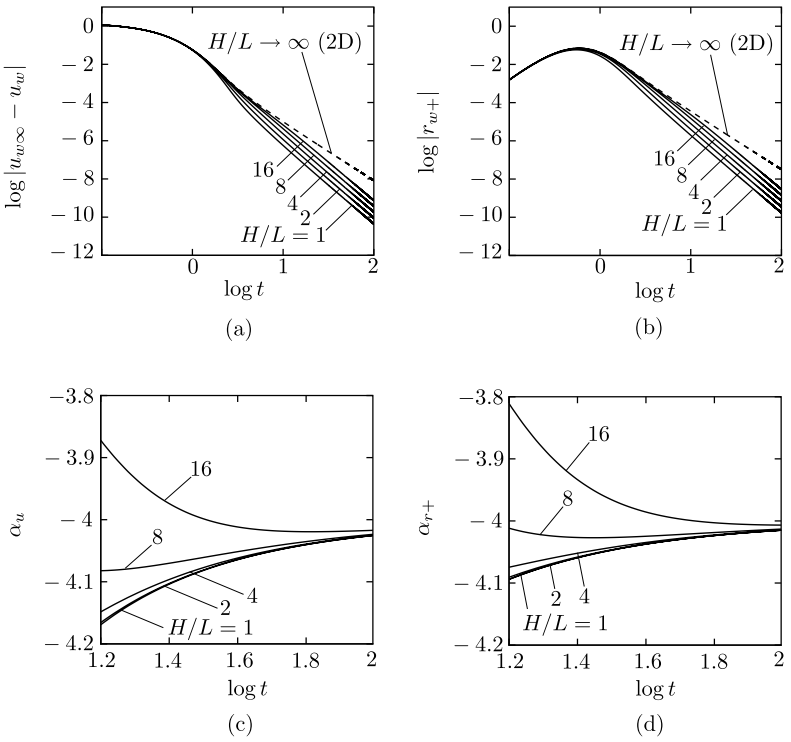

Fig. 1.8 Long-time behavior for Case 1 with various aspect ratios (three-dimensional problem). (a) $\log|u_{w\infty}-u_w|$ vs $\log t$, (b) $\log|r_{w+}|$ vs $\log t$, (c) α_u vs $\log t$, (d) α_{r+} vs $\log t$.

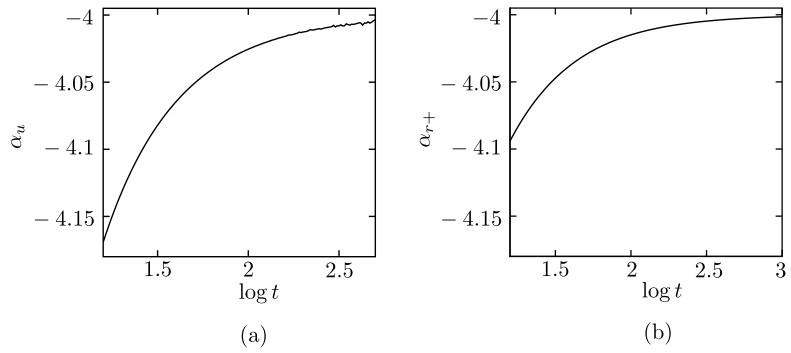

Fig. 1.9 Long-time behavior for Case 1 with $H/L = 1$ (square plate) (three-dimensional problem). (a) α_u vs $\log t$, (b) α_{r+} vs $\log t$.

Table 1.5 Values of $\alpha_u(t)$ and $\alpha_{r+}(t)$ at large times for Case 1 with $H/L = 1$ (square plate) (three-dimensional problem).

t	$\log t$	$-\alpha_u$	$-\alpha_{r+}$
15.85	1.2	4.169216	4.094073
31.62	1.5	4.082090	4.047232
100.00	2.0	4.025448	4.014949
316.23	2.5	4.008078	4.004729
1000.00	3.0	$\cdots$	4.001496

tractable mathematically, so that more rigorous results are available [8, 9, 10]. Therefore, studying the case of the diffuse reflection is more complementary. The second and main reason is that the computation is more difficult for the specular reflection. For the diffuse reflection, we need to store only $x_w(t_{(j)})$, $u_w(t_{(j)})$, and $\rho_{w\pm}(x_{2(l)}, t_{(j)})$ at all $t_{(j)}$, from which we can compute the velocity distribution function of the molecules leaving the plate. In contrast, for the specular reflection, we have to either store the velocity distribution function of the leaving molecules at all $t_{(j)}$ or trace back, at each $t_{(i)}$, the trajectories of the recolliding molecules until the initial distribution is reached. These processes, which are memory-consuming or time-consuming, make a long-time computation formidable.

In the computation for Fig. 1.5 and Fig. 1.6(d) in the 1D problem, we have set $\Delta t = 0.01$.

Table 1.6 Values of $u_\infty - u_w(t)$ for Case 1 with different Δt (one-dimensional problem).

		$u_\infty - u_w(t)$			
t	$\log t$	$\Delta t = 0.1$	$\Delta t = 0.05$	$\Delta t = 0.02$	$\Delta t = 0.01$
1	0.0	4.9198×10^{-2}	5.8070×10^{-2}	6.2945×10^{-2}	6.4500×10^{-2}
5	0.7	5.9364×10^{-4}	7.2347×10^{-4}	8.0840×10^{-4}	8.3765×10^{-4}
10	1.0	1.3178×10^{-4}	1.6031×10^{-4}	1.7893×10^{-4}	1.8533×10^{-4}
50	1.7	4.8105×10^{-6}	5.8464×10^{-6}	6.5211×10^{-6}	6.7529×10^{-6}
100	2.0	1.1892×10^{-6}	1.4451×10^{-6}	1.6118×10^{-6}	1.6690×10^{-6}
500	2.7	4.7144×10^{-8}	5.7286×10^{-8}	6.3889×10^{-8}	6.6157×10^{-8}
1000	3.0	1.1773×10^{-8}	1.4305×10^{-8}	1.5954×10^{-8}	1.6520×10^{-8}
t	$\log t$	$\Delta t = 0.005$	$\Delta t = 0.002$	$\Delta t = 0.001$	
1	0.0	6.5265×10^{-2}	6.5720×10^{-2}	6.5871×10^{-2}	
5	0.7	8.5243×10^{-4}	8.6135×10^{-4}	8.6433×10^{-4}	
10	1.0	1.8856×10^{-4}	1.9051×10^{-4}	1.9116×10^{-4}	
50	1.7	6.8699×10^{-6}	6.9404×10^{-6}	6.9639×10^{-6}	
100	2.0	1.6979×10^{-6}	1.7153×10^{-6}	1.7212×10^{-6}	
500	2.7	6.7301×10^{-8}	6.7996×10^{-8}	6.8221×10^{-8}	
1000	3.0	1.6806×10^{-8}	1.6978×10^{-8}	1.7036×10^{-8}	

Table 1.7 Values of $\alpha_u(t)$ for Case 1 with different Δt (one-dimensional problem).

		$-\alpha_u$			
t	$\log t$	$\Delta t = 0.1$	$\Delta t = 0.05$	$\Delta t = 0.02$	$\Delta t = 0.01$
31.62	1.5	2.032576	2.034489	2.035645	2.036055
100.00	2.0	2.010204	2.010803	2.011176	2.011302
316.23	2.5	2.003216	2.003407	2.003523	2.003564
1000.00	3.0	2.001017	2.001076	2.001113	2.001126
t	$\log t$	$\Delta t = 0.005$	$\Delta t = 0.002$	$\Delta t = 0.001$	
31.62	1.5	2.036443	2.036470	2.036479	
100.00	2.0	2.011416	2.011424	2.011427	
316.23	2.5	2.003599	2.003602	2.003603	
1000.00	3.0	2.001137	2.001138	2.001138	

However, for Figs. 1.6(a)–1.6(c), which require very accurate computation at short times, we used a smaller time step $\Delta t = 0.005$. We have also examined the effect of the time step Δt on the solution for Case 1. Some results are shown in Tables 1.6 and 1.7. Table 1.6 shows the values of $u_\infty - u_w(t)$ at different times for $\Delta t = 0.1$, 0.05, 0.02, 0.01, 0.005, 0.002, and 0.001, and Table 1.7 the values of α_u at large times for the same Δt's. Table 1.6 clearly shows the fact that our finite-difference scheme (1.22) is of first order in Δt. According to the same table, we need $\Delta t = 0.01$ to obtain the accuracy of 3%-relative error and $\Delta t = 0.005$ the accuracy of 1.5%-relative error. However, Table 1.7 shows that the decay exponent α_u is much less sensitive to Δt and that $\Delta t = 0.01$ is sufficient to obtain accurate values of α_u.

The 2D computation for the data in Fig. 1.7 was performed with $\Delta t = 0.01$ and $\Delta x_2 = 1/14$. Here, we have checked the effect of Δx_2 on the solution with finer grid points, $\Delta x_2 = 1/30$ and $1/62$, for Case 1. Some results are shown in Tables 1.8 and 1.9. To be more specific, Table 1.8 shows $u_\infty - u_w(t)$ at different times for $\Delta x_2 = 1/14$, $1/30$ and $1/62$, and Table 1.9 the corresponding values of α_u at some large times. As seen from these tables, $\Delta x_2 = 1/14$ gives a sufficiently accurate result.

Table 1.8 Values of $u_\infty - u_w(t)$ for Case 1 with different Δx_2 (two-dimensional problem).

		$u_\infty - u_w(t)$		
t	$\log t$	$\Delta x_2 = 1/14$	$\Delta x_2 = 1/30$	$\Delta x_2 = 1/62$
1	0.0	5.901367×10^{-2}	5.901460×10^{-2}	5.901480×10^{-2}
5	0.7	9.972841×10^{-5}	9.973847×10^{-5}	9.974059×10^{-5}
10	1.0	9.949553×10^{-6}	9.950565×10^{-6}	9.950777×10^{-6}
50	1.7	6.747572×10^{-8}	6.748259×10^{-8}	6.748403×10^{-8}
100	2.0	8.268005×10^{-9}	8.268846×10^{-9}	8.269023×10^{-9}
500	2.7	6.510437×10^{-11}	6.511103×10^{-11}	6.511236×10^{-11}
1000	3.0	8.121948×10^{-12}	8.122836×10^{-12}	8.123058×10^{-12}

Table 1.9 Values of $\alpha_u(t)$ for Case 1 with different Δx_2 (two-dimensional problem).

		$-\alpha_u$		
t	$\log t$	$\Delta x_2 = 1/14$	$\Delta x_2 = 1/30$	$\Delta x_2 = 1/62$
31.62	1.5	3.063329	3.0633287	3.0633287
100.00	2.0	3.019708	3.0197084	3.0197083
316.23	2.5	3.006202	3.0062039	3.0062040
1000.00	3.0	3.001961	3.0019547	3.0019512

The 3D computation, which is much heavier than 2D computation, prevents from using fine grid points in x_2 and x_3. Therefore, we have used $\Delta t = 0.01$ and $\Delta x_2 = \Delta x_3 = 1/6$ [i.e., $7 \times 7(H/L)$ points on the plate] for the preliminary result shown in Fig. 1.8, where Δx_3 is the grid size in the x_3 direction. However, in order to establish the reliable long time behavior, we carried out a computation with finer grid points in x_2 and x_3 for the square plate ($H/L = 1$, Case 1), i.e., a computation with $\Delta t = 0.01$ and $\Delta x_2 = \Delta x_3 = 1/14$. Figure 1.9 demonstrates such a result. In this connection, we have carried out the same computation with larger time steps, $\Delta t = 0.1$, 0.05, and 0.02, to see the effect of the time step. The results are shown in Tables 1.10 and 1.11.

The computation was carried out with quadruple precision. If we perform the 2D computation with double precision, the strong oscillation exhibited in Fig. 1.7(c) appears at much earlier times.

Table 1.10 Values of $u_\infty - u_w(t)$ for Case 1 ($H/L = 1$) with different Δt (three-dimensional problem).

		$u_\infty - u_w(t)$			
t	$\log t$	$\Delta t = 0.1$	$\Delta t = 0.05$	$\Delta t = 0.02$	$\Delta t = 0.01$
1	0.0	4.1660×10^{-2}	4.9610×10^{-2}	5.3867×10^{-2}	5.5210×10^{-2}
5	0.7	8.7286×10^{-6}	1.0632×10^{-5}	1.1883×10^{-5}	1.2317×10^{-5}
10	1.0	4.1238×10^{-7}	4.9498×10^{-7}	5.4796×10^{-7}	5.6604×10^{-7}
50	1.7	5.3709×10^{-10}	6.4109×10^{-10}	7.0732×10^{-10}	7.2982×10^{-10}
100	2.0	3.2744×10^{-11}	3.9065×10^{-11}	4.3088×10^{-11}	4.4454×10^{-11}
500	2.7	5.1292×10^{-14}	6.1284×10^{-14}	6.7502×10^{-14}	6.9722×10^{-14}
1000	3.0	3.1086×10^{-15}	3.7748×10^{-15}	4.2188×10^{-15}	4.4409×10^{-15}

Table 1.11 Values of $\alpha_u(t)$ for Case 1 ($H/L = 1$) with different Δt (three-dimensional problem).

		$-\alpha_u$			
t	$\log t$	$\Delta t = 0.1$	$\Delta t = 0.05$	$\Delta t = 0.02$	$\Delta t = 0.01$
15.85	1.2	4.149665	4.160207	4.166830	4.169216
31.62	1.5	4.073104	4.077973	4.081020	4.082090
100.00	2.0	4.022755	4.024270	4.025114	4.025448
158.49	2.2	4.013993	4.015431	4.015819	4.015973

It should be mentioned that we have employed a fast algorithm for the error function provided by T. Ooura, available from his home page (http://www.kurims.kyoto-u.ac.jp/~ooura/index.html). The algorithm is for double precision, but we have confirmed that it gives an accuracy of 19 significant figures if it is used in a quadruple-precision computation.

The computation has been carried out on a Personal Computer with CPU: Intel(R) Xeon(R) X5355 2.66GHz $\times$ 8.

6 Concluding remarks

In this paper we have investigated numerically an unsteady motion of a plate in a free-molecular gas at rest caused by a uniform external force and by a drag exerted by the gas molecules, with special interest in the rate of approach to the final steady motion. The study complements the preceding mathematical results [8, 9, 10, 11] on a similar problem (a circular disk or general convex body, rather than a plate, was considered in these works) that showed a slow approach in proportion to some inverse power of time. In these works it was also revealed that the slow approach is caused by the fact that some of the molecules that have been reflected by the body in the past are hit by the body again (recollision). The theoretical results, however, are based on the assumption that the initial velocity of the body is very close to its final velocity. In the present study we were able to provide some numerical evidences, in the case of diffuse reflection studied in [11], that the same result holds when the initial velocity of the body is quite different from the final velocity.

The motion of a body in a free-molecular gas is encountered in connection with the motion of nanoscale aerosol particles, that of satellites or spacecrafts, etc. When the motion is unsteady and undergoes acceleration, deceleration, rotation, etc., one expect that the gas molecules keep a memory from the initial stage because of the absence of intermolecular collisions that destroy the memory, and this fact may affect the motion of the body at later times. The present study, as well as the previous studies [8, 9, 10, 11], clarifies the basic properties of the effect of long memory, which manifests itself in the form of recollision of the molecules. There are some interesting studies of migrations of a convex body in a free-molecular gas caused by various kinds of forces (thermophoresis, shearing phoresis, etc.) [17, 18, 19]. However, in spite of the fact that these migrations contain unsteady motions of the body, the effect of recollision is not taken into account in these works. That is, the distribution function of the gas molecules impinging on the body is assumed to be given by that at infinity at any instant. If the effect of recollision is taken into account, it may change the trajectory of the body significantly. The present study provides a first step to tackle such problems.

References

[1] H. Grad, "Principles of the kinetic theory of gases," in *Handbuch der Physik*, edited by S. Flügge (Springer, Berlin, 1958), Band XII, pp. 205–294.

[2] M. N. Kogan, *Rarefied Gas Dynamics* (Plenum, New York, 1969).

[3] C. Cercignani, *The Boltzmann Equation and Its Applications* (Springer, New York, 1988).

[4] C. Cercignani, R. Illner, and M. Pulvirenti, *The Mathematical Theory of Dilute Gases* (Springer, New York, 1994).

[5] Y. Sone, *Kinetic Theory and Fluid Dynamics* (Birkäuser, Boston, 2002).

[6] Y. Sone, *Molecular Gas Dynamics: Theory, Techniques, and Applications* (Birkäuser, Boston, 2007).

[7] S. A. Schaaf and P. L. Chambré, "Flow of rarefied gases," in *Fundamentals of Gas Dynamics*, edited by H. W. Emmons (Princeton University Press, Princeton, 1958), Chap. H.

[8] S. Caprino, C. Marchioro, and M. Pulvirenti, "Approach to equilibrium in a microscopic model of friction," Commun. Math. Phys. **264**, 167–189 (2006).

[9] S. Caprino, G. Cavallaro, and C. Marchioro, "On a microscopic model of viscous friction," Math. Models Methods Appl. Sci. **17**, 1369–1403 (2007).

[10] G. Cavallaro, "On the motion of a convex body interacting with a perfect gas in the mean-field approximation," Rendiconti di Matematica. Ser. VII **27**, 123–145 (2007).

[11] K. Aoki, G. Cavallaro, C. Marchioro, and M. Pulvirenti, "On the motion of a body in thermal equilibrium immersed in a perfect gas," ESAIM: Math. Model. Num. Anal. **42**, 263–275 (2008).

[12] V. Balakrishnan, I. Bena, C. Van den Broeck, "Velocity correlations, diffusion and stochasticity in a one-dimensional system," Phys. Rev. E **65**, 031102 (2002).

[13] C. Gruber and J. Piasecki, "Stationary motion of the adiabatic piston," Physica A **268**, 412-423 (1999).

[14] J. L. Lebowitz, J. Piasecki, and Y. Sinai, "Scaling dynamics of a massive piston in an ideal gas," in *Hard Ball Systems and the Lorentz Gas*, Encycl. Math. Sci. Vol. 101 (Springer, 2000), pp. 217–227.

[15] P. Buttà, E. Caglioti, and C. Marchioro, "On the long time behavior of infinitely extended systems of particles interacting via Kac potential," J. Stat. Phys. **108**, 317–339 (2002).

[16] P. Buttà, E. Caglioti, and C. Marchioro, "On the motion of a charged particle interacting with an infinitely extended system," Commun. Math. Phys. **223**, 545–569 (2003).

[17] K. I. Borg, "Dynamics of bodies small compared to the mean free path in gases," Doctoral Thesis, Royal Institute of Technology, Stockholm, Sweden (2003).

[18] K. I. Borg and L. H. Söderholm, "Thermophoresis of axially symmetric bodies," in *Rarefied Gas Dynamics*, edited by T. J. Bartel and M. A. Gallis (AIP, Melvile, 2001), pp. 867–874.

[19] K. I. Borg and L. H. Söderholm, "Orbital effects of the Magnus force on a spinning spherical satellite in a rarefied atmosphere," Eur. J. Mech. B/Fluids **27**, 623–631 (2008).

Chapter 2

Relaxation of a free-molecular gas to equilibrium caused by interaction with vessel wall

Abstract A free-molecular gas contained in a static vessel with a uniform temperature is considered. The approach of the velocity distribution function of the gas molecules from a given initial distribution to the uniform equilibrium state at rest is investigated numerically under the diffuse reflection boundary condition. This relaxation is caused by the interaction of gas molecules with the vessel wall. It is shown that, for a spherical vessel, the velocity distribution function approaches the final uniform equilibrium distribution in such a way that their difference decreases in proportion to an inverse power of time. This is slower than the known result for a rarefied gas with molecular collisions.

1 Introduction

Let us consider an ideal rarefied gas contained in a vessel kept at a uniform temperature. In the absence of the gravity, the steady state of the gas is the uniform equilibrium at rest at the same temperature as the vessel. If the equilibrium is perturbed, the state of the gas approaches the equilibrium as time goes on. In the present paper, we are concerned with this approach.

When the mean free path of the gas molecules is not negligibly small compared with the size of the vessel, the continuum fluid dynamics is not valid, and we need to use kinetic theory to describe the above-mentioned approach to the equilibrium. That is, it is described by the Boltzmann equation with its initial and boundary conditions. It is intuitively clear that the velocity distribution function of the gas molecules, starting from a given initial distribution, approaches the global stationary Maxwellian distribution with a density given by the average density of the initial distribution and with the same temperature as the vessel, which we call the *final equilibrium state*. However, the mathematical proof of the statement is relatively recent [1, 2].

In recent years, the rate of approach to the final equilibrium state has been an important subject of mathematical study of the Boltzmann equation [3, 4, 5, 6, 7]. In [6], the following result is reported. Let t_* be the time variable, f_* the velocity distribution function of the gas molecules, and M_{w*} the final equilibrium distribution. If the boundary condition on the vessel wall is the diffuse

reflection, then, it holds that

$$\|f_* - M_{w*}\| = O(t_*^{-\delta}), \quad \text{as} \ \ t_* \to \infty, \tag{2.1}$$

with any positive number δ, where $\|\cdot\|$ is a suitably defined norm. The almost exponential decay estimate (2.1) is also true for some different types of boundary condition on the vessel wall, such as the specular reflection [3, 4] and the periodic condition [3, 4]. However, for these boundary conditions, the temperature of the final equilibrium state is determined by the initial condition. It should be mentioned that the exponential decay has been proven recently [7] for the above-mentioned boundary conditions with stronger mathematical results in the case where the solution is close to the final equilibrium state.

The approach to the equilibrium is caused by the two factors:

(i) The collisions between gas molecules.
(ii) The interaction between the gas molecules and the vessel wall.

The effect of factor (ii) is absent for the specular reflection and the periodic boundary condition.

Now let us consider the case where the gas is so rarefied that the interaction between the gas molecules is neglected. Such a gas is called the free-molecular gas or the Knudsen gas, characterized by infinitely large Knudsen number (the mean free path of the gas molecules divided by the characteristic length of the vessel). In this case, the approach to the final equilibrium state is caused only by the factor (ii). Therefore, the manner of approach may depend on the type of interaction between the gas molecules and the vessel wall, i.e., the boundary condition of the Boltzmann equation, as well as the shape and space dimension of the vessel. In fact, if the initial distribution is not an equilibrium state, the gas never approaches the final equilibrium state for the specular reflection and for the periodic condition, since these conditions have no thermalizing effect. Furthermore, even for the boundary conditions with thermalizing effect, the thermalization takes place nonuniformly in the molecular velocity space. That is, fast molecules hit the boundary and are thermalized quickly, whereas it takes long time for slow molecules to interact with the boundary. The nonuniform convergence of the velocity distribution function in the molecular velocity space may cause a slow approach of the velocity-averaged (or macroscopic) quantities to their equilibrium values.

The approach to the final equilibrium state for a free-molecular gas is a special case of the approach to the stationary solution when the wall temperature is not uniform. The latter problem has been studied by several authors: for instance, [2] for the diffuse reflection condition in the three-dimensional (3D) setting, [8, 9] for a more general boundary condition in the one-dimensional (1D) setting, and [10] for a discrete-velocity model in the 1D setting. In these works, however, the rate of the approach has not been discussed. To the best of the authors' knowledge, the only exception is the recent work by Yu [11], in which an interesting probabilistic method has been developed for the approach to the stationary solution in the 1D setting (in a slab) for the diffuse reflection. He was able to give detailed estimates for the rate of the non-uniform convergence of the velocity distribution function mentioned above. However, the optimal rate of approach to the final equilibrium state, which is comparable to Eq. (2.1), has not been found yet.

In the present study, we investigate this problem (the approach of a free-molecular gas to the final equilibrium state) numerically. We consider a free-molecular gas in a vessel, on the wall of which the gas molecules make the diffuse reflection. We restrict ourselves to a vessel of spherical shape of dimension d, i.e., a sphere for the 3D case ($d = 3$), a circular cylinder for the 2D case ($d = 2$), and a gap between two parallel plates for 1D case ($d = 1$). In addition, we are mainly concerned with the spherically symmetric case with a spatially uniform initial condition. These restrictions make the computation for the 2D and 3D cases feasible. We will investigate the decay rate to the

final equilibrium state of the velocity distribution function as well as the macroscopic quantities. As the result, we will give numerical evidence that the decay is in proportion to an inverse power of time, for instance,

$$\|f_* - M_{w*}\| \approx C^{(d)}/t_*^d, \qquad (d = 1, 2, 3), \tag{2.2}$$

as $t_* \to \infty$, where $\| \cdot \|$ is a kind of L^1 norm in the position and molecular velocity, and $C^{(d)}$ positive constants.

2 Formulation of the problem

2.1 Problem, assumptions, and notations

Consider a rarefied monatomic gas in a vessel kept at a uniform and constant temperature T_{w*}. If the state of the gas is given at the initial time $t_* = 0$, then it evolves in time and approaches the final equilibrium state, i.e., the uniform equilibrium state at rest with temperature T_{w*} and density the average density of the initial state. We investigate the process of approach numerically, with special interest in the asymptotic behavior of the gas, under the following assumptions:

(i) The behavior of the gas is described by the Boltzmann equation.
(ii) The gas is so rarefied that the effect of the collision between the gas molecules is negligible (free-molecular or Knudsen gas).
(iii) The interaction between the gas molecules and the vessel wall is described by the diffuse reflection. That is, the gas molecules leaving the wall are distributed according to the stationary Maxwellian distribution with temperature T_{w*}, and the condition of no net mass flux across the wall is satisfied.
(iv) The vessel is of spherical shape of dimension d with diameter L. To be more specific, the vessel is a sphere of diameter L for $d = 3$, a circular cylinder of diameter L for $d = 2$, and a gap of width L between two parallel plates for $d = 1$.

Let ρ_{0*} be the average density of the gas associated with the initial velocity distribution function. Then, the final equilibrium distribution M_{w*} is given by

$$M_{w*} = \frac{\rho_{0*}}{(2\pi R T_{w*})^{3/2}} \exp\left(-\frac{\xi_i^2}{2RT_{w*}}\right), \tag{2.3}$$

where ξ_i is the molecular velocity, and R is the gas constant per unit mass ($R = k/m$ with k the Boltzmann constant and m the mass of a molecule). We take

$$L, \quad T_{w*}, \quad \rho_{0*}, \quad c_{w*} = (2RT_{w*})^{1/2}, \quad t_{w*} = L/c_{w*}, \tag{2.4}$$

as the reference length, temperature, density, velocity, and time, respectively. Let X_i be the Cartesian coordinates in space, t_* the time variable (as already appeared), $f_*(X_i, \xi_i, t_*)$ the velocity distribution function of the gas molecules, $\rho_*(X_i, t_*)$ the density of the gas, $u_{i*}(X_i, t_*)$ the flow velocity, and $T_*(X_i, t_*)$ the temperature. Then, we introduce the dimensionless counterparts $[x_i, t, \zeta_i, f, M_w, \rho, u_i, T]$ of $[X_i, t_*, \xi_i, f_*(X_i, \xi_i, t_*), M_{w*}, \rho_*(X_i, t_*), u_{i*}(X_i, t_*), T_*(X_i, t_*)]$ by the following relations:

$$\begin{aligned} &X_i = Lx_i, \qquad t_* = t_{w*}t, \qquad \xi_i = c_{w*}\zeta_i, \\ &f_* = (\rho_{0*}/c_{w*}^3)\, f, \qquad M_{w*} = (\rho_{0*}/c_{w*}^3)\, M_w, \\ &\rho_* = \rho_{0*}\rho, \qquad u_{i*} = c_{w*}u_i, \qquad T_* = T_{w*}T. \end{aligned} \tag{2.5}$$

We suppose that the spherical vessel (of dimension d) is given by $S_d(x_i) = 0$ ($d = 1, 2, 3$) in the dimensionless x_i space and its inside (the region of the gas) is described by $\mathcal{D} = \{\, x_i \,|\, S_d(x_i) < 0 \,\}$. That is,

$$S_1(x_1) = x_1^2 - \frac{1}{4}, \tag{2.6a}$$

$$S_2(x_1, x_2) = x_1^2 + x_2^2 - \frac{1}{4}, \tag{2.6b}$$

$$S_3(x_1, x_2, x_3) = x_1^2 + x_2^2 + x_3^2 - \frac{1}{4}. \tag{2.6c}$$

In addition, $n_i(x_i) = -\nabla S_d/|\nabla S_d|$ denotes the unit normal vector to the surface of the vessel pointed to the gas.

2.2 Basic equation

The (dimensionless) Boltzmann equation for a free-molecular gas reads

$$\frac{\partial f}{\partial t} + \zeta_i \frac{\partial f}{\partial x_i} = 0. \tag{2.7}$$

The corresponding initial condition is given by

$$f(x_i,\, \zeta_i,\, 0) = f_0(x_i,\, \zeta_i), \tag{2.8}$$

and the boundary condition (diffuse reflection) on the vessel wall by

$$f(x_i,\, \zeta_i,\, t) = f_w(x_i,\, \zeta_i,\, t), \qquad \text{for } \; S_d(x_i) = 0, \;\; \zeta_i n_i > 0, \tag{2.9a}$$

$$f_w(x_i,\, \zeta_i, t) = \rho_w(x_i,\, t) M_w(\zeta_i), \tag{2.9b}$$

$$\rho_w(x_i,\, t) = -2\pi^{1/2} \int_{\zeta_j n_j < 0} \zeta_j n_j f(x_i,\, \zeta_i,\, t) \mathrm{d}\boldsymbol{\zeta}, \tag{2.9c}$$

where $\mathrm{d}\boldsymbol{\zeta} = \mathrm{d}\zeta_1 \mathrm{d}\zeta_2 \mathrm{d}\zeta_3$, and M_w is the dimensionless reference Maxwellian (i.e., the dimensionless final equilibrium distribution), i.e.,

$$M_w(\zeta_i) = \pi^{-3/2} \exp(-\zeta_i^2). \tag{2.10}$$

Here, we exclude the initial condition f_0 containing the Dirac delta centered at $\zeta_i = 0$.

The density ρ, flow velocity u_i, and temperature T are defined as the following moments of f:

$$\rho(x_i,\, t) = \int_{\text{all } \zeta_i} f \mathrm{d}\boldsymbol{\zeta}, \tag{2.11a}$$

$$u_i(x_i,\, t) = \frac{1}{\rho} \int_{\text{all } \zeta_i} \zeta_i f \mathrm{d}\boldsymbol{\zeta}, \tag{2.11b}$$

$$T(x_i,\, t) = \frac{2}{3\rho} \int_{\text{all } \zeta_i} (\zeta_i - u_i)^2 f \mathrm{d}\boldsymbol{\zeta}. \tag{2.11c}$$

In addition, we introduce the following quantity $W(f|M_w)$:

$$W(f|M_w) = \int_{\text{all } \zeta_i} f \ln(f/M_w) \mathrm{d}\boldsymbol{\zeta}, \tag{2.12}$$

the dimensional counterpart of which is given as

$$W_*(f_*|M_{w*}) = \rho_{0*} W(f|M_w) = \int_{\text{all }\xi_i} f_* \ln(f_*/M_{w*}) \mathrm{d}\boldsymbol{\xi}. \tag{2.13}$$

As time goes on, f approaches the final equilibrium state M_w except at $\zeta_i = 0$. Thus, we have

$$\lim_{t\to\infty} \rho_w(x_i, t) = 1, \tag{2.14}$$

and

$$\begin{aligned} &\lim_{t\to\infty} \rho(x_i,\, t) = 1, \quad \lim_{t\to\infty} u_i(x_i,\, t) = 0, \\ &\lim_{t\to\infty} T(x_i,\, t) = 1, \quad \lim_{t\to\infty} W(f|M_w) = 0. \end{aligned} \tag{2.15}$$

The fact that f approaches the unique limit M_w is intuitively obvious for a vessel of arbitrary shape. However, its mathematical proof is relatively recent [1, 2].

When f_* is a local Maxwellian distribution, W_*/ρ_* reduces to $\ln(\rho_*/\rho_{0*}) - (3/2)\ln(T_*/T_{w*}) + (3/2)(T_*/T_{w*}) + \text{const}$, which can be expressed as $(e_* - T_{w*}s_*)/RT_{w*} + \text{const}$, where e_* and s_* are the internal energy and entropy per unit mass, respectively. Since $F_* = e_* - T_* s_*$ is the Helmholtz free energy per unit mass, W_* is similar to it. In particular, F_* for $\rho_* = \rho_{0*}$ and $T_* = T_{w*}$ corresponds to $W_* = 0$. Let us denote by $\langle W \rangle$ the integral of W over the vessel, i.e.,

$$\langle W \rangle = \int_{\mathcal{D}} W \mathrm{d}\mathbf{x}, \tag{2.16}$$

with $\mathrm{d}\mathbf{x} = \mathrm{d}x_1\mathrm{d}x_2\mathrm{d}x_3$ and with the obvious interpretation in the 1D and 2D cases. Then, we can show, from Eqs. (2.7) and (2.9), that $\mathrm{d}\langle W \rangle/\mathrm{d}t \le 0$ and the equality sign holds if and only if $f = M_w$ (i.e., $W = 0$). This fact is consistent with the Helmholtz potential minimum principle in thermodynamics [12]. Since $\langle W \rangle$ has been used as a measure of deviation of f from M_w (e.g., [3, 4, 5, 6, 8]), we also use it for the same purpose.

3 Preliminaries

In this section, we carry out some preliminary analyses for the numerical analysis. The solution of the Boltzmann equation (2.7) for a free-molecular gas is expressed as

$$f(x_i,\, \zeta_i,\, t) = f(x_i - \zeta_i(t-s),\, \zeta_i,\, s), \qquad (0 \le s \le t). \tag{2.17}$$

That is, the velocity distribution function is constant along the trajectory of a molecule in the $(x_i,\, t)$ space. Therefore, one can obtain information on the velocity distribution function by tracing back the trajectory of the molecules. If we trace back, from a given point $(x_i,\, t)$ in the $(x_i,\, t)$ space, the trajectory of a molecule with a given velocity ζ_i, we either reach the initial time $t = 0$ without hitting the vessel wall or hit the wall at time s in the past. The time s, which is a function of x_i, ζ_i, and t, is obtained as follows.

Since the molecule with velocity ζ_i that left the vessel wall at time s reaches the position x_i at time t, the following relation holds (see Fig. 2.1).

$$x_i' = x_i - (t-s)\zeta_i, \qquad S_d(x_i') = 0. \tag{2.18}$$

Solving these equations for s, we obtain the departure time $s(x_i,\, \zeta_i,\, t)$ together with the departure point x_i'. If $s(x_i,\, \zeta_i,\, t)$ is negative, this means that the trajectory can be traced back to the initial

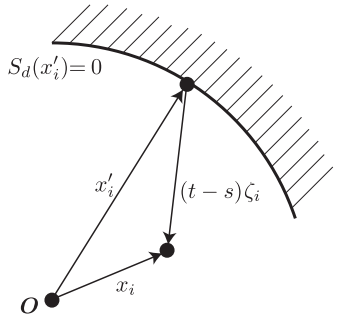

Fig. 2.1 Configuration. The relation between x_i in the gas and x_i' on the vessel wall in terms of the present time t, the time in the past s, and the molecular velocity ζ_i.

time without hitting the vessel wall. In such a case, the value of $f(x_i,\, \zeta_i,\, t)$ is given by the initial condition $f_0(x_i,\, \zeta_i)$.

From these facts, we can write the solution of the initial and boundary value problem (2.7)–(2.9) formally in the following form:

$$f(x_i,\, \zeta_i,\, t) = f_0(x_i - \zeta_i t,\, \zeta_i), \quad \text{for} \quad \zeta_i \in \Omega_0(x_i, t), \tag{2.19a}$$

$$\begin{aligned} f(x_i,\, \zeta_i,\, t) &= f_w(x_i - \zeta_i(t-s),\, \zeta_i, s) \\ &= \rho_w(x_i - \zeta_i(t-s),\, s) M_w(\zeta_i), \quad \text{for} \quad \zeta_i \in \Omega_w(x_i, t), \end{aligned} \tag{2.19b}$$

where Ω_0 is the set of ζ_i for which Eq. (2.18) gives a negative solution s ($s < 0$), and Ω_w the set of ζ_i for which Eq. (2.18) gives a non-negative solution ($0 \le s \le t$); s in Eq. (2.19b) is the non-negative solution $s(x_i,\, \zeta_i,\, t)$ of Eq. (2.18), i.e.,

$$S_d\Big(x_i - \zeta_i[t - s(x_i,\, \zeta_i,\, t)] \Big) = 0, \qquad 0 \le s(x_i,\, \zeta_i,\, t) \le t. \tag{2.20}$$

[See the next paragraph for the explicit form of $s(x_i,\, \zeta_i,\, t)$.] Since f_0 is given, we have the solution if ρ_w is found. Substitution of Eq. (2.19) into Eq. (2.9c) yields the following integral equation for ρ_w:

$$\begin{aligned} \frac{\rho_w(x_i, t)}{2\sqrt{\pi}} = &- \int_{\substack{\zeta_j n_j < 0 \\ \zeta_i \in \Omega_0(x_i,\, t)}} \zeta_j n_j f_0(x_i - \zeta_i t,\, \zeta_i)\, \mathrm{d}\boldsymbol{\zeta} \\ &- \int_{\substack{\zeta_j n_j < 0 \\ \zeta_i \in \Omega_w(x_i,\, t)}} \zeta_j n_j M_w(\zeta_i)\, \rho_w(x_i - \zeta_i(t-s),\, s)\, \mathrm{d}\boldsymbol{\zeta}, \\ &\qquad\qquad \text{for} \quad S_d(x_i) = 0, \end{aligned} \tag{2.21}$$

where s is given by Eq. (2.20). Once ρ_w is obtained from Eq. (2.21), one obtains f from Eq. (2.19) and then the macroscopic quantities from Eqs. (2.11) and (2.12).

Equation (2.18) yields the following explicit expressions for $s(x_i,\, \zeta_i,\, t)$, $\Omega_0(x_i,\, t)$, and

$\Omega_w(x_i,\, t)$ for the three-dimensional case ($d = 3$).

$$s(x_i,\, \zeta_i,\, t) = t - \frac{\zeta_j x_j}{\zeta_k^2} - \frac{1}{\zeta_k^2}\Big[(\zeta_j x_j)^2 - \zeta_k^2\Big(x_l^2 - \frac{1}{4}\Big)\Big]^{1/2}, \tag{2.22a}$$

$$\Omega_0(x_i,\, t) = \Big\{\, (\zeta_1, \zeta_2, \zeta_3) \;\Big|\; \Big(\zeta_j - \frac{x_j}{t}\Big)^2 < \frac{1}{4t^2} \,\Big\}, \tag{2.22b}$$

$$\Omega_w(x_i,\, t) = \Big\{\, (\zeta_1, \zeta_2, \zeta_3) \;\Big|\; \Big(\zeta_j - \frac{x_j}{t}\Big)^2 \geq \frac{1}{4t^2} \,\Big\}. \tag{2.22c}$$

The corresponding results for the two- and one-dimensional cases ($d = 2$ and 1) are omitted here.

4 Numerical analysis

This section is devoted to the description of the numerical solution method. We first describe the solution method for the integral equation (2.21) for ρ_w and then comment on the computation of the macroscopic quantities.

4.1 Integral equation

4.1.1 Special choice of initial condition and simplification

At this point, we consider, as the initial condition, the stationary Maxwellian distribution with temperature T_{0*} and density ρ_{0*}, namely, a uniform equilibrium state at rest with a temperature different from that of the vessel. Thus, its dimensionless form is given by

$$f_0(\zeta_i) = T_0^{-3/2}\, M_w(\zeta_i / T_0^{1/2}), \tag{2.23a}$$

$$T_0 = T_{0*}/T_{w*}, \tag{2.23b}$$

where $M_w(\zeta_i)$ is given in Eq. (2.10). Since the vessel is spherically symmetric, the initial condition (2.23), which is uniform in x_i and isotropic in ζ_i, yields a solution ρ_w of Eq. (2.21) that is independent of the position on the vessel wall:

$$\rho_w = \rho_w(t). \tag{2.24}$$

This fact can be seen from Eq. (2.21) with the explicit form of $s(x_i,\, \zeta_i,\, t)$, $\Omega_0(x_i,\, t)$, and $\Omega_w(x_i,\, t)$. It should be noted that the same is true for any spherically symmetric initial conditions. The case of a non-symmetric initial condition will be investigated for the one-dimensional problem ($d = 1$) in Sec. 6.

In these circumstances, Eq. (2.21) is simplified drastically and is reduced to the following integral equation:

$$\rho_w(t) = M_d(t) + \int_0^t k_d(t-s)\rho_w(s)\mathrm{d}s, \qquad (d = 1,\, 2,\, 3). \tag{2.25}$$

Here

$$\begin{aligned} M_1(t) &= \sqrt{T_0}\Big[1 - \exp\Big(-\frac{1}{T_0 t^2}\Big)\Big], \\ k_1(t) &= \frac{2}{t^3}\exp\Big(-\frac{1}{t^2}\Big), \end{aligned} \tag{2.26}$$

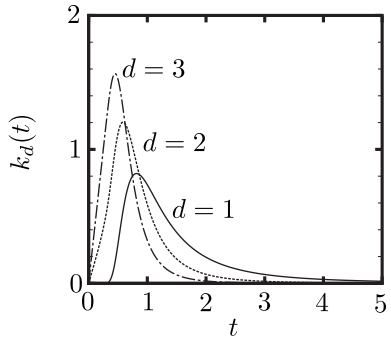

Fig. 2.2 The kernel functions $k_d(t)$ versus t for $d = 1, 2, 3$. The solid line indicates $k_1(t)$, the dotted line $k_2(t)$, and the dot-dashed line $k_3(t)$.

for $d = 1$,

$$\begin{aligned} M_2(t) =& -\frac{\sqrt{\pi}}{t}\bar{I}_1\Big(-\frac{1}{2T_0t^2}\Big), \\ k_2(t) =& \frac{\sqrt{\pi}}{t^4}\Big[\bar{I}_0\Big(-\frac{1}{2t^2}\Big) + (1+t^2)\bar{I}_1\Big(-\frac{1}{2t^2}\Big)\Big], \end{aligned} \tag{2.27}$$

for $d = 2$, and

$$\begin{aligned} M_3(t) =& \sqrt{T_0}\Big[1 - 2T_0t^2 + (1+2T_0t^2)\exp\Big(-\frac{1}{T_0t^2}\Big)\Big], \\ k_3(t) =& 4t - \Big(4t + \frac{4}{t} + \frac{2}{t^3}\Big)\exp\Big(-\frac{1}{t^2}\Big), \end{aligned} \tag{2.28}$$

for $d = 3$; $\bar{I}_n(y)$ in Eq. (2.27) is defined as

$$\bar{I}_n(y) = \exp(y) I_n(y), \tag{2.29a}$$

$$I_n(y) = \frac{1}{\pi}\int_0^\pi \cos(n\theta)\exp(y\cos\theta)\mathrm{d}\theta, \tag{2.29b}$$

where $I_n(y)$ is the modified Bessel function of the first kind of order n. The kernel functions $k_d(t)$ are shown in Fig. 2.2. As is seen easily, $M_d(t)$ and $k_d(t)$ decay as

$$M_d(t) \approx C_M^{(d)}/t^{d+1}, \qquad k_d(t) \approx C_k^{(d)}/t^{d+2}, \tag{2.30}$$

as $t \to \infty$, where $C_M^{(d)}$ and $C_k^{(d)}$ are positive constants. In addition, the following relation holds:

$$\int_0^\infty k_d(t)\mathrm{d}t = 1. \tag{2.31}$$

With the initial condition (2.23) and thus with Eq. (2.24), Eq. (2.19) reduces to a spherically symmetric solution. More specifically, for $d = 1$, $f = f(x_1, \zeta_1, \zeta_t, t)$ with $\zeta_t = (\zeta_2^2 + \zeta_3^2)^{1/2}$, satisfying the condition $f(x_1, \zeta_1, \zeta_t, t) = f(-x_1, -\zeta_1, \zeta_t, t)$ (symmetric with respect to the plane $x_1 = 0$ and without a flow parallel to the vessel wall); for $d = 2$, $f = f(\bar{r}, \zeta_{\bar{r}}, |\zeta_{\bar{\theta}}|, |\zeta_3|, t)$, where $(\bar{r}, \bar{\theta}, x_3)$ is the cylindrical coordinate system with $\bar{r} = (x_1^2 + x_2^2)^{1/2}$, and $\zeta_{\bar{r}}$ and $\zeta_{\bar{\theta}}$ are the $\bar{r}$ and $\bar{\theta}$ components of ζ_i (cylindrically symmetric and without axial or circumferential flow); for

$d = 3$, $f = f(r, \zeta_r, \zeta_\perp, t)$ with $\zeta_\perp = (\zeta_\theta^2 + \zeta_\varphi^2)^{1/2}$, where (r, θ, φ) is the spherical coordinate system with $r = (x_i^2)^{1/2}$, and ζ_r, ζ_θ, and ζ_φ are, respectively, the r, θ, and φ components of ζ_i.

In the practical computation, in order to reduce the cancellation error, we analyze the following equation for $U(t) = \rho_w(t) - 1$, which vanishes as $t \to \infty$ [see Eq. (2.14)], rather than Eq. (2.25):

$$U(t) = M_d(t) - M_d(t)\Big|_{T_0=1} + \int_0^t k_d(t-s)U(s)\mathrm{d}s. \tag{2.32}$$

The main purpose of the present study is to clarify the asymptotic behavior of the solution as $t \to \infty$. This means that we have to obtain very small values of $U = \rho_w - 1$ with extremely high accuracy for a very long time. In general, such a computation is formidable for the three-dimensional case and is very hard even for the two-dimensional case. Thanks to the initial condition (2.23), the integral equation for ρ_w has been reduced to the one-dimensional equation (2.25) or (2.32) irrespective of the dimension of the spherical vessel. This makes the two- and three-dimensional problems tractable, without harming the two and three dimensionality inherent to the problems.

4.1.2 Numerical method

Numerical analysis of the integral equation (2.32) is straightforward and simple. Let Δt be the time step, $t_n = n\Delta t$ ($n = 0, 1, 2, ...$) the discritized time variable, and $U_n = U(t_n)$. If the integral in Eq. (2.32) at $t = t_n$ is approximated in terms of U_m as

$$\sum_{m=0}^{n} A_m U_m, \tag{2.33}$$

where A_m depends on the quadrature for the numerical integration, then Eq. (2.32) at $t = t_n$ gives

$$U_n = \left[M_d(t_n) - M_d(t_n)\Big|_{T_0=1} + \sum_{m=0}^{n-1} A_m U_m \right] (1 - A_n)^{-1}. \tag{2.34}$$

The sequence $\{U_n\}$ ($n = 0, 1, 2, ...$) is determined by Eq. (2.34), and we suppose that U_n thus obtained is an approximate solution of $U(t)$ at $t = t_n$.

For the 1D case ($d = 1$), we use the simple trapezoidal rule to determine A_m in Eq. (2.33). For the 2D and 3D cases ($d = 2, 3$), we approximate $U(t)$ for $t \in [t_{m-1}, t_m]$ by the linear function, i.e., $U(t) \approx (U_m - U_{m-1})(t - t_{m-1})/\Delta t + U_{m-1}$, and carry out the integration for each interval $[t_{m-1}, t_m]$ ($m = 1, 2, ..., n$) analytically to obtain A_m in Eq. (2.33). The explicit form of A_m is omitted here.

4.1.3 Remark

The integral equation (2.25) is the classical renewal equation (see, e.g., [13, 14]), and the asymptotic behavior of the solution as $t \to \infty$ is studied in [13]. If we apply Theorem 4 in [13] to Eq. (2.25), we obtain the following estimate

$$|\rho_w(t) - 1| = o(t^{2-d}), \quad \text{as } t \to \infty, \tag{2.35}$$

for $d = 2$ and 3. The 1D case does not satisfy the condition of the Theorem (the boundedness of the first-order moment of the kernel). In Sec. 5.2.1, our numerical result will show a decay rate (2.46). Although the estimate (2.35) is not sharp at all, the decay rate (2.46) falls in the range expressed by Eq. (2.35). As for the 1D case, Theorem 2 of [11] gives the estimate

$$|\rho_w(t) - 1| = O(t^{-1/10}), \quad \text{as } t \to \infty. \tag{2.36}$$

Our numerical result (2.46) (with $d = 1$) is contained in this range, though it is not sharp enough, too.

4.2 Macroscopic quantities

4.2.1 Preliminaries

Before presenting the method of computation of the macroscopic quantities, we introduce some additional quantities whose numerical results will also be presented in Sec. 5.

We first define the following marginals of f and M_w for the 1D and 2D cases:

$$\widetilde{f}(x_1,\, \zeta_1,\, t) = \int_{-\infty}^{\infty}\int_{-\infty}^{\infty} f \mathrm{d}\zeta_2 \mathrm{d}\zeta_3, \tag{2.37a}$$

$$\widetilde{M}_w = \int_{-\infty}^{\infty}\int_{-\infty}^{\infty} M_w \mathrm{d}\zeta_2 \mathrm{d}\zeta_3 = \frac{1}{\sqrt{\pi}} \exp(-\zeta_1^2), \tag{2.37b}$$

for $d = 1$, and

$$\widetilde{f}^{(2)}(\bar{r},\, \zeta_{\bar{r}},\, |\zeta_{\bar{\theta}}|,\, t) = \int_{-\infty}^{\infty} f \mathrm{d}\zeta_3, \tag{2.38a}$$

$$\widetilde{M}_w^{(2)} = \int_{-\infty}^{\infty} M_w \mathrm{d}\zeta_3 = \frac{1}{\pi} \exp(-\zeta_{\bar{r}}^2 - \zeta_{\bar{\theta}}^2), \tag{2.38b}$$

for $d = 2$. In addition, we introduce the following L^1 norm of $\widetilde{f} - \widetilde{M}_w$ ($d = 1$) in ζ_1, that of $\widetilde{f}^{(2)} - \widetilde{M}_w^{(2)}$ ($d = 2$) in $(\zeta_{\bar{r}},\, \zeta_{\bar{\theta}})$, and that of $f - M_w$ ($d = 3$) in ζ_i, respectively:

$$\|\Delta f\|^{(1)}(|x_1|,\, t) = \int_{-\infty}^{\infty} |\widetilde{f} - \widetilde{M}_w| \mathrm{d}\zeta_1, \tag{2.39a}$$

$$\|\Delta f\|^{(2)}(\bar{r},\, t) = \int_{-\infty}^{\infty}\int_{-\infty}^{\infty} |\widetilde{f}^{(2)} - \widetilde{M}_w^{(2)}| \mathrm{d}\zeta_{\bar{r}} \mathrm{d}\zeta_{\bar{\theta}}, \tag{2.39b}$$

$$\|\Delta f\|^{(3)}(r,\, t) = \int_{-\infty}^{\infty}\int_{-\infty}^{\infty}\int_{-\infty}^{\infty} |f - M_w| \mathrm{d}\zeta_r \mathrm{d}\zeta_\theta \mathrm{d}\zeta_\varphi. \tag{2.39c}$$

We further introduce the average of the above L^1 norms in the vessel, i.e.,

$$\overline{\|\Delta f\|^{(d)}}(t) = 2^d d \int_0^{1/2} \|\Delta f\|^{(d)} \mathrm{d}\mu^{(d)}, \qquad (d = 1,\, 2,\, 3), \tag{2.40}$$

where $\mathrm{d}\mu^{(1)} = \mathrm{d}x_1$, $\mathrm{d}\mu^{(2)} = \bar{r}\mathrm{d}\bar{r}$, and $\mathrm{d}\mu^{(3)} = r^2 \mathrm{d}r$.

4.2.2 Numerical method

Once $\rho_w(t)$ is known, the macroscopic quantities ρ, u_i, T, and W are obtained by using Eq. (2.19) in Eqs. (2.11) and (2.12). In the present spherically symmetric case, we can calculate the macroscopic quantities at the point $(x_1,\, 0,\, 0)$ ($0 \le x_1 \le 1/2$). For instance, in the 3D case, $h(r,\, t)$ for $r = x_1$, any θ, and any φ ($h = \rho$, u_r, T, etc., where u_r is the r component of u_i) is given by $h(x_1,\, 0,\, 0,\, t)$ ($h = \rho$, u_1, T, etc.).

The macroscopic variables at $(x_1,\, 0,\, 0)$ $(0 \le x_1 \le 1/2)$ are expressed as

$$\rho = F_{(0,0,0)} + P_{(0,0,0)}, \quad u_1 = \frac{1}{\rho}\left(F_{(1,0,0)} + P_{(1,0,0)}\right), \tag{2.41a}$$

$$T = \frac{2}{3\rho}\left(F_{(2,0,0)} + F_{(0,2,0)} + F_{(0,0,2)} + P_{(2,0,0)} + P_{(0,2,0)} + P_{(0,0,2)} - \rho u_1^2\right), \tag{2.41b}$$

$$W = Q_{(0,0,0)} - \frac{3}{2}\ln T_0\, F_{(0,0,0)} + \left(1 - \frac{1}{T_0}\right)\left(F_{(2,0,0)} + F_{(0,2,0)} + F_{(0,0,2)}\right), \tag{2.41c}$$

where

$$F_{(n_1,n_2,n_3)} = \int_{\zeta_i \in \Omega_0} \zeta_1^{n_1}\zeta_2^{n_2}\zeta_3^{n_3} f_0(\zeta_i)\mathrm{d}\boldsymbol{\zeta}, \tag{2.42a}$$

$$P_{(n_1,n_2,n_3)} = \int_{\zeta_i \in \Omega_w} \zeta_1^{n_1}\zeta_2^{n_2}\zeta_3^{n_3} M_w(\zeta_i)\, \rho_w(s)\mathrm{d}\boldsymbol{\zeta}, \tag{2.42b}$$

$$Q_{(n_1,n_2,n_3)} = \int_{\zeta_i \in \Omega_w} \zeta_1^{n_1}\zeta_2^{n_2}\zeta_3^{n_3} M_w(\zeta_i)\, \rho_w(s)\, \ln \rho_w(s)\, \mathrm{d}\boldsymbol{\zeta}, \tag{2.42c}$$

Ω_0, Ω_w, and s, which have occurred in Eq. (2.21), are evaluated at $(x_1,\, 0,\, 0)$, and $u_{\bar{r}}$ (the $\bar{r}$ component of u_i) and u_r at $(x_1,\, 0,\, 0)$ are represented by u_1.

The $F_{(n_1,n_2,n_3)}$ contained in Eq. (2.41) can be obtained analytically in the form including the error and exponential functions for $d = 1$ and can be reduced to single integrals including the sinusoidal, error, and exponential functions for $d = 2$ and 3. On the other hand, the $P_{(n_1,n_2,n_3)}$ and $Q_{(n_1,n_2,n_3)}$ can be expressed in the form of convolution:

$$P_{(n_1,n_2,n_3)} = \int_0^t K_d(x_1,\, t-s)\rho_w(s)\mathrm{d}s, \tag{2.43a}$$

$$Q_{(n_1,n_2,n_3)} = \int_0^t K_d(x_1,\, t-s)\rho_w(s)\ln\rho_w(s)\,\mathrm{d}s, \tag{2.43b}$$

where s is the integration variable. The kernel K_d is expressed analytically in terms of the exponential function for $d = 1$ and is expressed in the form of a single integral of a function containing the sinusoidal and exponential functions for $d = 2$ and 3. The explicit form of $F_{(n_1,n_2,n_3)}$ and K_d are omitted for conciseness.

The single integrals in $F_{(n_1,n_2,n_3)}$ and K_d for $d = 2$ and 3 are evaluated numerically using the Gaussian quadrature, and the accuracy with an error less than 10^{-16} is attained. As for the convolutions (2.43), we use the values of ρ_w at $t = t_n$ [$\rho_w(t_n) = U_n + 1$] obtained in Sec. 4.1.2. More specifically, the integral with respect to s is divided into the integrals over small intervals $[s_{m-1},\, s_m]$ ($s_m = m\Delta t$), in each of which $\rho_w(s)$ is approximated by the linear function, and the integration over each interval is performed numerically using the Gaussian quadrature. The linear approximation of ρ_w is legitimate because the change of $\rho_w(s)$ is moderate and the behavior of the integrands $K_d(x_1,\, t-s)\rho_w(s)$ and $K_d(x_1,\, t-s)\rho_w(s)\ln\rho_w(s)$ is dominated by that of $K_d(x_1,\, t-s)$. In fact, as the point $(x_1,\, 0,\, 0)$ approaches the vessel wall ($x_1 \approx 1/2$), the change of K_d becomes steeper. In such a case, we ought to decrease the size of the small intervals $[s_{m-1},\, s_m]$, i.e., the time step Δt. That is, the smallness of the time step Δt in solving Eq. (2.32) is determined not only by the behavior of the solution itself but also by the requirement that the integrals (2.43) be

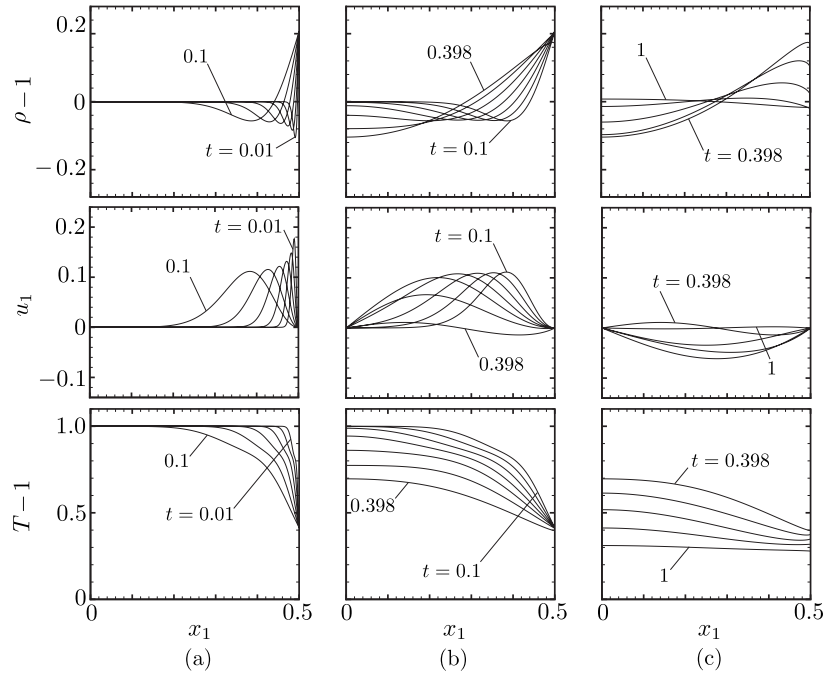

Fig. 2.3 Short-time behavior of ρ, u_1 and T for $T_0 = 2$ in the 1D case ($d = 1$): ρ, u_1, and T vs x_1 for $0 \le x_1 \le 0.5$. (a) $t = 0.01, 0.0158, 0.0251, 0.0398, 0.0631, 0.1$, (b) $t = 0.1, 0.125, 0.158, 0.199, 0.251, 0.398$, (c) $t = 0.398, 0.501, 0.631, 0.794, 1$.

obtained accurately even near the vessel wall. Incidentally, the values of the macroscopic quantities at the vessel wall ($x_1 = 1/2$) are obtained differently.

The computation of the L^1 norms (2.39) is similar to that of ρ. In fact, we can show that there is a time t_c (depending on d and T_0) such that, for $t > t_c$, the $f - M_w$, $\widetilde{f} - \widetilde{M}_w$, or $\widetilde{f}^{(2)} - \widetilde{M}_w^{(2)}$ in Eq. (2.39) does not change the sign. Therefore, if we restrict ourselves to the long-time behavior, the computation is essentially the same as that for ρ.

5 Results of numerical analysis

In this section, we summarize the results obtained by the numerical analysis.

5.1 Short- and intermediate-time behavior

First, we show some results for relatively short time. Figure 2.3 shows the time evolution of the profiles of the density, flow velocity, and temperature for $T_0 = 2$ in the 1D case ($d = 1$): Figs. 2.3(a), 2.3(b), and 2.3(c) are, respectively, for $0.01 \le t \le 0.1$, $0.1 \le t \le 0.398$, and $0.398 \le t \le 1$. Disturbances are created at the boundary and propagate in the interior domain. At $t = 1$, ρ and u_1 are already close to their final values ($\rho = 1$ and $u_1 = 0$), whereas T is still far from it ($T = 1$) though T is almost uniform. In the 2D and 3D cases, the result for which are omitted here, the disturbances are larger, but decay faster.

Figures 2.4 and 2.5 show the time evolution of the marginal velocity distribution function $\widetilde{f}$ defined by Eq. (2.37a) for the 1D case as the function of ζ_1 at the center of the gap $x_1 = 0$ and

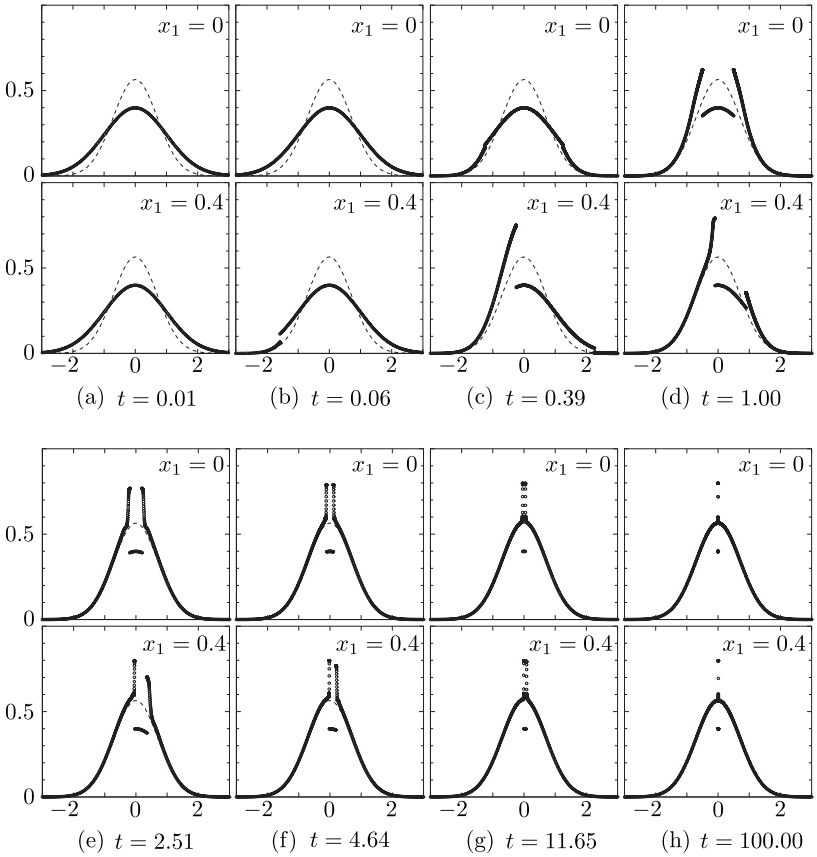

Fig. 2.4 Time evolution of the marginal velocity distribution function $\widetilde{f}(x_1, \zeta_1, t)$ for $T_0 = 2$ in the 1D case ($d = 1$). $\widetilde{f}$ vs ζ_1 is shown at different times. (a) $t = 0.01$, (b) $t = 0.06$, (c) $t = 0.39$, (d) $t = 1.00$, (e) $t = 2.51$, (f) $t = 4.64$, (g) $t = 11.65$, (h) $t = 100.00$. Here, the upper figures show the results at $x_1 = 0$, and the lower at $x_1 = 0.4$; the dashed line indicates $\widetilde{M}_w$.

at $x_1 = 0.4$; the upper figures show $\widetilde{f}$ at $x_1 = 0$, and the lower at $x_1 = 0.4$; Figs. 2.5(a)–(d) are enlarged figures of Figs. 2.4(e)–(h) near $\zeta_1 = 0$; the dashed line indicates the marginal $\widetilde{M}_w$ corresponding to the final steady state M_w [Eq. (2.37b)].

In the 1D case with the initial condition (2.23), the marginal $\widetilde{f}$ is expressed as [cf. Eq. (2.19)]

$$\widetilde{f}(x_1, \zeta_1, t) = \begin{cases} \dfrac{1}{\sqrt{\pi T_0}} \exp\Big(-\dfrac{\zeta_1^2}{T_0}\Big), & \Big(\dfrac{x_1 - 1/2}{t} < \zeta_1 < \dfrac{x_1 + 1/2}{t}\Big), \\ \dfrac{1}{\sqrt{\pi}} \rho_w\Big(t - \dfrac{x_1 - 1/2}{\zeta_1}\Big) \exp(-\zeta_1^2), & \Big(\zeta_1 < \dfrac{x_1 - 1/2}{t}\Big), \\ \dfrac{1}{\sqrt{\pi}} \rho_w\Big(t - \dfrac{x_1 + 1/2}{\zeta_1}\Big) \exp(-\zeta_1^2), & \Big(\dfrac{x_1 + 1/2}{t} < \zeta_1\Big). \end{cases} \tag{2.44}$$

Let us consider the evolution of $\widetilde{f}$ at $x_1 = 0$ (upper figures of Figs. 2.4 and 2.5), referring to Eq. (2.44). The molecules in the range $-1/2t < \zeta_1 < 1/2t$, which shrinks as time goes on, come directly from the initial distribution without interaction with the walls (see Figs. 2.4 and 2.5). At the initial stages, the molecules distributed according to the initial distribution impinge on the walls

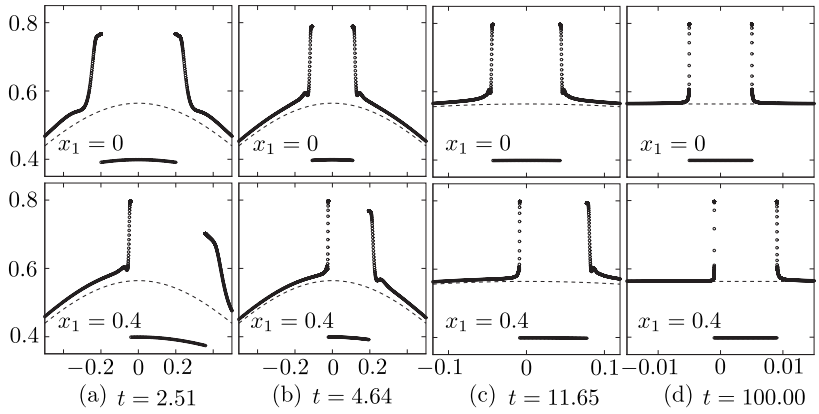

Fig. 2.5 Time evolution of the marginal velocity distribution function $\widetilde{f}(x_1, \zeta_1, t)$ for $T_0 = 2$ in the 1D case ($d = 1$). (a) $t = 2.51$, (b) $t = 4.64$, (c) $t = 11.65$, (d) $t = 100.00$. Figures (a), (b), (c) and (d) are enlarged figure of Fig. 2.4 (e), (f), (g) and (h), respectively. See the caption of Fig. 2.4.

and reflected. Since $T_0 > 1$ in Figs. 2.4 and 2.5, the reflected molecules are cooled down. In other words, less fast molecules (the molecules with large $|\zeta_1|$) and more slow molecules (the molecules with small $|\zeta_1|$) are produced by the reflection. At an early time [Fig. 2.4(c)], only the less-crowded fast molecules among the reflected molecules can reach the point $x_1 = 0$. Therefore, the high-speed tail of the distribution is lowered compared with the initial distribution. At a later time [Fig. 2.4(d)], the more-crowded slow molecules with speed $|\zeta_1| \approx 1/2t$ ($1/2t < |\zeta_1| < 1/2t + \delta$ with δ a small number) reflected at the initial stages reach the point $x_1 = 0$. This results in the significant increase of $\widetilde{f}$ for this speed range. At large times [Figs. 2.4(e)–(h) and Figs. 2.5(a)–(d)], the range of the more-crowded slow molecules with speed $|\zeta_1| \approx 1/2t$ reflected at the initial stages is more and more localized because slightly faster molecules have already experienced many reflections, so that they are well accommodated with the walls (or they have approached the final equilibrium distribution). At $x_1 = 0.4$, the more-crowded slow molecules reflected on the right wall ($x_1 = 1/2$) at the initial stages reach much earlier than the corresponding molecules from the left wall. However, except the non-symmetry, the manner of the deformation of $\widetilde{f}$ is the same.

The localized deviation in $\widetilde{f}$ in the neighborhood of $\zeta_1 = (x_1 \pm 1/2)/t$ exists forever though the range shrinks as time goes on. This is a sort of long-memory effect originating from the very initial stages, which leads to the slow decay of the velocity-averaged quantities, as we will see in Sec. 5.2.

A mathematical description (estimate) corresponding to the deformation of the velocity distribution function explained in the preceding paragraphs is given in [11]. The effect of the slow molecules (or molecules moving parallel to the boundary) also manifests itself in the diffusion limit where the thickness of the channel containing a free-molecular gas is led to zero [15, 16, 17]. It should also be mentioned that a different type of long-memory effect, arising in the unsteady motion of a body in a free-molecular gas, has been investigated in [18, 19, 20, 21].

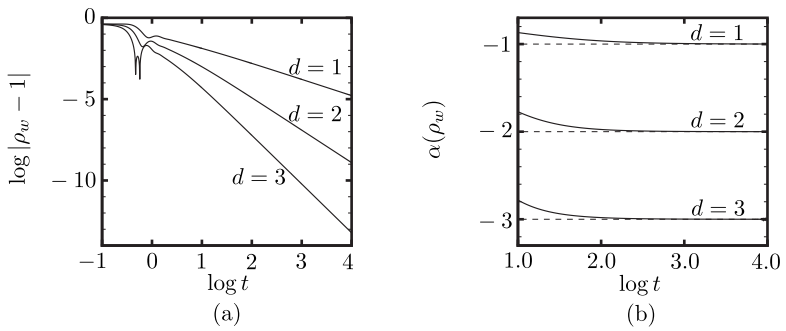

Fig. 2.6 Long-time behavior of ρ_w for different dimension $d = 1$, 2, and 3 for $T_0 = 2$. (a) $\log|\rho_w - 1|$ vs $\log t$, (b) $\alpha(\rho_w)$ vs $\log t$.

5.2 Long-time behavior and approach to equilibrium

Next, we investigate the long-time behavior and the approach to the final equilibrium state, which is the main purpose of the present study. In what follows, the logarithm $\log(\cdot)$ indicates the common logarithm with base 10.

5.2.1 $\rho_w(t)$

The crucial quantity is $\rho_w(t)$, from which the velocity distribution function and thus all the macroscopic quantities can be obtained. The long-time behavior of ρ_w is shown in Fig. 2.6 and Table 2.1 for the 1D, 2D, and 3D cases. Figure 2.6(a) shows $\log|\rho_w - 1|$ versus $\log t$ for $T_0 = 2$, and Fig. 2.6(b) the gradients of the curves in Fig. 2.6(a) versus $\log t$. Here, $\alpha(h)$ for a function $h(t)$ is defined by

$$\alpha(h) = \mathrm{d}\log|h(t) - h_\infty|/\mathrm{d}\log t, \tag{2.45}$$

where h_∞ indicates the equilibrium value of $h(t)$, e.g., $\rho_{w\infty} = 1$. Table 2.1 contains the values of $\alpha(\rho_w)$ at large times for different T_0. From these results, it is highly probable that $\rho_w - 1$ decays as

$$|\rho_w - 1| \approx C_w^{(d)}/t^d, \qquad (d = 1,\ 2,\ 3), \tag{2.46}$$

with positive constants $C_w^{(d)}$.

5.2.2 Global quantities

Next, we show the long time behavior of the global quantities, $\overline{\|\Delta f\|^{(d)}}(t)$ [Eq. (2.40)] and $\overline{W}(t)$, where $\overline{W}(t)$ is defined by Eq. (2.40) with $\|\Delta f\|^{(d)}$ replaced by W [Eq. (2.12)] [note that $W = W(|x_1|,\, t)$ for $d = 1$, $W = W(\bar{r},\, t)$ for $d = 2$, and $W = W(r,\, t)$ for $d = 3$ in the present case]. It should be noted that

$$\overline{W} = \langle W\rangle/\mathrm{vol}(\mathcal{D}), \tag{2.47}$$

where $\langle W\rangle$ is defined in Eq. (2.16), $\mathrm{vol}(\mathcal{D})$ is the volume of the vessel (with the obvious interpretation in the 1D and 2D cases) in the dimensionless x_i space. Figure 2.7(a) shows $\log|\overline{W}|$ versus $\log t$ for $-2 \le \log t \le 3$, and Fig. 2.7(b) the gradients $\alpha(\overline{W})$ [cf. Eq. (2.45)] of the curves in Fig. 2.7(a) versus $\log t$; Fig. 2.7(c) shows $\log\overline{\|\Delta f\|^{(d)}}$ versus $\log t$ for $1 \le \log t \le 3$, and Fig. 2.7(d) the gradients $\alpha(\overline{\|\Delta f\|^{(d)}})$ of the curves in Fig. 2.7(c) versus $\log t$. Table 2.2 shows the

Table 2.1 Values of $\alpha(\rho_w)$ at large times for different T_0.

		$-\alpha(\rho_w)$ $(d=1)$			
t	$\log t$	$T_0=0.5$	$T_0=0.8$	$T_0=1.5$	$T_0=2.0$
316	2.5	0.984778	0.984559	0.984292	0.984178
1000	3.0	0.993830	0.993760	0.993673	0.993637
3162	3.5	0.997626	0.997604	0.997576	0.997565
10000	4.0	0.999117	0.999110	0.999101	0.999098
		$-\alpha(\rho_w)$ $(d=2)$			
t	$\log t$	$T_0=0.5$	$T_0=0.8$	$T_0=1.5$	$T_0=2.0$
316	2.5	1.993056	1.992784	1.992415	1.992248
1000	3.0	1.997843	1.997756	1.997638	1.997585
3162	3.5	1.999323	1.999295	1.999258	1.999241
10000	4.0	⋯	⋯	⋯	1.999760
		$-\alpha(\rho_w)$ $(d=3)$			
t	$\log t$	$T_0=0.5$	$T_0=0.8$	$T_0=1.5$	$T_0=2.0$
316	2.5	2.995022	2.994742	2.994320	2.994118
1000	3.0	2.998437	2.998348	2.998214	2.998150
3162	3.5	⋯	⋯	⋯	2.999415
5011	3.7	⋯	⋯	⋯	2.999626

Table 2.2 Values of $\alpha(\overline{W})$ and $\alpha(\overline{\|\Delta f\|^{(d)}})$ at $t=10000$ for $d=1$ and $t=1000$ for $d=2$ and 3.

			$-\alpha(\overline{W})$			
d	t	$\log t$	$T_0=0.5$	$T_0=0.8$	$T_0=1.5$	$T_0=2.0$
1	10^4	4	1.000028	1.000027	1.000025	1.000025
2	10^3	3	⋯	⋯	⋯	2.000194
3	10^3	3	⋯	⋯	⋯	3.000163
			$-\alpha(\overline{\|\Delta f\|^{(d)}})$			
d	t	$\log t$	$T_0=0.5$	$T_0=0.8$	$T_0=1.5$	$T_0=2.0$
1	10^4	4	0.999999	0.999999	0.999999	0.999999
2	10^3	3	⋯	⋯	⋯	1.999997
3	10^3	3	⋯	⋯	⋯	2.999998

values of the gradients $\alpha(\overline{W})$ and $\alpha(\overline{\|\Delta f\|^{(d)}})$ at $t=10000$ for $T_0=0.5$, 0.8, 1.5, and 2 in the 1D case and those at $t=1000$ for $T_0=2$ in the 2D and 3D cases. As mentioned in the last paragraph in Sec. 2.2, $\langle W\rangle$ and thus $\overline{W}$ decrease monotonically. In order to demonstrate this property, the curves in Fig. 2.7(a) are plotted from a very short time ($t=0.01$). Figure 2.7 and Table 2.2 provide numerical evidence that $\overline{W}$ and $\overline{\|\Delta f\|^{(d)}}$ decay as

$$|\overline{W}| \approx \overline{C}_W^{(d)}/t^d, \qquad \overline{\|\Delta f\|^{(d)}} \approx \overline{C}_\Delta^{(d)}/t^d, \qquad (d=1,\,2,\,3), \tag{2.48}$$

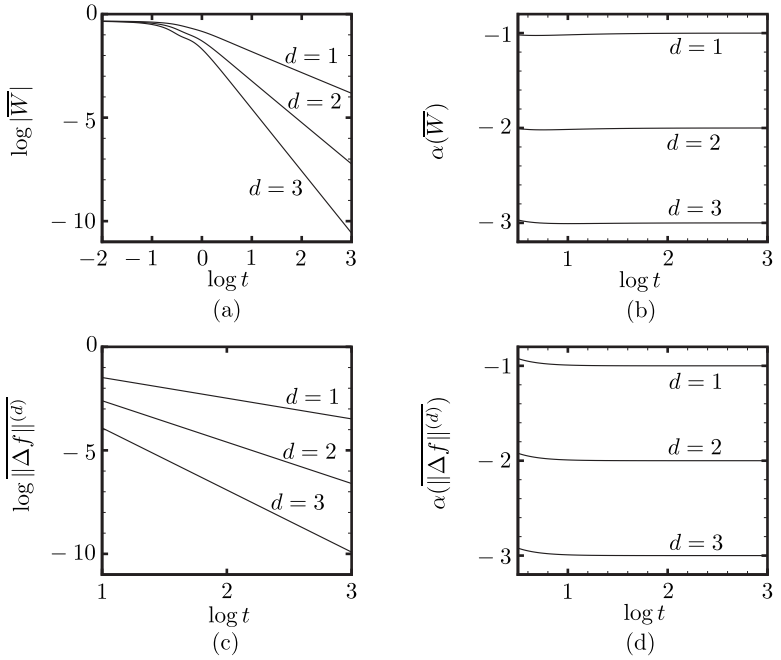

Fig. 2.7 Long-time behavior of $\overline{W}$ and $\overline{\|\Delta f\|^{(d)}}$ for different dimension $d = 1$, 2, and 3 for $T_0 = 2$. (a) $\log|\overline{W}|$ vs $\log t$, (b) $\alpha(\overline{W})$ vs $\log t$, (c) $\log\overline{\|\Delta f\|^{(d)}}$ vs $\log t$, (d) $\alpha(\overline{\|\Delta f\|^{(d)}})$ vs $\log t$.

where $\overline{C}_W^{(d)}$ and $\overline{C}_\Delta^{(d)}$ are positive constants, that is, the evidence that Eq. (2.2) is true.

5.2.3 Local macroscopic quantities

Finally, we show the long-time behavior of the local macroscopic quantities. Figure 2.8(a) shows $\log|W|$ versus $\log t$, Fig. 2.8(b) the gradients $\alpha(W)$ [cf. Eq. (2.45)] of the curves in Fig. 2.8(a) versus $\log t$, Fig. 2.8(c) $\log\|\Delta f\|^{(1)}$ versus $\log t$, and Fig. 2.8(d) the gradients $\alpha(\|\Delta f\|^{(1)})$ [cf. Eq. (2.45)] of the curves in Fig. 2.8(c) versus $\log t$, at several x_1 for $T_0 = 2$ in the 1D case ($d = 1$). In Fig. 2.9, we show the behavior of the density ρ, flow velocity u_1, and temperature T at some points for $T_0 = 2$ in the 1D case ($d = 1$); Fig. 2.9(a) is the plot of $\log|h - h_\infty|$ versus $\log t$, where $h = \rho$, u_1, and T ($\rho_\infty = T_\infty = 1$, $u_{1\infty} = 0$), and Figs. 2.9(b), 2.9(c), and 2.9(d) show the gradients of the curves in 2.9(a) for ρ, u_1, and T, respectively. Figures 2.10(a), 2.10(b), and 2.10(c) are the figures in the 2D case ($d = 2$) and Figs. 2.11(a), 2.11(b), and 2.11(c) those in the 3D case ($d = 3$) corresponding to Figs. 2.8(a), 2.8(c), and 2.9(a) [the curves at less points are shown in Figs. 2.10(a), 2.10(b), 2.11(a), and 2.11(b)]. The curves for the evolution of the gradients corresponding to Figs. 2.8(b), 2.8(d), 2.9(b), 2.9(c), and 2.9(d) are omitted for the 2D and 3D cases. Table 2.3 contains the values of the gradients $\alpha(h)$ with $h = W$, $\|\Delta f\|^{(d)}$, ρ, u_1 ($d = 1$), $u_{\bar{r}}$ ($d = 2$), u_r ($d = 3$), and T at a point ($x_1 = 0.2$ for $d = 1$, $\bar{r} = 0.2$ for $d = 2$, and $r = 0.2$ for $d = 3$) for various T_0 at a long time ($t = 10000$ for $d = 1$, $t = 3162$ for $d = 2$, and $t = 1000$ for $d = 3$). From these results, we observe that $\alpha(W)$, $\alpha(\|\Delta f\|^{(d)})$, and $\alpha(T)$ tend to approach $-d$, whereas $\alpha(\rho)$ tends to approach $-(d + 1)$. In addition, $\alpha(u_1)$, $\alpha(u_{\bar{r}})$, and $\alpha(u_r)$ tend to approach

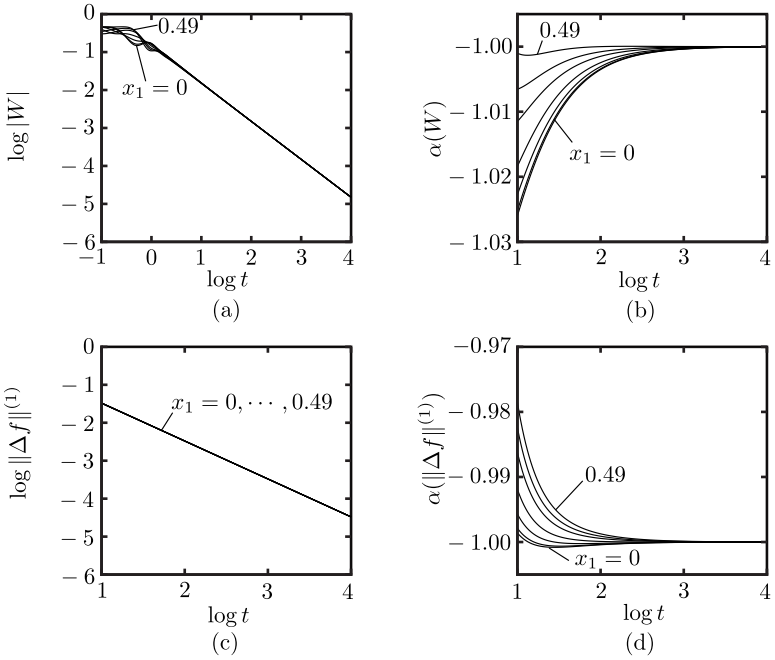

Fig. 2.8 Long-time behavior of W and $\|\Delta f\|^{(1)}$ at $x_1 = 0$, 0.1, 0.2, 0.3, 0.4, 0.45, 0.49 for $T_0 = 2$ ($d = 1$). (a) $\log|W|$ vs $\log t$, (b) $\alpha(W)$ vs $\log t$, (c) $\log\|\Delta f\|^{(d)}$ vs $\log t$, (d) $\alpha(\|\Delta f\|^{(1)})$ vs $\log t$.

-3, -4, and -5, respectively. This gives numerical evidence of the following decay rates:

$$
\begin{aligned}
&|W| \approx C_W^{(d)}/t^d, \quad \|\Delta f\|^{(d)} \approx C_\Delta^{(d)}/t^d, \\
&|T-1| \approx C_T^{(d)}/t^d, \quad |\rho - 1| \approx C_\rho^{(d)}/t^{d+1}, \\
&|u_1| \approx C_1^{(1)}/t^3, \quad |u_{\bar{r}}| \approx C_{\bar{r}}^{(2)}/t^4, \quad |u_r| \approx C_r^{(3)}/t^5,
\end{aligned}
\tag{2.49}
$$

where $C_W^{(d)}$, $C_\Delta^{(d)}$, etc. are positive constants, depending on the position in space. As we can see from Figs. 2.8–2.11, it is likely that $C_W^{(d)}$, $C_\Delta^{(d)}$, and $C_T^{(d)}$ are independent of the position. It should be noted that the density and flow velocity decay faster than the temperature, W, and $\|\Delta f\|^{(d)}$.

5.2.4 Remarks on accuracy of computation

The accuracy of the numerical solution of Eq. (2.32) depends on the quadrature for numerical integration (2.33) and the time step Δt. The results in Table 2.1 are obtained with $\Delta t = 0.002$. In the case of $T_0 = 2$, we have also carried out the computation with different time steps, $\Delta t = 0.01$, 0.005, and 0.001, until $\log t = 4$ ($d = 1$) and 3 ($d = 2,\ 3$). The results for $\alpha(\rho_w)$ based on different time steps agree until the seventh decimal place. Therefore, it is highly probable that all the values in Table 2.1 are accurate until the last decimal place. In the 3D case, the decay of $|\rho_w - 1|$ is faster, and it becomes less than 10^{-13} at $\log t = 4$. Therefore, it becomes very difficult to obtain the gradient of the curve accurately by the method described in the last paragraph in this subsection. In fact, the curve for $d = 3$ in Fig. 2.6(b) exhibits small oscillation for $\log t$ close to 4. This is the reason why $\alpha(\rho_w)$ for $d = 3$ and $T_0 = 2$ is shown only up to $\log t = 3.7$ in Table 2.1.

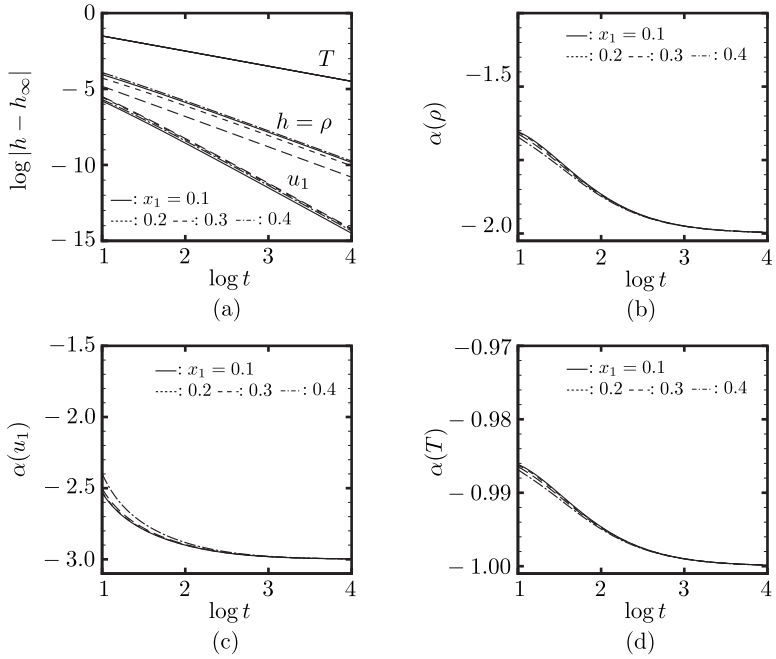

Fig. 2.9 Long-time behavior of ρ, u_1 and T at $x_1 = 0.1, 0.2, 0.3, 0.4$ for $T_0 = 2$ ($d = 1$). (a) $\log|h - h_\infty|$ vs $\log t$, where $h = \rho$, u_1 and T, (b) $\alpha(\rho)$ vs $\log t$, (c) $\alpha(u_1)$ vs $\log t$, (d) $\alpha(T)$ vs $\log t$. Here, the solid line indicates the quantities at $x_1 = 0.1$, the dashed line at $x_1 = 0.2$, the long-dashed line at $x_1 = 0.3$, and the dot-dashed line at $x_1 = 0.4$.

As explained in the second from last paragraph in Sec. 4.2.2, if we want to obtain the macroscopic quantities accurately near the vessel wall, we need a time step smaller than required by Eq. (2.32) itself. The time step $\Delta t = 0.002$, which might appear unnecessarily small, is chosen in such a way that the macroscopic variables at $(0.49,\ 0,\ 0)$ are obtained accurately.

The results in Table 2.3 are also based on $\Delta t = 0.002$. At $\log t = 3$ and at $x_1 = 0$, 0.2, and 0.4 ($x_2 = x_3 = 0$), the gradients $\alpha(W)$, $\alpha(\|\Delta f\|^{(d)})$, and $\alpha(T)$ with $\Delta t = 0.002$ agree with those with $\Delta t = 0.001$ up to the fifth decimal place for $d = 1$, 2, and 3. But, the agreement is one or two less decimal places for $\alpha(\rho)$ and $\alpha(u)$ ($u = u_1$, $u_{\bar{r}}$, or u_r).

The values of $\alpha(\overline{W})$ and $\alpha(\overline{\|\Delta f\|^{(d)}})$ in Table 2.2 are also based on the data obtained with $\Delta t = 0.002$. Here, the integration with respect to the space variable [cf. (2.40)] is carried out analytically for $d = 1$ and numerically for $d = 2$ and 3. In the latter, Simpson's rule with a uniform interval Δx ($x = \bar{r}$ or r) is used. The data for $d = 2$ and 3 in Table 2.2 are obtained with $\Delta x = 0.005$. However, the results obtained with $\Delta x = 0.025$ and 0.01 do not show any difference from the values in Table 2.2.

The gradients $\alpha(\rho_w)$ [cf. Eq. (2.45)] shown in Fig. 2.6(b) and Table 2.1 are evaluated by the simple linear approximation, i.e., $\alpha(\rho_w)(t_n) = (\log|U_n| - \log|U_{n-1}|)/(\log t_n - \log t_{n-1})$. On the other hand, once $\rho_w(t)$ is obtained, we can obtain the macroscopic quantities at any point in space and at any t. We evaluate the macroscopic quantities at discrete t's, say $t = \bar{t}_m$, which are distributed uniformly in $\log t$ (50 points in the interval $n < \log t \le n + 1$ with n being integer). Then, the gradient $\alpha(h)$ is obtained by the simple linear approximation.

The computation was carried out with quadruple precision. If we perform the computation

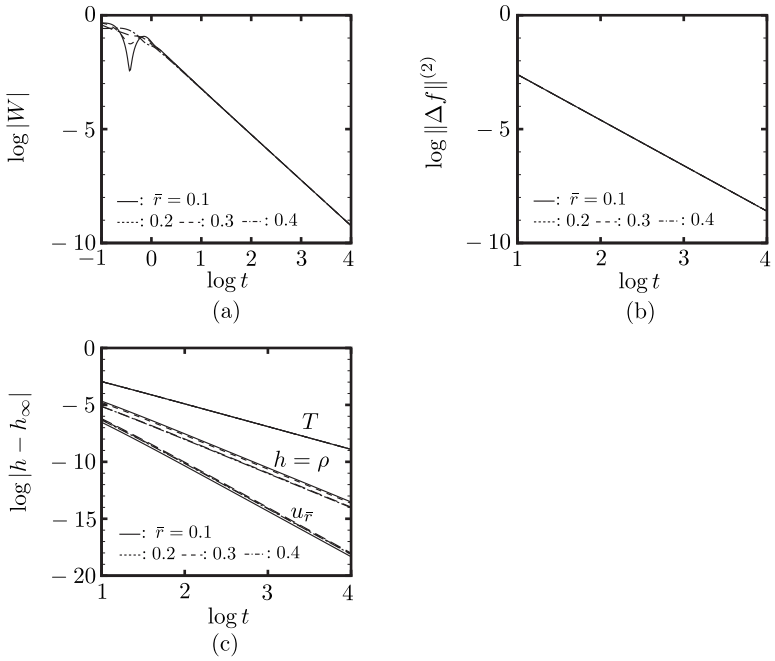

Fig. 2.10 Long-time behavior of W, $\|\Delta f\|^{(2)}$, ρ, $u_{\bar{r}}$, and T at $\bar{r} = 0.1$, 0.2, 0.3, 0.4 for $T_0 = 2$ ($d = 2$). (a) $\log|W|$ vs $\log t$. (b) $\log\|\Delta f\|^{(2)}$ vs $\log t$. (c) $\log|h - h_\infty|$ vs $\log t$, where $h = \rho$, $u_{\bar{r}}$, and T. Here, the solid line indicates the quantities at $\bar{r} = 0.1$, the dashed line at $\bar{r} = 0.2$, the long-dashed line at $\bar{r} = 0.3$, and the dot-dashed line at $\bar{r} = 0.4$.

with double precision, we are not able to show the convergence of the gradients $\alpha(\rho_w)$, $\alpha(W)$, $\alpha(\rho)$, etc. It should be mentioned that we have employed fast algorithms for the error and Bessel functions provided by T. Ooura, available from his home page (http://www.kurims.kyoto-u.ac.jp/~ooura/index.html). The algorithms are for double precision, but we have confirmed that they give an accuracy of 19 significant figures if they are used in a quadruple-precision computation.

The computation has been carried out on a PC cluster with CPU: Intel(R) Core 2 Extreme QX9650 3.0GHz(4CPU)×8.

6 Non-symmetric initial condition (one-dimensional case)

In Secs. 4 and 5, we investigated the time evolution of the solution with the initial condition (2.23), i.e., a uniform equilibrium state at rest with a temperature different from the temperature of the vessel wall. In this section, restricting ourselves to the 1D case, we repeat the same computation with a non-symmetric initial condition. Our initial condition is

$$f_0(x_1,\zeta_i) = \frac{\rho^{\rm in}(x_1)}{[\pi T^{\rm in}(x_1)]^{3/2}} \exp\Big(-\frac{[\zeta_1 - u_1^{\rm in}(x_1)]^2 + \zeta_2^2 + \zeta_3^2}{T^{\rm in}(x_1)}\Big), \tag{2.50}$$

where

$$\rho^{\rm in}(x_1) = 1 + a_\rho \cos(2\pi m_\rho x_1 + b_\rho), \tag{2.51a}$$

$$u_1^{\rm in}(x_1) = a_u \cos(2\pi m_u x_1 + b_u), \tag{2.51b}$$

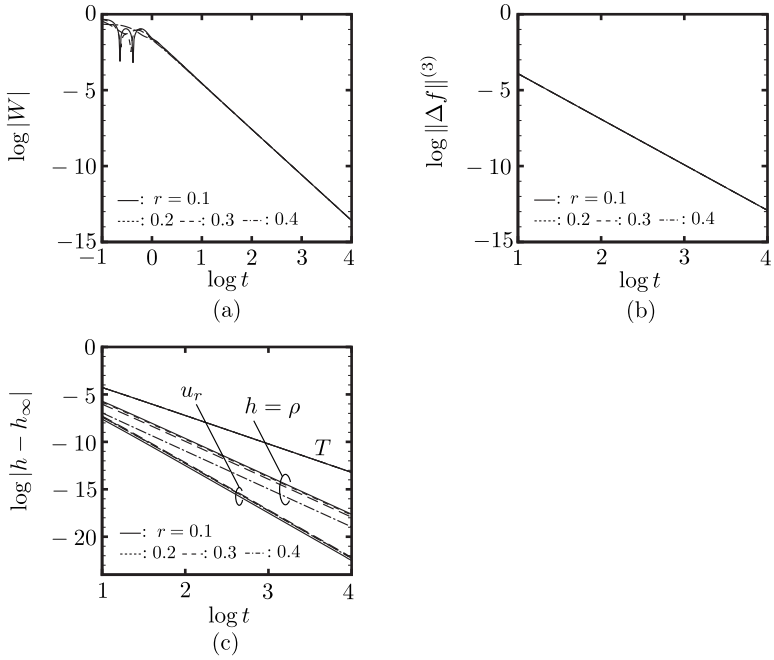

Fig. 2.11 Long-time behavior of W, $\|\Delta f\|^{(3)}$, ρ, u_r, and T at $r = 0.1$, 0.2, 0.3, 0.4 for $T_0 = 2$ ($d = 3$). (a) $\log|W|$ vs $\log t$. (b) $\log\|\Delta f\|^{(3)}$ vs $\log t$. (c) $\log|h - h_\infty|$ vs $\log t$, where $h = \rho$, u_r, and T. Here, the solid line indicates the quantities at $r = 0.1$, the dashed line at $r = 0.2$, the long-dashed line at $r = 0.3$, and the dot-dashed line at $r = 0.4$.

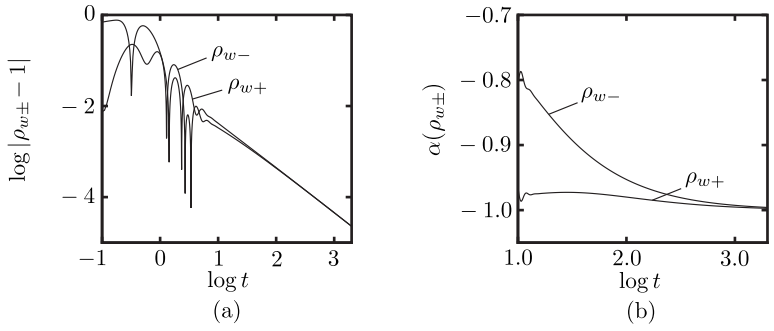

Fig. 2.12 Long-time behavior of $\rho_{w-}(t)$ and $\rho_{w+}(t)$ for the non-symmetric initial condition ($d = 1$). (a) $\log|\rho_{w\pm} - 1|$ vs $\log t$. (b) $\alpha(\rho_{w\pm})$ vs $\log t$.

$$T^{\rm in}(x_1) = 1 + a_T \cos(2\pi m_T x_1 + b_T). \tag{2.51c}$$

Equation (2.50) is the local Maxwellian distribution with density $\rho^{\rm in}(x_1)\rho_{0*}$, flow velocity $(u_1^{\rm in}(x_1)\, c_{w*},\ 0,\ 0)$, and temperature $T^{\rm in}(x_1)T_{w*}$. In this case, Eq. (2.21) yields a coupled integral equation of renewal type for $\rho_{w-}(t) \equiv \rho_w(\text{at}\ \ x_1 = -1/2)$ and $\rho_{w+}(t) \equiv \rho_w(\text{at}\ \ x_1 = 1/2)$ in place of Eq. (2.25) with Eq. (2.26). We have carried out computations for different values of the parameters a_ρ, m_ρ, etc. Here, we give only the result for the long-time behavior of one case: $(a_\rho,\, b_\rho,\, m_\rho) = (0.5, 1, 1)$, $(a_u,\, b_u,\, m_u) = (0.5, 1, 1)$, $(a_T,\, b_T,\, m_T) = (0.5, 2, 1.5)$.

Table 2.3 Values of $\alpha(h)$ at large t for different T_0 ($d = 1, 2, 3$).

	$-\alpha(h)$ $(d=1,\ x_1=0.2,\ t=10000)$			
h	$T_0 = 0.5$	$T_0 = 0.8$	$T_0 = 1.5$	$T_0 = 2.0$
W	1.000040	1.000064	1.000006	1.000014
$\|\Delta f\|^{(1)}$	0.999994	0.999994	0.999994	0.999994
ρ	1.998055	1.997862	1.998454	1.998414
u_1	2.997527	2.998085	2.996390	2.996803
T	0.999811	0.999824	0.999844	0.999854
	$-\alpha(h)$ $(d=2,\ \bar{r}=0.2,\ t=3162)$			
h	$T_0 = 0.5$	$T_0 = 0.8$	$T_0 = 1.5$	$T_0 = 2.0$
W	1.999919	1.999677	2.000857	2.000198
$\|\Delta f\|^{(2)}$	2.000031	2.000031	2.000030	2.000030
ρ	2.998974	2.999090	2.998970	2.998987
$u_{\bar{r}}$	3.998626	3.998776	3.998653	3.998672
T	1.999657	1.999657	1.999638	1.999626
	$-\alpha(h)$ $(d=3,\ r=0.2,\ t=1000)$			
h	$T_0 = 0.5$	$T_0 = 0.8$	$T_0 = 1.5$	$T_0 = 2.0$
W	2.999493	2.998174	3.001350	3.000942
$\|\Delta f\|^{(3)}$	3.000166	3.000166	3.000166	3.000167
ρ	3.998371	3.998527	3.998369	3.998338
u_r	4.997977	4.998174	4.998001	4.997962
T	2.999152	2.999049	2.998942	2.998874

We show the long-time behavior of $\rho_{w\pm}(t)$ in Fig. 2.12: Fig. 2.12(a) shows $\log|\rho_{w\pm} - 1|$ versus $\log t$, and Fig. 2.12(b) the gradients $\alpha(\rho_{w\pm})$ [cf. Eq. (2.45)] versus $\log t$. The values of the gradients $\alpha(\rho_{w\pm})$ at some large times are shown in Table 2.4. It is seen from these results that $\rho_{w\pm}(t) - 1$ tend to decay as Eq. (2.46) with $d = 1$. Figure 2.13(a) is the plots of $\log|\overline{W}|$ and $\log\overline{\|\Delta f\|^{(1)}}$ versus $\log t$, and Fig. 2.13(b) the gradients $\alpha(\overline{W})$ and $\alpha(\overline{\|\Delta f\|^{(1)}})$ versus $\log t$. Figures 2.14(a), 2.14(b), and 2.14(c) are the figures corresponding to Figs. 2.8(a), 2.8(c), and 2.9(a) [the curves at less points are shown in Figs. 2.14(a) and 2.14(b)]. The curves for the evolution of the gradients corresponding to Figs. 2.8(b), 2.8(d), 2.9(b), 2.9(c), and 2.9(d) are omitted in the present case. Table 2.5 shows the values of the gradients $\alpha(h)$ with $h = W$, $\|\Delta f\|^{(1)}$, ρ, u_1, and T at a point ($x_1 = 0.2$) at a long time ($t = 2000$). It is seen from these results that the manner of approach to the final equilibrium state expressed by Eqs. (2.48) and (2.49) is also true in the present case.

It should be noted that, with the non-symmetric initial condition (2.50), the computation becomes more difficult than that in Secs. 4 and 5 to obtain an accurate solution [even with Eq. (2.50), if $\rho^{\rm in}(x_1)$, $u_1^{\rm in}(x_1)$, and $T^{\rm in}(x_1)$ are chosen in such a way that $\rho_{w-}(0) = \rho_{w+}(0)$ holds at $t = 0$, it becomes easier to get an accurate result]. Therefore, a smaller time step and a more accurate interpolation formula have been used to obtain the results shown in this section. For instance, $\Delta t = 0.001$ is used, and the quartic approximation, rather than the linear approximation, is used for $\rho_{w\pm}$

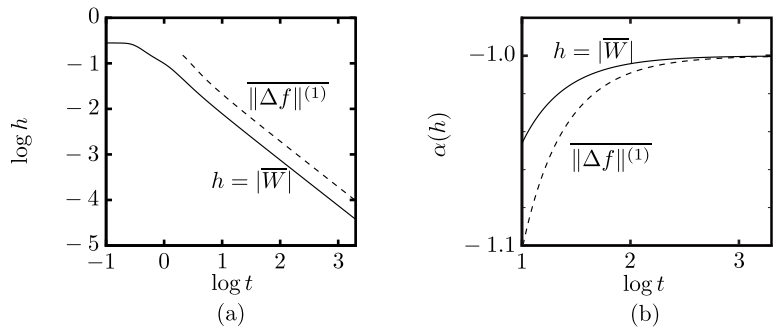

Fig. 2.13 Long-time behavior of $\overline{W}$ and $\overline{\|\Delta f\|^{(1)}}$ for the non-symmetric initial condition ($d = 1$). (a) $\log|\overline{W}|$ and $\log\overline{\|\Delta f\|^{(1)}}$ vs $\log t$. (b) $\alpha(\overline{W})$ and $\alpha(\overline{\|\Delta f\|^{(1)}})$ vs $\log t$. Here, solid line indicates the quantities of $\overline{W}$, and the dashed line those of $\overline{\|\Delta f\|^{(1)}}$.

Table 2.4 Values of $\alpha(\rho_{w\pm})$ at large t for the non-symmetric initial condition ($d = 1$).

t	$\log t$	$-\alpha(\rho_{w-})$	$-\alpha(\rho_{w+})$
50	1.698	0.921745	0.974493
100	2.000	0.952926	0.979931
500	2.698	0.986831	0.992228
1000	3.000	0.992608	0.995298
2000	3.301	0.995904	0.997245

Table 2.5 Values of $\alpha(h)$ at $x_1 = 0.2$ at a large t ($t = 2000$) for the non-symmetric initial condition.

$-\alpha(h)$ $(d = 1,\ x_1 = 0.2,\ t = 2000)$				
$h = W$	$h = \|\Delta f\|^{(1)}$	$h = \rho$	$h = u_1$	$h = T$
1.000148	1.000487	2.014651	3.035255	0.997015

when performing the numerical integration in the integral equations corresponding to Eq. (2.32). In this step, we have used a fast argorithm for the exponential integral $E_1(x) = \int_x^\infty (1/t)\exp(-t)\mathrm{d}t$ provided by J. Jin (see http://jin.ece.uiuc.edu/routines/routines.html).

7 Concluding remarks

In the present study, we have investigated numerically the unsteady behavior of a free-molecular (or Knudsen) gas contained in a vessel with a uniform and constant temperature with special interest in the rate of approach to the final equilibrium state at rest. We assumed the diffuse reflection as the boundary condition on the vessel wall and restricted ourselves to a vessel of spherical shape of dimension d, i.e., a sphere for the 3D case, a circular cylinder for the 2D case, and a gap between two parallel plates for the 1D case. Then, we mainly considered the spherically symmetric case assuming the initial condition to be the uniform equilibrium state at rest with a different temperature from the vessel wall. Such restrictions have made the computation for the 2D and 3D cases tractable. We have investigated the rate of approach to the final equilibrium state for the velocity

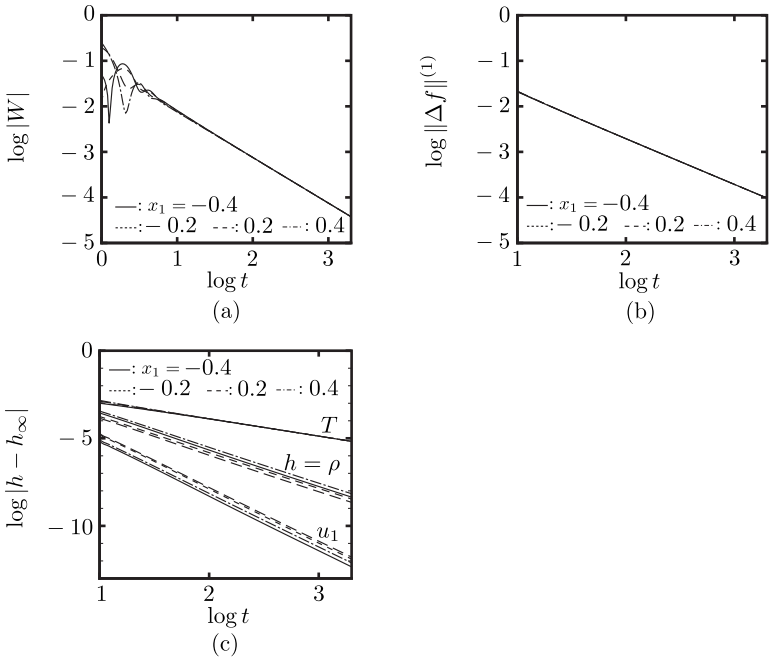

Fig. 2.14 Long-time behavior of macroscopic quantities W, $\|\Delta f\|^{(1)}$, ρ, u_1 and T at $x_1 = -0.4$, -0.2, 0.2, and 0.4 for the non-symmetric initial condition ($d = 1$). (a) $\log|W|$ vs $\log t$. (b) $\log\|\Delta f\|^{(1)}$ vs $\log t$. (c) $\log|h - h_\infty|$ vs $\log t$, where $h = \rho$, u_1 and T. Here, the solid line indicates the quantities at $x_1 = -0.4$, the dashed line at $x_1 = -0.2$, the long-dashed line at $x_1 = 0.2$, and the dot-dashed line at $x_1 = 0.4$.

distribution function as well as for the macroscopic quantities. The numerical results give evidence that the approach is slow and in proportion to an inverse power of time as given by Eq. (2.2). This conclusion is also supported by additional computations using a nonuniform initial condition in the 1D case.

References

[1] Desvillettes, L.: Convergence to equilibrium in large time for Boltzmann and B.G.K. equations. Arch. Rational Mech. Anal., **110**, 73–91 (1990).

[2] Arkeryd, L., Nouri, A.: Boltzmann asymptotics with diffuse reflection boundary conditions. Mh. Math., **123**, 285–298 (1997).

[3] Villani, C.: A review of mathematical topics in collisional kinetic theory. In: Friedlander, S., Serre, D. (eds.) Handbook of Mathematical Fluid Dynamics, vol. 1, pp. 71–305. Elsevier, Amsterdam (2002).

[4] Desvillettes, L., Villani, C.: On the trend to global equilibrium for spatially inhomogeneous kinetic systems: The Boltzmann equation. Invent. Math., **159**, 245–316 (2005).

[5] Villani, C.: Convergence to equilibrium: Entropy production and hypocoercivity. In: Capitelli, M. (ed.) Rarefied Gas Dynamics, pp. 8–25. AIP, Melville (2005).

[6] Villani, C.: Hypocoercivity. Mem. Amer. Math. Soc., **202**, No. 950 (2009).

[7] Guo, Y.: Decay and continuity of the Boltzmann equation in bounded domains. Arch. Rational Mech. Anal., published online (2009).

[8] Lebowitz, J. L., Frisch, H. L.: Model of nonequilibrium ensemble: Knudsen gas. Phys. Rev., **107**, 917–923 (1957).

[9] Arkeryd, L., Ianiro, N., Triolo, L.: The trend to a stationary state for the Lebowitz stick model. Math. Methods App. Sci., **16**, 739–757 (1993).

[10] Bose, C., Grzegorczyk, P., Illner, R.: Asymptotic bahavior of one-dimensional discrete-velocity models in a slab. Arch. Rational Mech. Anal., **127**, 337–360 (1994).

[11] Yu, S.-H.: Stochastic formulation for the initial-boundary value problems of the Boltzmann equation. Arch. Rational Mech. Anal., **192**, 217–274 (2009).

[12] Callen, H. B.: Thermodynamics, Chap. 6, Sec. 6.1. John Wiley and Sons, New York (1960).

[13] Feller, W.: On the integral equation of renewal theory. Ann. Math. Stat., **12**, 243–267 (1941).

[14] Feller, W.: An Introduction to Probability Theory and Its Applications, 2nd ed., Vol. 2, Chap. XI. John Wiley and Sons, New York (1971).

[15] Babovsky, H.: On Knudsen flows within thin tubes. J. Stat. Phys., **44**, 865–878 (1986).

[16] Babovsky, H., Bardos, C., Platkowski, T.: Diffusion approximation for a Knudsen gas in a thin domain with accommodation on the boundary. Asymptotic Anal., **3**, 265–289 (1991).

[17] Golse, F.: Anomalous diffusion limit for the Knudsen gas. Asymptotic Anal., **17**, 1–12 (1998).

[18] Caprino, S., Marchioro, C., Pulvirenti, M.: Approach to equilibrium in a microscopic model of friction. Commun. Math. Phys., **264**, 167–189 (2006).

[19] Caprino, S., Cavallaro, G., Marchioro, C.: On a microscopic model of viscous friction. Math. Models Methods Appl. Sci., **17**, 1369–1403 (2007).

[20] Aoki, K., Cavallaro, G., Marchioro, C., Pulvirenti, M.: On the motion of a body in thermal equilibrium immersed in a perfect gas. Math. Model. Num. Anal., **42**, 263–275 (2008).

[21] Aoki, K., Tsuji, T., Cavallaro, G.: Approach to steady motion of a plate moving in a free-molecular gas under a constant external force. Phys. Rev. E., **80**, 016309 (2009).

Chapter 3

Decay of a linear pendulum in a free-molecular gas and in a special Lorentz gas

Abstract A circular disk without thickness is placed in a gas, and an external force, obeying Hooke's law, is acting perpendicularly on the disk. If the disk is displaced perpendicularly from its equilibrium position and released, then it starts an oscillatory or non-oscillatory unsteady motion, which decays as time goes on because of the drag exerted by the gas molecules. This unsteady motion, i.e., the decay of this linear pendulum, is investigated numerically, under the diffuse reflection condition on the surface of the disk, with special interest in the manner of its decay, for two kinds of gases: one is a collisionless gas (or Knudsen gas) and the other is a special Lorentz gas interacting with a background. It is shown that the decay of the displacement of the disk is slow and is in proportion to an inverse power of time for the collisionless gas. The result complements the existing mathematical study of a similar problem [S. Caprino, *et al.*, *Math. Models. Meth. Appl. Sci.* **17**, 1369–1403 (2007)] in the case of non-oscillatory decay. It is also shown that the manner of the decay changes significantly for the special Lorentz gas.

1 Introduction

Let us consider a body in an infinite expanse of a gas. The body is supposed to be subject to an external force that obeys Hooke's law (i.e., a restoring force in proportion to the displacement from the equilibrium position) and be movable only in the direction parallel to the force (linear pendulum). If the body is displaced and released with an initial velocity, then it starts an unsteady motion, e.g., an oscillation around the equilibrium position, but the motion attenuates as time goes on because of the drag force exerted on the body by the surrounding gas. We are concerned with the rate of decay of the motion of the body.

If the drag force is proportional to the speed of the body, the motion of the body (e.g., the amplitude of the oscillation) decays exponentially in time. However, the drag exerted by the gas is not so simple, and we may expect a different decay rate. This problem, together with the case

in which the body is subject to a constant external force and approaches a final steady motion, has been studied extensively [1, 2, 3, 4, 5, 6] when the surrounding gas is a collisionless gas (a free-molecular gas or the Knudsen gas), i.e., a gas that is so rarefied that collisions between gas molecules can be neglected.

For instance, the case where the body is a circular disk and the external force, obeying Hooke's law, acts perpendicularly on the disk was studied mathematically in [2]. To be more specific, let us denote by t_* the time variable and by $X_w(t_*)$ the displacement (with sign) of the disk from the equilibrium position. Then, the force is expressed as $-\kappa X_w(t_*)$ with a positive constant κ. The gas molecules are assumed to undergo specular reflection on the disk. Initially, the disk is fixed with displacement X_{w0}, and the gas is in a uniform equilibrium state at rest. At time $t_* = 0$, it is released with an initial velocity (parallel to the external force). Then, the disk starts an unsteady motion, and as time goes on, the motion decays, i.e., $X_w(t_*) \to 0$. In [2], it is proved that there exist cases where $X_w(t_*)$ decays monotonically (without oscillation) and that the decay is slow and algebraic in such cases, i.e., it is described as

$$|X_w(t_*)| \approx C_s/t_*^{d+2}, \tag{3.1}$$

for sufficiently large t_*, where d is the dimension of the problem and C_s is a positive constant. A subsequent numerical study [6] confirmed an algebraic decay even in the case with many oscillations for the one-dimensional problem ($d = 1$). Here, it should be mentioned that, since the diffuse-reflection condition, rather than the specular-reflection condition, was employed in [6], the decay rate was different and was proportional to $1/t_*^2$, which is slower than Eq. (3.1) with $d = 1$. These algebraically slow decays are attributed to a long-memory effect peculiar to a collisionless gas. In such a gas, the molecules that are reflected by the disk at early times may hit the disk again at later times. In contrast to a gas with intermolecular collisions, such molecules transfer information about the disk at an early stage directly to the disk at a later stage and may affect the motion of the disk long time later. In other words, they give rise to a long-memory effect.

The aim of the present study is twofold. One is to extend the numerical study in [6] to two- and three-dimensional problems and provide numerical evidence of the decay rate described by

$$|X_w(t_*)| \approx C_f/t_*^{d+1}, \tag{3.2}$$

with a positive constant C_f, under the diffuse-reflection boundary condition. The other is to see the change of the decay rate when the long-memory effect is destroyed by introducing a sort of interaction of gas molecules with a background. For this purpose, we consider a special Lorentz gas explained in the main text and consider the resulting kinetic equation (a toy model). We study the decay of the unsteady motion of the disk numerically and show that the decay rate changes significantly.

2 Formulation of the Problem

2.1 Problem

Let us consider an infinite expanse of a rarefied gas in an equilibrium state at rest at temperature T_{*0} and density ρ_{*0}. What kind of gas (i.e., what kind of kinetic equation) we are considering will be specified in Sec. 2.2. A circular disk with diameter L_* and without thickness, kept at temperature T_{*0}, is placed in the gas, and an external force, obeying Hooke's law (elastic force), is acting on the disk perpendicularly to its surface. In the present study, we consider d-dimensional problems with $d = 1$, 2, and 3: The disk is a circular disk with diameter L_* when $d = 3$ [Fig. 3.1(a)], an

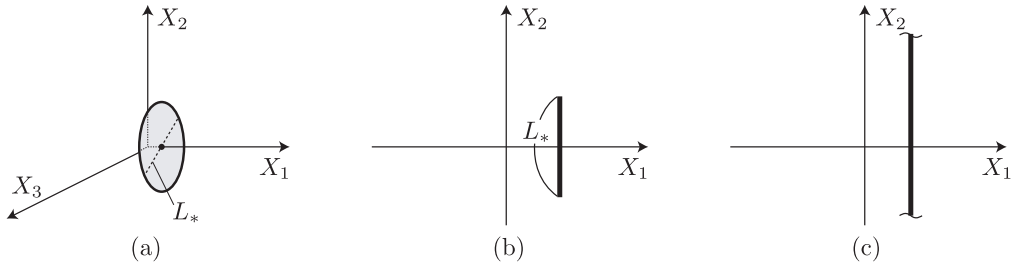

Fig. 3.1 A circular disk of d dimension ($d = 1, 2, 3$) without thickness in a gas. (a) Circular disk with diameter L_* ($d = 3$), (b) infinite plate with finite width L_* ($d = 2$), and (c) infinite plate ($d = 1$).

infinite plate with finite width L_* when $d = 2$ [Fig. 3.1(b)], and an infinitely wide plate when $d = 1$ [Fig. 3.1(c)]. Let t_* be the time variable and X_i be the Cartesian coordinates in space with the X_i axes taken as in Fig. 3.1. That is, X_1 axis is taken parallel to the elastic force, and $X_1 = 0$ indicates the equilibrium position of the disk. Therefore, the elastic force F_1 per unit area of the disk is expressed as

$$F_1 = -M_* \omega_*^2 X_w(t_*), \tag{3.3}$$

where $X_w(t_*)$ is the position (X_1 coordinate) of the disk at time t_*, M_* is the mass density of the disk (the mass of the disk per unit surface), and ω_* is the proper frequency of the elastic force.

At time $t_* = 0$, the disk is released from a position $X_1 = X_{w0}$ with an initial velocity V_{w0} in the X_1 direction. Then, it starts an unsteady motion (e.g., an oscillatory motion), but the motion decays as time goes on because of the drag exerted on the disk by the surrounding gas. We investigate this unsteady motion of the disk numerically, with special interest in the long-time behavior and the manner of the decay, assuming that the disk moves only along the X_1 axis and does not change its attitude.

2.2 Choice of the gas

In the present study, we consider the following two types of gas as the gas surrounding the disk. We denote by ξ_i the molecular velocity and by $f_*(X_i, \xi_i, t_*)$ the velocity distribution function of the gas molecules.

2.2.1 Collisionless gas

The collisionless gas is a gas that is so rarefied that collisions between gas molecules can be neglected. It is also called the free-molecular gas or the Knudsen gas. In this case, the basic equation is the Boltzmann equation without the collision term, i.e., the free-transport equation:

$$\frac{\partial f_*}{\partial t_*} + \xi_j \frac{\partial f_*}{\partial X_j} = 0. \tag{3.4}$$

That is, f_* is constant along the molecular trajectory.

2.2.2 A kind of the Lorentz gas

In addition to the collisionless gas, we consider a gas that is described by the following equation.

$$\frac{\partial f_*}{\partial t_*} + \xi_i \frac{\partial f_*}{\partial X_i} = \nu(\xi_i)(f_{*\infty} - f_*), \tag{3.5}$$

where

$$\nu(\xi_i) = \frac{\pi(r+r_s)^2}{m_s} \int_{\mathbb{R}^3} |\boldsymbol{\xi} - \boldsymbol{\xi}_s| f_{*s}(\xi_{si}) d\boldsymbol{\xi}_s, \tag{3.6a}$$

$$f_{*\infty}(\xi_i) = \frac{\pi(r+r_s)^2}{m_s \nu(\xi_i)} \int_{\mathbb{R}^3} |\boldsymbol{\xi} - \boldsymbol{\xi}_s| f_{*s}(\xi_{si}) f_{*v}(\xi_i - \xi_{si}) d\boldsymbol{\xi}_s, \tag{3.6b}$$

with $d\boldsymbol{\xi}_s = d\xi_{s1} d\xi_{s2} d\xi_{s3}$. Here, $f_{*v}(\xi_i)$ and $f_{*s}(\xi_i)$ are given functions of ξ_i, and r, r_s, and m_s are given constants. A physical model that leads to this equation is the following.

Let us suppose that the gas is a vapor of a substance and its molecule is a hard sphere with mass m and radius r. In the gas, there are randomly distributed spherical obstacles (droplets) of mass m_s and radius r_s, which are made of the condensed phase of the same substance as the vapor. The obstacles are moving with velocity ξ_{si}, and their velocity is distributed according to a given distribution $f_{*s}(\xi_{si})$ that is uniform in X_i and constant in t_*. We assume that the vapor molecules hitting an obstacle are absorbed and reemitted with a velocity distribution $f_{*v}(\xi_i - \xi_{si})$, which is a given function of $\xi_i - \xi_{si}$, uniform in X_i, and constant in t_*. We neglect the collisions between vapor molecules and consider their interaction with the obstacles only. Then, we arrive at Eq. (3.5). See Appendix for more details.

In the actual analysis, we use an equation that is a further simplification of Eq. (3.5), derived under the assumption that f_{*v} and f_{*s} are Maxwellians and the average speed of motion of the obstacles are much smaller than that of the gas molecules (see Appendix).

2.3 Assumptions

We investigate the problem stated in Sec. 2.1 under the following assumptions:

(i) The behavior of the gas is described by Eq. (3.4) or the model equation Eq. (3.12) shown later, which is a simplified version of Eq. (3.5).

(ii) The gas molecules undergo diffuse reflection on the surface of the disk. That is. the molecules reflected by the disk are distributed according to the Maxwellian distribution characterized by the temperature and velocity of the disk, and there is no net mass flux across the disk surface.

In the two-dimensional (2D) problem ($d = 2$), f_* is independent of X_3; in the one-dimensional (1D) problem ($d = 1$), f_* is independent of X_2 and X_3.

3 Basic Equations

In this section, we summarize the basic equations in dimensionless form. We restrict ourselves to the three-dimensional problem, since the two- and one-dimensional cases are essentially the same.

3.1 Dimensionless variables and notations

In the preceding sections, we have introduced dimensional variables t_*, X_i, ξ_i, f_*, X_w, and V_w and dimensional quantities T_{*0}, ρ_{*0}, L_*, M_*, ω_*, X_{w0}, and V_{w0}. In addition, let us denote by $G_*[f_*]$ the drag acting on the disk divided by its area and by f_{*0} the Maxwellian distribution at rest at density ρ_{*0} and temperature T_{*0}.

Then we introduce the dimensionless quantities t, x_i, ζ_i, f, x_w, v_w, L, M, x_{w0}, v_{w0}, $G[f]$, and

f_0 by the following relations:

$$
\begin{aligned}
&t_* = (1/\omega_*)\, t, \quad X_i = (\sqrt{2R_*T_{*0}}/\omega_*)\, x_i, \quad \xi_i = \sqrt{2R_*T_{*0}}\, \zeta_i, \\
&f_*(X_i, \xi_i, t_*) = [\rho_{*0}/(2R_*T_{*0})^{3/2}]\, f(x_i, \zeta_i, t), \\
&X_w(t_*) = (\sqrt{2R_*T_{*0}}/\omega_*)\, x_w(t), \quad V_w(t_*) = \sqrt{2R_*T_{*0}}\, v_w(t), \\
&L_* = (\sqrt{2R_*T_{*0}}/\omega_*)\, L, \quad M_* = (\rho_{*0}\sqrt{2R_*T_{*0}}/\omega_*)\, M, \\
&X_{w0} = (\sqrt{2R_*T_{*0}}/\omega_*)\, x_{w0}, \quad V_{w0} = \sqrt{2R_*T_{*0}}\, v_{w0}, \\
&G_*[f_*] = \rho_{0*}(2R_*T_{*0})\, G[f], \\
&f_{*0}(|\boldsymbol{\xi}|) = [\rho_{*0}/(2R_*T_{*0})^{3/2}]\, f_0(|\boldsymbol{\zeta}|),
\end{aligned}
\tag{3.7}
$$

where R_* is the gas constant per unit mass ($R_* = k_B/m$ with k_B the Boltzmann constant and m the mass of a gas molecule), and thus f_0 is given by

$$
f_0(|\boldsymbol{\zeta}|) = \pi^{-3/2} \exp(-|\boldsymbol{\zeta}|^2). \tag{3.8}
$$

We further introduce some additional notations for later convenience: c_1 is the molecular velocity relative to the velocity of the disk in the x_1 direction, i.e.,

$$
c_1 = \zeta_1 - v_w(t), \tag{3.9}
$$

$\partial S_\pm(t)$ is the surface of the disk, i.e.,

$$
\partial S_\pm(t) = \{\, x_i \in \mathbb{R}^3 \,|\, x_1 = x_w(t) \pm 0,\ x_2^2 + x_3^2 < L^2/4 \,\}, \tag{3.10}
$$

and $\Omega_\pm(t)$ is the range of molecular velocity defined by

$$
\Omega_\pm(t) = \{\, \zeta_i \in \mathbb{R}^3 \,|\, c_1 \gtrless 0 \,\}. \tag{3.11}
$$

In Eqs. (3.10) and (3.11) and in what follows, the upper (or lower) signs go together.

3.2 Basic equations in dimensionless form

Our basic equation is Eq. (3.82) in Appendix, which is a toy model and is a simplified version of Eq. (3.5), i.e.,

$$
\frac{\partial f}{\partial t} + \zeta_i \frac{\partial f}{\partial x_i} = \frac{\nu_\epsilon(|\boldsymbol{\zeta}|)}{\mathrm{Kn}}(f_0 - f). \tag{3.12}
$$

The case of a collisionless gas [Eq. (3.4)] is included in this equation as a special case ($\mathrm{Kn} \to \infty$). In Eq. (3.12), the dimensionless collision frequency $\nu_\epsilon(|\boldsymbol{\zeta}|)$ is defined by the following function $\nu_\epsilon(x)$:

$$
\nu_\epsilon(x) = \frac{\epsilon}{\sqrt{\pi}} \Big[\exp\left(-\frac{x^2}{\epsilon^2}\right) + \sqrt{\pi} \left(\frac{x}{\epsilon} + \frac{\epsilon}{2x}\right) \mathrm{erf}\left(\frac{x}{\epsilon}\right) \Big], \quad \text{for} \quad x > 0, \tag{3.13}
$$

with $\mathrm{erf}(x)$ the error function given by

$$
\mathrm{erf}(x) = \frac{2}{\sqrt{\pi}} \int_0^x \exp(-y^2) dy, \tag{3.14}
$$

and the Knudsen number Kn is defined as

$$
\mathrm{Kn} = [\pi n_{*s}(r + r_s)^2]^{-1} (\sqrt{2R_*T_{*0}}/\omega_*)^{-1}, \tag{3.15}
$$

with n_{*s} a positive constant [the number density of the obstacles; cf. Eq. (3.62)]. Here, ϵ is a small parameter, and the Kn is the ratio between the mean free path of a gas molecule for the collisions against obstacles [see Eqs. (3.81) and (3.82c)] and the characteristic length $(\sqrt{2R_*T_{*0}}/\omega_*)$. See Appendix for the details of the derivation of Eq. (3.12) and the physical meaning of the parameters and conditions.

The corresponding initial condition is given by

$$f(x_i, \zeta_i, 0) = f_0(\zeta_i), \tag{3.16}$$

and the boundary condition (diffuse reflection) on the surface of the disk $\partial S_\pm(t)$ is given by

$$f(x_i,\, \zeta_i,\, t) = f_{w\pm}(x_2,\, x_3,\, \zeta_i,\, t), \quad \text{for} \quad x_i \in \partial S_\pm(t),\ \ \zeta_i \in \Omega_\pm(t). \tag{3.17}$$

where

$$f_{w\pm}(x_2,\, x_3,\, \zeta_i,\, t) = \pi^{-3/2}\rho_{w\pm}(x_2,\, x_3,\, t)\exp(-c_1^2 - \zeta_2^2 - \zeta_3^2), \tag{3.18a}$$

$$\rho_{w\pm}(x_2,\, x_3,\, t) = \mp 2\sqrt{\pi}\int_{\Omega_\mp(t)} c_1 f(x_i,\, \zeta_i,\, t)d\boldsymbol{\zeta}, \quad \text{for}\ \ x_i \in \partial S_\pm(t), \tag{3.18b}$$

with the notation $d\boldsymbol{\zeta} = d\zeta_1 d\zeta_2 d\zeta_3$.

The equation of motion of the disk is given as

$$\frac{dx_w(t)}{dt} = v_w(t), \qquad \frac{dv_w}{dt} = -x_w - \frac{1}{M}G[f], \tag{3.19}$$

with the initial condition

$$x_w(0) = x_{w0}, \qquad v_w(0) = v_{w0}. \tag{3.20}$$

The dimensionless average drag $G[f]$ per unit area is expressed in terms of the velocity distribution function on the disk:

$$G[f] = G_+[f] + G_-[f], \tag{3.21}$$

where

$$G_\pm[f] = \pm\frac{1}{\pi(L/2)^2}\int_{x_2^2+x_3^2<L^2/4}\left(\int_{\Omega_\mp(t)} c_1^2 f(x_w(t) \pm 0,\, x_2,\, x_3,\, \zeta_i,\, t)d\boldsymbol{\zeta} + \int_{\Omega_\pm(t)} c_1^2 f_{w\pm}(x_2,\, x_3,\, \zeta_i,\, t)d\boldsymbol{\zeta}\right) dx_2 dx_3. \tag{3.22}$$

We solve the coupled system Eqs. (3.12)–(1.8) and Eqs. (3.19)–(1.10) numerically with special interest in the manner of decay of the motion of the disk, i.e., the decay of $|x_w|$. The parameters contained in the present problem are

$$L, \quad M, \quad x_{w0}, \quad v_{w0}, \quad \mathrm{Kn}, \quad \epsilon. \tag{3.23}$$

Recall that $\mathrm{Kn} = \infty$ recovers the collisionless gas Eq. (3.4).

4 Preliminaries

4.1 Integral form

In the numerical analysis, we solve Eqs. (3.12)–(1.8) and Eqs. (3.19)–(1.10) in a time-marching manner. For this purpose, it is more convenient to use the expression of $\rho_{w\pm}(x_2,\, x_2,\, t)$ in terms of the integrals containing information about $\rho_{w\pm}$, x_w, and v_w in the past. In order to derive the integral form of $\rho_{w\pm}$, let us fix the time t and assume that $\rho_{w\pm}$, x_w, and v_w are known for the time s in the past ($0 \le s < t$). In addition, we consider x_i on the disk [$x_i \in \partial S_\pm(t)$].

For each velocity ζ_i for the molecules incident on the disk [$\zeta_i \in \Omega_\mp(t)$ for $x_i \in \partial S_\pm(t)$], we trace back the corresponding molecular trajectory. Then, we either (i) reach the initial time without hitting the disk, or (ii) encounter the disk at a time t^b in the past ($0 < t^b < t$) at a point $(x_w(t^b) \pm 0,\, x_2^b,\, x_3^b)$ on the disk. To be more specific, $t^b(\zeta_1,\, t)$ is given by

$$t^b = \max\{s \in (0,\, t) \,|\, x_1 - \zeta_1(t-s) = x_w(s)\}, \tag{3.24}$$

and $x_2^b(x_2,\, \zeta_2,\, t,\, t^b)$ and $x_3^b(x_3,\, \zeta_3,\, t,\, t^b)$ by

$$x_2^b = x_2 - \zeta_2(t-t^b), \qquad x_3^b = x_3 - \zeta_3(t-t^b), \tag{3.25}$$

under the condition that $(x_2^b)^2 + (x_3^b)^2 < (L/2)^2$. The latter condition restricts the range of ζ_i and is stated more precisely that

$$\zeta_i \in \Gamma_\pm(x_2,\, x_3,\, t), \tag{3.26a}$$

$$\Gamma_\pm = \left\{\zeta_i \in \mathbb{R}^3 \;\middle|\; {}^\exists t^b > 0,\ (x_2^b)^2 + (x_3^b)^2 < (L/2)^2,\ x_i \in \partial S_\pm(t)\right\}. \tag{3.26b}$$

Now let us define $\tau_\pm^b(x_i,\, \zeta_i,\, t)$ by

$$\tau_\pm^b = \begin{cases} t^b, & \text{for} \quad \zeta_i \in \Gamma_\pm, \\ 0, & \text{for} \quad \zeta_i \notin \Gamma_\pm. \end{cases} \tag{3.27}$$

This quantity is similar to the *backward exit time* for free-transport particles in a closed domain. Then, integrating Eq. (3.12) along the characteristic line, one can write

$$\begin{aligned} f(x_i,\, \zeta_i,\, t) = f_0 + \left[f(x_i - \zeta_i(t-\tau_\pm^b),\, \zeta_i,\, \tau_\pm^b) - f_0\right] \\ \times \exp\left(-\frac{\nu_\epsilon(|\boldsymbol{\zeta}|)}{\mathrm{Kn}}\,(t-\tau_\pm^b)\right). \end{aligned} \tag{3.28}$$

Here, the term $f(x_i - \zeta_i(t-\tau_\pm^b),\, \zeta_i,\, \tau_\pm^b)$ is expressed more explicitly as

$$f(x_i - \zeta_i(t-\tau_\pm^b),\, \zeta_i,\, \tau_\pm^b) = \begin{cases} f_{w\pm}(x_2^b,\, x_3^b,\, \zeta_i,\, t^b), & \text{for} \quad \zeta_i \in \Gamma_\pm, \\ f_0, & \text{for} \quad \zeta_i \notin \Gamma_\pm. \end{cases} \tag{3.29}$$

If we substitute Eq. (3.28) into Eq. (3.18b), then we have

$$\begin{aligned} \mp\frac{\rho_{w\pm}(x_2,\, x_3,\, t)}{2\sqrt{\pi}} = \int_{\Omega_\mp} c_1 f_0 d\boldsymbol{\zeta} + \int_{\Gamma_\pm \cap \Omega_\mp} c_1 f_0 \exp\left(-\frac{\nu_\epsilon(|\boldsymbol{\zeta}|)}{\mathrm{Kn}}(t-t^b)\right) \\ \times \left[\rho_{w\pm}^b \exp\left(\zeta_1^2 - [\zeta_1 - v_w^b]^2\right) - 1\right] d\boldsymbol{\zeta}, \\ \text{for} \quad x_i \in \partial S_\pm(t), \end{aligned} \tag{3.30}$$

where

$$\rho^b_{w\pm} = \rho_{w\pm}(x^b_2,\, x^b_3,\, t^b), \qquad v^b_w = v_w(t^b). \tag{3.31}$$

Equation (3.30) yields the expression of $\rho_{w\pm}(x_2,\, x_3,\, t)$ in terms of $\rho_{w\pm}$, x_w, and v_w in the past. It could be interpreted as the integral equation for $\rho_{w\pm}$ if we suppose that x_w and v_w are known. Equation (3.30) is the key equation for our time-marching solution of the original system.

4.2 Axisymmetry

In the three-dimensional case ($d = 3$), we assume that the problem is axisymmetric with respect to the x_1 axis and reduce the number of the independent variables. Let us introduce the cylindrical coordinate system $(x_1,\, r,\, \theta)$ for x_i as

$$x_1 = x_1, \qquad x_2 = r\cos\theta, \qquad x_3 = r\sin\theta, \tag{3.32}$$

with $r \in [0,\, \infty)$ and $\theta \in [0,\, 2\pi)$, and assume that $\rho_{w\pm}$ is independent of θ in the cylindrical coordinate system, i.e.,

$$\tilde{\rho}_{w\pm}(r, t) = \rho_{w\pm}(x_2, x_3, t). \tag{3.33}$$

We further introduce some additional notations:

$$\partial\tilde{S}_\pm(t) = \{\, (x_1,\, r,\, \theta) \in \mathbb{R}\times\mathbb{R}_+\times[0,\, 2\pi) \,|\, x_1 = x_w(t) \pm 0,\, r < L/2 \,\}, \tag{3.34a}$$

$$\Gamma^\perp_\pm = \left\{ \zeta_1 \in \mathbb{R} \;\middle|\; {}^\exists t^b > 0,\, (x_1,\, r,\, \theta) \in \partial\tilde{S}_\pm(t) \right\}, \tag{3.34b}$$

$$\Omega^\perp_\pm = \left\{ \zeta_1 \in \mathbb{R} \;\middle|\; \zeta_1 \gtrless v_w(t) \right\}. \tag{3.34c}$$

If we express x^b_2 and x^b_3 as

$$x^b_2 = r^b\cos(\theta + \theta^b), \qquad x^b_3 = r^b\sin(\theta + \theta^b), \tag{3.35}$$

using the polar coordinates in the x_2x_3 plane, then Eq. (3.25) is recast as

$$r^b\cos(\theta + \theta^b) = r\cos\theta - \zeta_2(t - t^b), \tag{3.36a}$$

$$r^b\sin(\theta + \theta^b) = r\sin\theta - \zeta_3(t - t^b). \tag{3.36b}$$

Let us transform the integration variables from $(\zeta_1,\, \zeta_2,\, \zeta_3)$ to $(\zeta_1,\, r^b,\, \theta^b)$ in Eq. (3.30) by the use of Eq. (3.36), noting that $t^b = t^b(\zeta_1,\, t)$. Then, we have

$$\mp\frac{\tilde{\rho}_{w\pm}(r,\, t)}{2\sqrt{\pi}} = H_{1\pm}(t) + P_{1\pm}[\tilde{\rho}_{w\pm}](r,\, t), \quad \text{for} \quad (x_1,\, r,\, \theta) \in \partial\tilde{S}_\pm, \tag{3.37}$$

where $H_{1\pm}(t)$ and $P_{1\pm}[\tilde{\rho}_{w\pm}](r,\, t)$ are the function and the operator, which are defined in a more general form in the following.

The function $H_{n\pm}(t)$ is defined by

$$H_{n\pm}(t) = \int_{\Omega_\mp} c_1^n f_0 d\boldsymbol{\zeta}, \tag{3.38a}$$

or, more explicitly,

$$H_{1\pm}(t) = \mp\frac{1}{2\sqrt{\pi}}\exp(-v_w^2(t)) - \frac{1}{2}v_w(t)\mathrm{erfc}(\mp v_w(t)), \tag{3.38b}$$

$$H_{2\pm}(t) = \pm\frac{v_w(t)}{2\sqrt{\pi}}\exp(-v_w^2(t)) + \frac{1}{2}\left[v_w(t) + \frac{1}{2}\right]\mathrm{erfc}(\mp v_w(t)), \tag{3.38c}$$

where erfc(x) is the complementary error function:

$$\mathrm{erfc}(x) = \frac{2}{\sqrt{\pi}} \int_x^\infty \exp(-y^2) dy = 1 - \mathrm{erf}(x). \tag{3.39}$$

The operator $P_{n\pm}[\tilde{\rho}_{w\pm}](r,\, t)$ is defined as

$$P_{n\pm}[\tilde{\rho}_{w\pm}](r,\, t) = \int_{\Omega_{\mp}^{\pm} \cap \Gamma_{\pm}^{\perp}} c_1^n F[\tilde{\rho}_{w\pm}](r,\, \zeta_1,\, t;\, t^b)\, d\zeta_1, \tag{3.40}$$

where

$$\begin{aligned} F[\tilde{\rho}_{w\pm}](r,\, \zeta_1,\, t;\, t^b) = &\int_0^{L/2} K(|\zeta_1|,\, r^b,\, r,\, t - t^b;\, \mathrm{Kn},\, \epsilon) \\ &\times \left[\tilde{\rho}_{w\pm}(r^b,\, t^b) \exp(\zeta_1^2 - [\zeta_1 - v_w^b]^2) - 1\right] dr^b, \end{aligned} \tag{3.41a}$$

$$\begin{aligned} &K(|\zeta_1|,\, r^b,\, r,\, t - t^b;\, \mathrm{Kn},\, \epsilon) \\ &\quad = \frac{2r^b}{\pi^{3/2}(t - t^b)^2} \int_0^\pi \exp\left(-\zeta^2(\theta^b) - \frac{\nu_\epsilon(\zeta(\theta^b))}{\mathrm{Kn}}(t - t^b)\right) d\theta^b, \end{aligned} \tag{3.41b}$$

$$\zeta(\theta^b) = \sqrt{\zeta_1^2 + \frac{(r - r^b)^2 + 2r^b r(1 - \cos\theta^b)}{(t - t^b)^2}}. \tag{3.41c}$$

With these notations, the average drag acting on the disk per unit area (3.22) is recast as

$$\begin{aligned} \pm G_\pm(t) = &\frac{8}{L^2} \int_0^{L/2} \left[H_{2\pm}(t) + P_{2\pm}[\tilde{\rho}_{w\pm}](r,\, t) + \frac{1}{4}\tilde{\rho}_{w\pm}(r,\, t)\right] r dr, \\ &\text{for} \quad (x_1,\, r,\, \theta) \in \partial\tilde{S}_\pm. \end{aligned} \tag{3.42}$$

For a collisionless gas [Eq. (3.4)], which is given by the limit as $\mathrm{Kn} \to \infty$ in the special Lorentz gas [Eq. (3.12)], we have the analytic expression of K [Eq. (3.41b)], i.e.,

$$\begin{aligned} K_\infty &\equiv K(|\zeta_1|,\, r^b,\, r,\, t - t^b;\, \infty,\, \epsilon) \\ &= \frac{2r^b}{(t - t^b)^2\sqrt{\pi}} \exp\left(-\zeta_1^2 - \left(\frac{r - r^b}{t - t^b}\right)^2\right) \bar{I}_0\left(\frac{2r^b r}{(t - t^b)^2}\right), \end{aligned} \tag{3.43}$$

where $\bar{I}_0(x)$ is defined by

$$\bar{I}_0(x) = \exp(-|x|) I_0(x), \tag{3.44a}$$

$$I_0(x) = \frac{1}{\pi} \int_0^\pi \exp(x\cos\theta) d\theta. \tag{3.44b}$$

Here, $I_0(x)$ is the modified Bessel function of the first kind of order zero.

5 Numerical Analysis

In this section, we explain the numerical solution method for the three-dimensional (axisymmetric) case.

5.1 Numerical scheme for equation of motion

We first consider the equation of motion of the disk (3.19). Let us introduce the following discrete variables:

$$t^{(n)} = n\Delta t, \quad x_w^{(n)} = x_w(t^{(n)}), \quad v_w^{(n)} = v_w(t^{(n)}), \quad G^{(n)} = G[f(\cdot\,, t^{(n)})], \tag{3.45}$$

where Δt is a constant (time interval). Suppose that all the quantities have been obtained up to $t = t^{(n)}$. Then, we compute the position $x_w^{(n+1)}$ and velocity $v_w^{(n+1)}$ of the disk as well as the drag $G^{(n+1)}$ at $t = t^{(n+1)}$ by the predictor-corrector method explained below.

For brevity, we introduce the notation

$$\mathsf{X} = \begin{bmatrix} x_w \\ v_w \end{bmatrix}, \qquad \mathsf{F} = \begin{bmatrix} v_w \\ -x_w - M^{-1}G[f] \end{bmatrix}, \tag{3.46a}$$

$$\mathsf{X}^{(n)} = \begin{bmatrix} x_w^{(n)} \\ v_w^{(n)} \end{bmatrix}, \qquad \mathsf{F}^{(n)} = \begin{bmatrix} v_w^{(n)} \\ -x_w^{(n)} - M^{-1}G^{(n)} \end{bmatrix}, \tag{3.46b}$$

and write the equation of motion (3.19) as

$$\frac{d\mathsf{X}}{dt} = \mathsf{F}, \tag{3.47}$$

which leads to

$$\mathsf{X}^{(n+1)} = \mathsf{X}^{(n)} + \int_{t^{(n)}}^{t^{(n+1)}} \mathsf{F}\, dt. \tag{3.48}$$

We first obtain the predicted value $\widehat{\mathsf{X}}^{(n+1)}$ of $\mathsf{X}^{(n+1)}$ by approximating F in Eq. (1.23) by the l_P-degree polynomial of t based on the values $\mathsf{F}^{(n)}$, $\mathsf{F}^{(n-1)}$, ..., $\mathsf{F}^{(n-l_P)}$, i.e.,

$$\widehat{\mathsf{X}}^{(n+1)} = \mathsf{X}^{(n)} + \Delta t \sum_{l=0}^{l_P} w_P^{(n-l)} \mathsf{F}^{(n-l)}, \tag{3.49}$$

where the weights $w_P^{(n)}$, ..., $w_P^{(n-l_P)}$ are determined according to the polynomial approximation mentioned above. We set $l_P = 3$ in this paper ($l_p = n$ for $n \le 2$). With this $\widehat{\mathsf{X}}^{(n+1)}$, we compute the predicted value $\widehat{\mathsf{F}}^{(n+1)}$ (or $\widehat{G}^{(n+1)}$) by the procedure that will be described in Sec. 5.2. Then, we compute $\mathsf{X}^{(n+1)}$ by approximating F in Eq. (1.23) by the l_C-degree polynomial of t based on the values $\widehat{\mathsf{F}}^{(n+1)}$, $\mathsf{F}^{(n)}$, ..., $\mathsf{F}^{(n+1-l_C)}$, i.e.,

$$\mathsf{X}^{(n+1)} = \mathsf{X}^{(n)} + \Delta t \left(w_C^{(n+1)} \widehat{\mathsf{F}}^{(n+1)} + \sum_{l=0}^{l_C-1} w_C^{(n-l)} \mathsf{F}^{(n-l)} \right), \tag{3.50}$$

where the weights $w_C^{(n+1)}$, ..., $w_C^{(n+1-l_C)}$ are determined similarly. We set $l_C = 4$ in the present paper ($l_C = n$ for $n \le 3$). Finally, with the new value $\mathsf{X}^{(n+1)}$, we compute $G^{(n+1)}$ (see Sec. 5.2) to prepare for the next step.

Once $x_w^{(n+1)}$ and $v_w^{(n+1)}$ are obtained, we approximate the trajectory $x_w(t)$ in the time interval $t \in [t^{(n)}, t^{(n+1)}]$ by the cubic polynomial $\psi_n(t)$ determined by the following conditions:

$$\begin{aligned} &\psi_n(t^{(n)}) = x_w^{(n)}, && \psi_n(t^{(n+1)}) = x_w^{(n+1)}, \\ &\left.\frac{d\psi_n}{dt}\right|_{t=t^{(n)}} = v_w^{(n)}, && \left.\frac{d\psi_n}{dt}\right|_{t=t^{(n+1)}} = v_w^{(n+1)}. \end{aligned} \tag{3.51}$$

The approximated trajectory $x_w(t) = \psi_n(t)$ in the interval $t \in [t^{(n)}, t^{(n+1)}]$ $(n = 0,\ 1,\ 2,\ ...)$ will be used in Sec. 5.3.

5.2 Numerical scheme for computation of the drag force

In this subsection, we describe the method of computation of the drag force $G^{(n+1)}$ at $t = t^{(n+1)}$, supposing that the quantities at previous time steps $(t = t^{(k)},\ k = 0,\ 1,\ ...,\ n)$ are all known and that $x_w^{(n+1)}$ and $v_w^{(n+1)}$ are also known [cf. Sec. 5.1]. We first introduce grid points in the r and θ coordinates in the cylindrical coordinate system (3.32), i.e.,

$$r^{(i)} = (L/2)\,(i/N_r), \qquad (i = 0,\ ...,\ N_r), \tag{3.52}$$

$$\theta^{(j)} = \pi\,(j/N_\theta), \qquad (j = 0,\ ...,\ N_\theta), \tag{3.53}$$

and denote

$$\tilde{\rho}_{w\pm}^{(i,k)} = \tilde{\rho}_{w\pm}(r^{(i)},\ t^{(k)}). \tag{3.54}$$

In addition, we choose the grid points $\zeta_1^{(k)}$ for ζ_1 in such a way that $t^b(\zeta_1^{(k)},\ t^{(n+1)})$ [Eq. (3.24)] falls on the discrete time $t^{(k)}$.

The first step is to obtain $\tilde{\rho}_{w\pm}^{(i,n+1)}$ by the use of Eq. (3.37) at $r = r^{(i)}$ and $t = t^{(n+1)}$. Since $H_{1\pm}(t^{(n+1)})$ can be obtained from the explicit expression (3.38b), our major concern is to compute $P_{1\pm}[\tilde{\rho}_{w\pm}](r^{(i)},\ t^{(n+1)})$ [Eq. (3.40)], for which we need to compute $F[\tilde{\rho}_{w\pm}](r^{(i)},\ \zeta_1^{(k)}, t^{(n+1)};\ t^b(\zeta_1^{(k)},\ t^{(n+1)}))$. This can be computed for $k = 0,\ 1,\ ...,\ n$ from Eq. (3.41) because $\rho_{w\pm}^{(i,k)}$ and $v_w(t^{(k)})$ are known for $i = 0,\ ...,\ N_r$ and $k = 0,\ ...,\ n$ [Note that $v_w^b = v_w(t^b(\zeta_1^{(k)}, t^{(n+1)}))$ in Eq. (3.41)]. The integration with respect to θ^b in Eq. (3.41b) and that with respect to r^b in Eq. (3.41a) are carried out by the Simpson rule. Then $P_{1\pm}[\tilde{\rho}_{w\pm}](r^{(i)},\ t^{(n+1)})$ is computed from Eq. (3.40), where the integration with respect to ζ_1 is performed by the trapezoidal rule. In this integration, $F[\tilde{\rho}_{w\pm}](r^{(i)}, \zeta_1^{(k)},\ t^{(n+1)}; t^b(\zeta_1^{(k)}, t^{(n+1)}))$ at $k = n + 1$, which corresponds to the end point of the range of integration with respect to ζ_1, is not required, since the integrand vanishes there because of the factor c_1. It should be noted that $t^b(\zeta_1,\ t^{(n+1)})$, as a function of ζ_1, exhibits discontinuities depending on the shape of the trajectory in the past, $x_w(s)$ for $s \in [0,\ t)$. Therefore, for accurate numerical integration, we need the precise locations of the discontinuities as well as the values of the integrand at both sides of the discontinuities. The detailed description how to handle the discontinuities will be given in the next subsection.

Once we obtain $\tilde{\rho}_{w\pm}^{(i,n+1)}$ by the procedure mentioned above, we can compute $G_\pm(t^{(n+1)})$ from Eq. (3.42). Here, $H_{2\pm}(t^{n+1})$ is obtained from Eq. (3.38c), and $P_{2\pm}[\tilde{\rho}_{w\pm}](r^{(i)},\ t^{(n+1)})$ is computed from Eq. (3.40), in the same way as $P_{1\pm}[\tilde{\rho}_{w\pm}]\ (r^{(i)},\ t^{(n+1)})$ in the preceding paragraph. Then, the integration with respect to r in Eq. (3.42) is carried out by the Simpson rule. Then, the average drag $G^{(n+1)}$ at $t = t^{(n+1)}$ is obtained as the sum of $G_+(t^{(n+1)})$ and $G_-(t^{(n+1)})$ [Eq. (3.21)].

The predicted value $\widehat{G}^{(n+1)}$ of $G^{(n+1)}$, which appeared in Sec. 5.1, can be obtained in the same way as $G^{(n+1)}$, using the predicted values $\widehat{\mathsf{X}}^{(n+1)}$ (i.e., the predicted values of $x_w^{(n+1)}$ and $v_w^{(n+1)}$) instead of $x_w^{(n+1)}$ and $v_w^{(n+1)}$.

5.3 Numerical scheme for computation of discontinuity

As we mentioned in Sec. 5.2, $t^b(\zeta_1,\ t^{(n+1)})$ may be a piecewise continuous function of ζ_1 with (a finite number of) discontinuities. In this subsection, we will give a brief sketch how to obtain the

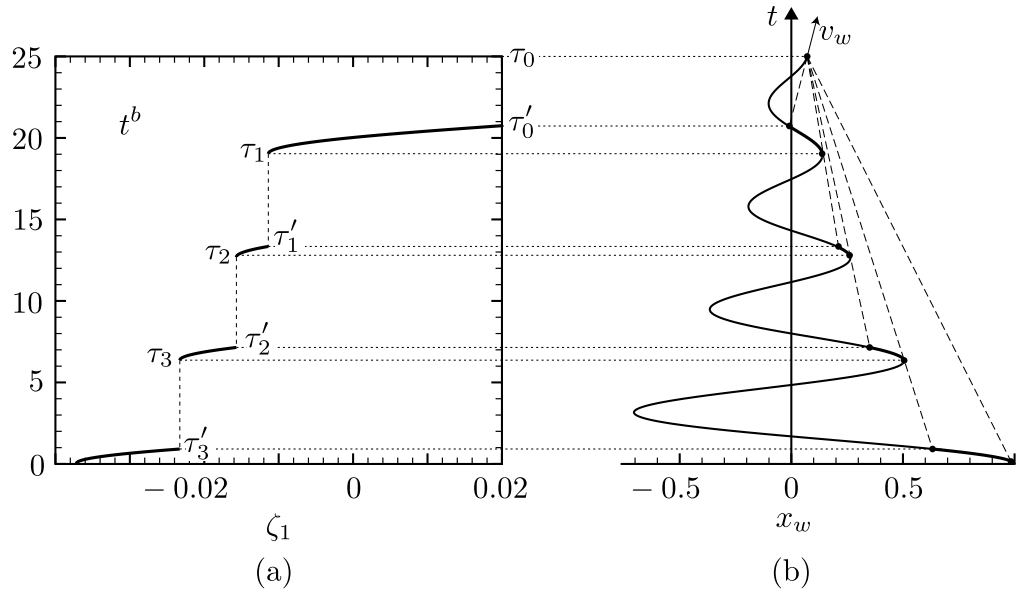

Fig. 3.2 The discontinuities of the function $t^b(\zeta_1,\, t)$ at a given t. (a) The $t^b(\zeta_1,\, t)$ at $t = 25$ as the function of ζ_1. (b) The trajectory $x_w(t)$ of the disk for $0 \le t \le 25$. The parameters are set as $d = 3$, $M = 4$, $L = 1$, $x_{w0} = 1$, $v_{w0} = 0$, and $\mathrm{Kn} = \infty$ (collisionless gas).

positions of discontinuities and the values of t^b at both sides of the discontinuities. For simplicity, we discuss only the "+" side, i.e., for $x_i \in \partial\tilde{S}_+(t^{(n+1)})$. The situation is shown in Fig. 3.2, i.e., the actual trajectory $x_w(t)$ [$0 \le t \le t^{(n+1)} = 25$] is shown for $d = 1$, $M = 4$, $L = 1$, $x_{w0} = 1$, $v_{w0} = 0$, and $\mathrm{Kn} = \infty$ (collisionless gas) in Fig. 3.2(b), and the corresponding t^b at $t = 25$ is shown as the function of ζ_1 in Fig. 3.2(a). Then, it is obvious that the positions of the discontinuities and the values of t^b there are obtained by inspecting the tangential lines of the trajectory. To be more specific, we first solve the following equation to obtain τ:

$$x_w^{(n+1)} - t^{(n+1)} \left.\frac{d\psi_k}{dt}\right|_{t=\tau} = \psi_k(\tau) - \tau \left.\frac{d\psi_k}{dt}\right|_{t=\tau}, \quad \text{for} \quad k = 0,\, ...,\, n, \tag{3.55}$$

recalling that the trajectory $x_w(t)$ for $t \in [0,\, t^{(n+1)}]$ has been approximated piecewisely by cubic polynomials ψ_k ($k = 0,\, ...,\, n$) [cf. the last paragraph of Sec. 5.1]. If τ satisfies the condition for t^b [Eq. (3.24) with $t = t^{(n+1)}$] and $\tau \in [t^{(k)},\, t^{(k+1)}]$, then t^b is discontinuous at $\zeta_1 = \eta$ such that $t^b(\eta,\, t^{(n+1)}) = \tau$. By definition, τ is the value of $t^b(\zeta_1,\, t^{(n+1)})$ at $\zeta_1 = \eta + 0$. If we denote by τ' the value of $t^b(\zeta_1,\, t^{(n+1)})$ at $\zeta_1 = \eta - 0$, then it is obtained as

$$\tau' = \max\left\{ \psi_k(\tau) - \tau \left.\frac{d\psi_k}{dt}\right|_{t=\tau} = \psi_{k'}(\tau') - \tau' \left.\frac{d\psi_k}{dt}\right|_{t=\tau} \right\},$$
$$\left(\tau \in [t^{(k)},\, t^{(k+1)}],\;\; \tau' \in [t^{(k')},\, t^{(k'+1)}],\;\; k \ge k'\right). \tag{3.56}$$

If there is no k' satisfying Eq. (3.56), then $\tau' = 0$. In Fig. 3.2(a), τ's and τ''s are numbered as $t^{(n+1)} = \tau_0 > \tau_0' > \tau_1 > \tau_1' > \tau_2 > \tau_2' > \cdots$. Equations (3.55) and (3.56) are solved by the Newton method.

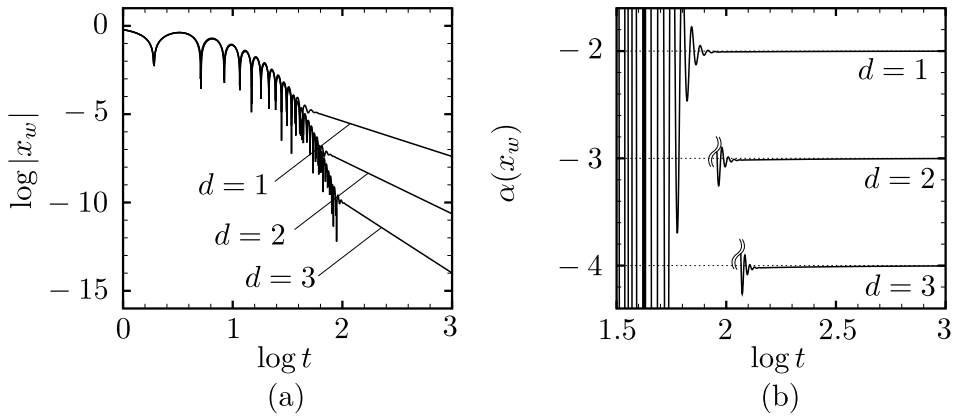

Fig. 3.3 The decay of the displacement $x_w(t)$ for $d = 1$, 2, and 3 in the case of $M = 4$, $L = 1$ ($d = 2$ and 3), $x_{w0} = 1$, and $v_{w0} = 0$ (collisionless gas: $\mathrm{Kn} = \infty$). (a) $\log_{10} |x_w|$ vs $\log_{10} t$. (b) The gradient $\alpha(x_w)$ of the curve in panel (a) vs $\log_{10} t$.

5.4 Data for computation

The numerical results that will be shown in Sec. 6 are based on $\Delta t = 0.02$ and $N_r = 16$ and $N_\theta = 32$ for $d = 3$. We have confirmed, with computations using different grid systems, that this sytem is enough for necessary accuracy. The computation was carried out with quadruple precision. We have used fast algorithms for the error and Bessel functions provided by T. Ooura, available from his home page (http://www.kurims.kyoto-u.ac.jp/~ooura/index.html). The algorithms are for double precision, but we have confirmed that they give an accuracy of 19 significant figures if they are used in a quadruple-precision computation.

The computation has been carried out on a PC cluster with CPU: Intel(R) Core 2 Extreme QX9650 3.0GHz(4CPU)×8.

6 Results

In this section, we present some numerical results, focusing our attention on the manner of decay of the displacement $x_w(t)$ of the disk at long times.

6.1 Collisionless gas

First, we show the results for the collisionless gas (cf. Sec. 2.2.1), which can also be regarded as the special case $\mathrm{Kn} = \infty$ of Eq. (3.12). Figure 3.3 contains the decay properties of the displacement $x_w(t)$ of the disk at long times for the d-dimensional problems ($d = 1$, 2, and 3; see Fig. 3.1) in the case of $M = 4$, $L = 1$ ($d = 2$ and 3), $x_{w0} = 1$, and $v_{w0} = 0$: Fig. 3.3(a) shows the plot $\log_{10} |x_w(t)|$ versus $\log_{10} t$, and Fig. 3.3(b) shows the gradient $\alpha(x_w)$ of the curve in Fig. 3.3(a), i.e.,

$$\alpha(x_w) = d \log_{10} |x_w(t)| / d \log_{10} t. \tag{3.57}$$

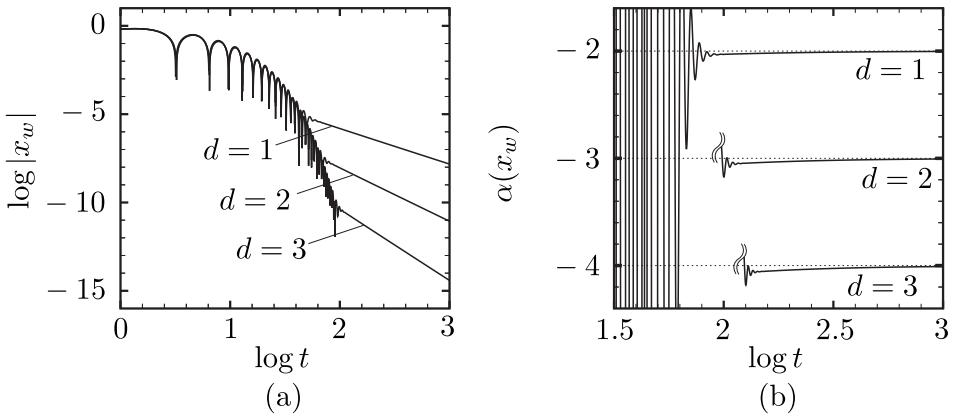

Fig. 3.4 The decay of the displacement $x_w(t)$ for $d = 1$, 2, and 3 in the case of $M = 4$, $L = 1$ ($d = 2$ and 3), $x_{w0} = 0$, and $v_{w0} = 1$ (collisionless gas: $\mathrm{Kn} = \infty$). (a) $\log_{10} |x_w|$ vs $\log_{10} t$. (b) The gradient $\alpha(x_w)$ of the curve in panel (a) vs $\log_{10} t$.

Table 3.1 The values of the gradient $\alpha(x_w)$ of the curve $\log_{10} |x_w|$ vs $\log_{10} t$ for $d = 1$, 2, and 3 and for $M = 1$, 4, and 10 in the case of $L = 1$ ($d = 2$ and 3), $x_{w0} = 1$, and $v_{w0} = 0$ (collisionless gas: $\mathrm{Kn} = \infty$). See Fig. 3.3 for $M = 4$.

		$-\alpha(x_w)$								
		$d = 1$			$d = 2$			$d = 3$		
t	$\log t$	$M = 10$	$M = 4$	$M = 1$	$M = 10$	$M = 4$	$M = 1$	$M = 10$	$M = 4$	$M = 1$
10.00	1.0	—*	—*	3.6368	—*	—*	7.5391	—*	—*	8.5635
31.62	1.5	—*	—*	2.1620	—*	—*	3.3034	—*	—*	4.4575
100.00	2.0	—*	2.0074	2.0463	—*	3.0476	3.0813	—*	—*	4.1167
316.23	2.5	1.9821	2.0029	2.0143	2.9941	3.0066	3.0246	—*	4.0100	4.0351
398.11	2.6	1.9860	2.0024	2.0113	2.9863	3.0053	3.0195	3.9896	4.0081	4.0277
630.96	2.8	1.9914	2.0015	2.0071	2.9916	3.0034	3.0122	3.9916	4.0052	4.0174
1000.00	3.0	1.9946	2.0010	2.0045	2.9948	3.0022	3.0077	3.9952	4.0036	4.0113
1995.26	3.3	1.9974	⋯	2.0022	2.9974	⋯	3.0038	⋯	⋯	⋯
3162.28	3.5	1.9983	⋯	2.0014	⋯	⋯	⋯	⋯	⋯	⋯
10000.00	4.0	1.9995	⋯	2.0004	⋯	⋯	⋯	⋯	⋯	⋯

*Values are omitted because of the strong oscillation of $\alpha(x_w)$ [see e.g. Fig. 3.3(b)].

Table 3.1 shows the values of $\alpha(x_w)$ corresponding to Fig. 3.3(b) as well as its values for $M = 1$ and 10. Figure 3.4 is the counterpart of Fig. 3.3 with different initial conditions of the disk, $x_{w0} = 0$ and $v_{w0} = 1$, and Table 3.2 shows the numerical values of $\alpha(x_w)$ corresponding to Fig. 3.4(b). These figures and tables supplement our earlier work [6], in which only the case of $d = 1$ is investigated.

The results contained in Figs. 3.3 and 3.4 and Tables 3.1 and 3.2, together with those of other cases that are not shown in this paper, provide some pieces of numerical evidence for the decay

Table 3.2 The values of the gradient $\alpha(x_w)$ of the curve $\log_{10}|x_w|$ vs $\log_{10} t$ for $d = 1$, 2, and 3 in the case of $M = 4$, $L = 1$ ($d = 2$ and 3), $x_{w0} = 0$, and $v_{w0} = 1$ (collisionless gas: $\mathrm{Kn} = \infty$). See Fig. 3.4.

		$-\alpha(x_w)$		
t	$\log t$	$d = 1$	$d = 2$	$d = 3$
100.00	2.0	2.0309	3.1730	—*
158.49	2.2	2.0197	3.0364	4.0521
251.19	2.4	2.0127	3.0233	4.0333
398.11	2.6	2.0081	3.0148	4.0212
630.96	2.8	2.0052	3.0094	4.0135
1000.00	3.0	2.0033	3.0059	4.0092

*Values are omitted because of the strong oscillation of $\alpha(x_w)$ [see e.g. Fig. 3.4(b)].

rate (3.2), i.e.,

$$|x_w(t)| \approx C/t^{d+1}, \tag{3.58}$$

for large t, where and hereafter C symbolically denotes a constant with respect to t that may depend on other parameters.

As was proven mathematically in [1, 2, 3, 4] and then confirmed numerically in [5, 6], the slow algebraic decay is attributed to the long-memory effect caused by multiple collisions of a gas molecule with the disk. In general, when a body is moving freely in a collisionless gas under the action of an external force, the body is accelerated or decelerated by the force. In this situation, the molecules that are reflected by the body at early times may hit the body again and again at later times. Such molecules transfer information about the body at early stages directly to the body at later times and may affect the motion of the body long time later. That is, they give rise to a long-memory effect. In fact, if the effect of the multiple collisions is neglected, the decay is exponential in time [1, 2]. Our next interest is how the decay rate is modified if the long-memory effect is destroyed by some means. This is the reason why we consider the toy model Eq. (3.12) based on the special Lorentz gas.

6.2 Special Lorentz gas: Case of resting obstacles

We first consider Eq. (3.12) with $\epsilon = 0$, which corresponds to the case where the obstacles are at rest in the special Lorentz gas. We show some results in this case in Figs. 3.5 and 3.6 as well as Tables 3.3 and 3.4. Figure 3.5(a) shows the curves $\log_{10}|x_w(t)|$ versus $\log_{10} t$ in the one-dimensional problem ($d = 1$) with initial condition $x_{w0} = 1$ and $v_{w0} = 0$ for $M = 1$ (monotonic decay) and 10 (oscillatory decay) and for $\mathrm{Kn} = 10$ and 10^2 together with the collisionless case ($\mathrm{Kn} = \infty$), and the gradient $\alpha(x_w)$ of each curve is plotted versus $\log_{10} t$ in Fig. 3.5(b). Some values of $\alpha(x_w)$ at large times are shown in Table 3.3. Figure 3.6 is the corresponding figure in the three-dimensional problem ($d = 3$) with initial condition $x_{w0} = 1$ and $v_{w0} = 0$ for $M = 1$ and $L = 1$ and for $\mathrm{Kn} = 1$, 10, 10^2 and ∞ (collisionless gas). Table 3.4 shows some values of the gradient $\alpha(x_w)$ in Fig. 3.6 at large times.

From these results, it is likely that the displacement $x_w(t)$ of the disk decays as

$$|x_w(t)| \approx C/t^4, \tag{3.59}$$

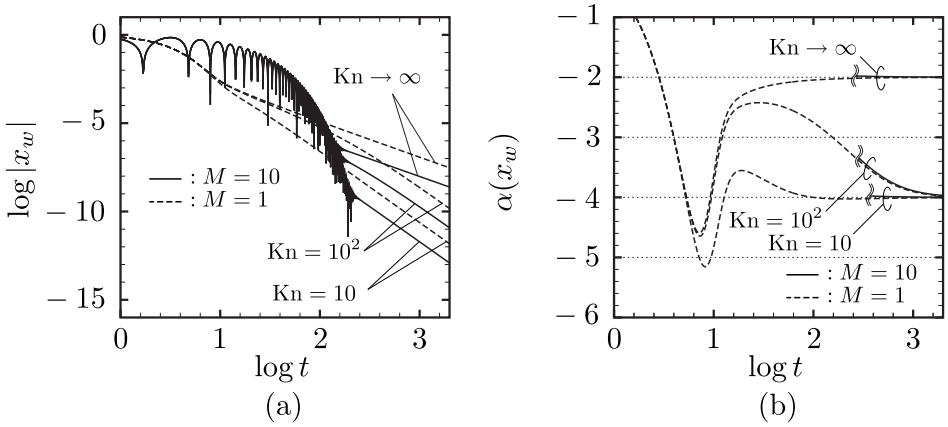

Fig. 3.5 The decay of the displacement $x_w(t)$ for $d = 1$, $x_{w0} = 1$, and $v_{w0} = 0$ [special Lorentz gas with resting obstacle: Eq. (3.12) with $\epsilon = 0$]. (a) $\log_{10}|x_w|$ vs $\log_{10} t$. (b) The gradient $\alpha(x_w)$ of the curve in panel (a) vs $\log_{10} t$. The solid line is for $M = 10$ (oscillatory decay), and the dashed line is for $M = 1$ (monotonic decay). The results for $\mathrm{Kn} = 10$, 10^2, and ∞ (collisionless gas) are shown in the figures.

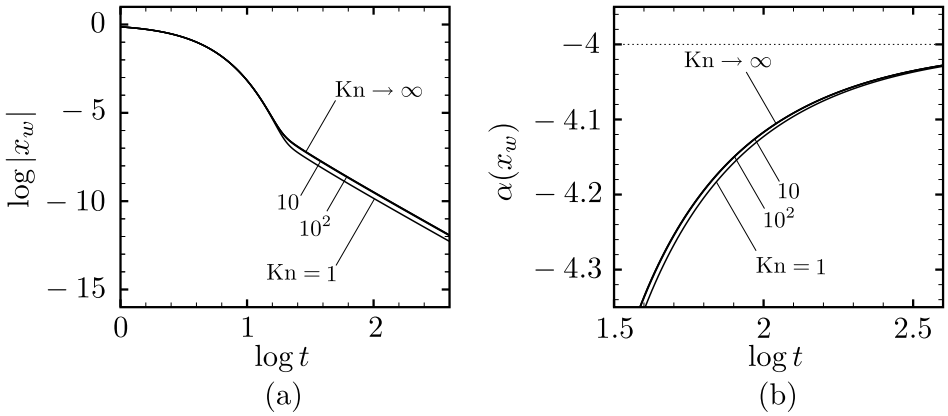

Fig. 3.6 The decay of the displacement $x_w(t)$ for $d = 3$, $M = 1$, $L = 1$, $x_{w0} = 1$, and $v_{w0} = 0$ [special Lorentz gas with resting obstacle: Eq. (3.12) with $\epsilon = 0$]. (a) $\log_{10}|x_w|$ vs $\log_{10} t$. (b) The gradient $\alpha(x_w)$ of the curve in panel (a) vs $\log_{10} t$. The results for $\mathrm{Kn} = 1$, 10, 10^2, and ∞ (collisionless gas) are shown in the figures.

for large t, independent of the dimension d of the problem. This is different from Eq. (3.58) for a collisionless gas, but the rate is still algebraic. Unlike the collisionless case, the gas molecules reflected by the disk generally hit the obstacles before hitting the disk again. Therefore, the long-memory effect in the collisionless gas is destroyed in the present case. However, since the obstacles are at rest, slow molecules among the reflected molecules may not interact with the obstacles before they are hit again by the disk. In this sense, the long-memory effect is not completely destroyed. This may be the reason why we still have an algebraic decay. In the present setting, the obstacles are three dimensional (spheres of uniform size) and randomly distributed in the three-dimensional space, irrespective of the dimension d of the problem shown in Fig. 3.1. Therefore, it is natural

Table 3.3 The values of the gradient $\alpha(x_w)$ of the curve $\log_{10}|x_w|$ vs $\log_{10} t$ for $d = 1$, $x_{w0} = 1$, and $v_{w0} = 0$ [special Lorentz gas with resting obstacle: Eq. (3.12) with $\epsilon = 0$]. See Fig. 3.5.

		$-\alpha(x_w)$					
		Kn $\to \infty$		Kn $= 10^2$		Kn $= 10$	
t	$\log t$	$M = 10$	$M = 1$	$M = 10$	$M = 1$	$M = 10$	$M = 1$
316.23	2.5	1.9821	2.0143	3.4116	3.4517	3.9827	4.0229
1000.00	3.0	1.9946	2.0045	3.8891	3.9041	3.9938	4.0097
1995.26	3.3	1.9974	2.0022	3.9684	3.9762	3.9972	4.0052
10000.00	4.0	1.9995	2.0004	...	...	...	...

Table 3.4 The values of the gradient $\alpha(x_w)$ of the curve $\log_{10}|x_w|$ vs $\log_{10} t$ for $d = 3$, $M = 1$, $L = 1$, $x_{w0} = 1$, and $v_{w0} = 0$ [special Lorentz gas with resting obstacle: Eq. (3.12) with $\epsilon = 0$]. See Fig. 3.6.

		$-\alpha(x_w)$			
t	$\log t$	Kn$\to \infty$	Kn$= 10^2$	Kn$= 10$	Kn$= 1$
10.00	1.0	8.5635	8.5641	8.5698	8.6089
25.12	1.4	4.8025	4.8041	4.8192	5.0253
63.10	1.8	4.1942	4.1943	4.1952	4.2043
158.49	2.2	4.0716	4.0716	4.0719	4.0752
398.11	2.6	4.0277	4.0277	4.0279	4.0291

that the decay rate (3.59) is independent of d. For instance, the rate may change if the obstacles are two-dimensional cylinders distributed randomly in the x_1x_2 space in the two dimensional problem ($d = 2$).

6.3 Special Lorentz gas: Case of moving obstacles

Finally we consider Eq. (3.12) with non-zero ϵ, which corresponds to the case where the obstacles are moving with low speed (cf. Appendix). Some results for the decay property of the displacement are shown in Figs. 3.7–3.9 as well as Tables 3.5– 3.7. Figure 3.7(a) shows the curves $\log_{10}|x_w(t)|$ versus $\log_{10} t$ in the one-dimensional problem ($d = 1$) with initial condition $x_{w0} = 1$ and $v_{w0} = 0$ for $M = 1$ (monotonic decay), $\mathrm{Kn} = 10$ and ∞ (collisionless case), and various values of ϵ including $\epsilon = 0$ (case of resting obstacles). The gradient $\alpha(x_w)$ of each curve in Fig. 3.7(a) is plotted versus $\log_{10} t$ in Fig. 3.7(b), and some values of $\alpha(x_w)$ at large times are shown in Table 3.5. Figure 3.8 and Table 3.6 are the corresponding figure and table for oscillatory decay, that is, for $d = 1$, $M = 10$, $\mathrm{Kn} = 10$ and ∞, and various ϵ with initial condition $x_{w0} = 1$ and $v_{w0} = 0$. Then, Fig. 3.9 and Table 3.7 show the corresponding results in the three-dimensional problem ($d = 3$) for $M = 1$ (monotonic decay), $L = 1$, $\mathrm{Kn} = 10$ and ∞, and various ϵ with initial condition $x_{w0} = 1$ and $v_{w0} = 0$.

It is seen from these results that, when $\epsilon \neq 0$, the gradient $\alpha(x_w)$ decreases faster and faster as time t increases for large t. This suggests that the decay rate is exponential in t. To see it more clearly, we plot, in Fig. 3.10(a), $\log_{10}|t^4 x_w(t)|$ versus t in the same case as in Fig. 3.9 and, in

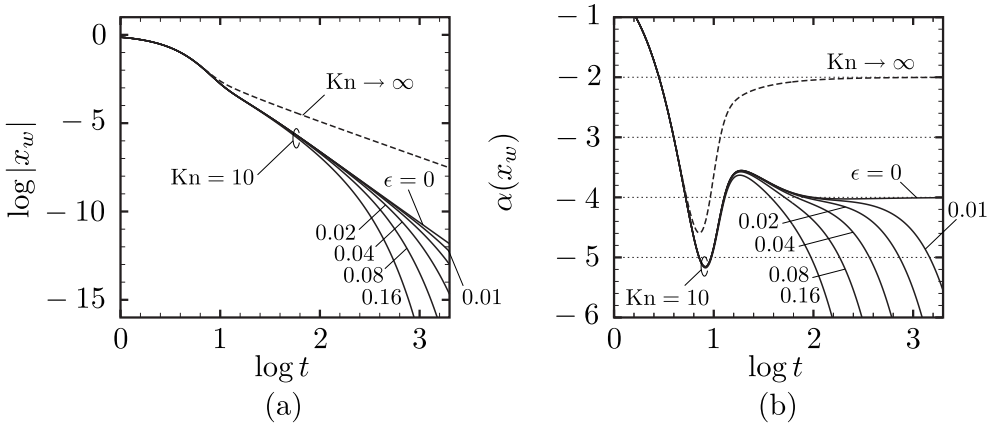

Fig. 3.7 The decay of the displacement $x_w(t)$ for $d = 1$, $M = 1$, $x_{w0} = 1$, and $v_{w0} = 0$ [special Lorentz gas with moving obstacle: Eq. (3.12)]. (a) $\log_{10}|x_w|$ vs $\log_{10} t$. (b) The gradient $\alpha(x_w)$ of the curve in panel (a) vs $\log_{10} t$.

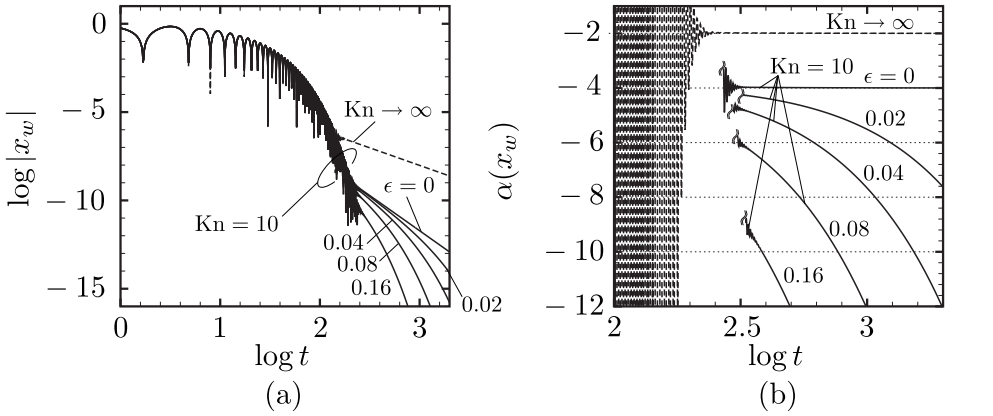

Fig. 3.8 The decay of the displacement $x_w(t)$ for $d = 1$, $M = 10$, $x_{w0} = 1$, and $v_{w0} = 0$ [special Lorentz gas with moving obstacle: Eq. (3.12)]. (a) $\log_{10}|x_w|$ vs $\log_{10} t$. (b) The gradient $\alpha(x_w)$ of the curve in panel (a) vs $\log_{10} t$.

Fig. 3.10(b), the gradient of the curve in Fig. 3.10(a), i.e.,

$$\beta(x_w) = d \log_{10} |t^4 x_w(t)|/dt. \tag{3.60}$$

Figure 3.10(b) indicates that the gradient $\beta(x_w)$ tends to approach a non-zero constant value, depending on ϵ, when $\epsilon \neq 0$. For $\epsilon = 0.16$, the curve deviates from the constant value for t larger than about 400. This may be due to the numerical error, since $|x_w(t)|$ is too small for accurate computation in this case [see Fig. 3.9(a)]. Some values of $\beta(x_w)$ are shown for large t in Table 3.8. From these results, the decay of $x_w(t)$ for large t is likely to be

$$|x_w(t)| \approx C t^{-4} \exp(-\overline{\beta}\, t), \tag{3.61}$$

with constant $\overline{\beta}$ (depending on the parameters) for $d = 3$. However, for $d = 1$ and 2, the numerical result does not show clear decay property as in the case of $d = 3$.

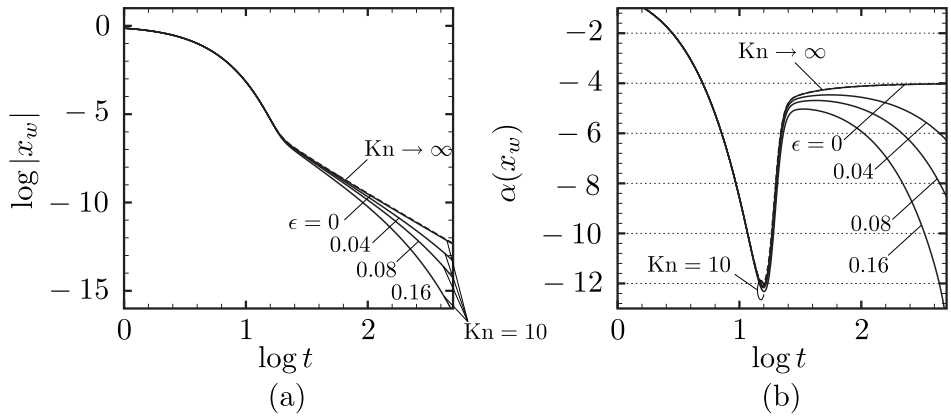

Fig. 3.9 The decay of the displacement $x_w(t)$ for $d = 3$, $M = 1$, $L = 1$, $x_{w0} = 1$, and $v_{w0} = 0$ [special Lorentz gas with moving obstacle: Eq. (3.12)]. (a) $\log_{10}|x_w|$ vs $\log_{10} t$. (b) The gradient $\alpha(x_w)$ of the curve in panel (a) vs $\log_{10} t$.

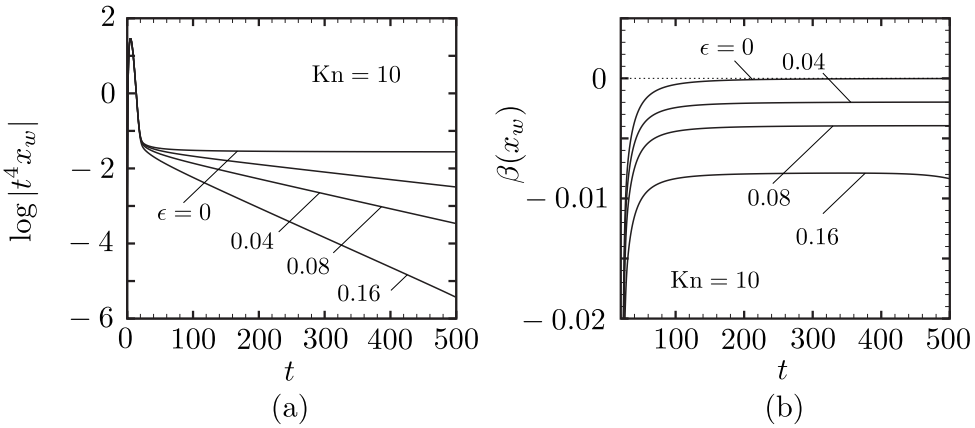

Fig. 3.10 The decay of $t^4 x_w(t)$ in the case of Fig. 3.9 and Table 3.7. (a) $\log_{10}|t^4 x_w|$ vs t. (b) The gradient $\beta(x_w)$ of the curve in panel (a) vs t.

Contrary to the case of resting obstacles, even slow molecules among the reflected molecules are hit by the moving obstacles in the present case of $\epsilon \neq 0$. Therefore, almost no information about the motion of the disk is transmitted directly to the later time. In other words, the long-memory effect caused by multiple collisions of a gas molecule with the disk is eliminated. As the consequence, we have a faster decay, such as given by Eq. (3.61). The decay is faster for larger ϵ because the obstacles moving with higher speed have more chances to collide with the gas molecules.

7 Concluding remarks

In the present study, we have investigated unsteady motion of a disk in a gas under the action of an external force obeying Hooke's law, with special interest in the manner of decay of the motion caused by the drag force exerted by the gas. We first considered the case where the gas is a

highly rarefied collisionless gas (free-molecular gas or the Knudsen gas) and provided some pieces of numerical evidence for the decay of the displacement described by Eq. (3.2) or (3.58). These results complement our previous numerical results for the one-dimensional case ($d = 1$) [6] as well as the rigorous mathematical results for the case of non-oscillatory decay [2] [specular reflection rather than diffuse reflection is employed in [2], so that the decay rate is given by Eq. (3.1)]. The slow algebraic decay is attributed to the long-memory effect caused by multiple collisions of a gas molecules with the disk, as proven mathematically in [1, 2, 3, 4] and confirmed numerically in [5, 6]. In fact, the decay becomes exponentially fast if the multiple collisions are neglected by assuming that all the molecules incident on the disk come from the initial velocity distribution.

Our next interest was to see how the decay rate is modified when the long-memory effect is destroyed by some means. For this purpose, we have introduced a toy model, Eq. (3.12), whose physical basis is a type of the Lorentz gas consisting of free-streaming gas (vapor) molecules and randomly distributed spherical obstacles (droplets of the liquid or solid phase of the vapor) with which the gas molecules interact. Our numerical results show the following: The decay rate is still algebraic when $\epsilon = 0$ in Eq. (3.12), which corresponds to the case of resting obstacles, but we have a faster decay rate that is likely to be exponential in time when $\epsilon \neq 0$, which corresponds to the case of moving obstacles. This result seems to be natural, since the moving obstacles destroy the memory of the gas molecules almost completely. However, if we consider a real gas with collisions between gas molecules, the manner of decay of the motion of the disk may be different from the case of the present toy model. In this connection, it should be mentioned that the decay rate of translational and rotational motion (monotonic and oscillatory decay) of a spherical body

Table 3.5 The values of the gradient $\alpha(x_w)$ of the curve $\log_{10}|x_w|$ vs $\log_{10} t$ for $d = 1$, $M = 1$, $x_{w0} = 1$, and $v_{w0} = 0$ [special Lorentz gas with moving obstacle: Eq. (3.12)]. See Fig. 3.7.

		$-\alpha(x_w)$						
		Kn$\to\infty$	Kn$=10$					
t	$\log t$	—	$\epsilon = 0$	$\epsilon = 0.01$	$\epsilon = 0.02$	$\epsilon = 0.04$	$\epsilon = 0.08$	$\epsilon = 0.16$
316.23	2.5	2.0143	4.0229	4.1044	4.2963	4.8191	6.0808	8.8256
630.96	2.8	2.0071	4.0143	4.2839	4.8181	6.0871	8.8150	14.4522
1000.00	3.0	2.0045	4.0097	4.5708	5.5291	7.6797	12.1092	$\cdots$
1995.26	3.3	2.0022	4.0052	5.5526	7.6319	12.0896	$\cdots$	$\cdots$

Table 3.6 The values of the gradient $\alpha(x_w)$ of the curve $\log_{10}|x_w|$ vs $\log_{10} t$ for $d = 1$, $M = 10$, $x_{w0} = 1$, and $v_{w0} = 0$ [special Lorentz gas with moving obstacle: Eq. (3.12)]. See Fig. 3.8.

		$-\alpha(x_w)$					
		Kn$\to\infty$	Kn$=10$				
t	$\log t$	—	$\epsilon = 0$	$\epsilon = 0.02$	$\epsilon = 0.04$	$\epsilon = 0.08$	$\epsilon = 0.16$
316.23	2.5	1.9821	3.9827	4.2596	4.7898	6.0830	9.2442
630.96	2.8	1.9914	3.9888	4.7939	6.0642	8.7931	14.4310
1000.00	3.0	1.9946	3.9938	5.5144	7.6655	12.0959	$\cdots$
1995.26	3.3	1.9974	3.9972	7.6254	12.0866	$\cdots$	$\cdots$

Table 3.7 The values of the gradient $\alpha(x_w)$ of the curve $\log_{10}|x_w|$ vs $\log_{10} t$ for $d = 3$, $M = 1$, $L = 1$, $x_{w0} = 1$, and $v_{w0} = 0$ [special Lorentz gas with moving obstacle: Eq. (3.12)]. See Fig. 3.9.

		$-\alpha(x_w)$				
		Kn$\to\infty$	Kn$=10$			
t	$\log t$	—	$\epsilon = 0$	$\epsilon = 0.04$	$\epsilon = 0.08$	$\epsilon = 0.16$
100.00	2.0	4.1167	4.1173	4.5613	5.0168	5.9224
158.49	2.2	4.0716	4.0719	4.7827	5.5006	6.9332
251.19	2.4	4.0444	4.0446	5.1755	6.3109	8.5797
398.11	2.6	4.0277	4.0279	5.8230	7.6214	11.2453

Table 3.8 The values of the gradient $\beta(x_w)$ of the curve $\log_{10}|t^4 x_w|$ vs t in the case of Fig. 3.9 and Table 3.7.

		$-\beta(x_w)$			
t	$\log t$	$\epsilon = 0$	$\epsilon = 0.04$	$\epsilon = 0.08$	$\epsilon = 0.16$
100.00	2.000	5.0957×10^{-4}	2.4379×10^{-3}	4.4162×10^{-3}	8.3495×10^{-3}
149.97	2.176	2.2075×10^{-4}	2.1668×10^{-3}	4.1350×10^{-3}	8.0610×10^{-3}
199.99	2.301	1.2260×10^{-4}	2.0749×10^{-3}	4.0396×10^{-3}	7.9631×10^{-3}
250.03	2.398	7.7865×10^{-5}	2.0330×10^{-3}	3.9961×10^{-3}	7.9188×10^{-3}
299.92	2.477	5.3861×10^{-5}	2.0106×10^{-3}	3.9728×10^{-3}	7.8965×10^{-3}
349.95	2.544	3.9427×10^{-5}	1.9971×10^{-3}	3.9590×10^{-3}	—*
399.94	2.602	3.0113×10^{-5}	1.9884×10^{-3}	3.9503×10^{-3}	—*
449.78	2.653	2.3771×10^{-5}	1.9825×10^{-3}	3.9450×10^{-3}	—*
498.88	2.698	1.9299×10^{-5}	1.9785×10^{-3}	3.9426×10^{-3}	—*

*Values are omitted because of the loss of accuracy [see Fig. 3.10(b)].

was investigated mathematically when the surrounding fluid is the viscous Stokes fluid [8, 9]. In this case, the decay rate was proven to be algebraic in time. This fact also provides a motivation to study the present problem for the gas with intermolecular collisions. This will be a subject of the next stage of our study.

Finally, it should be remarked that the present problem has some similarity to the so-called piston problem, which is a fundamental problem in statistical physics (see [14, 15, 16] and the references therein). In [17, 18], for instance, an unsteady motion of a piston has been investigated numerically, using particle methods, when the movable piston is placed in a closed container, the gas is collisionless, and the boundary condition is specular reflection. In this case, the oscillating motion of the piston is caused by instability of a mechanical equilibrium [19], rather than an external force as considered in the present paper.

A Special Lorentz gas: Derivation of Eqs. (3.5) and (3.12)

In this section, we consider a physical model that can be said to be a special version of the Lorentz gas [10, 11] and give a physical derivation of the corresponding equations, Eqs. (3.5) and

(3.12), along the same line as the original derivation of the Boltzmann equation [12]. In particular, we follow the argument in [13].

A.1 Physical model

We consider, as in the main text, a gas composed of hard-sphere molecules of mass m and radius r, whose velocity distribution function is denoted by $f_*(X_i,\, \xi_i,\, t_*)$. In the gas, spherical obstacles of uniform size (mass m_s and radius r_s) are distributed randomly. We suppose that the gas is the vapor of a substance and the obstacles are made of the condensed phase of the same substance, so that evaporation and condensation of the gas may take place on the surface of the obstacles. A physical image may be given by a system composed of a dilute water vapor and tiny water droplets suspended in it, though only a monatomic gas is considered in the present paper. As described in Sec. 2.2.2, the obstacles are moving with velocity ξ_{si}. Our assumptions on the model are as follows:

1. Gas molecules hitting an obstacle are absorbed in it.
2. The obstacles emit the gas molecules according to a given velocity distribution $f_{*v}(\xi_i - \xi_{si})$, which is uniform in space and constant in time.
3. The motion of the obstacles are not affected by the interaction with the gas molecules or other obstacles, and their velocities ξ_{si} are distributed according to a given velocity distribution $f_{*s}(\xi_{si})$, which is uniform in space and constant in time.
4. Collisions between gas molecules can be neglected.
5. No external force acts on the gas molecules.

The first and second assumptions correspond to the usual boundary condition for the Boltzmann equation on the interface on which evaporation or condensation is taking place (for instance, the complete condensation condition [7]). The fourth assumption is realized when the number density of the gas molecules n_* and that of the obstacles n_{*s}, defined by

$$n_* = \frac{1}{m}\int_{\mathbb{R}^3} f_* d\boldsymbol{\xi}, \qquad n_{*s} = \frac{1}{m_s}\int_{\mathbb{R}^3} f_{*s} d\boldsymbol{\xi_s}, \tag{3.62}$$

satisfy the condition

$$\max_{X_i\in\mathbb{R}^3,\, t\in\mathbb{R}_+} n_* r^2 \ll n_{*s} r_s^2, \tag{3.63}$$

as will be discussed in Sec. A.2.2.

A.2 Kinetic equations for the model

We first derive the general form of the kinetic equation for the physical model introduced in Sec. A.1 (Sec. A.2.1). Then we simplify the kinetic equation with the help of special choices of f_{*s} and f_{*v} (Sec. A.2.3). In the mean time, the discussion about the mean free path will be given in Sec. A.2.2.

A.2.1 General Form

Proposition 1 *For the physical model described in Sec. A.1 (the special Lorentz gas), the velocity distribution function of the gas molecules $f_*(X_i,\, \xi_i,\, t_*)$ satisfies Eqs.* (3.5) *and* (3.6)*.*

Proof Let $d\boldsymbol{X}d\boldsymbol{\xi}$ denote a small neighborhood of (X_i, ξ_i) in the six-dimensional phase space. Then, $(f_*/m)d\boldsymbol{X}d\boldsymbol{\xi}$ represents the number of gas molecules in $d\boldsymbol{X}d\boldsymbol{\xi}$. Suppose that the volume $d\boldsymbol{X}d\boldsymbol{\xi}$ is moving according to the equation of motion:

$$\frac{dX_i}{dt_*} = \xi_i, \qquad \frac{d\xi_i}{dt_*} = 0. \tag{3.64}$$

Therefore, the volume $d\boldsymbol{X}d\boldsymbol{\xi}$ at time t_* moves to the volume $d\overline{\boldsymbol{X}}d\overline{\boldsymbol{\xi}}$ at time $\bar{t}_* = t_* + dt_*$, which is a small neighborhood of the point

$$\overline{X}_i = X_i + \xi_i dt_*, \qquad \overline{\xi}_i = \xi_i, \tag{3.65}$$

where dt_* is a small increment of time. Since $d\boldsymbol{X}d\boldsymbol{\xi} = d\overline{\boldsymbol{X}}d\overline{\boldsymbol{\xi}}$ holds, the difference between the number of molecules in $d\overline{\boldsymbol{X}}d\overline{\boldsymbol{\xi}}$ and that in $d\boldsymbol{X}d\boldsymbol{\xi}$ is given by

$$\begin{aligned}&\frac{1}{m}f_*(\overline{X}_i,\, \overline{\xi}_i,\, \bar{t}_*)d\overline{\boldsymbol{X}}d\overline{\boldsymbol{\xi}} - \frac{1}{m}f_*(X_i,\, \xi_i,\, t_*)d\boldsymbol{X}d\boldsymbol{\xi}\\ =&\frac{1}{m}\left[\frac{\partial f_*}{\partial t_*} + \xi_i\frac{\partial f_*}{\partial X_i} + O(dt_*)\right]d\boldsymbol{X}d\boldsymbol{\xi}dt_*.\end{aligned} \tag{3.66}$$

This is equal to the increase of the number of molecules in the volume $d\boldsymbol{X}d\boldsymbol{\xi}$ minus its decrease during the time interval dt_* because of collisions with the obstacles, which can be expressed as

$$\frac{1}{m}J_{\mathrm{gain}}(\overline{X}_i,\, \overline{\xi}_i,\, \bar{t}_*)d\overline{\boldsymbol{X}}d\overline{\boldsymbol{\xi}}dt_* - \frac{1}{m}J_{\mathrm{loss}}(X_i,\, \xi_i,\, t_*)d\boldsymbol{X}d\boldsymbol{\xi}dt_*. \tag{3.67}$$

More precisely, the first term in Eq. (3.67) (the gain term) indicates the number of molecules that are contained in the volume $d\overline{\boldsymbol{X}}d\overline{\boldsymbol{\xi}}$ at time $\bar{t}_*$ and have emitted from the obstacles during dt_*. The second term in Eq. (3.67) (the loss term) indicates the number of molecules that were contained in the volume $d\boldsymbol{X}d\boldsymbol{\xi}$ at time t_* and have hit the obstacles during dt_*. We recall here that we have neglected the collision between gas molecules (see Sec. A.2.2).

Now we try to derive the explicit form of J_{loss} and J_{gain}.

Loss Term : J_{loss} Consider an obstacle moving with a velocity $\boldsymbol{\xi}_s$ contained in the volume $d\boldsymbol{X}$. We denote a unit vector at the center of the obstacle by $\boldsymbol{\alpha}$ and the solid-angle element around $\boldsymbol{\alpha}$ by $d\Omega(\boldsymbol{\alpha})$. The number of the molecules with velocity in the small neighborhood $d\boldsymbol{\xi}$ around $\boldsymbol{\xi}$ and hitting the obstacle during dt_* is given by the number of the molecules contained in the cylinder with height $|(\boldsymbol{\xi} - \boldsymbol{\xi}_s)\cdot\boldsymbol{\alpha}|dt_*$ and the base area $d_s^2\Omega(\boldsymbol{\alpha})$ ($d_s = r + r_s$) in Fig. 3.11(a), i.e.,

$$\frac{1}{m}f_*(X_i,\, \xi_i,\, t_*)d\boldsymbol{\xi} \times |(\boldsymbol{\xi} - \boldsymbol{\xi}_s)\cdot\boldsymbol{\alpha}|dt_* \times d_s^2 d\Omega(\boldsymbol{\alpha}) \times \mathbf{1}_{\{(\boldsymbol{\xi}-\boldsymbol{\xi}_s)\cdot\boldsymbol{\alpha}<0\}}, \tag{3.68}$$

where $\mathbf{1}_A$ is the characteristic function of a set A. By integrating Eq. (3.68) for all $\boldsymbol{\alpha}$, we obtain the total number of the gas molecules with velocity in $d\boldsymbol{\xi}$ hitting the obstacle during dt_*, i.e.,

$$\left(\int_{\mathrm{all}\,\boldsymbol{\alpha}} \frac{1}{m}f_*|(\boldsymbol{\xi} - \boldsymbol{\xi}_s)\cdot\boldsymbol{\alpha}|\mathbf{1}_{\{(\boldsymbol{\xi}-\boldsymbol{\xi}_s)\cdot\boldsymbol{\alpha}<0\}}d_s^2 d\Omega(\boldsymbol{\alpha})\right)d\boldsymbol{\xi}dt_* = \frac{1}{m}\pi d_s^2|\boldsymbol{\xi} - \boldsymbol{\xi}_s|f_*d\boldsymbol{\xi}dt_*. \tag{3.69}$$

Since the number of the obstacles contained in the small neighborhood $d\boldsymbol{X}d\boldsymbol{\xi}_s$ around $(X_i,\, \xi_{si})$ is given by $(1/m_s)f_{*s}(\boldsymbol{\xi_s})d\boldsymbol{X}d\boldsymbol{\xi}_s$, the total number of the gas molecules contained in $d\boldsymbol{X}d\boldsymbol{\xi}$ and hitting the obstacles during dt_*, i.e., $(1/m)J_{\mathrm{loss}}d\boldsymbol{X}d\boldsymbol{\xi}dt_*$, is obtained as

$$\begin{aligned}\frac{1}{m}J_{\mathrm{loss}}d\boldsymbol{X}d\boldsymbol{\xi}dt_* &= \int_{\xi_{si}\in\mathbb{R}^3}\left(\frac{1}{m}\pi d_s^2|\boldsymbol{\xi} - \boldsymbol{\xi}_s|f_*d\boldsymbol{\xi}dt_*\right)\frac{1}{m_s}f_{*s}(\xi_{si})d\boldsymbol{X}d\boldsymbol{\xi}_s\\ &= \frac{1}{m}\frac{\pi d_s^2}{m_s}\left(\int_{\xi_{si}\in\mathbb{R}^3}|\boldsymbol{\xi} - \boldsymbol{\xi}_s|f_{*s}(\xi_{si})d\boldsymbol{\xi}_s\right)f_*d\boldsymbol{X}d\boldsymbol{\xi}dt_*.\end{aligned} \tag{3.70}$$

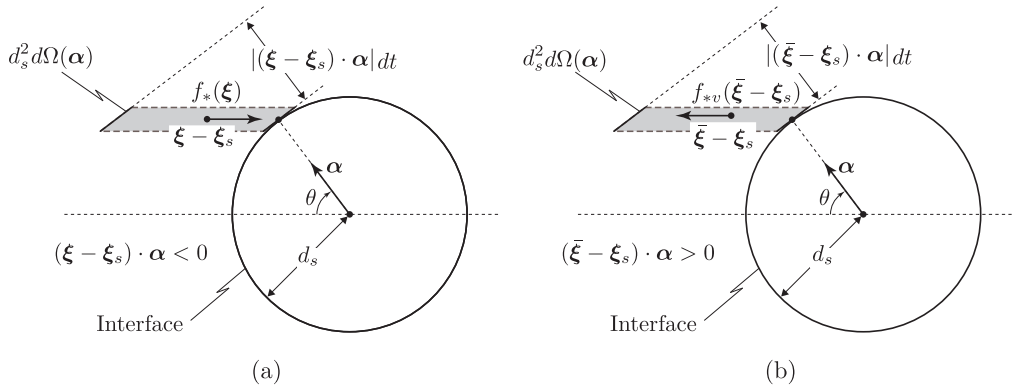

Fig. 3.11 Configuration of the collision between gas molecules and an obstacle with velocity ξ_{si}. (a) The loss term. (b) The gain term.

Gain Term : $J_{\rm gain}$ We count the number of gas molecules with velocity in a small neighborhood $d\overline{\boldsymbol{\xi}}$ around $\overline{\boldsymbol{\xi}}$, emitted from an obstacle during dt_*. Since the distribution function for the emitted vapor molecules is a given function, the same discussion as the loss term holds. The only difference is that f_* is replaced by $f_{*v}(\overline{\xi}_i-\xi_{si})$ and $\mathbf{1}_{\{(\boldsymbol{\xi}-\boldsymbol{\xi}_s)\cdot\boldsymbol{\alpha}<0\}}$ by $\mathbf{1}_{\{(\bar{\boldsymbol{\xi}}-\boldsymbol{\xi}_s)\cdot\boldsymbol{\alpha}>0\}}$ in Eq. (3.68) [see Fig. 3.11(b)]. Noting that $\overline{\xi}_i=\xi_i$ [Eq. (3.65)] and $d\overline{\boldsymbol{X}}d\overline{\boldsymbol{\xi}}=d\boldsymbol{X}d\boldsymbol{\xi}$, we obtain

$$\begin{aligned}\frac{1}{m}J_{\rm gain}d\overline{\boldsymbol{X}}d\overline{\boldsymbol{\xi}}dt_* &= \int_{\xi_{si}\in\mathbb{R}^3}\left(\frac{1}{m}\pi d_s^2|\overline{\boldsymbol{\xi}}-\boldsymbol{\xi}_s|f_{*v}(\overline{\xi}_i-\xi_{si})d\overline{\boldsymbol{\xi}}dt_*\right)\frac{1}{m_s}f_{*s}(\xi_s)d\overline{\boldsymbol{X}}d\boldsymbol{\xi}_s\\ &= \frac{1}{m}\frac{\pi d_s^2}{m_s}\left(\int_{\xi_{si}\in\mathbb{R}^3}|\boldsymbol{\xi}-\boldsymbol{\xi}_s|f_{*s}(\xi_{si})f_{*v}(\xi_i-\xi_{si})d\boldsymbol{\xi}_s\right)d\boldsymbol{X}d\boldsymbol{\xi}dt_*. \qquad (3.71)\end{aligned}$$

Equating Eq. (3.66) and Eq. (3.67) with Eqs. (3.70) and (3.71) and neglecting higher-order terms of dt_*, we obtain Eqs. (3.5) and (3.6). □

A.2.2 Mean free path

In order to discuss the mean free paths of the gas molecules, we consider the case where the gas is in the equilibrium state at rest at temperature T_{*0} and density ρ_{*0} (or molecular number density n_{*0}), i.e.,

$$f_* = \frac{mn_{*0}}{(2\pi R_*T_{*0})^{3/2}}\exp\left(-\frac{|\boldsymbol{\xi}|^2}{2R_*T_{*0}}\right). \qquad (3.72)$$

Then, the mean free path l_* of a gas molecule for the collisions against gas molecules is given by [7]

$$l_* = 1/\sqrt{2}\pi(2r)^2n_{*0}. \qquad (3.73)$$

On the other hand, from the consideration in Sec. A.2.1, the mean free path l_{*s} of a gas molecules for the collisions against the obstacles is obtained as follows:

$$l_{*s} = \left[\frac{\pi d_s^2}{m_s}\int_{\mathbb{R}^3}f_{*s}(\xi_{si})\Phi\left(\frac{|\boldsymbol{\xi}_s|}{\sqrt{2R_*T_{*0}}}\right)d\boldsymbol{\xi}_s\right]^{-1}, \qquad (3.74a)$$

$$\Phi(x) = \frac{1}{2}\left[\exp(-x^2)+\sqrt{\pi}\left(x+\frac{1}{2x}\right)\mathrm{erf}(x)\right]. \qquad (3.74b)$$

Let us consider the ratio l_{*s}/l_* under the condition (3.63). Then it can be estimated as

$$\frac{l_{*s}}{l_*} = \sqrt{2}\pi(2r)^2 n_{*0}\left[\frac{\pi d_s^2}{m_s}\int_{\mathbb{R}^3} f_{*s}(\xi_{si})\Phi\left(\frac{|\boldsymbol{\xi}_s|}{\sqrt{2R_*T_{*0}}}\right)d\boldsymbol{\xi}_s\right]^{-1}$$
$$\leq 4\sqrt{2}\frac{n_{*0}r^2}{n_{*s}(r+r_s)^2} \ll 1, \tag{3.75}$$

where the first inequality is due to the property $\Phi(x) \geq 1$, and the second one due to Eq. (3.63). If we choose the characteristic length $(\sqrt{2R_*T_{*0}}/\omega_*)$ (cf. Sec 3.1) much shorter than l_* but comparable to or longer than l_{*s}, we can neglect the effect of collisions between gas molecules. This legitimates the assumption 4 in Sec. A.1.

A.2.3 Special choice of f_{*s} and f_{*v}

Finally, we derive the simplified version (3.12) of the kinetic equation (3.5) with the help of special choices of f_{*v} and f_{*s} and a further assumption.

Let us choose the following Maxwellians as f_{*v} and f_{*s}:

$$f_{*v}(\xi_i - \xi_{si}) = \frac{mn_{*0}}{(2\pi R_*T_{*0})^{3/2}}\exp\left(-\frac{|\boldsymbol{\xi}-\boldsymbol{\xi}_s|^2}{2R_*T_{*0}}\right), \tag{3.76a}$$

$$f_{*s}(\xi_{si}) = \frac{m_s n_{*s}}{(2\pi\Theta_s)^{3/2}}\exp\left(-\frac{|\boldsymbol{\xi}_s|^2}{2\Theta_s}\right), \tag{3.76b}$$

where Θ_s is a positive constant, and introduce the following ϵ:

$$\epsilon = \sqrt{\frac{\Theta_s}{R_*T_{*0}}}. \tag{3.77}$$

Then, Eqs. (3.6a) and (3.6b) are reduced to

$$\nu(\xi_i) = 2\sqrt{\pi}\, n_{*s}(r+r_s)^2\sqrt{2\Theta_s}\,\phi(0, |\boldsymbol{\xi}|/\sqrt{2\Theta_s}), \tag{3.78a}$$

$$f_{*\infty}(\xi_i) = \frac{\phi(\epsilon, |\boldsymbol{\xi}|/\sqrt{2\Theta_s})}{\phi(0, |\boldsymbol{\xi}|/\sqrt{2\Theta_s})}\,\frac{mn_{*0}}{(2\pi R_*T_{*0})^{3/2}}\exp\left(-\frac{\epsilon^2}{1+\epsilon^2}\frac{|\boldsymbol{\xi}|^2}{2\Theta_s}\right), \tag{3.78b}$$

where $\phi(a,\, x)$ is a dimensionless function defined by

$$\phi(a,x) = \frac{1}{2}(1+a^2)^{-2}\left[\exp\left(-\bar{x}^2\right) + \sqrt{\pi}\left(\bar{x}+\frac{1}{2\bar{x}}\right)\mathrm{erf}\,(\bar{x})\right]\Bigg|_{\bar{x}=x/\sqrt{1+a^2}}. \tag{3.79}$$

By the use of the dimensionless variables in Eq. (3.7), Eq. (3.5) is recast as

$$\frac{\partial f}{\partial t} + \zeta_i\frac{\partial f}{\partial X_i} = \frac{1}{\mathrm{Kn}_\epsilon}\left(\frac{2}{\sqrt{\pi}}\frac{\epsilon}{\sqrt{1+\epsilon^2}}\right)\phi(0,\epsilon^{-1}|\boldsymbol{\zeta}|)$$
$$\times\left[\frac{\phi(\epsilon,\epsilon^{-1}|\boldsymbol{\zeta}|)}{\phi(0,\epsilon^{-1}|\boldsymbol{\zeta}|)}\,\frac{1}{\pi^{3/2}}\exp\left(-\frac{|\boldsymbol{\zeta}|^2}{1+\epsilon^2}\right) - f\right], \tag{3.80}$$

where Kn_ϵ is defined as [see Eq. (3.74a)]

$$\mathrm{Kn}_\epsilon = l_{*s}/(\sqrt{2R_*T_{*0}}/\omega_*) = [\pi n_{*s}(r+r_s)^2\sqrt{1+\epsilon^2}]^{-1}(\sqrt{2R_*T_{*0}}/\omega_*)^{-1}. \tag{3.81}$$

We now assume $\epsilon \ll 1$, which means that the speed of motion of the obstacles is much lower than that of the thermal motion of the gas molecules, and neglect the terms of $O(\epsilon^2)$. Then, we finally obtain the equation that is studied in the main text, i.e.,

$$\frac{\partial f}{\partial t} + \zeta_i \frac{\partial f}{\partial x_i} = \frac{\nu_\epsilon(|\boldsymbol{\zeta}|)}{\mathrm{Kn}} \left[\frac{1}{\pi^{3/2}} \exp\left(-|\boldsymbol{\zeta}|^2\right) - f \right], \tag{3.82a}$$

where

$$\nu_\epsilon(x) = \frac{2}{\sqrt{\pi}} \epsilon \phi(0,\, \epsilon^{-1} x) = \frac{\epsilon}{\sqrt{\pi}} \left[\exp\left(-\frac{x^2}{\epsilon^2}\right) + \sqrt{\pi} \left(\frac{x}{\epsilon} + \frac{\epsilon}{2x}\right) \mathrm{erf}\left(\frac{x}{\epsilon}\right) \right], \tag{3.82b}$$

$$\mathrm{Kn} = l_{*s}(\epsilon = 0) / (\sqrt{2 R_* T_{*0}} / \omega_*) = [\pi n_{*s} (r + r_s)^2]^{-1} (\sqrt{2 R_* T_{*0}} / \omega_*)^{-1}. \tag{3.82c}$$

References

[1] Caprino, S., Marchioro, C., Pulvirenti, M.: Approach to equilibrium in a microscopic model of friction. Commun. Math. Phys. **264**, 167–189 (2006).

[2] Caprino, S., Cavallaro, G., Marchioro, C.: On a microscopic model of viscous friction. Math. Models Methods Appl. Sci. **17**, 1369–1403 (2007).

[3] Cavallaro, G.: On the motion of a convex body interacting with a perfect gas in the mean-field approximation. Rendiconti di Matematica. Ser. VII **27**, 123–145 (2007).

[4] Aoki, K., Cavallaro, G., Marchioro, C., Pulvirenti, M.: On the motion of a body in thermal equilibrium immersed in a perfect gas. Math. Model. Num. Anal. **42**, 263–275 (2008).

[5] Aoki, K., Tsuji, T., Cavallaro, G.: Approach to steady motion of a plate moving in a free-molecular gas under a constant external force. Phys. Rev. E. **80**, 016309 (2009).

[6] Tsuji, T., Aoki, K.: Decay of an oscillating plate in a free-molecular gas. In: Levin, D. A., Wysong, I. J., Garcia, A. L. (eds.) *Rarefied Gas Dynamics*. AIP, Melville (2011). pp. 140–145.

[7] Sone, Y.: *Molecular Gas Dynamics: Theory, Techniques, and Applications*. Birkäuser, Boston (2007); Supplementary Notes and Errata: Kyoto University Research Information Repository (http://hdl.handle.net/2433/66098).

[8] Cavallaro, G., Marchioro, C.: On the approach to equilibrium for a pendulum immersed in a Stokes fluid. Math. Models Methods Appl. Sci. **20**, 1999–2019 (2010).

[9] Cavallaro, G., Marchioro, C., Tsuji, T.: Approach to equilibrium of a rotating sphere in a Stokes flow. Ann. Univ. Ferrara **57**, 211–228 (2011).

[10] Gallavotti, G.: *Statistical Mechanics: A Short Treatise*. Springer, Berlin (1999).

[11] Caglioti, E., Golse, F.: On the Boltzmann-Grad limit for the two dimensional periodic Lorentz gas. J. Stat. Phys. **141**, 264–317 (2010).

[12] Boltzmann, L.: *Lectures on Gas Theory*. Dover, New York (1995).

[13] Takata, S.: Invitation to the kinetic theory. J. Jpn. Soc. Fluid Mech. (Nagare) **27**, 387–396 (2008) (in Japanese).

[14] Gruber, Ch., Piasecki, J.: Stationary motion of the adiabatic piston. Physica A **268**, 412–423 (1999).

[15] Chernov, N., Lebowitz, J. L., Sinai, Ya.: Scaling dynamics of a massive piston in a cube filled with ideal gas: Exact results. J. Stat. Phys. **109**, 529–548 (2002).

[16] Lebowitz, J. L., Piasecki, J., Sinai, Ya.: in *Hard Ball Systems and the Lorentz Gas*, Encyclopedia of Mathematical Sciences Vol. 101 (Springer, New York, 2000), pp. 217–227.

[17] Kestemont, E., Van den Broeck, C., Mansour, M. M.: The "adiabatic" piston: And yet it moves. Europhys. Lett. **49**, 143–149 (2000).

[18] Chernov, N., Lebowitz, J. L.: Dynamics of a massive piston in an ideal gas: Oscillatory motion and approach to equilibrium. J. Stat. Phys. **109**, 507–527 (2002).

[19] Caglioti, E., Chernov, N., Lebowitz, J. L.: Stability of solutions of hydrodynamic equations describing the scaling limit of a massive piston in an ideal gas. Nonlinearity **17**, 897–923 (2004).

Chapter 4

Part 1: Moving boundary problems in a rarefied gas

Abstract Unsteady flows of a rarefied gas in a full space caused by a longitudinal oscillation of an infinitely wide plate is investigated numerically on the basis of the Bhatnagar-Gross-Krook (BGK) model of the Boltzmann equation. The paper aims at showing properties and difficulties inherent to moving boundary problems in kinetic theory of gases using a simple one-dimensional setting. More specifically, the following two problems are considered: (Problem I) the plate starts a forced harmonic oscillation (forced motion); (Problem II) the plate, which is subject to an external restoring force obeying Hooke's law, is displaced from its equilibrium position and released (free motion). The physical interest in Problem I lies in the propagation of nonlinear acoustic waves in a rarefied gas, whereas that in Problem II in the decay rate of the oscillation of the plate. An accurate numerical method, which is capable of describing singularities caused by the oscillating plate, is developed on the basis of the method of characteristics and is applied to the two problems mentioned above. As a result, the unsteady behavior of the solution, such as the propagation of discontinuities and some weaker singularities in the molecular velocity distribution function, are clarified. Some results are also compared with those based on the existing method.

1 Introduction

Moving boundary problems are one of the hot subjects in kinetic theory of gases and have been investigated extensively, in particular, in connection with micro electro mechanical systems (MEMS) [1]. The examples include the force on vibrating micro components exerted by the surrounding gas, the propagation of a sound wave generated by high-frequency oscillation of the boundary, the motion of vanes of the Crookes radiometer, etc. For moving boundary problems, which are essentially time-dependent, the prevailing direct simulation Monte Carlo (DSMC) method [2, 3] is not an optimal method because one has to take the ensemble average over many independent runs in order to reduce the fluctuation inherent to the method (see, for instance, [4, 5, 6] for the application of DSMC method to moving boundary problems). Therefore, deterministic methods based on the model Boltzmann equations are usually employed with the help of known techniques in computational fluid dynamics (CFD), such as the moving mesh technique and the immersed boundary method [7, 8].

In time-independent problems where the boundary is not moving in the normal direction, the molecular velocity distribution function on the plane or convex boundary (convex toward the domain of gas) is discontinuous at the molecular velocities tangent to the boundary (here, we are considering the case in which no external force acts on the gas molecules). For the convex boundary, this discontinuity propagates into the gas along the characteristics of the Boltzmann equation [9, 10, 11]. In contrast, for the plane boundary, the discontinuity stays on the boundary without propagating into the gas. The same is true when the plane boundary is moving in any direction with a constant velocity. However, if the boundary is accelerated in the direction opposite to the domain of the gas, the discontinuity is left in the gas even for the plane boundary, since the characteristics tangent to the boundary at a time go into the gas domain subsequently. If the boundary oscillates in the normal direction, therefore, the velocity distribution function may exhibit highly complex shape with many discontinuities as well as steep changes even for the plane boundary. To the best of the authors' knowledge, no attention has been paid to this point in the literature.

In the present study, we consider this problem. Restricting ourselves to spatially one-dimensional problems, we try to develop an accurate numerical method that is capable of describing the discontinuities in the molecular velocity distribution function generated by a moving plane boundary, on the basis of the Bhatnagar-Gross-Krook (BGK) model [12, 13] of the Boltzmann equation. More specifically, we consider two problems: One is the unsteady gas motion in a half space produced by a forced harmonic oscillation of the plane wall, and the other is the decay of a one-dimensional oscillator (linear pendulum) caused by the drag force exerted by the gas. The former is nothing but the problem of nonlinear acoustic wave propagation [5, 14]. In the latter problem, which is a sort of free-boundary problem and has been investigated extensively for a free-molecular (or Knudsen) gas [15, 16], our final purpose is to find the correct decay rate of the amplitude of the oscillator.

The aim of the present paper is not to develop an efficient numerical scheme but to solve the above basic problems faithfully and establish reliable numerical solutions that may serve as reference solutions when efficient numerical methods are devised.

The paper is organized as follows. We first formulate the two problems in Sec. 2. Section 3 is devoted to some preliminary discussions for numerical analysis. In Sec. 4, we develop the numerical method, and the results of numerical analysis are summarized in Sec. 5. Some concluding remarks are given in Sec. 6.

2 Formulation of the problem

2.1 Problem, assumptions, and notations

Let us consider an infinitely wide plate without thickness, kept at temperature T_{0*} and immersed in an infinite expanse of a rarefied ideal monatomic gas in an equilibrium state at rest with temperature T_{0*} and density ρ_{0*}. We take X_1 axis of the Cartesian coordinate system X_i perpendicular to the plate. At time $t_* = 0$, where t_* is the time variable, the plate is set into motion in the X_1 direction in a manner described below. We investigate the subsequent motion of the gas numerically under the following assumptions:

(i) The behavior of the gas is described by the BGK model [12, 13] of the Boltzmann equation.

(ii) The gas molecules undergo diffuse reflection on the plate. More specifically, the velocity of the reflected molecules on the boundary are distributed according to the (half-range) Maxwellian distribution being characterized by the velocity and temperature of the plate and having the density determined in such a way that there is no instantaneous net mass flow across the plate (see e.g., [10, 11]).

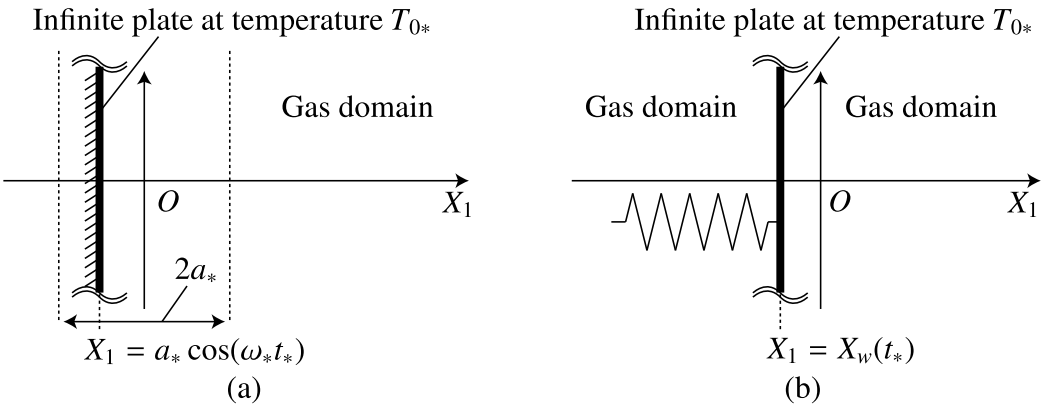

Fig. 4.1 Configuration of the problem. (a) Forced motion (Problem I), (b) free motion (Problem II).

Let us denote by $X_w(t_*)$ the position (X_1 coordinate) of the plate and by $V_w(t_*)$ its velocity, i.e., $V_w(t_*) = \dot{X}_w(t_*)$ where $\dot{}$ indicates the time derivative. In the present study, we consider the following two types of motion of the plate:

[Problem I] (forced motion): The plate starts a forced harmonic oscillation given by

$$X_w(t_*) = a_* \cos \omega_* t_*, \tag{4.1}$$

at $t_* = 0$ [see Fig. 4.1(a)], where a_* and ω_* are the amplitude and angular frequency of the oscillation. In this problem, we practically consider the half space $X_1 \geq X_w(t_*)$.

[Problem II] (free motion): The plate is subject to an external restoring force obeying Hooke's law. The plate is originally displaced from its equilibrium position $X_1 = 0$ and released at $t_* = 0$. Then, it undergoes, in general, an oscillatory motion, which decays as time proceeds because of the drag exerted by the surrounding gas [see Fig. 4.1(b)]. In this problem, the motion of the plate, which is determined together with the motion of the gas, is described by the following equation of motion and initial condition:

$$\dot{X}_w(t_*) = V_w(t_*), \qquad \dot{V}_w(t_*) = -\omega_*^2 X_w(t_*) - G_*/\mathcal{M}_*, \tag{4.2a}$$

$$X_w(0) = a_*, \qquad V_w(0) = 0, \tag{4.2b}$$

where ω_* is a constant (characteristic frequency of the motion), a_* is the initial position of the plate, $\mathcal{M}_*$ is the mass of the plate per unit area, and G_* is the drag force per unit area exerted by the surrounding gas. The term $-\omega_*^2 X_w(t_*)$ in Eq. (4.2) indicates the restoring force obeying Hooke's law, and G_* depends on the motion of the plate as well as the behavior of the gas [see Eq. (4.15) below].

Before presenting the basic equations, let us summarize the notations that will be used in the paper.

First, we introduce (and repeat) dimensional variables: t_* is the time variable, X_i the Cartesian coordinate system in space, ξ_i the molecular velocity, X_w the position of the plate (X_1 coordinate), and V_w the velocity of the plate (X_1 direction); ρ_* is the density of the gas, u_{1*} the flow velocity of the gas in the X_1 direction (the other two components u_{2*} and u_{3*} are assumed to be zero), T_* the temperature of the gas, and $p_* = R\rho_* T_*$ the pressure of the gas, where R is the gas constant

per unit mass ($R = k_B/m_g$ with the Boltzmann constant k_B and the mass of a gas molecule m_g); G_* is the drag force acting on the plate per unit area, $\mathcal{M}_*$ the mass of the plate per unit area, a_* the amplitude of the harmonic oscillation of the plate (Problem I) or the initial position of the plate (Problem II), and f_* the velocity distribution function of gas molecules. Then, adopting the time and length scales given respectively by

$$1/\omega_*, \qquad c_{0*}/\omega_*, \tag{4.3}$$

where $c_{0*} = (2RT_{0*})^{1/2}$, we introduce the dimensionless counterparts, t, x_i, ζ_i, x_w, v_w, ρ, u_1, T, p, G, $\mathcal{M}$, a, and f as follows:

$$\begin{aligned}
&t = t_*/(1/\omega_*), \quad x_i = X_i/(c_{0*}/\omega_*), \quad \zeta_i = \xi_i/c_{0*},\\
&x_w = X_w/(c_{0*}/\omega_*), \quad v_w = V_w/c_{0*},\\
&\rho = \rho_*/\rho_{0*}, \quad u_1 = u_{1*}/c_{0*}, \quad T = T_*/T_{0*}, \quad p = p_*/p_{0*},\\
&G = G_*/(\rho_{0*}c_{0*}^2), \quad \mathcal{M} = \mathcal{M}_*/(\rho_{0*}c_{0*}/\omega_*), \quad a = a_*/(c_{0*}/\omega_*),\\
&f = f_*/(\rho_{0*}c_{0*}^3),
\end{aligned} \tag{4.4}$$

where $p_{0*} = R\rho_{0*}T_{0*}$.

We further introduce some additional notations. We denote by l_{0*} and ν_{0*}, respectively, the mean free path and the mean collision frequency of gas molecules at the equilibrium state at rest at temperature T_{0*} and density ρ_{0*}. For the standard BGK model, they are expressed as

$$l_{0*} = (2/\sqrt{\pi})\,(c_{0*}/\nu_{0*}), \qquad \nu_{0*} = A_c\rho_{0*}. \tag{4.5}$$

where A_c is a constant. Then, we define the Knudsen number Kn as

$$\mathrm{Kn} = l_{0*}/(c_{0*}/\omega_*). \tag{4.6}$$

2.2 Basic equations

The present problem is a spatially one-dimensional problem, in which the independent variables are $(x_1,\, \zeta_1,\, \zeta_2,\, \zeta_3,\, t)$ in dimensionless variables. It is well known that in such a problem, one can eliminate the molecular velocity components ζ_2 and ζ_3 parallel to the plate [17]. More specifically, in the present problem, if we multiply the original BGK equation and the initial and boundary conditions by 1 and $\zeta_2^2 + \zeta_3^2$ and integrate the resulting equations over the whole space of ζ_2 and ζ_3, we obtain the initial- and boundary-value problem of the coupled integro-differential equations of BGK type for the following marginal velocity distribution functions g and h:

$$g(x_1,\, \zeta_1,\, t) = \int_{\mathbb{R}^2} f(x_1,\, \zeta_1,\, \zeta_2,\, \zeta_3,\, t)\,\mathrm{d}\zeta_2\mathrm{d}\zeta_3, \tag{4.7a}$$

$$h(x_1,\, \zeta_1,\, t) = \int_{\mathbb{R}^2} (\zeta_2^2 + \zeta_3^2) f(x_1,\, \zeta_1,\, \zeta_2,\, \zeta_3,\, t)\,\mathrm{d}\zeta_2\mathrm{d}\zeta_3. \tag{4.7b}$$

That is, with the notations

$$\Phi = \begin{bmatrix} g \\ h \end{bmatrix}, \qquad \lambda = \begin{bmatrix} 1 \\ T \end{bmatrix}, \qquad \delta = \begin{bmatrix} 1 \\ 1 \end{bmatrix}, \tag{4.8}$$

the equations are written as

$$(\partial_t + \zeta_1 \partial_{x_1})\Phi = \frac{2}{\sqrt{\pi}} \frac{1}{\mathrm{Kn}} \rho \left(\lambda M - \Phi\right), \tag{4.9a}$$

$$M = \frac{\rho}{(\pi T)^{1/2}} \exp\left(-\frac{(\zeta_1 - u_1)^2}{T}\right), \tag{4.9b}$$

$$\rho = \int_{\mathbb{R}} g \mathrm{d}\zeta_1, \quad u_1 = \frac{1}{\rho} \int_{\mathbb{R}} \zeta_1 g \mathrm{d}\zeta_1, \quad T = \frac{2}{3\rho} \int_{\mathbb{R}} [(\zeta_1 - u_1)^2 g + h] \mathrm{d}\zeta_1, \tag{4.9c}$$

the initial condition is

$$\Phi(x_1,\, \zeta_1,\, 0) = \pi^{-1/2} \exp(-\zeta_1^2)\, \delta, \tag{4.10}$$

and the boundary condition on the plate is given by

$$\Phi(x_1,\, \zeta_1,\, t) = M_{w\pm}(\zeta_1,\, t)\, \delta, \quad \text{at} \quad x_1 = x_w(t) \pm 0, \quad \text{for} \quad \zeta_1 - v_w(t) \gtrless 0, \tag{4.11}$$

where

$$M_{w\pm}(\zeta_1,\, t) = \pi^{-1/2} \sigma_{w\pm}(t) \exp\left(-[\zeta_1 - v_w(t)]^2\right), \tag{4.12a}$$

$$\sigma_{w\pm}(t) = \mp 2\sqrt{\pi} \int_{\zeta_1 - v_w(t) \lessgtr 0} [\zeta_1 - v_w(t)] g(x_w(t) \pm 0,\, \zeta_1,\, t) \mathrm{d}\zeta_1. \tag{4.12b}$$

In Eqs. (4.11) and (4.12), the upper signs indicate the condition on the right surface of the plate, and the lower signs that on its left surface. Here and in what follows, the upper (or lower) signs go together.

In Problem I (forced motion), the position of the plate $x_w(t)$ is given by

$$x_w(t) = a \cos t. \tag{4.13}$$

In Problem II (free motion), $x_w(t)$ is unknown and described by

$$\dot{x}_w(t) = v_w(t), \qquad \dot{v}_w(t) = -x_w(t) - G/\mathcal{M}, \tag{4.14a}$$

$$x_w(0) = a, \qquad v_w(0) = 0, \tag{4.14b}$$

where $\dot{}$ indicates the derivative with respect to t, and the drag in Eq. (4.14a) is expressed in terms of g as

$$G = G_+ + G_-, \tag{4.15a}$$

$$G_\pm = \pm \int_{\zeta_1 - v_w(t) \lessgtr 0} [\zeta_1 - v_w(t)]^2 g(x_w(t) \pm 0,\, \zeta_1,\, t) \mathrm{d}\zeta_1 \pm \int_{\zeta_1 - v_w(t) \gtrless 0} [\zeta_1 - v_w(t)]^2 M_{w\pm}(\zeta_1,\, t) \mathrm{d}\zeta_1. \tag{4.15b}$$

We numerically solve Eqs. (4.9)–(4.12) with Eq. (4.13) for Problem I (forced motion) and the coupled system, Eqs. (4.9)–(4.12) and Eqs. (4.14) and (4.15), for Problem II (free motion). In Problem I, we only consider the half space $x_1 \in [x_w,\, \infty)$.

The dimensionless parameters are a and Kn in Problem I and a, $\mathcal{M}$, and Kn in Problem II. In the present study, we focus our attention mainly on the effect of Kn on the solution.

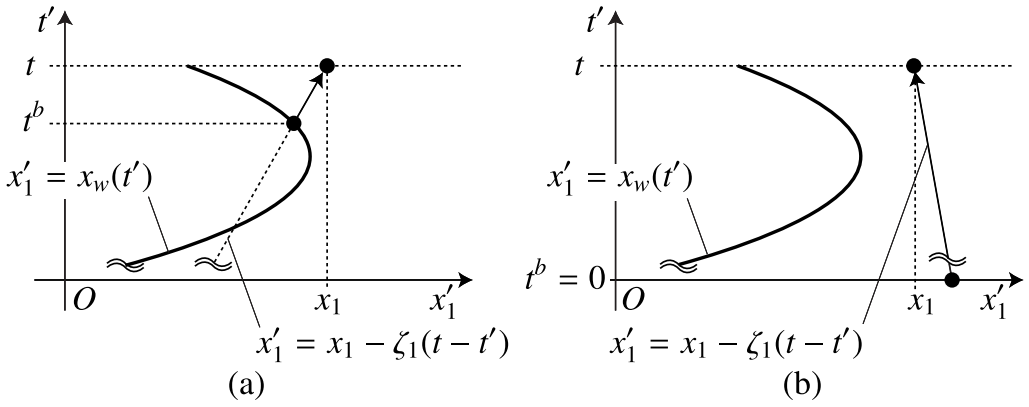

Fig. 4.2 (x_1', t') plane and the backward exit time $t^b(x_1, \zeta_1, t)$. (a) Case of $t^b \neq 0$, (b) case of $t^b = 0$. See Eq. (4.18).

3 Preliminaries

3.1 Integral form of the BGK equation

In this and following sections, it is convenient to consider the situation in the (x_1, t) plane. For further convenience, we call this plane the (x_1', t') plane using the current coordinates x_1' and t' and express a fixed point in the plane by (x_1, t) (e.g., see Fig. 4.2).

Let us define the operator T_p^q on a function $F(x_1, t)$ with variables x_1 and t by

$$\mathsf{T}_p^q[F(x_1, t)] = F(x_1 - p(t - q), q). \tag{4.16}$$

where other variables such as ζ_1 in $\Phi(x_1, \zeta_1, t)$ [see Eqs. (4.7) and (4.8)], if any, are unchanged and thus omitted.

Then, by integrating both sides of Eq. (4.9a) along the characteristic line $x_1' = x_1 - \zeta_1(t - t')$ under conditions (4.10) and (4.11), we obtain

$$\Phi = \mathsf{T}_{\zeta_1}^{t^b}[\Phi] + \frac{2}{\sqrt{\pi}} \frac{1}{\mathrm{Kn}} \int_{t^b}^{t} \mathsf{T}_{\zeta_1}^{\tau}[\rho\,(\lambda M - \Phi)]\mathrm{d}\tau, \tag{4.17}$$

where t^b is the backward exit time defined by

$$t^b(x_1, \zeta_1, t) = \begin{cases} \max\{t' \in (0, t)\,|\,x_1 - \zeta_1(t - t') = x_w(t')\}, \\ 0, \quad \text{if } x_1 - \zeta_1(t - t') \neq x_w(t'), \quad \text{for} \quad {}^\forall t' \in (0, t), \end{cases} \tag{4.18}$$

(see Fig. 4.2). Thus, $\mathsf{T}_{\zeta_1}^{t^b}[\Phi]$ is the value of Φ at the "foot" of the characteristic line, i.e.,

$$\mathsf{T}_{\zeta_1}^{t^b}[\Phi] = \begin{cases} M_{w\pm}(\zeta_1, t^b)\,\delta, \quad \text{for} \quad t^b \in (0, t), \quad x_1 \gtrless x_w(t), \\ \\ \pi^{-1/2} \exp(-\zeta_1^2)\,\delta, \quad \text{for} \quad t^b = 0, \end{cases} \tag{4.19}$$

where δ is defined in Eq. (4.8). We are going to discuss the *singularities* caused by the motion of the plate using Eq. (4.17) with Eqs. (4.18) and (4.19) in the following subsection.

3.2 Singularities in the velocity distribution function

In time-independent boundary-value problems of the Boltzmann equation, the molecular velocity distribution function is, in general, discontinuous in the space and molecular velocity variables around convex boundary (here, convex means convex toward the region of the gas). That is, the velocity distribution function on the boundary is discontinuous at the molecular velocities tangential to the boundary, and this discontinuity propagates into the gas along the characteristics corresponding to the tangential velocity. This fact has been well understood physically as well as in the level of formal analysis [9, 10, 11]. Mention should also be made of recent progress in rigorous mathematical theory [18].

In the present problem, when the trajectory of the plate $x_1' = x_w(t')$ in the $(x_1',\, t')$ plane is convex toward the side of the gas, the same mechanism works. That is, the characteristic line tangent to the trajectory in the $(x_1',\, t')$ plane carries the discontinuity in the gas. We classify this type of singularity as Type-1 singularity in the following. In addition to this, we also need to pay attention to different types of (weaker) singularities, which we will call Type-2 and Type-3 singularities. In this section, we only consider the half space $x_1' \in [x_w(t'), \infty)$. We also note that our discussion is based on formal analysis and physical intuition.

3.2.1 Type-1 singularity: discontinuity

Let us consider the case where there exists a positive backward exit time $t^b \in (0,\, t)$ [Eq. (4.18)]. Then, its derivatives with respect to x_1, ζ_1, and t, i.e.,

$$\frac{\partial t^b}{\partial x_1} = \frac{1}{v_w(t^b) - \zeta_1}, \quad \frac{\partial t^b}{\partial \zeta_1} = -\frac{t - t^b}{v_w(t^b) - \zeta_1}, \quad \frac{\partial t^b}{\partial t} = -\frac{\zeta_1}{v_w(t^b) - \zeta_1}, \tag{4.20}$$

suggest that t^b is singular for x_1, ζ_1, and t satisfying $\zeta_1 = v_w(t^b(x_1,\, \zeta_1,\, t))$. Let us assume that there exists a ζ_1 satisfying $\zeta_1 = v_w(t^b(x_1,\, \zeta_1,\, t))$ for given x_1 and t and denote it by ζ_d, i.e., $\zeta_d = v_w(t^b(x_1,\, \zeta_d,\, t))$. We further assume that $\dot{v}_w(t^b(x_1, \zeta_d, t)) \neq 0$. In other words, the characteristic line $x_1' = x_1 - \zeta_d(t - t')$ passing the point $(x_1,\, t)$ is tangent to the trajectory of the plate $x_1' = x_w(t')$ at $(x_w(t^b),\, t^b)$, which is not an inflexion point of the trajectory. Then, we define the following $s_\pm$ (see Fig. 4.3):

$$\begin{aligned} s_+ &= \lim_{\zeta_1 \to \zeta_d + 0} t^b(x_1,\, \zeta_1,\, t) \\ &= \max\{t' \in (0,\, t) \,|\, x_1 - \zeta_1(t - t') = x_w(t'),\, \zeta_1 = v_w(t')\}, \end{aligned} \tag{4.21a}$$

$$\begin{aligned} s_- &= \lim_{\zeta_1 \to \zeta_d - 0} t^b(x_1,\, \zeta_1,\, t) \\ &= \begin{cases} \max\{t' \in (0,\, s_+) \,|\, x_1 - \zeta_1(t - t') = x_w(t')\}, \\ 0, \quad \text{if } \; x_1 - \zeta_1(t - t') \neq x_w(t') \quad \text{for } \; {}^\forall t' \in (0,\, s_+). \end{cases} \end{aligned} \tag{4.21b}$$

Since t^b jumps from s_+ to s_-, it is likely from Eq. (4.17) that $\Phi(x_1,\, \zeta_1,\, t)$ exhibits a jump at $\zeta_1 = \zeta_d$. To see this, we take the limits $\zeta_1 \to \zeta_d \pm 0$ in Eq. (4.17). Then, using Eq. (4.21), we obtain the following relations:

$$\begin{aligned} \Phi_+ &\equiv \lim_{\zeta_1 \to \zeta_d + 0} \Phi(x_1,\, \zeta_1,\, t) \\ &= \mathsf{T}^{s_+}_{\zeta_d + 0}[\Phi] + \frac{2}{\sqrt{\pi}} \frac{1}{\mathrm{Kn}} \int_{s_+}^{t} \mathsf{T}^{\tau}_{\zeta_d + 0}[\rho(\lambda M - \Phi)] \mathrm{d}\tau, \end{aligned} \tag{4.22a}$$

$$\Phi_- \equiv \lim_{\zeta_1 \to \zeta_d - 0} \Phi(x_1,\, \zeta_1,\, t)$$

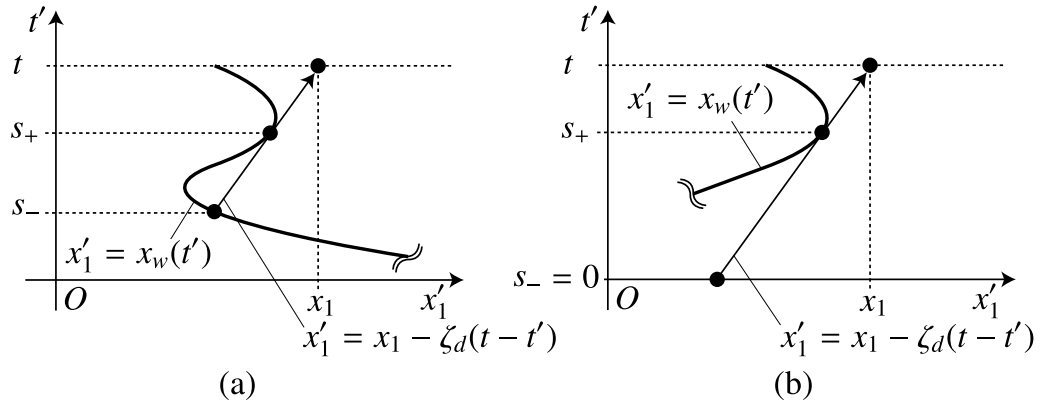

Fig. 4.3 Definition of s_+ and s_- in the $(x'_1,\, t')$ plane. (a) Case of $s_- \neq 0$, (b) case of $s_- = 0$. See Eq. (4.21).

$$= \mathsf{T}^{s_-}_{\zeta_d-0}[\Phi] + \frac{2}{\sqrt{\pi}}\frac{1}{\mathrm{Kn}}\left(\int_{s_-}^{s_+} + \int_{s_+}^{t}\right)\mathsf{T}^{\tau}_{\zeta_d-0}[\rho(\lambda M - \Phi)]\mathrm{d}\tau. \tag{4.22b}$$

Here, we assume that the macroscopic quantities $\rho(x'_1,\, t')$, $u_1(x'_1,\, t')$, $T(x'_1,\, t')$, etc., which are the moments of Φ [Eq. (4.9c)], are continuous in x'_1 and t' for all x'_1 $[> x_w(t')]$ and t' (> 0) even if Φ is discontinuous. This is a physical realization of the celebrated averaging lemma [19]. Thus, we have

$$\mathsf{T}^{\tau}_{\zeta_d+0}[\rho] - \mathsf{T}^{\tau}_{\zeta_d-0}[\rho] = 0, \qquad \mathsf{T}^{\tau}_{\zeta_d+0}[\rho\lambda M] - \mathsf{T}^{\tau}_{\zeta_d-0}[\rho\lambda M] = 0. \tag{4.23}$$

Therefore, we have, from Eq. (4.22), the following expressions for the jump:

$$\begin{aligned}\Phi_+ - \Phi_- =& \mathsf{T}^{s_+}_{\zeta_d+0}[\Phi] - \mathsf{T}^{s_+}_{\zeta_d-0}[\Phi] \\ &- \frac{2}{\sqrt{\pi}}\frac{1}{\mathrm{Kn}}\int_{s_+}^{t}\mathsf{T}^{\tau}_{\zeta_d}[\rho](\mathsf{T}^{\tau}_{\zeta_d+0}[\Phi] - \mathsf{T}^{\tau}_{\zeta_d-0}[\Phi])\mathrm{d}\tau,\end{aligned} \tag{4.24}$$

where use has been made of the relationship

$$\begin{aligned}\mathsf{T}^{s_+}_{\zeta_d+0}[\Phi] - \left(\mathsf{T}^{s_-}_{\zeta_d-0}[\Phi] + \frac{2}{\sqrt{\pi}}\frac{1}{\mathrm{Kn}}\int_{s_-}^{s_+}\mathsf{T}^{\tau}_{\zeta_d-0}[\rho(\lambda M - \Phi)]\right)\mathrm{d}\tau \\ = \mathsf{T}^{s_+}_{\zeta_d+0}[\Phi] - \mathsf{T}^{s_+}_{\zeta_d-0}[\Phi].\end{aligned} \tag{4.25}$$

Equation (4.24) is equivalent to

$$\Phi_+ - \Phi_- = (\mathsf{T}^{s_+}_{\zeta_d+0}[\Phi] - \mathsf{T}^{s_+}_{\zeta_d-0}[\Phi])\exp\left(-\frac{2}{\sqrt{\pi}}\frac{1}{\mathrm{Kn}}\int_{s_+}^{t}\mathsf{T}^{\tau}_{\zeta_d}[\rho]\mathrm{d}\tau\right). \tag{4.26}$$

The $\mathsf{T}^{s_+}_{\zeta_d+0}[\Phi]$ is given by the boundary condition on the plate at $(x_w(s_+),\, s_+)$ in the $(x'_1,\, t')$ plane, whereas $\mathsf{T}^{s_+}_{\zeta_d-0}[\Phi]$ is the velocity distribution function in the gas at the same point, which consists of information at $(x_w(s_-),\, s_-)$ and the effect of molecular collisions along the characteristic line for $t' \in (s_-,\, s_+)$. Thus, they are in general different ($\mathsf{T}^{s_+}_{\zeta_d+0}[\Phi] \neq \mathsf{T}^{s_+}_{\zeta_d-0}[\Phi]$). This means that Φ exhibits a discontinuity at $\zeta_1 = \zeta_d$ for the fixed $(x_1,\, t)$, i.e., $\Phi_+ \neq \Phi_-$.

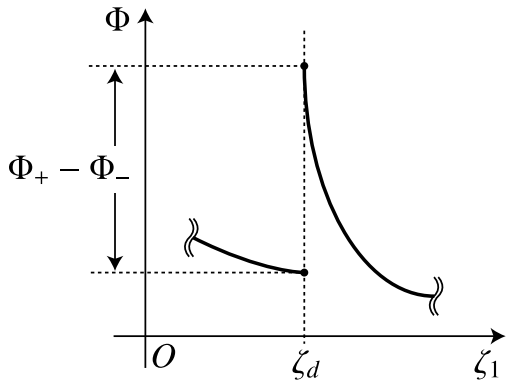

Fig. 4.4 Schematic view of Type-1 singularity (discontinuity). Φ at $(x_1,\, t)$ exhibits a discontinuity at $\zeta_1 = \zeta_d$. The limit of the derivative $\partial_{\zeta_1}\Phi$ as $\zeta_1 \to \zeta_d + 0$ diverges for a free-molecular gas ($\mathrm{Kn} \to \infty$).

If we assume that $\rho > \rho_c = O(1)$ along the characteristic line, we have

$$\int_{s_+}^{t} \mathsf{T}^{\tau}_{\zeta_d}[\rho]\mathrm{d}\tau > \rho_c(t - s_+), \tag{4.27}$$

and thus

$$|\Phi_+ - \Phi_-| < \left|\mathsf{T}^{s_+}_{\zeta_d+0}[\Phi] - \mathsf{T}^{s_+}_{\zeta_d-0}[\Phi]\right| \exp\left(-\frac{2}{\sqrt{\pi}}\frac{1}{\mathrm{Kn}}\rho_c(t - s_+)\right). \tag{4.28}$$

Therefore, the discontinuity in Φ decays exponentially as t/Kn becomes large.

Next, we consider the derivative of Φ with respect to ζ_1 for a free-molecular gas ($\mathrm{Kn} = \infty$) when there exists a positive t^b. Then, we have, from Eq. (4.17),

$$\begin{aligned}\frac{\partial\Phi}{\partial\zeta_1} &= \frac{\partial}{\partial\zeta_1} M_{w+}(\zeta_1,\, t^b(x_1,\, \zeta_1,\, t))\,\delta \\ &= M_{w+}(\zeta_1,\, t^b)\left\{\frac{\dot\sigma_w(t^b)}{\sigma_w(t^b)}\frac{\partial t^b}{\partial\zeta_1} - 2[\zeta_1 - v_w(t^b)] + 2\dot v_w(t^b)(t - t^b)\right\}\delta,\end{aligned} \tag{4.29}$$

which is unbounded when $\zeta_1 \to \zeta_d + 0$ [see Eq. (4.20)], i.e.,

$$\lim_{\zeta_1\to\zeta_d+0}\frac{\partial\Phi}{\partial\zeta_1} = \mathrm{sgn}(\dot\sigma_{w+}(s_+))\,\delta\times\infty. \tag{4.30}$$

This divergence has been observed in [15]. On the other hand, when there are collisions between gas molecules ($\mathrm{Kn} < \infty$), we are not able to obtain explicit information about the behavior of $\partial\Phi/\partial\zeta_1$. Nevertheless, we expect that the derivative $\partial\Phi/\partial\zeta_1$ may become very large in the limit $\zeta_1 \to \zeta_d + 0$, at least for large Kn. This situation is schematically shown in Fig. 4.4.

It is needless to say that we should deal with the discontinuity in Φ correctly in the actual numerical computation to obtain necessary accuracy. In addition, we should also pay attention to the steep change in Φ near the limit $\zeta_1 \to \zeta_d + 0$ in order to obtain the correct behavior of the macroscopic quantities.

In the above discussion, we investigated the behavior of Φ as a function of ζ_1 for fixed x_1 and t. If we change x_1 for fixed ζ_1 and t or change t for fixed x_1 and ζ_1, we can observe a similar singularity in x_1 or in t. In other words, the singularity of Φ (the discontinuity in Φ and the divergence of its derivative) is present in the three-dimensional space $(x_1,\, \zeta_1,\, t)$. The same comment applies to Secs. 3.2.2 and 3.2.3.

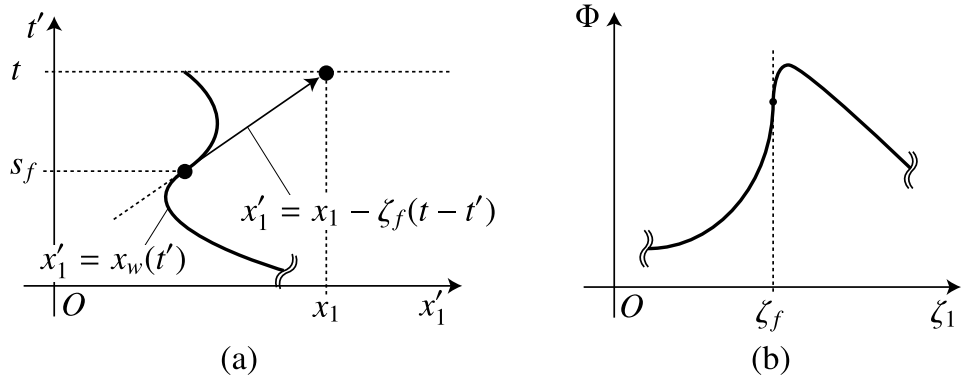

Fig. 4.5 Schematic view of Type-2 singularity. (a) Definition of s_f in the (x_1', t') plane, (b) Φ at $(x_1,\, t)$ as a function of ζ_1. The derivative $\partial_{\zeta_1}\Phi$ becomes infinity at $\zeta_1 = \zeta_f$ for a free-molecular gas ($\mathrm{Kn} \to \infty$).

3.2.2 Type-2 singularity

As in Sec. 3.2.1, we consider the case where there exists a positive backward exit time $t^b \in (0,\, t)$ [Eq. (4.18)]. As mentioned just after Eq. (4.20), t^b is singular for x_1, ζ_1, and t satisfying $\zeta_1 = v_w(t^b(x_1,\, \zeta_1,\, t))$. Here, we assume that there exists a ζ_1 satisfying not only $\zeta_1 = v_w(t^b(x_1,\, \zeta_1,\, t))$ but also $\dot{v}_w(t^b(x_1, \zeta_1, t)) = 0$ and denote it by ζ_f; that is, $\zeta_f = v_w(t^b(x_1,\, \zeta_f,\, t))$ and $\dot{v}_w(t^b(x_1, \zeta_f, t)) = 0$. In other words, the characteristic line $x_1' = x_1 - \zeta_f(t - t')$ passing the point $(x_1,\, t)$ is tangent to the trajectory of the plate $x_1' = x_w(t')$ at $(x_w(t^b),\, t^b)$, which is also an inflexion point of the trajectory. Then, we define the following s_f [see Fig. 4.5(a)]:

$$\begin{aligned} s_f &= t^b(x_1,\, \zeta_f,\, t) \\ &= \max\{t' \in (0,\, t) \,|\, x_1 - \zeta_1(t - t') = x_w(t'),\, \zeta_1 = v_w(t'),\, \dot{v}_w(t') = 0\}. \end{aligned} \tag{4.31}$$

At the point $(x_w(s_f),\, s_f)$ in the $(x_1',\, t')$ plane, t^b is continuous in ζ_1, but its derivative $\partial t^b/\partial\zeta_1$ diverges. Therefore, for a free-molecular gas ($\mathrm{Kn} = \infty$), it is seen from Eq. (4.29) that the derivative $\partial\Phi/\partial\zeta_1$ diverges at $\zeta_1 = \zeta_f$, i.e.,

$$\lim_{\zeta_1 \to \zeta_f} \frac{\partial \Phi}{\partial \zeta_1} = \mathrm{sgn}(\dot{\sigma}_{w+}(s_f))\, \delta \times \infty, \tag{4.32}$$

though Φ itself is continuous there. Therefore, as is the case of the limit as $\zeta_1 \to \zeta_d + 0$ in Sec. 3.2.1, we should expect a steep change in Φ in the vicinity of $\zeta_1 = \zeta_f$ even when there are collisions between gas molecules ($\mathrm{Kn} < \infty$). This situation is schematically shown in Fig. 4.5(b).

We also need to handle this steep change in Φ in the vicinity of $\zeta_1 = \zeta_f$ in order to describe the behavior of the macroscopic quantities correctly.

3.2.3 Type-3 singularity

As pointed out in [20, 21] (see also [22]), if the limit of the boundary condition on the plate as $t \to 0+$ is different from the corresponding part of the initial condition at the location of the plate, this difference propagates into the gas as a discontinuity in the molecular velocity distribution function. In the present problem, since the velocity distribution function on the plate as $t \to 0+$ is the same as the initial condition, we are free from the discontinuity mentioned above, as we will

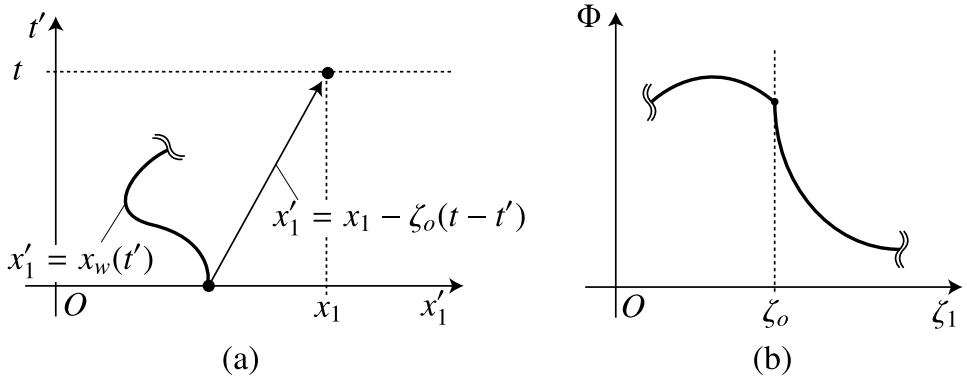

Fig. 4.6 Schematic view of Type-3 singularity. (a) Definition of ζ_o in the (x_1', t') plane, (b) Φ at $(x_1,\, t)$ as a function of ζ_1. The derivative $\partial_{\zeta_1}\Phi$ is discontinuous at $\zeta_1 = \zeta_o$ for a free-molecular gas ($\mathrm{Kn} \to \infty$).

see below. However, there appears a weaker singularity of which care should be exercised in the practical computation.

In both Problems I and II, $x_w(0) = a$ and $v_w(0) = 0$ [see Eqs. (4.13) and (4.14)], so that the trajectory of the plate $x_1' = x_w(t')$ starts perpendicularly to the x_1' axis in the $(x_1',\, t')$ plane [see Fig. 4.6(a)]. Let us suppose that, for a fixed x_1 and t, there is a ζ_1 such that the characteristic line $x_1' = x_1 - \zeta_1(t - t')$ passing the point $(x_1,\, t)$ intersects with the trajectory of the plate $x_w(t')$ only at the initial point $(x_w(0),\, 0)$ [see Fig. 4.6(a)], and let us denote it by ζ_o, i.e., $x_1 - \zeta_o t = x_w(0)$ and $x_1 - \zeta_o(t - t') \neq x_w(t')$ for ${}^\forall t' \in (0, t)$.

From Eq. (4.17), we have

$$\begin{aligned}\lim_{\zeta_1 \to \zeta_o + 0} \Phi &= M_{w+}(\zeta_o,\, 0)\, \delta + \frac{2}{\sqrt{\pi}} \frac{1}{\mathrm{Kn}} \int_0^{t_o} \mathsf{T}^{\tau}_{\zeta_o + 0}[\rho\,(\lambda M - \Phi)]\mathrm{d}\tau \\ &= \pi^{-1/2} \exp(-\zeta_o^2)\, \delta + \frac{2}{\sqrt{\pi}} \frac{1}{\mathrm{Kn}} \int_0^{t_o} \mathsf{T}^{\tau}_{\zeta_o + 0}[\rho\,(\lambda M - \Phi)]\mathrm{d}\tau, \end{aligned} \tag{4.33}$$

and

$$\begin{aligned}\lim_{\zeta_1 \to \zeta_o - 0} \Phi &= \Phi(x_w(0),\, \zeta_o,\, 0) + \frac{2}{\sqrt{\pi}} \frac{1}{\mathrm{Kn}} \int_0^{t_o} \mathsf{T}^{\tau}_{\zeta_o - 0}[\rho\,(\lambda M - \Phi)]\mathrm{d}\tau \\ &= \pi^{-1/2} \exp(-\zeta_o^2)\, \delta + \frac{2}{\sqrt{\pi}} \frac{1}{\mathrm{Kn}} \int_0^{t_o} \mathsf{T}^{\tau}_{\zeta_o - 0}[\rho\,(\lambda M - \Phi)]\mathrm{d}\tau. \end{aligned} \tag{4.34}$$

Thus, Φ is continuous at $\zeta_1 = \zeta_o$ because of Eq. (4.23). However, if we consider the free-molecular gas ($\mathrm{Kn} = \infty$), we obtain the following limiting values of the derivative $\partial\Phi/\partial\zeta_1$:

$$\lim_{\zeta_1 \to \zeta_o + 0} \frac{\partial \Phi}{\partial \zeta_1} = \left\{ \pi^{-1/2} \exp(-\zeta_o^2) \left[\dot{\sigma}_w(0) \frac{t}{\zeta_o} - 2at \right] - 2\pi^{-1/2} \zeta_o \exp(-\zeta_o^2) \right\} \delta, \tag{4.35a}$$

$$\lim_{\zeta_1 \to \zeta_o - 0} \frac{\partial \Phi}{\partial \zeta_1} = \lim_{\zeta_1 \to \zeta_o - 0} \frac{\partial}{\partial \zeta_1}\, \pi^{-1/2} \exp(-\zeta_1^2)\, \delta = -2\pi^{-1/2} \zeta_o \exp(-\zeta_o^2)\, \delta, \tag{4.35b}$$

where the first equation is obtained by taking the limit $t^b \to 0$ in Eq. (4.29). Therefore, these two limits are generally different, and thus the velocity distribution function behaves as shown schematically in Fig. 4.6(b). When there are collisions between gas molecules ($\mathrm{Kn} < \infty$), the

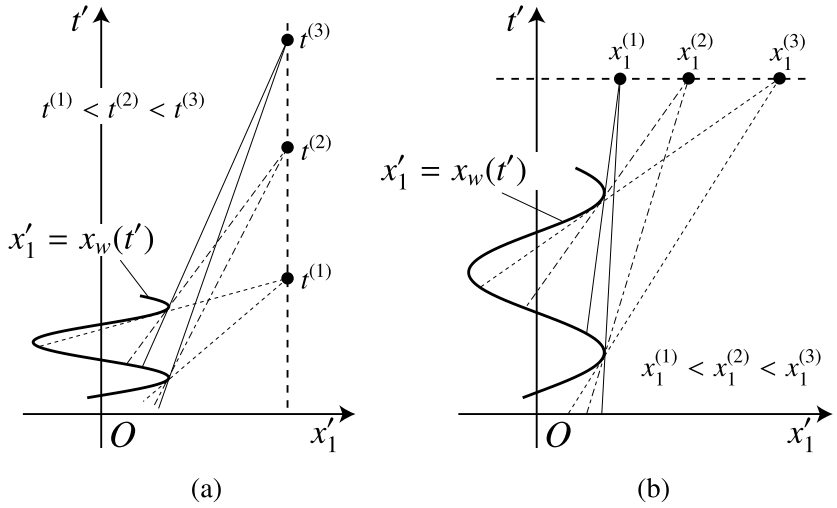

Fig. 4.7 Illustrative figure showing the localization of discontinuities in Φ. (a) $t' = t^{(1)} < t^{(2)} < t^{(3)}$ and a fixed x_1', (b) $x_1' = x_1^{(1)} < x_1^{(2)} < x_1^{(3)}$ and a fixed (large) t'. The interval between two neighboring velocities at which Φ is discontinuous shrinks as time goes on [(a)], or at positions in a zone close to the plate [(b)].

discontinuity in the derivative at $\zeta_1 = \zeta_o$ is likely to decay as t becomes large. However, in order to obtain accurate solution at the initial stage, we should pay attention to this behavior in the numerical computation.

3.2.4 Localization of discontinuities

The trajectory of the plate $x_1' = x_w(t')$ is a sinusoidal curve in the $(x_1',\, t')$ plane in Problem I and can be a decaying oscillatory curve in Problem II. In these cases, when t is large, multiple discontinuities (Type-1 singularities) may accumulate in a localized interval in ζ_1. Figure 4.7 is an illustrative figure showing this localization of discontinuities. It is clear from Fig. 4.7(a) that, for a fixed x_1', the interval between two velocities at which the velocity distribution function is discontinuous shrinks as t' becomes large. Figure 4.7(b) shows that, for a fixed t' large enough, the interval is also small at x_1' in a zone close to the plate. For the free-molecular gas ($\mathrm{Kn} = \infty$), more and more discontinuities accumulate in a shrinking interval in ζ_1 as time goes on. When there are inter-molecular collisions, aged discontinuities die out. Therefore, the structure of the velocity distribution function is less complex than in the free-molecular case. However, since young discontinuities are always present in a localized interval, the structure is complex enough except in the case of small Kn. This accumulation of discontinuities is problematic, since any discontinuity-capturing numerical method does not work unless extremely fine mesh is used. To avoid this difficulty, we will propose an adaptive grid system that resolves the localized structure of the velocity distribution function in Sec. 4. The result will be compared with that obtained by a standard discontinuity-capturing scheme, such as the ENO scheme [23], in Sec. 5.

4 Numerical analysis

In this section, we describe the numerical method used in the present paper. It is designed in such a way that no interpolation (or extrapolation) is needed for the velocity distribution function, since it has discontinuities and some weaker singularities as shown in Sec. 3.2. For brevity, we

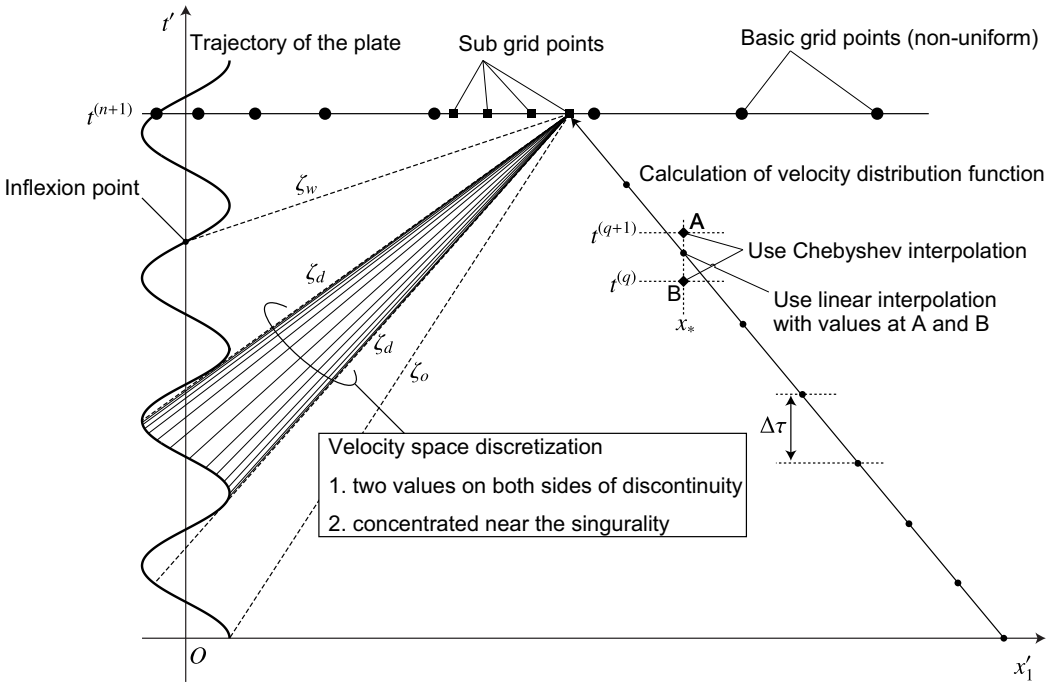

Fig. 4.8 Expository figure for the numerical method in the case of Problem I (forced oscillation).

only consider the region $x_1 \in [x_w(t), \infty)$ and omit the plus sign that indicates the right side of the plate, e.g., M_{w+} and σ_{w+} in Eq. (4.12) are denoted by M_w and σ_w, respectively. Figure 4.8, which will be referred frequently in the following, is an expository figure prepared for the help of explanation in this section.

4.1 Grid points and interpolation

Let us introduce the discretized time valuable $t^{(n)}$ and corresponding discrete values of x_w, v_w, and σ_w as

$$t^{(n)} = n\Delta t, \quad x_w^{(n)} = x_w(t^{(n)}), \quad v_w^{(n)} = v_w(t^{(n)}), \quad \sigma_w^{(n)} = \sigma_w(t^{(n)}), \\ (n = 0,\, 1,\, 2,\, ...). \tag{4.36}$$

Then, for each $t^{(n)}$, we introduce the basic grid points $x^{(n,i)}$ in x_1 that are more concentrated near the plate and uniformly distributed in the far field by the following relation:

$$x^{(n,i)} = x_w^{(n)} + L_\eta(n,\, i), \qquad (i = 0,\, 1,\, 2,\, ...,\, N_x), \tag{4.37}$$

where the grid function $L_\eta(n,\, i)$ is defined by Eq. (4.56) in A, and $x^{(n,0)} = x_w^{(n)}$ holds because $L_\eta(n,\, 0) = 0$. Note that the basic grid points $x^{(n,i)}$ depends on the time $t^{(n)}$. In addition, we introduce sub grid points $z^{(k,n,i)}$ $(k = 0,\, 1,\, ...,\, N_{\rm ch})$ on each interval $I^{(n,i)} = [x^{(n,i)},\, x^{(n,i+1)}]$ for the Chebyshev interpolation by the following formula:

$$z^{(k,n,i)} = \frac{1}{2}[1 - \cos(k\pi/N_{\rm ch})](x^{(n,i+1)} - x^{(n,i)}) + x^{(n,i)}, \\ (k = 0,\, 1,\, 2,\, ...,\, N_{\rm ch}), \tag{4.38}$$

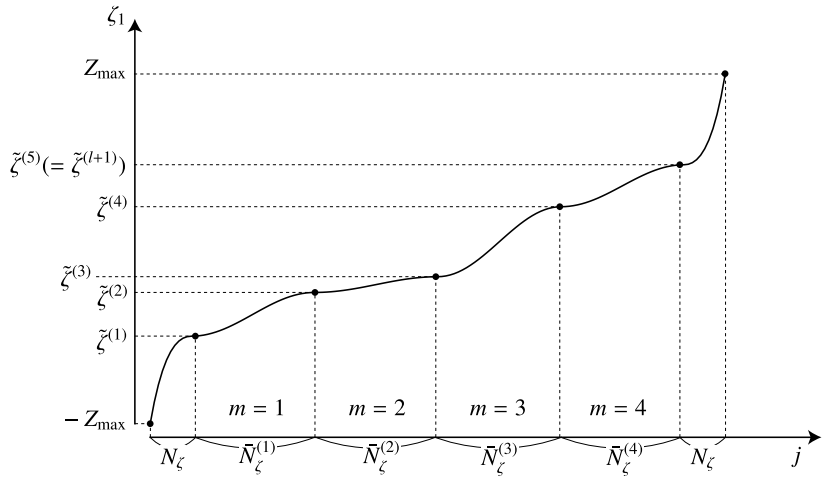

Fig. 4.9 Schematic shape of the grid function $\zeta_1 = L_\zeta(j)$ vs (continuous) j [see Eqs. (4.60) and (4.61)]. The figure shows an example with $l = 4$, $\tilde{\zeta}^{(1)} = -2.5$, $\tilde{\zeta}^{(2)} = -1.25$, $\tilde{\zeta}^{(3)} = -0.8$, $\tilde{\zeta}^{(4)} = 1.2$, $\tilde{\zeta}^{(5)} = 2.4$, and $Z_{\max} = 5$.

where $z^{(0,n,i)} = x^{(n,i)}$ and $z^{(N_{\rm ch},n,i)} = z^{(0,n,i+1)} = x^{(n,i+1)}$ hold (see Fig. 4.8). In our computation, the velocity distribution function Φ and thus the macroscopic quantities will be computed at the grid points $(z^{(k,n,i)},\, t^{(n)})$ $(i = 0,\, 1,\, 2,\, ...,\, N_x - 1;\, k = 0,\, 1,\, ...,\, N_{\rm ch} - 1)$ and $(x^{(n,N_x)},\, t^{(n)})$ for $n = 0,\, 1,\, 2,\, ...$ in the $(x_1',\, t')$ plane.

Let U stand for the macroscopic quantities ρ, u_1, and T $(U = \rho,\, u_1,\, T)$. Once U is obtained at all points $x_1' = z^{(k,n,i)}$ $(i = 0,\, 1,\, 2,\, ...,\, N_x - 1;\, k = 0,\, 1,\, ...,\, N_{\rm ch} - 1)$ and $x_1' = x^{(n,N_x)}$ for a given time $t' = t^{(n)}$, we can obtain U at any point $x_1' = x_1$ for the same $t^{(n)}$ by the Chebyshev interpolation. More specifically, if the point x_1 belongs to the interval $I^{(n,i')}$, then we have

$$U(x_1,\, t^{(n)}) = \sum_{k=0}^{N_{\rm ch}} a_{\rm ch}^{(k,n,i')} T_{N_{\rm ch}-k}(x_1'), \qquad x_1' = 2\frac{x_1 - x^{(n,i')}}{x^{(n,i'+1)} - x^{(n,i')}} - 1. \tag{4.39}$$

Here, $T_k(\theta)$ is the Chebyshev polynomial of the first kind of degree k, defined by

$$T_k(\theta) = \cos(k \arccos\theta), \tag{4.40}$$

and the Chebyshev coefficients $a_{\rm ch}^{(k,n,i')}$ are obtained in terms of U at $x_1 = z^{(k,n,i')}$ by

$$a_{\rm ch}^{(k,n,i')} = L_a(k, U^{(k,n,i')}), \tag{4.41}$$

where

$$U^{(k,n,i)} = U(z^{(k,n,i)},\, t^{(n)}), \tag{4.42}$$

and L_a is the function defined in Eq. (4.57) in A.

4.2 Grid points in molecular velocity space

Our grid points in the molecular velocity ζ_1 are associated with each grid point in $(z^{(k,n,i)},\, t^{(n)})$ in the $(x_1',\, t')$ plane and thus depend on n, i, and k. For simplicity, we denote any grid point in the $(x_1',\, t')$ plane by $(x_1,\, t)$ and omit the indices n, i, and k in the explanation of the grid points in ζ_1.

In Sec. 3.2, we have seen that for a fixed grid point $(x_1,\, t)$, there may exist singular velocities ζ_d, ζ_f, and ζ_o. We need two grid points at $\zeta_1 = \zeta_d \pm 0$ to express the discontinuity and use fine grid points in ζ_1 near these singular velocities to resolve steep changes. Now we denote by ζ_w the molecular velocity corresponding to the gradient of the characteristic line connecting the grid point $(x_1,\, t)$ and an inflection point of the trajectory $x_1' = x_w(t')$ [we assume that the line segment between the two points is contained in the gas region $x_1' \geq x_w(t')$ in the $(x_1',\, t')$ plane]. When this characteristic line is tangent to the trajectory at the inflection point, ζ_w becomes ζ_f. Therefore, the probability of having ζ_f is much less than having ζ_d or ζ_o. However, if ζ_w is close to ζ_f, we expect a steep change of Φ near $\zeta_1 = \zeta_w$, so that we need fine grid points there, too. Therefore, we extend the set of the singular velocities from $\{\zeta_d,\, \zeta_f,\, \zeta_o\}$ to $\{\zeta_d,\, \zeta_w,\, \zeta_o\}$ and concentrate the grid points in ζ_1 around these extended singular velocities (see Fig. 4.8).

Let $\tilde{\zeta}^{(1)}$, $\tilde{\zeta}^{(2)}$, ..., $\tilde{\zeta}^{(l+1)}$ be the all elements of the set of the extended singular velocities $\{\zeta_d,\, \zeta_w,\, \zeta_o\}$ such that $\tilde{\zeta}^{(m)} < \tilde{\zeta}^{(m+1)}$. We first restrict the infinite range $-\infty < \zeta_1 < \infty$ to a finite range $-Z_{\max} \leq \zeta_1 \leq Z_{\max}$. The constant $Z_{\max}$ is to be chosen in such a way that the velocity distribution function Φ is negligibly small at $\zeta_1 = \pm Z_{\max}$. Then, our grid points $\zeta^{(j)}$ in ζ_1 ($j = 0,\, 1,\, 2,\, ...,\, M_\zeta$; $\zeta^{(0)} = -Z_{\max}$ and $\zeta^{(M_\zeta)} = Z_{\max}$) are chosen in the following way.

We divide each of the end intervals $[-Z_{\max},\, \tilde{\zeta}^{(1)}]$ and $[\tilde{\zeta}^{(l+1)},\, Z_{\max}]$ into N_ζ small intervals with grid points more concentrated at $\tilde{\zeta}^{(1)}$ and $\tilde{\zeta}^{(l+1)}$. Then, we divide each interval $[\tilde{\zeta}^{(m)},\, \tilde{\zeta}^{(m+1)}]$ $(m = 1, ..., l)$ into $\bar{N}_\zeta^{(m)}$ small intervals with grid points more concentrated at both ends $\tilde{\zeta}^{(m)}$ and $\tilde{\zeta}^{(m+1)}$. Thus, $M_\zeta = 2N_\zeta + \sum_{m=1}^{l} \bar{N}_\zeta^{(m)}$. More specifically, the grid points $\zeta^{(j)}$ are defined by using a grid function $L_\zeta(j)$:

$$\zeta^{(j)} = L_\zeta(j). \tag{4.43}$$

The explicit form of $L_\zeta(j)$ is given in Eq. (4.60) in A, but its schematic shape as a function of (continuous) j is shown in Fig. 4.9. The concentration of the grid points at $\tilde{\zeta}^{(m)}$ is made by the use of the cosine function (or the exponential function in the left-most and right-most intervals) [see Eq. (4.60)].

When ζ_w is not close to ζ_f, the concentration of the grid points at ζ_w is the waste of grid points. However, it helps simplification of the computer programme. This grid system in ζ_1 enables us to capture the singular behavior of the velocity distribution function, as we will see in Sec. 5.

4.3 Outline of numerical method

In Problem I, the motion of the plate is given, whereas in Problem II, it is determined together with the solution Φ. In this subsection, we give the outline of the numerical method for Problem II. Then, that for Problem I is rather trivial. In our previous paper [16], we considered Problem II for a free-molecular (or Knudsen) gas. The difference in the numerical procedure between [16] and the present paper lies in the way how to obtain the velocity distribution function Φ. Once Φ is obtained on the plate, then the procedure to obtain the motion of the plate is the same as that in [16]. Therefore, we put the method for obtaining Φ in the next subsection and summarize the other processes here, referring to [16] for the process of obtaining the motion of the plate.

Let

$$\Phi^{(k,n,i,j)} = \Phi(z^{(k,n,i)},\, \zeta^{(j)},\, t^{(n)}), \tag{4.44}$$

for the following discussion, and suppose that the quantities $x_w^{(q)}$, $v_w^{(q)}$, $U^{(k,q,i)}$, $\sigma_w^{(q)}$, and $G_\pm^{(q)} \equiv G_\pm(t^{(q)})$ for $q = 0,\, ...,\, n$, $i = 0,\, ...,\, N_x$, and $k = 0,\, ...,\, N_{\rm ch}$ have been obtained. Our method for obtaining those quantities at $q = n + 1$ is the so-called predictor-corrector method, in which a predicted value $\hat{h}$ of the quantity h (h stands for $x_w^{(n+1)}$, $v_w^{(n+1)}$, $\sigma_w^{(n+1)}$, etc.) is first obtained

by using a suitable extrapolation, and then its corrected value h is obtained using $\hat{h}$. To be more specific,

1. Compute the predicted values $\hat{x}_w^{(n+1)}$ and $\hat{v}_w^{(n+1)}$, using $G_\pm(t^{(n)})$ (see Sec. 5.1 in [16] for the details).
2. Compute the predicted distribution function $\hat{\Phi}^{(k,n+1,i,j)}$ by the procedure that will be described in Sec. 4.4.
3. Compute the predicted values $\hat{U}^{(k,n+1,i)}$, $\hat{\sigma}_w^{(n+1)}$, and $\hat{G}^{(n+1)}$, using $\hat{\Phi}^{(k,n+1,i,j)}$ in Eqs. (4.9c), (4.12b), and (4.15), respectively (we use a second-order quadrature for the numerical integration).
4. Compute the corrected values $x_w^{(n+1)}$ and $v_w^{(n+1)}$, using $\hat{G}_\pm(t^{(n+1)})$ (see Sec. 5.1 in [16] for the details).
5. Compute the corrected distribution function $\Phi^{(k,n+1,i,j)}$ by the procedure that will be described in Sec. 4.4.
6. Compute the corrected values $U^{(k,n+1,i)}$, $\sigma_w^{(n+1)}$, and $G^{(n+1)}$, using $\Phi^{(k,n+1,i,j)}$ in Eqs. (4.9c), (4.12b), and (4.15), respectively (we use a second-order quadrature for the numerical integration).

We repeat the above processes, starting from the initial condition, until the required time is reached.

4.4 Calculation of velocity distribution function

We suppose that the quantities $x_w^{(q)}$, $v_w^{(q)}$, $U^{(k,q,i)}$, $\sigma_w^{(q)}$, and $G_\pm^{(q)} \equiv G_\pm(t^{(q)})$ for $q = 0, ..., n$, $i = 0, ..., N_x$, and $k = 0, ..., N_{\text{ch}}$ are all known. Let us consider fixed i, k, and j and try to compute $\Phi^{(k,n+1,i,j)}$ [cf. Eq. (4.44)]. Then, the characteristic line passing the grid point $(z^{(k,n+1,i)}, t^{(n+1)})$ in the (x_1', t') is determined and thus $t^b(z^{(k,n+1,i)}, \zeta^{(j)}, t^{(n+1)})$ is obtained [cf. Eq. (4.18)]. In this subsection, we denote the discretized local Maxwellian [Eq. (4.9b)] by

$$M^{(k,n,i,j)} = M(z^{(k,n,i)}, \zeta^{(j)}, t^{(n)}), \tag{4.45}$$

and use the notations (4.42) and (4.44).

We divide the interval $[t^b, t^{(n+1)}]$ into N_t equal small intervals with width $\Delta\tau$ by grid points $t' = \tau^{(m_t)}$ in t' variable ($m_t = 0, ..., N_t$), i.e.,

$$\tau^{(0)} = t^b < \tau^{(1)} < \cdots < \tau^{(m_t)} < \cdots < \tau^{(N_t)} = t^{(n+1)}, \tag{4.46}$$

with $\tau^{(m_t+1)} - \tau^{(m_t)} = \Delta\tau$ (see Fig. 4.8). Note that N_t may be different depending on $z^{(k,n+1,i)}$, $\zeta^{(j)}$, and $t^{(n+1)}$. Here, we choose N_t as

$$N_t = \max\left(\tilde{N}_t, \left[\frac{(t^{(n+1)} - t^b)}{\Delta\tau_{\min}}\right]_{\text{int}} + 1\right), \tag{4.47}$$

where $[x]_{\text{int}}$ indicates the integer part of x, and $\tilde{N}_t$ and $\Delta\tau_{\min}$ are parameters to be specified. More precisely, $\Delta\tau_{\min}$ is a standard small time interval, but when $t^{(n+1)} - t^b$ is comparable to or smaller than $\Delta\tau_{\min}$, then we divide the interval $[t^b, t^{(n+1)}]$ into $\tilde{N}_t$ small intervals.

Now suppose that Φ is known at $t = \tau^{(0)}, \tau^{(1)}, ..., \tau^{(m)}$ along the characteristic line ($0 \le m \le N_t - 1$). In other words,

$$\mathsf{T}^{\tau^{(0)}}_{\zeta^{(j)}}[\Phi^{(k,n+1,i,j)}],\ \mathsf{T}^{\tau^{(1)}}_{\zeta^{(j)}}[\Phi^{(k,n+1,i,j)}],\ ...,\ \mathsf{T}^{\tau^{(m)}}_{\zeta^{(j)}}[\Phi^{(k,n+1,i,j)}], \tag{4.48}$$

are known [cf. Eq. (4.16)]. If we integrate both sides of Eq. (4.9a) from $t' = \tau^{(m)}$ to $\tau^{(m+1)}$ along the characteristic line, we obtain [cf. Eq. (4.17)]

$$\mathsf{T}^{\tau^{(m+1)}}_{\zeta^{(j)}}[\Phi^{(k,n+1,i,j)}] = \mathsf{T}^{\tau^{(m)}}_{\zeta^{(j)}}[\Phi^{(k,n+1,i,j)}] + \frac{2}{\sqrt{\pi}}\frac{1}{\mathrm{Kn}}\int_{\tau^{(m)}}^{\tau^{(m+1)}} \mathsf{T}^{\tau}_{\zeta^{(j)}}\left[H^{(k,n+1,i,j)} - \rho^{(k,n+1,i)}\Phi^{(k,n+1,i,j)}\right]\mathrm{d}\tau. \tag{4.49}$$

where

$$H^{(k,n+1,i,j)} = \rho^{(k,n+1,i)}\lambda^{(k,n+1,i)}M^{(k,n+1,i,j)}, \quad \lambda^{(k,n+1,i)} = \left[\frac{1}{T^{(k,n+1,i)}}\right]. \tag{4.50}$$

If we apply the trapezoidal rule for the integral over the small interval $[\tau^{(m)}, \tau^{(m+1)}]$ in Eq. (4.49), we obtain $\mathsf{T}^{\tau^{(m+1)}}_{\zeta^{(j)}}[\Phi^{(k,n+1,i,j)}]$ in terms of the known quantities $\mathsf{T}^{\tau^{(m)}}_{\zeta^{(j)}}[\Phi^{(k,n+1,i,j)}]$, $\mathsf{T}^{\tau^{(m+1)}}_{\zeta^{(j)}}[U^{(k,n+1,i,j)}]$, and $\mathsf{T}^{\tau^{(m)}}_{\zeta^{(j)}}[U^{(k,n+1,i,j)}]$, that is,

$$\mathsf{T}^{\tau^{(m+1)}}_{\zeta^{(j)}}[\Phi^{(\,\cdot\,)}] = \left(1 + \frac{1}{\sqrt{\pi}}\frac{\Delta\tau}{\mathrm{Kn}}\mathsf{T}^{\tau^{(m+1)}}_{\zeta^{(j)}}[\rho^{(\,\cdot\,)}]\right)^{-1} \times \left[\mathsf{T}^{\tau^{(m)}}_{\zeta^{(j)}}[\Phi^{(\,\cdot\,)}] + \frac{1}{\sqrt{\pi}}\frac{\Delta\tau}{\mathrm{Kn}}\left(\mathsf{T}^{\tau^{(m)}}_{\zeta^{(j)}}\left[H^{(\,\cdot\,)} - \rho^{(\,\cdot\,)}\Phi^{(\,\cdot\,)}\right] + \mathsf{T}^{\tau^{(m+1)}}_{\zeta^{(j)}}\left[H^{(\,\cdot\,)}\right]\right)\right]. \tag{4.51}$$

where the superscript $(\,\cdot\,)$ indicates either the superscript $(k, n+1, i, j)$ or $(k, n+1, i)$.

On the other hand, $\mathsf{T}^{\tau^{(0)}}_{\zeta^{(j)}}[\Phi^{(k,n+1,i,j)}] = \mathsf{T}^{t^b}_{\zeta^{(j)}}[\Phi^{(k,n+1,i,j)}]$ is known from initial or boundary condition. More precisely,

$$\mathsf{T}^{t^b}_{\zeta^{(j)}}[\Phi^{(k,n+1,i,j)}] = \begin{cases} \pi^{-1/2}\sigma_w(t^b)\exp(-[\zeta^{(j)} - v_w(t^b)]^2), & \text{for} \quad t^b \neq 0, \\ \pi^{-1/2}\exp(-[\zeta^{(j)}]^2), & \text{for} \quad t^b = 0. \end{cases} \tag{4.52}$$

In the actual computation, t^b is obtained by the Newton method as in [16], $v_w(t^b)$ is interpolated by the method given in [16], and $\sigma_w(t^b)$ is linearly interpolated by using $\sigma_w(t^{(q)})$ and $\sigma_w(t^{(q+1)})$ when $t^b \in [t^{(q)}, t^{(q+1)}]$. If $q = n$, we use extrapolation to obtain $\sigma_w(t^b)$.

Then, applying Eq. (4.51) successively for $m = 0, 1, \ldots, N_t - 1$, we obtain $\Phi^{(k,n+1,i,j)} = \mathsf{T}^{\tau^{(N_t)}}_{\zeta^{(j)}}[\Phi^{(k,n+1,i,j)}]$. In this process, we need the macroscopic quantities at $\tau = \tau^{(m)}$, i.e., $\mathsf{T}^{\tau^{(m)}}_{\zeta^{(j)}}[U^{(k,n+1,i,j)}]$. If $\tau^{(m)} \leq t^{(n)}$ (say, $\tau^{(m)} \in [t^{(q)}, t^{(q+1)}]$ with $q \leq n-1$), we obtain the values by the linear interpolation in t' using $U(x_*, t^{(q)})$ and $U(x_*, t^{(q+1)})$, where

$$x_* = z^{(k,n,i)} - \zeta^{(j)}(t^{(n+1)} - \tau^{(m)}), \tag{4.53}$$

and the values of $U(x_*, t^{(q)})$ are obtained by the interpolation in x'_1 as described in Sec. 4.1 (see Fig. 4.8). If $t^{(n)} < \tau^{(m)} \leq t^{(n+1)}$, we obtain the values $\mathsf{T}^{\tau^{(m)}}_{\zeta^{(j)}}[U^{(k,n+1,i,j)}]$ by extrapolation. The $\Phi^{(k,n+1,i,j)}$ thus obtained is the predicted distribution function $\hat{\Phi}^{(k,n+1,i,j)}$ in Process 2 in Sec. 4.3. Once we obtain the predicted values $\hat{U}^{(k,n+1,i)}$ and $\hat{\sigma}_w^{(n+1)}$ in Process 3 in Sec. 4.3 and the corrected values $x_w^{(n+1)}$ and $v_w^{(n+1)}$ in Process 4 there, we can repeat the same procedure to obtain the corrected distribution function $\Phi^{(k,n+1,i,j)}$ using interpolation only (without any extrapolation), which is Process 5 in Sec. 4.3.

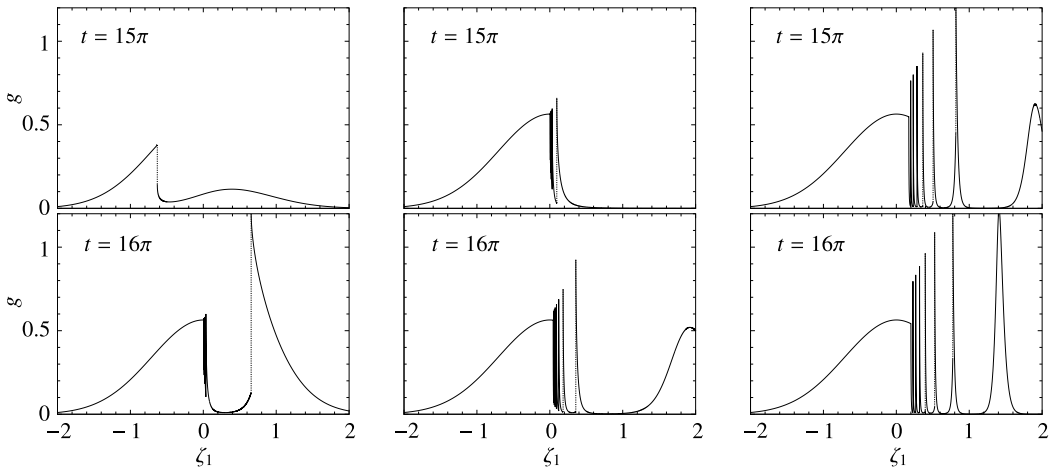

Fig. 4.10 The velocity distribution function $g(x_1, \zeta_1, t)$ vs ζ_1 for $\mathsf{K} = \infty$ and $a = 1$. (a) $x_1 = x_w(t) + 0.2243$, (b) $x_1 = x_w(t) + 2.3052$, and (c) $x_1 = x_w(t) + 10.05$. The upper figures are at $t = 15\pi$, and the lower figures at $t = 16\pi$.

5 Results of numerical analysis

In this section, we show some results of numerical analysis. For convenience, we use the following K, in place of the Knudsen number Kn, as the measure of gas rarefaction:

$$\mathsf{K} = (\sqrt{\pi}/2)\mathrm{Kn}. \tag{4.54}$$

Since our interest is a correct description of the singularities explained in Sec. 3.2, we are mainly concerned with the cases of non-small Knudsen numbers where the singularities are more eminent. We also make a comparison of the results by the present method with those by a finite-difference method with ENO scheme [23] (cf. B). Accuracy checks for the present method as well as the ENO scheme will be made in C.

5.1 Problem I (forced motion)

We first consider Problem I in Sec. 2.1. Here, emphasis is placed on the description of the velocity distribution function of complex shape.

5.1.1 Velocity distribution function

Here, we only consider the marginal velocity distribution function $g(x_1, \zeta_1, t)$ [Eq. (4.7a)]. Figure 4.10 shows g as a function of ζ_1 at two different times and three different positions for free-molecular flow ($\mathsf{K} = \infty$) and $a = 1$. Panels (a), (b), and (c) are, respectively, the results at the points $x_1 = x_w(t) + 0.2243$, $x_1 = x_w(t) + 2.3052$, and $x_1 = x_w(t) + 10.05$ with fixed distances from the moving plate; the upper and lower figures in each panel show the results at $t = 15\pi$ and $t = 16\pi$. Panel (a) is for a close neighborhood of the plate, and panel (c) for a relatively far field. The specified times $t = 15\pi$ and 16π correspond to the middle and the end of the eighth period, respectively. In all panels, one observes discontinuities that are shown by vertical dashed lines.

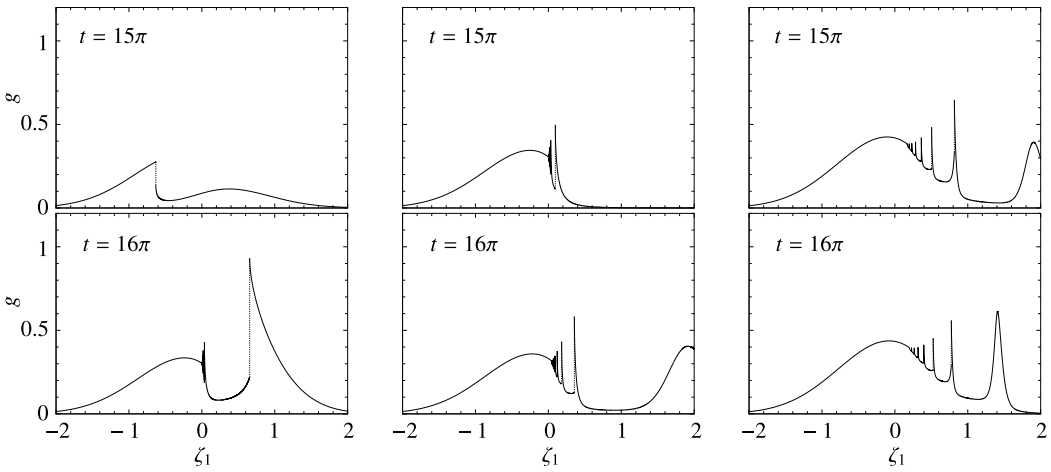

Fig. 4.11 The velocity distribution function $g(x_1, \zeta_1, t)$ vs ζ_1 for $\mathsf{K} = 10$ and $a = 1$. (a) $x_1 = x_w(t) + 0.2243$, (b) $x_1 = x_w(t) + 2.3052$, and (c) $x_1 = x_w(t) + 10.05$. The upper figures are at $t = 15\pi$, and the lower figures at $t = 16\pi$.

In addition, the gradient $\partial g/\partial \zeta_1$ is very large at the right-hand sides of the discontinuities (see Sec. 3.2.1).

Figure 4.11 is the corresponding figure for $\mathsf{K} = 10$, and Fig. 4.12 for $\mathsf{K} = 1$. Note that the locations of the discontinuities in ζ_1 (i.e., $\zeta_1 = \zeta_d$; see Sec. 3.2.1) are the same in Figs. 4.10–4.12. When $\mathsf{K} = 10$, there is the effect of collisions between gas molecules though it is not strong. This effect can be seen clearly by comparing Figs. 4.10 and 4.11. More specifically, the shape of the function g is globally similar in both figures, but the discontinuities are weaker in Fig. 4.11. In particular, the older discontinuities produced at earlier times, which are located closer to $\zeta_1 = 0$, have decayed more. However, when $\mathsf{K} = 1$, the effect of inter-molecular collisions becomes more eminent and makes the shape of g much smoother, as seen in Fig. 4.12. In fact, the discontinuities are hardly seen far away from the plate [Fig. 4.12(c)]. In the vicinity of the plate shown by Fig. 4.12(a), only the youngest discontinuity, produced in the nearest past, is observed clearly. These properties are well described by Eq. (4.28).

Figures 4.13(a), 4.13(b), and 4.13(c) show, respectively, the magnified figures of the upper figures of Figs. 4.10(b), 4.11(b), and 4.12(b) for the range $0 \le \zeta_1 \le 0.1$. We can observe the discontinuities (Type-1 singularities) more clearly in these magnified figures. In addition, we can also see the Type-3 singularity, originating from the initial condition (see Sec. 3.2.3), at $\zeta_1 \approx 0.006$ in Fig. 4.13(a), as noted in the figure. The same singularity can still be identified by a close look in Fig. 4.13(b) for $\mathsf{K} = 10$, whereas it is not visible in Fig. 4.13(c) for $\mathsf{K} = 1$.

As explained in the second paragraph in Sec. 4.2, Type-2 singularities arise rarely. For instance, when $a = 1$, it arises only for $(x_1,\, \zeta_1) = (\pi/2,\, 1)$ and $(5\pi/2,\, 1)$ at time $t = 4\pi$, since $(x_1',\, t') = (0,\, 3\pi/2)$ and $(0,\, 7\pi/2)$ are only the inflection points of the trajectory $x_1' = x_w(t')$ with $t' \le t = 4\pi$. However, at the grid points in the $(x_1',\, t')$ plane located in the neighborhood of the tangential line at an inflection point of the trajectory, the molecular velocity ζ_w (the velocity corresponding to the characteristic line connecting the grid point and the inflection point; see Sec. 4.2) becomes close to ζ_f (see Secs. 3.2.2 and 4.2). Therefore, we expect steep changes in the velocity distribution function at these ζ_w. Figure 4.14 demonstrates this situation for $a = 1$. More precisely, we plot the velocity distribution function $g(x_1,\, \zeta_1,\, t)$ at $t = 4\pi$ and $x_1 \approx \pi/2$ as a function of ζ_1 for

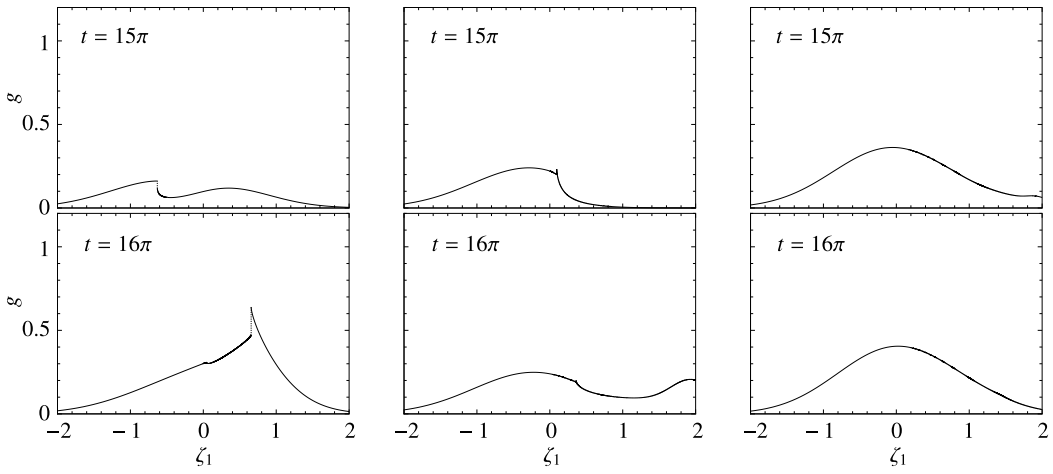

Fig. 4.12 The velocity distribution function $g(x_1, \zeta_1, t)$ vs ζ_1 for $\mathsf{K} = 1$ and $a = 1$. (a) $x_1 = x_w(t) + 0.2243$, (b) $x_1 = x_w(t) + 2.3052$, and (c) $x_1 = x_w(t) + 10.05$. The upper figures are at $t = 15\pi$, and the lower figures at $t = 16\pi$.

$\mathsf{K} = \infty$ [panel (a)], $\mathsf{K} = 10$ [panel (b)], and $\mathsf{K} = 1$ [panel (c)]. The upper figures show the overall shape at $x_1 = \pi/2 = 1.57080$ (the exact value of $\pi/2$ is $1.570796...$); thus the dashed vertical line indicates the location of the Type-2 singularity. The lower figures show the magnification of the upper figures in the vicinity of $\zeta_1 = 1$, together with some additional curves for x_1 very close to $\pi/2$. More specifically, the curve for $x_1 = 1.57080$ shows the Type-2 singularity at $\zeta_1 = 1$, and the curves for $x_1 = 1.5688$ and 1.5698 exhibit Type-1 singularities (discontinuities), as indicated by the dotted vertical line. On the other hand, the curves for 1.5718 and 1.5728 do not contain any singularities. It is seen from the figures that the gradient $|\partial g/\partial \zeta_1|$ at (the right side of) Type-1 singularity and that at Type-2 singularity are very large not only for $\mathsf{K} = \infty$ [cf. Eqs. (4.30) and (4.32)] but also for $\mathsf{K} = 10$ and 1 [the curve seems to have a cusp at $\zeta_1 = 1$ in the upper figures of panels (a) and (b)]. In addition, the curves for 1.5718 and 1.5728 still have very large gradients near the points $\zeta_1 = \zeta_w$. This is the reason why we have regarded $\zeta_1 = \zeta_w$ as singular velocities (see the second paragraph in Sec. 4.2). Otherwise we would miss the true shape of the velocity distribution function.

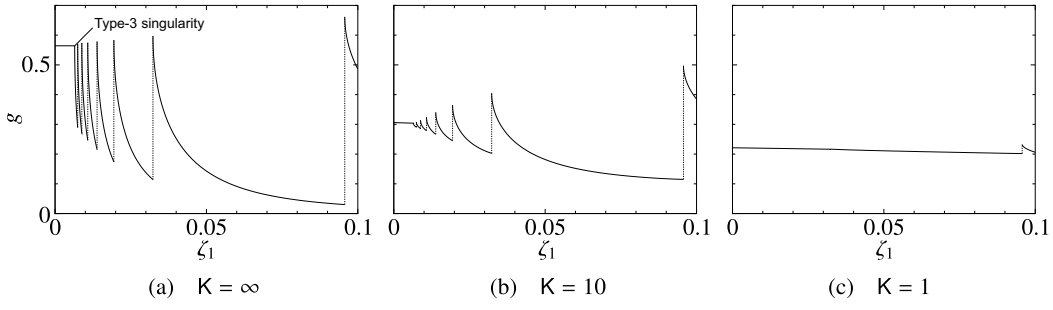

Fig. 4.13 The velocity distribution function $g(x_1, \zeta_1, t)$ vs ζ_1 for $a = 1$ at $x_1 = x_w(t) + 2.3052$ and $t = 15\pi$ (magnified). (a) $\mathsf{K} = \infty$, (b) $\mathsf{K} = 10$, and (c) $\mathsf{K} = 1$. Panels (a), (b), and (c) are the closeups of the upper figures of Figs. 4.10(b), 4.11(b), and 4.12(b), respectively.

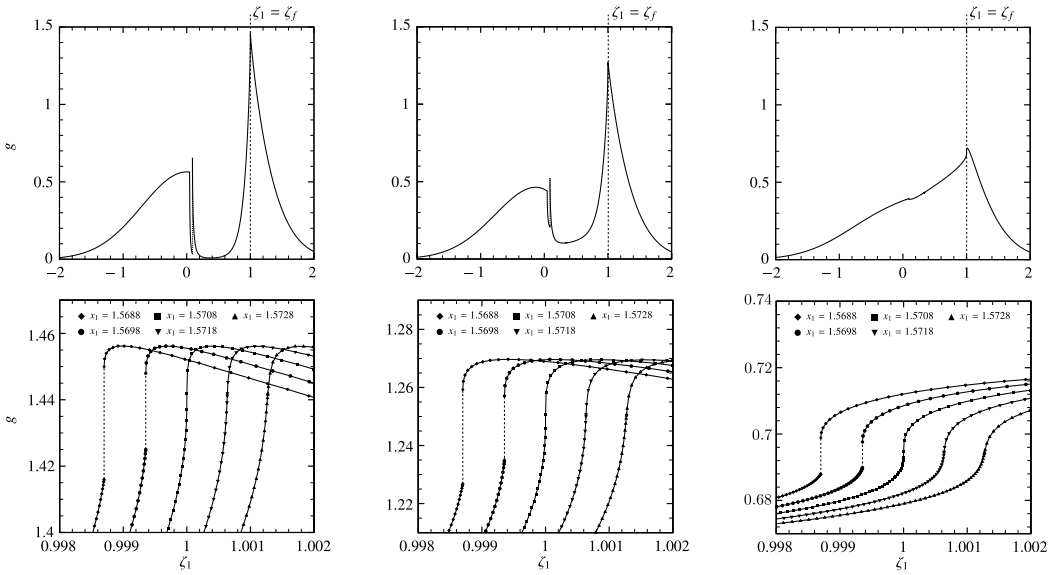

(a) $\mathsf{K} = \infty$ (b) $\mathsf{K} = 10$ (c) $\mathsf{K} = 1$

Fig. 4.14 The velocity distribution function $g(x_1, \zeta_1, t)$ at $t = 4\pi$. (a) $\mathsf{K} = \infty$, (b) $\mathsf{K} = 10$, and (c) $\mathsf{K} = 1$. The upper figures show g at $x_1 = 1.5708$, where $\zeta_1 = \zeta_f$ (Type-2 singularity) is indicated by the dashed vertical line. Lower figures show the closeups of the upper figures in the neighborhood of $\zeta_1 = 1$, together with g at some x_1 near $x_1 = \pi/2$ $(= 1.570796...)$, i.e., at $x_1 = 1.5688$, 1.5698, 1.5708, 1.5718, and 1.5728.

Finally, we compare the result of present computation with that obtained by the finite-difference method with the ENO scheme in Figs. 4.15 and 4.16. Figure 4.15 shows the comparison of $g(x_1, \zeta_1, t)$ at $t = 16\pi$ for $a = 1$ and for $\mathsf{K} = \infty$ [(a)], 10 [(b)], and $= 1$ [(c)], where the *solid line* indicates the present result and the *circle* the ENO result. The upper figures are for $x_1 = x_w(t) + 0.2243$ [near the oscillating plate; note that $x_w(16\pi) = a = 1$], and lower figures for $x_1 = x_w(t) + 22.3111$ (far field). It is seen that the ENO scheme (with fixed grid points in the molecular velocity space) can neither resolve the singularities nor the sharp changes for large K [panels (a) and (b)]. The same is true for $\mathsf{K} = 1$ near the plate [the upper figure of panel (c)]. However, in the far field, where the velocity distribution function is smooth, the ENO scheme gives a correct result [the lower figure of panel (c)]. The upper figures of Fig. 4.16 are the corresponding figures to the upper figures of Fig. 4.15 when the amplitude of oscillation is small. That is, $g(x_1, \zeta_1, t)$ for $a = 0.1$ and at $t = 16\pi$ and $x_1 = x_w(t) + 0.2243$ is plotted versus ζ_1. The lower figures of Fig. 4.16 are the closeup around $\zeta_1 = 0$ of the upper figures. The ENO result gives a better agreement in this case. However, its difference from the present result is quite visible for $\mathsf{K} = \infty$ and 10. When the amplitude a is small, the deviation of the velocity distribution function from the reference equilibrium state is small. In this case, one need to handle the deviation itself to describe physical phenomena using, e.g., the linearized Boltzmann equation. It is seen from the lower figures of Figs. 4.16(a) and (b) that the error of the ENO result is of the same order of magnitude as the deviation itself.

5.1.2 Macroscopic quantities

Next, we show some results for the macroscopic quantities, which illustrate the propagation of nonlinear acoustic waves in a rarefied gas. We will present only limited cases because the detailed

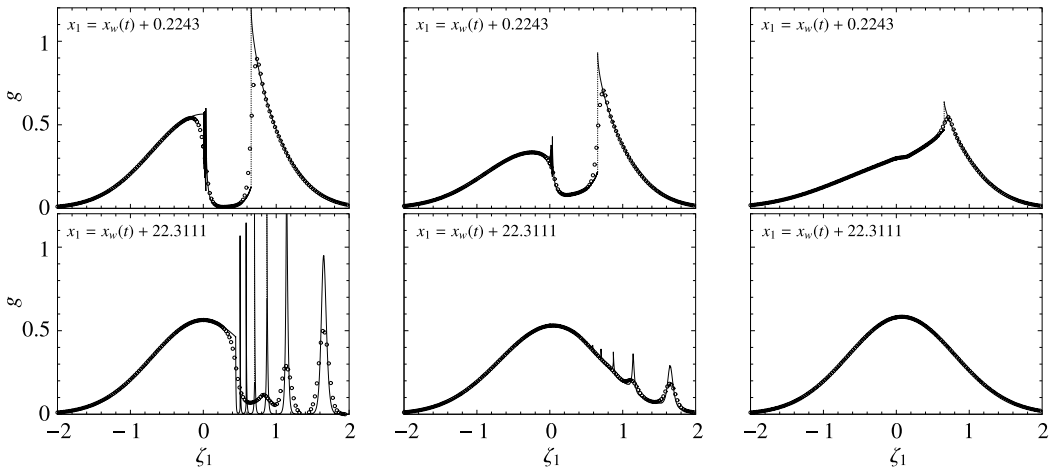

Fig. 4.15 The velocity distribution function $g(x_1,\, \zeta_1,\, t)$ at $t = 16\pi$ for $a = 1$. (a) $\mathsf{K} = \infty$, (b) $\mathsf{K} = 10$, and (c) $\mathsf{K} = 1$. The upper figures show the results at the position $x_1 = x_w(t) + 0.2243$, while the lower figures those at $x_1 = x_w(t) + 22.3111$. The results obtained by the ENO scheme (*circles*) are shown together with those by the present method (*Solid lines*).

discussions on the physical behavior are not the main purpose of the present paper and moreover, some of them are included in [24].

Figures 4.17, 4.18, and 4.19 show the profiles of the macroscopic quantities in the eighth period ($14\pi \le t \le 16\pi$) for $(\mathsf{K},\, a) = (\infty,\, 1)$, $(\infty,\, 0.1)$, and $(1,\, 0.1)$, respectively. In the figures, $\rho - 1$ is shown in panels (a), $T - 1$ in panels (b), u_1 panels (c), and $p - 1$ in panels (d). The behavior during a period can be followed as *bold dashed line* ($t = 14\pi$) $\rightarrow$ *dashed line* ($t = 14.5\pi$) $\rightarrow$ *dot-dashed line* ($t = 15\pi$) $\rightarrow$ *dot-dot-dashed line* ($t = 15.5\pi$) $\rightarrow$ *solid line* ($t = 16\pi$). Since the curves for $t = 14\pi$ and $t = 16\pi$ are almost the same, an almost periodic state has been established near the plate after the transient behavior. In the case of free-molecular flow (Figs. 4.17 and 4.18), the wave caused by the oscillating plate decays rapidly with the distance from the plate. This tendency remains when the Knudsen number is of the order of unity (Fig. 4.19). This strong decay was already recognized in some early works based on the linearized setting (see, e.g., [25, 26, 27, 28, 29]). In Fig. 4.17, one observes a weak streaming motion (i.e., a positive u_1) in the far field, as observed in earlier works based on the nonlinear setting (see, e.g., [5, 14, 24, 30]). In Figs. 4.18 and 4.19 for a small amplitude ($a = 0.1$), the nonlinearity is weak, so that the profiles are almost symmetric with respect to the reference equilibrium values. The reader is referred to [24] for the profiles for small K.

In Fig. 4.20, we compare the density profile, more precisely, $(\rho - 1)/a$, obtained by the present method and that by the ENO scheme for $(\mathsf{K},\, a) = (\infty,\, 1)$ [(a)], $(\infty,\, 0.1)$ [(b)], $(\infty,\, 0.01)$ [(c)], and $(10,\, 0.1)$ [(d)]. Here, the *solid line* indicates the present result, and the *dashed line* the ENO result. In each panel, the left figure shows the closeup near the oscillating plate (at $t = 14\pi$, 14.16π, 14.32π, 14.48π, 15.6π, 15.76π, 15.92π), and the right figure is for the far field (at $t = 16\pi$). The ENO scheme (with decent numerical parameters, see Sec. C.2 and B) gives good results near the plate except for a slight deviation in Fig. 4.20(a). It also gives the correct result for the far field in Fig. 4.20(a). This is surprising because the velocity distribution function for $\mathsf{K} = \infty$ obtained by the ENO scheme is far from the correct one, in particular, for the far field [see Fig. 4.15(a)]. In Figs. 4.20(a) and 4.20(b) for small amplitudes, the ENO results show visible oscillations. In

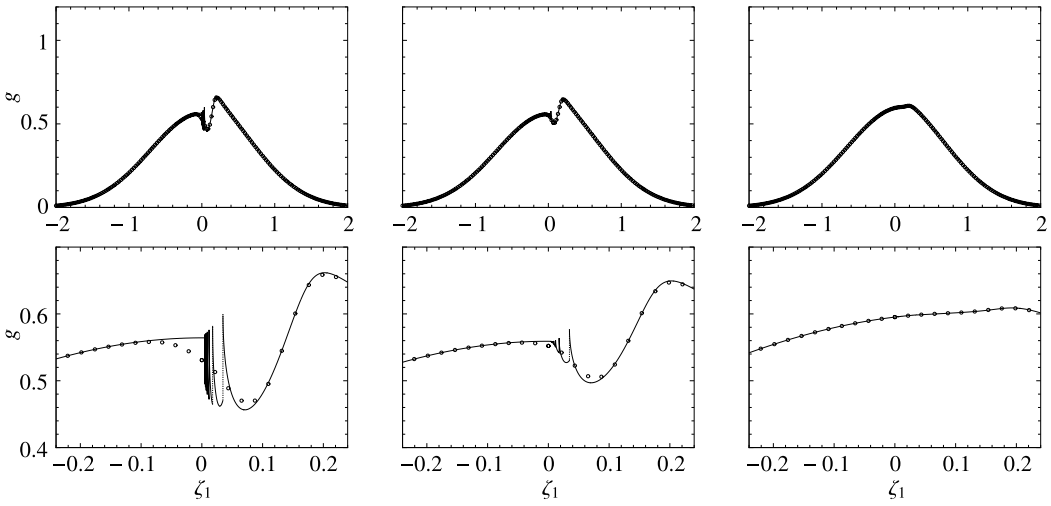

(a) $\mathsf{K} = \infty$ (b) $\mathsf{K} = 10$ (c) $\mathsf{K} = 1$

Fig. 4.16 The velocity distribution function $g(x_1, \zeta_1, t)$ at $t = 16\pi$ for $a = 0.1$. (a) $\mathsf{K} = \infty$, (b) $\mathsf{K} = 10$, and (c) $\mathsf{K} = 1$. The upper figures show the results at the position $x_1 = x_w(t) + 0.2243$, and the lower figures are the closeup of the upper figures around $\zeta_1 = 0$. The results obtained by the ENO scheme (*circle*) are shown together with those by the present method (*Solid line*).

Fig. 4.20(d), where the effect of collisions between gas molecules are included, the ENO scheme gives good results even for the far field as is expected from the comparison in Sec. 5.1.1.

5.2 Problem II (free motion)

In Problem II, the displacement of the plate $x_w(t)$ decays to zero as time proceeds because of the drag force exerted by the surrounding gas. We focus our attention on the rate of the decay. In the present paper, we let $\mathcal{M} = 2$ and change a and K as $a = 1$, 0.1, and 0.01, and $\mathsf{K} = \infty$, 10, and 1. The case of $\mathsf{K} = \infty$ and that of $\mathsf{K} = 10$ and 1 will be discussed separately.

5.2.1 Case of $\mathsf{K} = \infty$

For $\mathsf{K} = \infty$ (free-molecular flow), there exists a rigorous mathematical study [31], which has proven that the decay of $|x_w(t)|$ is proportional to an inverse power of time. The proof is restricted to the case of non-oscillatory decay. The algebraic decay has then confirmed numerically also for the oscillatory case [16]. In these works, linear motion of a three-dimensional body (a circular disk) is considered, and the one-dimensional case in [16] exactly corresponds to the present Problem II. According to [16], the asymptotic behavior of the displacement of the plate is

$$|x_w(t)| \approx Ct^{-2}, \qquad \text{for} \quad t \gg 1, \tag{4.55}$$

where C is a positive constant. Here we note that the method in [16] is specialized to a free-molecular gas and different from the present method. In Fig. 4.21, we show the displacement $|x_w(t)|$ versus t in double logarithmic scale for $\mathsf{K} = \infty$ and for $a = 1$ [(a)], 0.1 [(b)], and 0.01 [(c)]. Here, the *solid line* indicates the results obtained by the present method, the *bold dashed line* those by the ENO scheme, and the *bold dot-dashed line* and the *bold dot-dot-dashed line* in panel (a) those by the ENO scheme with coarser grid systems (the grid for the *bold dot-dot-dashed*

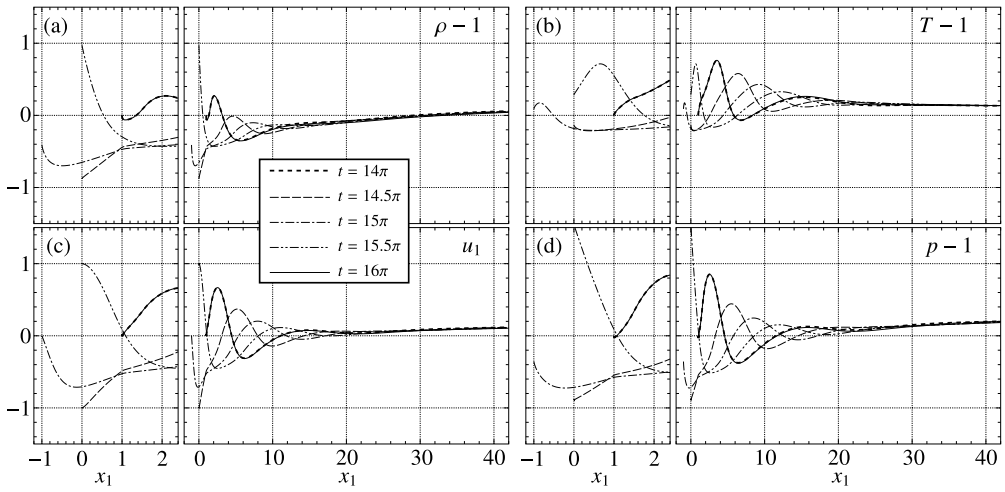

Fig. 4.17 Profiles of the macroscopic quantities at different times in $14\pi \leq t \leq 16\pi$ for $\mathsf{K} = \infty$ and $a = 1$. (a) $\rho - 1$, (b) $T - 1$, (c) u_1, and (d) $p - 1$. The results are shown at $t = 14\pi$ (*bold dashed line*), 14.5π (*dashed line*), 15π (*dot-dashed line*), 15.5π (*dot-dot-dashed line*), and 16π (*solid line*). In each panel, the left figure shows the closeup near the oscillating plate.

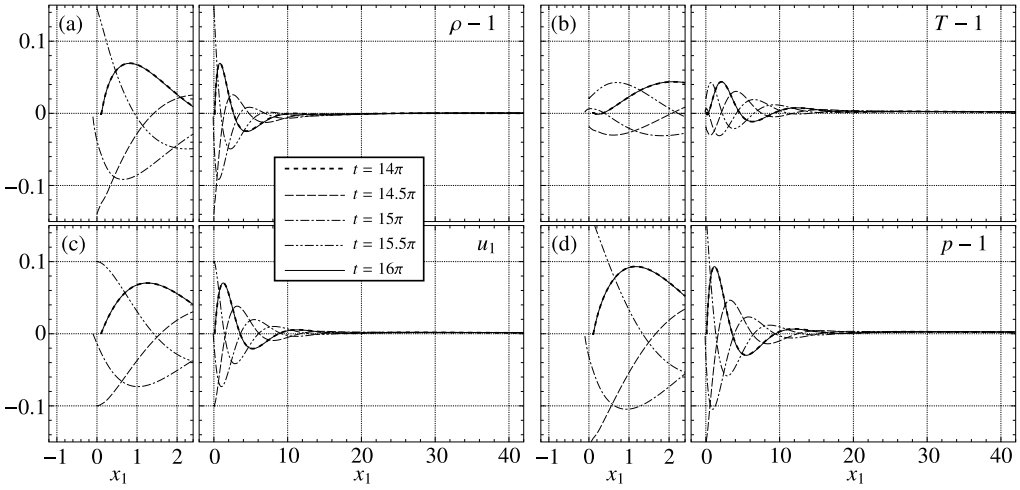

Fig. 4.18 Profiles of the macroscopic quantities at different times in $14\pi \leq t \leq 16\pi$ for $\mathsf{K} = \infty$ and $a = 0.1$. (a) $\rho - 1$, (b) $T - 1$, (c) u_1, and (d) $p - 1$. The results are shown at $t = 14\pi$ (*bold dashed line*), 14.5π (*dashed line*), 15π (*dot-dashed line*), 15.5π (*dot-dot-dashed line*), and 16π (*solid line*). In each panel, the left figure shows the closeup near the oscillating plate.

line is 2.5 times coarser than that for the *bold dashed line*). For both schemes, numerical systems slightly coarser than those for Problem I are used because the computation for a longer time is required in this problem (up to $t = 200$ in Fig. 4.21). In each panel, a straight line corresponding to $const(> 0) \times t^{-2}$ is shown by the dotted line. Panel (a) for $a = 1$ shows that the result by the present method tends to be parallel to the straight line for large t, which means that it captures the decay given by Eq. (4.55). In contrast, the results by the ENO scheme fails to capture it. The same is true in panel (b) for a smaller initial displacement ($a = 0.1$). However, in panel (c), where the

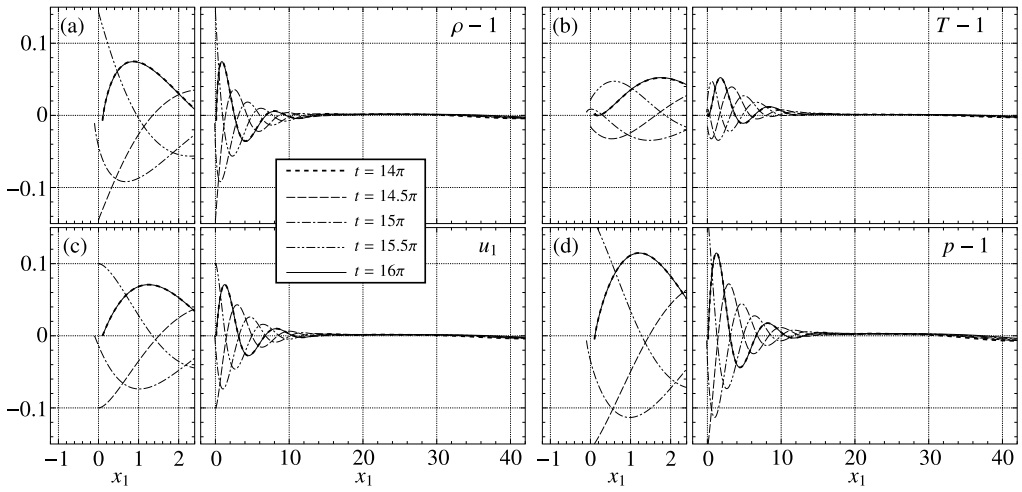

Fig. 4.19 Profiles of the macroscopic quantities at different times in $14\pi \leq t \leq 16\pi$ for $\mathsf{K} = 1$ and $a = 1$. (a) $\rho - 1$, (b) $T - 1$, (c) u_1, and (d) $p - 1$. The results are shown at $t = 14\pi$ (*bold dashed line*), 14.5π (*dashed line*), 15π (*dot-dashed line*), 15.5π (*dot-dot-dashed line*), and 16π (*solid line*). In each panel, the left figure shows the closeup near the oscillating plate.

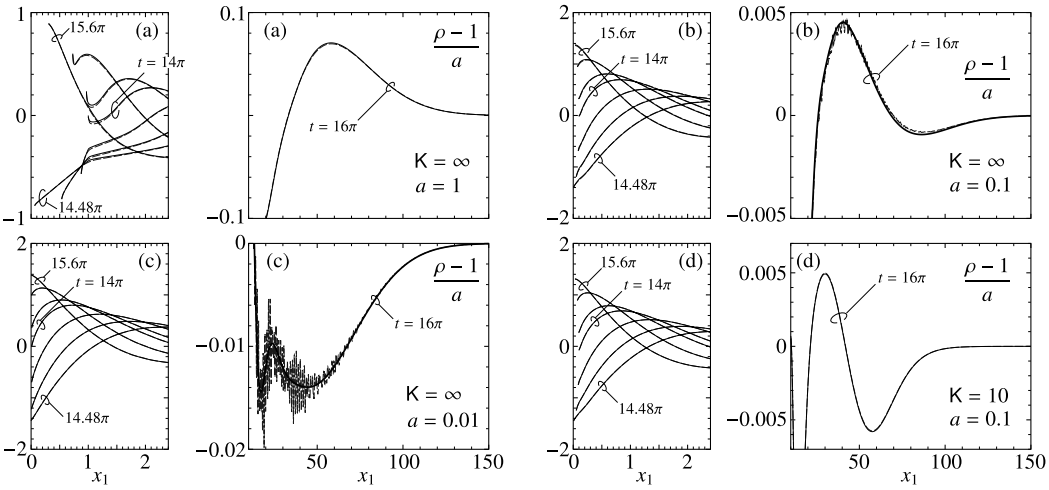

Fig. 4.20 Profiles of $(\rho - 1)/a$ at several different times in $14\pi \leq t \leq 16\pi$ for four sets of $(\mathsf{K},\, a)$. (a) $(\mathsf{K},\, a) = (\infty,\, 1)$, (b) $(\mathsf{K},\, a) = (\infty,\, 0.1)$, (c) $(\mathsf{K},\, a) = (\infty,\, 0.01)$, (d) $(\mathsf{K},\, a) = (10,\, 0.1)$. The *solid line* indicates the solution by the present method, and the *dashed line* that by the ENO scheme. In each panel, the left figure shows the closeup near the oscillating plate at $t = 14\pi$, 14.16π, 14.32π, 14.48π, 15.6π, 15.76π, 15.92π, and the right figure for the far field at $t = 16\pi$. In panels (b) and (c) for the far field, the solid line is thickened in order that it is distinguishable from the oscillatory dashed line.

initial displacement is so small ($a = 0.01$) that accurate computation is very hard, even the present method has a difficulty in describing the behavior given by Eq. (4.55). As discussed in [16], the power-law decay (4.55) is attributed to the localized steep changes in the velocity distribution function. Therefore, there is little hope to capture the correct decay rate by the ENO scheme even with finer grid systems.

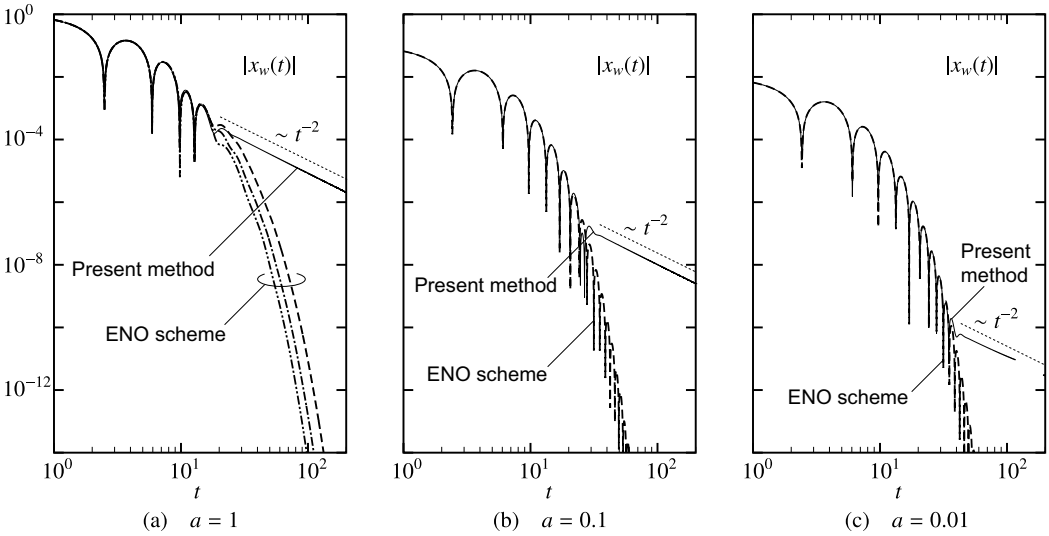

Fig. 4.21 The displacement $|x_w(t)|$ vs t in double logarithmic scale for $\mathsf{K} = \infty$. (a) $a = 1$, (b) $a = 0.1$, and (c) $a = 0.01$. The *solid line* indicates the results obtained by the present method, the *bold dashed line* those by the ENO scheme, and the *bold dot-dashed line* and the *bold dot-dot-dashed line* in panel (a) those by the ENO scheme with coarser grid systems.

5.2.2 Case of finite K

For finite K with the effect of inter-molecular collisions, nothing is known about the rate of the decay of the displacement. Figures 4.22 and 4.23 are, respectively, the figures for $\mathsf{K} = 10$ and $\mathsf{K} = 1$, corresponding to Fig. 4.21. In contrast to Fig. 4.21, the result by the ENO scheme is very close to that by the present method. In Problem II, the motion of the plate attenuates as time goes on, so that the singularities created by the moving plate at later time are weaker than those created at earlier times. Since the stronger singularities produced at earlier times has decayed at later times because of the effect of inter-molecular collisions, the velocity distribution function for finite K (even for $\mathsf{K} = 10$) is much milder than that for $\mathsf{K} = \infty$. This may be the reason why the ENO scheme works this time. For $\mathsf{K} = 10$ (Fig. 4.22), the computation up to time $t = 200$ is not enough to obtain a clear decay rate. On the contrary, for $\mathsf{K} = 1$ and $a = 0.1$ and 0.01 [panels (b) and (c) in Fig. 4.23], the curves tend to approach the straight line corresponding to $const(> 0) \times t^{-3/2}$. Therefore, it is likely in these cases that $x_w(t)$ decays as $|x_w(t)| \approx const(> 0) \times t^{-3/2}$ as $t \to \infty$. This is slower than in the case of $\mathsf{K} = \infty$. However, to arrive at a more definite conclusion, we need more intensive computation until longer times. The ENO scheme, which is computationally less expensive than the present method, could be useful for this purpose.

6 Concluding remarks

In the present study, we are concerned with moving boundary problems in kinetic theory of gases. We focused our attention to the singularities in the velocity distribution function created by the moving boundary and to the numerical method capable of describing the propagation of the singularities in the gas. In order to single out the essence of the problems without being bothered by other complexities, we employed the BGK model of the Boltzmann equation instead of the full Boltzmann equation and restricted ourselves to spatially one-dimensional problems: the propaga-

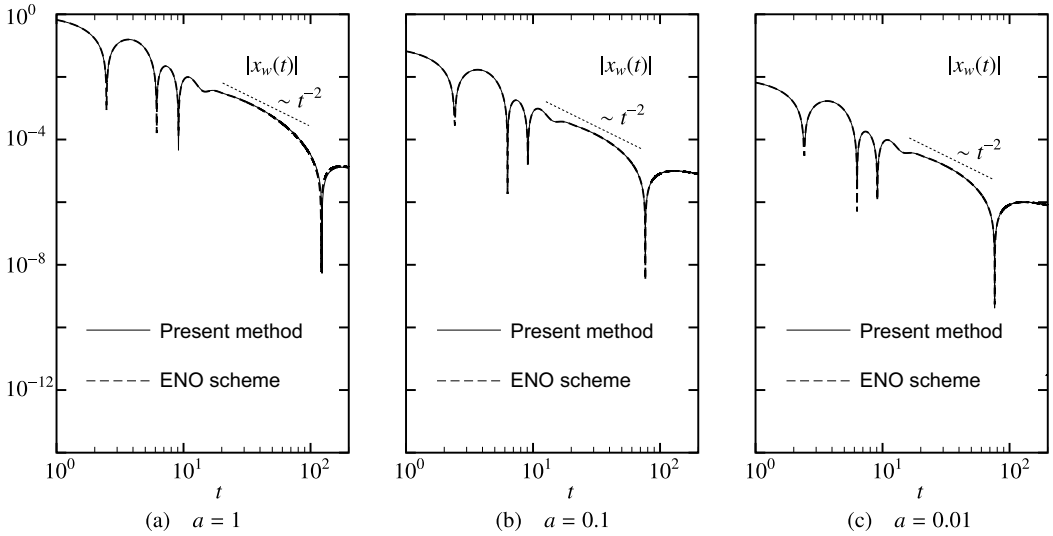

Fig. 4.22 The displacement $|x_w(t)|$ vs t in double logarithmic scale for $\mathsf{K} = 10$. (a) $a = 1$, (b) $a = 0.1$, and (c) $a = 0.01$. The *solid line* indicates the results obtained by the present method, the *bold dashed line* those by the ENO scheme, and the *bold dot-dashed line* and the *bold dot-dot-dashed line* in panel (a) those by the ENO scheme with coarser grid systems.

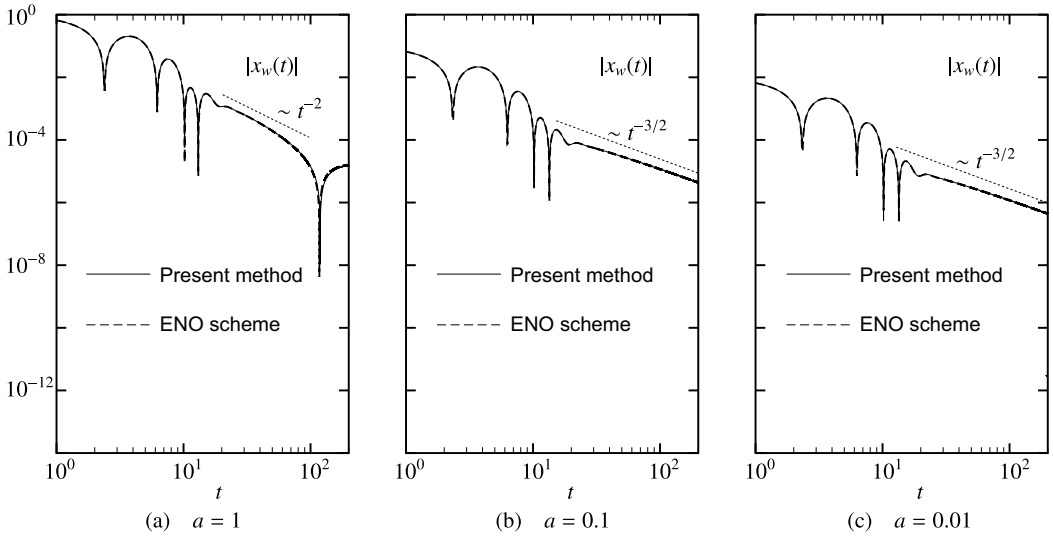

Fig. 4.23 The displacement $|x_w(t)|$ vs t in double logarithmic scale for $\mathsf{K} = 1$. (a) $a = 1$, (b) $a = 0.1$, and (c) $a = 0.01$. The *solid line* indicates the results obtained by the present method, the *bold dashed line* those by the ENO scheme, and the *bold dot-dashed line* and the *bold dot-dot-dashed line* in panel (a) those by the ENO scheme with coarser grid systems.

tion of nonlinear acoustic waves in a semi-infinite expense of a rarefied gas caused by the sudden start of harmonic oscillation of a plate (Problem I), and the decay of the displacement of a linear pendulum in a rarefied gas (Problem II) (Sec. 2). With the help of physical and formal mathematical arguments, we have clarified possible types of singularities introduced by the moving plate (Sec. 3). On the basis of the knowledge obtained in Sec. 3, we have constructed a numerical method that can describe the singularities and steep changes in the velocity distribution function (Sec. 4).

The results of numerical analysis are shown in Sec. 5.

For Problem I, we have put special emphasis on the complex shape of the velocity distribution function at large Knudsen numbers made up of accumulating singularities and steep changes (Sec. 5.1.1). This complex shape is very difficult to capture by standard numerical methods for kinetic equations, as exemplified by the numerical result using a finite-difference method with the ENO scheme. The behavior of the time evolution of the macroscopic quantities are then discussed (Sec. 5.1.2). In spite of the fact that the ENO scheme totally fails to describe the complex shape of the velocity distribution function for large Knudsen numbers, it gives surprisingly correct result for the macroscopic quantities. This may give a hope that, as far as the macroscopic quantities are concerned, standard methods can be used for moving boundary problems. The present results would serve as a reference solution or a benchmark for other methods devised to tackle the moving boundary problems. We should also emphasize that the present results give an insight for mathematical study of moving boundary problems for the Boltzmann equation. For instance, a mathematical theory based on the assumption that the solution of the Boltzmann equation is smooth does not make any practical sense.

For Problem II, we have focused our attention on the rate of the decay of the displacement (or amplitude) of an oscillating plate (Sec. 5.2). In the case of a free-molecular gas, the present method was able to reproduce the slow algebraic decay [Eq. (4.55)], obtained by an accurate numerical analysis specialized to a free-molecular gas, whereas the finite-difference method with the ENO scheme failed to capture it. In contrast, when there is the effect of inter-molecular collisions, the ENO scheme seemed to give correct result for the time evolution of the displacement of the plate. In addition, some results suggest that the decay rate is even slower than the free-molecular case. The definite clarification of the decay rate will be the subject of future research. It should be mentioned that similar decay problems (decay of a pendulum and of a rotating sphere) have been studied for a Stokes fluids [32, 33]. It would be interesting to study the present Problems I and II for a (compressible) Navier–Stokes fluids.

A Details for grid systems and interpolation

The grid function L_η occurring in Eq. (4.37) is defined as follows:

$$L_\eta(n,i) = \begin{cases} A^{(n)} i \exp(B^{(n)} i), & \text{for} \quad i = 0, \cdots, \bar{N}, \\ C^{(n)} i + D^{(n)}, & \text{for} \quad i = \bar{N}+1, \cdots, N_x, \end{cases} \tag{4.56a}$$

$$C^{(n)} = \Delta x_{\max}, \quad D^{(n)} = D_{\max} - x_w^{(n)} - C^{(n)} N_x, \tag{4.56b}$$

$$B^{(n)} = \frac{1}{\bar{N}} \left(\frac{C^{(n)} \bar{N}}{C^{(n)} \bar{N} + D^{(n)}} - 1 \right), \quad A^{(n)} = \frac{C^{(n)} \bar{N} + D^{(n)}}{\bar{N}} \exp(-B^{(n)} \bar{N}), \tag{4.56c}$$

where $\bar{N}$, $D_{\max}$, and $\Delta x_{\max}$ are the parameters: $\bar{N}$ controls the density of the grid points in the neighborhood of the plate, $D_{\max}$ the size of the domain of computation, and $\Delta x_{\max}$ the maximum of the width of the intervals $I^{(n,i)}$.

The function L_a appearing in Eq. (4.41) is defined as

$$L_a(k,\, U^{(k,n,i)}) = \frac{1}{N_{\text{ch}} e_{\text{ch}}^{(k)}} \sum_{m=0}^{N_{\text{ch}}-1} \left[U^{(m,n,i)} T_{N_{\text{ch}}-k}(y^{(m)}) + U^{(m+1,n,i)} T_{N_{\text{ch}}-k}(y^{(m+1)}) \right], \tag{4.57a}$$

$$e_{\text{ch}}^{(k)} = \begin{cases} 2, & \text{for} \quad k = 0 \text{ and } N_{\text{ch}}, \\ 1, & \text{otherwise}, \end{cases} \tag{4.57b}$$

$$y^{(m)} = \cos(m\pi/N_{\rm ch}). \tag{4.57c}$$

The grid function $L_\zeta(j)$ in Eq. (4.43) is defined as follows. We choose the number of small intervals $\bar{N}_\zeta^{(m)}$ in the interval $[\tilde{\zeta}^{(m)},\ \tilde{\zeta}^{(m+1)}]$ in the following way:

$$\bar{N}_\zeta^{(m)} = \max\left(\tilde{N}_\zeta,\ \left[\frac{\pi}{2}\frac{\tilde{\zeta}^{(m+1)} - \tilde{\zeta}^{(m)}}{\Delta\zeta_{\max}}\right]_{\rm int} + 1\right), \tag{4.58}$$

where $[x]_{\rm int}$ indicates the integer part of x, and $\tilde{N}_\zeta$ and $\Delta\zeta_{\max}$ are numbers that are chosen suitably. More specifically, $\Delta\zeta_{\max}$ is, in principle, the size of the largest small intervals in $[\tilde{\zeta}^{(m)},\ \tilde{\zeta}^{(m+1)}]$ for all m, but when the size of the interval $[\tilde{\zeta}^{(m)},\ \tilde{\zeta}^{(m+1)}]$ is comparable to or smaller than $\Delta\zeta_{\max}$, we put $\tilde{N}_\zeta$ small intervals there. Then, we define the cumulative number of the grid points by

$$\bar{C}^{(m-1)} = N_\zeta + \sum_{q=1}^{m-1} \bar{N}_\zeta^{(q)}, \qquad (m = 1,\ 2,\ ...,\ l+1), \tag{4.59}$$

with $\bar{C}^{(0)} = N_\zeta$, so that we have $\zeta^{(\bar{C}^{(m)})} = \tilde{\zeta}^{(m+1)}$. With these symbols, the grid function $L_\zeta(j)$ is given by

$$L_\zeta(j) = \begin{cases} A_0 j \exp(B_0 j) + C_0, & \text{for} \quad 0 \le j \le N_\zeta, \\ A_m \cos(B_m(j - C_m)) + D_m, & \text{for} \quad \bar{C}^{(m-1)} < j \le \bar{C}^{(m)}, \\ & \qquad (m = 1,\ 2,\ ...,\ l) \\ -A_{l+1} j' \exp(B_{l+1} j') - C_{l+1}, & j' = N_\zeta - \left(j - \bar{C}^{(l)}\right), \\ & \qquad \text{for} \quad \bar{C}^{(l)} < j \le \bar{C}^{(l)} + N_\zeta, \end{cases} \tag{4.60}$$

where

$$\begin{aligned} &A_0 = (Z_{\max} + \tilde{\zeta}^{(1)})\exp(1)/N_\zeta, \qquad B_0 = -1/N_\zeta, \qquad C_0 = -Z_{\max}, \\ &A_m = (\tilde{\zeta}^{(m+1)} - \tilde{\zeta}^{(m)})/2, \qquad B_m = \pi/\bar{N}_\zeta^{(m)}, \\ &C_m = \bar{C}^{(m)}, \qquad D_m = (\tilde{\zeta}^{(m+1)} + \tilde{\zeta}^{(m)})/2, \\ &A_{l+1} = (Z_{\max} - \tilde{\zeta}^{(l+1)})\exp(1)/N_\zeta, \quad B_{l+1} = -1/N_\zeta, \quad C_{l+1} = -Z_{\max}. \end{aligned} \tag{4.61}$$

In summary, the parameters to be set for the velocity grid $\zeta^{(j)}$ are $Z_{\max}$, N_ζ, $\tilde{N}_\zeta$, and $\Delta\zeta_{\max}$. It should be noted that the grid system $\zeta^{(j)}$, thus the parameters $Z_{\max}$, N_ζ, $\tilde{N}_\zeta$, and $\Delta\zeta_{\max}$, can be different depending on the grid points (x_1, t). For instance, we can use large N_ζ near the plate and small N_ζ for the far field.

B Basic equation for finite-difference method with ENO scheme

The ENO scheme employed in this paper is based on [23]. Since it is a well-known method, we will omit its description. However, because we are considering a moving boundary problem here, some preliminary analysis is necessary. More specifically, we introduce the space coordinate relative to $x_w(t)$ and the molecular velocity relative to $v_w(t)$, i.e.,

$$\check{x}_1 = x_1 - x_w(t), \quad \check{\zeta}_1 = \zeta_1 - v_w(t), \quad \check{t} = t. \tag{4.62}$$

and let

$$\check{\alpha}(\check{x}_1,\,\check{\zeta}_1,\,\check{t}) = \alpha(\check{x}_1 + x_w(\check{t}),\,\check{\zeta}_1 + v_w(\check{t}),\,\check{t}) \qquad (\text{with } \alpha = g,\ h,\ \text{or } \Phi), \tag{4.63a}$$

$$\check{\beta}(\check{x}_1,\,\check{t}) = \beta(\check{x}_1 + x_w(\check{t}),\,\check{t}) \qquad (\text{with } \beta = \rho \text{ or } T), \tag{4.63b}$$

$$\check{u}_1(\check{x}_1,\,\check{t}) = u_1(\check{x}_1 + x_w(\check{t}),\,\check{t}) - v_w(\check{t}). \tag{4.63c}$$

Then, the BGK equation (4.9) is recast as

$$\left[\partial_{\check{t}} + \check{\zeta}_1\partial_{\check{x}_1} - \dot{v}_w(\check{t})\partial_{\check{\zeta}_1}\right]\check{\Phi} = \frac{2}{\sqrt{\pi}}\frac{1}{\mathrm{Kn}}\check{\rho}\left(\begin{bmatrix}1\\ \check{T}\end{bmatrix}\check{M} - \check{\Phi}\right), \tag{4.64a}$$

$$\check{M} = \frac{\check{\rho}}{(\pi\check{T})^{1/2}}\exp\left(-\frac{(\check{\zeta}_1 - \check{u}_1)^2}{\check{T}}\right), \tag{4.64b}$$

$$\check{\rho} = \int_{\mathbb{R}}\check{g}\mathrm{d}\check{\zeta}_1, \quad \check{u}_1 = \frac{1}{\check{\rho}}\int_{\mathbb{R}}\check{\zeta}_1\check{g}\mathrm{d}\check{\zeta}_1, \quad \check{T} = \frac{2}{3\check{\rho}}\int_{\mathbb{R}}[(\check{\zeta}_1 - \check{u}_1)^2\check{g} + \check{h}]\mathrm{d}\check{\zeta}_1. \tag{4.64c}$$

The initial condition (4.10) and the boundary condition (4.11) are, respectively, written as

$$\check{\Phi} = \pi^{-1/2}\exp(-[\check{\zeta}_1 + v_w(0)]^2)\,\delta = \pi^{-1/2}\exp(-\check{\zeta}_1^2)\,\delta, \qquad (\check{t} = 0), \tag{4.65}$$

and

$$\check{\Phi}(\check{x}_1,\,\check{\zeta}_1,\,\check{t}) = \check{M}_{w\pm}(\check{\zeta}_1,\,\check{t})\,\delta, \qquad \text{at} \quad \check{x}_1 = \pm 0, \quad \text{for} \quad \check{\zeta}_1 \gtrless 0, \tag{4.66a}$$

$$\begin{cases} \check{M}_{w\pm}(\check{\zeta}_1,\,\check{t}) = \pi^{-1/2}\check{\sigma}_{w\pm}(\check{t})\exp\left(-\check{\zeta}_1^2\right), \\ \check{\sigma}_{w\pm}(\check{t}) = \mp 2\sqrt{\pi}\displaystyle\int_{\check{\zeta}_1 \lessgtr 0}\check{\zeta}_1\check{g}(\pm 0,\,\check{\zeta}_1,\,\check{t})\mathrm{d}\check{\zeta}_1. \end{cases} \tag{4.66b}$$

We solve this initial- and boundary-value problem by a finite-difference method with the ENO procedure, which automatically avoids the use of sharp gradients in finite differences. A first-order time discretization (the forward Euler scheme) with constant $\Delta\check{t}$ is used. For both $\check{x}_1$ and $\check{\zeta}_1$, we employ a third-order finite difference, using non-uniform grid systems concentrated at $\check{x}_1 \approx 0$ and $\check{\zeta}_1 \approx 0$. For the integration in velocity space, a second-order quadrature is used.

C Accuracy checks

C.1 Accuracy of the results by the present method

First, we numerically estimate the error contained in the results obtained by the present method by varying the numerical parameters, such as the grid size, in Problem I. Recall that the numerical parameters involved in this case are Δt for time discretization, N_x, $\bar{N}$, $D_{\max}$, $\Delta x_{\max}$, N_{ch} for space discretization, $Z_{\max}$, $\tilde{N}_\zeta$, $\Delta\zeta_{\max}$, N_ζ for molecular-velocity discretization, and $\Delta\tau_{\min}$, $\tilde{N}_t$ for the integration along characteristics. We fix some of them as follows:

$$\begin{aligned} &N_x = 110, \quad \bar{N} = 40, \quad D_{\max} = 120\times 2\pi, \quad \Delta x_{\max} = 9.1, \\ &Z_{\max} = 5, \quad \tilde{N}_\zeta = 40, \quad \Delta\tau_{\min} = \Delta t, \quad \tilde{N}_t = 5. \end{aligned} \tag{4.67}$$

The error coming from the choice of $Z_{\max}$ has been confirmed to be smaller than the error discussed below.

The error is measured by the quantities defined as follows. Let $\mathcal{P}(t)$ and $\mathcal{E}(t)$ be the (non-dimensional) momentum and energy fluxes per unit area and time across the oscillating plate.

Then, they are expressed as

$$\mathcal{P}(t) = p_{11}(x_w(t),\, t), \quad \mathcal{E}(t) = q_1(x_w(t),\, t) + p_{11}(x_w(t),\, t)v_w(t), \tag{4.68a}$$

$$p_{11}(x_1,\, t) = 2\int_{\mathbb{R}^3} (\zeta_1 - u_1)^2 f(x_1,\, \zeta_i,\, t)\mathrm{d}\zeta_1\mathrm{d}\zeta_2\mathrm{d}\zeta_3, \tag{4.68b}$$

$$q_1(x_1,\, t) = \int_{\mathbb{R}^3} (\zeta_1 - u_1)(\zeta_i - u_i)^2 f(x_1,\, \zeta_i,\, t)\mathrm{d}\zeta_1\mathrm{d}\zeta_2\mathrm{d}\zeta_3. \tag{4.68c}$$

We define their one-period averages $\bar{\mathcal{P}}_k$ and $\bar{\mathcal{E}}_k$ over k-th period, normalized by a, as

$$\bar{\mathcal{P}}_k = \frac{1}{2\pi a}\int_{2\pi(k-1)}^{2\pi k} \mathcal{P}(t')\mathrm{d}t', \quad \bar{\mathcal{E}}_k = \frac{1}{2\pi a}\int_{2\pi(k-1)}^{2\pi k} \mathcal{E}(t')\mathrm{d}t'. \tag{4.69}$$

Then, we introduce the following quantities $\mathcal{P}_{\text{err}}$ and $\mathcal{E}_{\text{err}}$ as a measure of the error:

$$\mathcal{P}_{\text{err}} = \frac{1}{8}\sum_{k=1}^{8} |\bar{\mathcal{P}}_k^{(\text{ref})} - \bar{\mathcal{P}}_k|, \quad \mathcal{E}_{\text{err}} = \frac{1}{8}\sum_{k=1}^{8} |\bar{\mathcal{E}}_k^{(\text{ref})} - \bar{\mathcal{E}}_k|, \tag{4.70}$$

where the superscript (ref) indicates $\bar{\mathcal{P}}_k$ and $\bar{\mathcal{E}}_k$ of the reference solution specified later. The quantities $\mathcal{P}_{\text{err}}$ and $\mathcal{E}_{\text{err}}$ are, roughly speaking, the average over 8 periods of the difference between the reference solution and the solution under consideration.

Let us first consider the effect of Δt. Our reference solution is the solution obtained with the following parameter setting:

$$\text{R1:} \quad \Delta t = 10^{-3}, \quad N_{\text{ch}} = 4, \quad \Delta\zeta_{\max} = 5\times 10^{-4}, \quad N_\zeta = 360. \tag{4.71}$$

In Table 4.1, the results for larger Δt are compared with the reference solution (with R1 setting) in the cases of $(\mathsf{K},\, a) = (\infty,\, 1)$, $(\infty,\, 0.01)$, $(1,\, 1)$, and $(1,\, 0.01)$. In all four cases, the error coming from the size of Δt is satisfactorily small.

Next, we consider the effect of the grid size in the molecular velocity space, i.e., the parameters $\Delta\zeta_{\max}$ and N_ζ. Our reference solution for this error estimate is the solution obtained with the following parameter setting:

$$\text{R2:} \quad \Delta t = 4\times 10^{-3}, \quad N_{\text{ch}} = 4, \quad \Delta\zeta_{\max} = 5\times 10^{-4}, \quad N_\zeta = 360. \tag{4.72}$$

We compare the results of $\mathcal{E}_{\text{err}}$ for larger $\Delta\zeta_{\max}$ and smaller N_ζ in Table 4.2. It is seen that the error coming from the choice of $\Delta\zeta_{\max}$ and N_ζ is small. For $(\mathsf{K},\, a) = (\infty,\, 0.01)$, the size of $\Delta\zeta_{\max}$ does not change the result. This can be explained as follows. We notice from Eq. (4.58) that, if $\tilde{\zeta}^{(m+1)} - \tilde{\zeta}^{(m)}$ is small, the size of $\Delta\zeta_{\max}$ does not affect $\bar{N}_\zeta^{(m)}$ and thus the result unless $\Delta\zeta_{\max}$ is small enough to make $[(\pi/2)(\tilde{\zeta}^{(m+1)} - \tilde{\zeta}^{(m)})/\Delta\zeta_{\max}] + 1$ ($= \tilde{\tilde{N}}_\zeta$ say) larger than $\tilde{N}_\zeta$. In fact, when $\Delta\zeta_{\max} = 1\times 10^{-4}$ or larger, $\tilde{N}_\zeta = 40$ is always larger than $\tilde{\tilde{N}}_\zeta$, so that the effect of the size $\Delta\zeta_{\max}$ does not appear.

Finally, we consider the effect of the grid size in the space variable x_1. Here, we have fixed the main grid points as Eq. (4.67). The minimum of the intervals at time $t = 0$, i.e., $x^{(0,1)} - x^{(0,0)}$ [see Eq. (4.37)], is about 3×10^{-3} with these parameters. Our reference solution for this error estimate is the solution obtained with the following parameter setting:

$$\text{R3:} \quad \Delta t = 4\times 10^{-3}, \quad N_{\text{ch}} = 5, \quad \Delta\zeta_{\max} = 5\times 10^{-4}, \quad N_\zeta = 360. \tag{4.73}$$

We change the value of N_{ch}, which is the number of the sub grid points, as $N_{\text{ch}} = 2$, 3, and 4. We summarize the results in the cases of $(\mathsf{K},\, a) = (10,\, 1)$, $(10,\, 0.01)$, $(1,\, 1)$, and $(1,\, 0.01)$ in Table 4.3. For large K, we need less grid points in physical space.

Table 4.1 $\mathcal{P}_{\text{err}}$ and $\mathcal{E}_{\text{err}}$ for different Δt. The reference solution is the solution obtained by the present method with R1 parameter setting.

	$\mathsf{K}=\infty$, $a=1$		$\mathsf{K}=\infty$, $a=0.01$	
Δt	$\mathcal{P}_{\text{err}}$	$\mathcal{E}_{\text{err}}$	$\mathcal{P}_{\text{err}}$	$\mathcal{E}_{\text{err}}$
$\Delta t = 10^{-3} \times 1.5625$	2.3328(-6)†	1.5425(-6)	1.0485(-7)	4.3386(-8)
$\Delta t = 10^{-3} \times 2.5$	8.5853(-6)	5.7321(-6)	2.9381(-7)	1.2408(-7)
$\Delta t = 10^{-3} \times 4$	2.4097(-5)	1.6210(-5)	6.3311(-7)	2.7711(-7)
	$\mathsf{K}=1$, $a=1$		$\mathsf{K}=1$, $a=0.01$	
Δt	$\mathcal{P}_{\text{err}}$	$\mathcal{E}_{\text{err}}$	$\mathcal{P}_{\text{err}}$	$\mathcal{E}_{\text{err}}$
$\Delta t = 10^{-3} \times 1.5625$	6.5225(-5)	1.0359(-4)	1.1801(-5)	2.8746(-5)
$\Delta t = 10^{-3} \times 2.5$	2.2507(-4)	3.3878(-4)	2.2044(-5)	2.5759(-4)
$\Delta t = 10^{-3} \times 4$	6.4364(-4)	8.5192(-4)	5.3475(-5)	9.9085(-4)

† read as 2.3328×10^{-6}.

Table 4.2 $\mathcal{E}_{\text{err}}$ for different $\Delta\zeta_{\max}$ and N_ζ. The reference solution is the solution obtained by the present method with R2 parameter setting.

	$\mathsf{K}=\infty$		$\mathsf{K}=1$	
	$a=1$	$a=0.01$	$a=1$	$a=0.01$
$\Delta\zeta_{\max} = 5 \times 10^{-4} \times 2$	4.1223(-9)†	2.1398(-9)	2.0276(-7)	1.6878(-6)
$\Delta\zeta_{\max} = 5 \times 10^{-4} \times 4$	2.1832(-7)	2.1398(-9)	7.8101(-7)	4.5371(-6)
$\Delta\zeta_{\max} = 5 \times 10^{-4} \times 8$	9.1535(-7)	2.1398(-9)	2.5030(-6)	7.8966(-6)
$N_\zeta = 360 \times (6/9)$	6.4550(-7)	5.6307(-7)	2.1314(-6)	4.3095(-5)
$N_\zeta = 360 \times (4/9)$	2.0741(-6)	2.2062(-6)	1.1308(-5)	1.8328(-4)
$N_\zeta = 360 \times (2/9)$	1.7939(-5)	1.7903(-5)	1.0500(-4)	1.6191(-3)

† read as 4.1223×10^{-9}.

Table 4.3 $\mathcal{E}_{\text{err}}$ for different N_{ch}. The reference solution is the solution obtained by the present method with R3 parameter setting.

	$\mathsf{K}=10$		$\mathsf{K}=1$	
	$a=1$	$a=0.01$	$a=1$	$a=0.01$
$N_{\text{ch}} = 4$	5.1879(-8)†	1.3194(-8)	2.0746(-7)	1.3386(-6)
$N_{\text{ch}} = 3$	9.6869(-8)	5.9826(-7)	4.1121(-6)	3.3980(-5)
$N_{\text{ch}} = 2$	3.6278(-6)	7.9736(-6)	1.2553(-5)	4.0008(-4)

† read as 5.1879×10^{-8}.

Table 4.4 $\|\rho\|$ at $t = 16\pi$.

	$\mathsf{K} = \infty$			$\mathsf{K} = 10$			$\mathsf{K} = 1$		
a	1	0.1	0.01	1	0.1	0.01	1	0.1	0.01
Present	6.1(-5)†	7.9(-6)	5.0(-6)	6.6(-5)	1.3(-5)	6.0(-7)	1.0(-5)	6.1(-5)	3.0(-5)
ENO	2.0(-3)	5.0(-2)	5.9(-2)	3.8(-3)	5.1(-2)	6.0(-2)	1.4(-2)	4.6(-2)	9.2(-2)

† read as 6.1×10^{-5}.

C.2 Accuracy of the results by the finite-difference method

In this subsection, we discuss the accuracy of the results for Problem I obtained by using the ENO scheme. For this purpose, we consider $\mathcal{P}_{\text{err}}$ and $\mathcal{E}_{\text{err}}$ formed by the ENO solution with different grid sizes and the reference solution obtained by the present method with R1 setting [see Eq. (4.71)]. We truncate the physical space as $0 \le \check{x}_1 \le 200$ and the molecular velocity space as $-6 \le \check{\zeta}_1 \le 6$. We vary the numerical parameters contained in the ENO scheme, i.e., the time step $\Delta\check{t}$, the number of grid points in the physical space $\check{N}_x$, and the number of grid points in the molecular velocity space $\check{N}_\zeta$, as

$$\Delta\check{t}/2\pi = \Delta \times 10^{-4}, \quad \check{N}_x = (1/\Delta) \times 4000, \quad \check{N}_\zeta = (1/\Delta) \times 400, \\ (0.625 \le \Delta \le 6.25). \tag{4.74}$$

That is, we change the values of $\Delta\check{t}$, $\check{N}_x$, and $\check{N}_\zeta$ at the same time by varying Δ. The grid size in physical space $\Delta\check{x}_1$ and that in the molecular velocity space $\Delta\check{\zeta}_1$ for $\Delta = 1$ are $0.02236 \le \Delta\check{x}_1 \le 0.07763$ and $0.0217 \le \Delta\check{\zeta}_1 \le 0.03892$, respectively (recall that we use the non-uniform grid system). Figure 4.24 shows $\mathcal{P}_{\text{err}}$ (upper figures) and $\mathcal{E}_{\text{err}}$ (lower figures) versus $\Delta\check{t}$ for $\mathsf{K} = \infty$ [(a)], $\mathsf{K} = 10$ [(b)], and $\mathsf{K} = 1$ [(c)]. The symbols *circle*, *square*, and *inverted triangle* indicate, respectively, the case of $a = 1$, $a = 0.1$, and $a = 0.01$. It is seen from the figure that $\mathcal{P}_{\text{err}}$ and $\mathcal{E}_{\text{err}}$ decrease in proportion to $\Delta\check{t}$ or $(\Delta\check{t})^2$, depending on a and K, except in the case of $(\mathsf{K}, a) = (\infty, 0.01)$, where the rate is slower than $\Delta\check{t}$.

Finally, we show the conservation of mass, which gives another measure of accuracy. The quantity $\|\rho\|(t)$ defined as

$$\|\rho\|(t) = \frac{1}{a}\left|\int_{x_w(t)}^{\infty} [\rho(x_1, t) - 1]\mathrm{d}x_1\right|, \tag{4.75}$$

should vanish for all t, i.e., the total mass of the gas is conserved. However, since both of our present method and the finite-difference method with the ENO scheme are not conservative, $\|\rho\|(t)$ does not vanish in the actual computation. In Table 4.4, the values of $\|\rho\|(t)$ at time $t = 16\pi$ are shown for both methods. Here, we have used the parameter setting R1 for the present method and $\Delta = 1$ for the ENO scheme. The present method conserves the total mass relatively well compared with the ENO scheme.

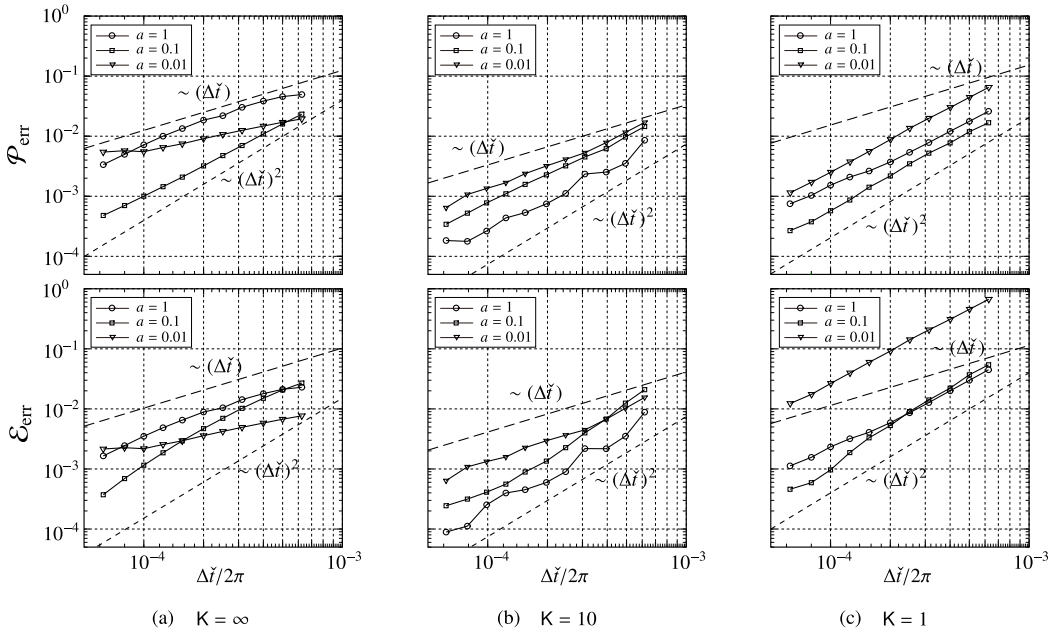

Fig. 4.24 $\mathcal{P}_{\rm err}$ and $\mathcal{E}_{\rm err}$ obtained by the ENO scheme vs $\Delta\check{t}$. (a) $\mathsf{K} = \infty$, (b) $\mathsf{K} = 10$, and (c) $\mathsf{K} = 1$. Here, the reference solution is the solution obtained by the present method with the R1 parameter setting. The symbols *circles*, *squares*, and *inverted triangles* indicate, respectively, the cases of $a = 1$, $a = 0.1$, and $a = 0.01$.

References

[1] G. Karniadakis, A. Beskok, N. Aluru, Microflows and Nanoflows: Fundamentals and Simulation, Springer, New York, 2005.

[2] G. A. Bird, Molecular Gas Dynamics, Oxford Univ. Press, Oxford, 1976.

[3] G. A. Bird, Molecular Gas Dynamics and the Direct Simulation of Gas Flows, Oxford Univ. Press, Oxford, 1994.

[4] S. Stefanov, P. Gospodinov, C. Cercignani, Monte Carlo simulation and Navier-Stokes finite difference calculation of unsteady-state rarefied gas flows, Phys. Fluids 10, (1998) 289–300.

[5] T. Ohwada, M. Kunihisa, Direct simulation of a flow produced by a plane wall oscillating in its normal direction, in: A.D. Ketsdever, E.P. Muntz (Eds.), Rarefied Gas Dynamics, AIP, Melville, 2003, pp. 202–209.

[6] D. J. Radar, M. A. Gallis, J. R. Torczynski, DSMC moving-boundary algorithms for simulating MEMS geometries with opening and closing gaps, in: D. A. Levin, et. al. (Eds), Rarefied Gas Dynamics, AIP, Melville, 2011, pp. 760–765.

[7] G, Russo, F. Filbet, Semilagrangian schemes applied to moving boundary problems for the BGK model of rarefied gas dynamics, Kinet. Relat. Models 2, (2009) 231–250.

[8] G. Dechristé, L. Mieussens, Numerical simulation of micro flows with moving obstacles, J. Phys.: Conf. Ser. 362, 012030.

[9] Y. Sone, S. Takata, Discontinuity of the velocity distribution function in a rarefied gas around a convex body and the S layer at the bottom of the Knudsen layer, Transp. Theory Stat. Phys. 21 (1992) 501–530.

[10] Y. Sone, Kinetic Theory and Fluid Mechanics, Birkäuser, Boston, 2002.

[11] Y. Sone, Molecular Gas Dynamics: Theory, Techniques, and Applications, Birkäuser, Boston, 2007.

[12] P. L. Bhatnagar, E. P. Gross, M. Krook, A model for collision processes in gases. I. Small amplitude processes in charged and neutral one-component systems, Phys. Rev. 94 (1954) 511–525.

[13] P. Welander, On the temperature jump in a rarefied gas, Ark. Fys. 7 (1954) 507–553.

[14] Y. Inoue, T. Yano, Propagation of strongly nonlinear plane waves, J. Acoust. Soc. Am. 94 (1993) 1632–1642.

[15] T. Tsuji, K. Aoki, Decay of an oscillating plate in a free-molecular gas, in: D.A. Levin, I. Wysong, A.L. Garcia, L.A. Gochberg (Eds.), Rarefied Gas Dynamics, AIP, Melville, 2011, pp. 140–145.

[16] T. Tsuji, K. Aoki, Decay of a linear pendulum in a free-molecular gas and in a special Lorentz gas, J. Stat. Phys. 146 (2012) 620–645.

[17] C. K. Chu, Kinetic-theoretic description of the formation of a shock wave, Phys. Fluids 8 (1965) 12–22.

[18] C. Kim, Formation and propagation of discontinuity for Boltzmann equation in non-convex domains, Commun. Math. Phys. 308 (2011) 641–701.

[19] F. Golse, P. L. Lions, B. Perthame, R. Sentis, Regularity of the moments of the solution of a transport equation, J. Func. Anal. 76 (1988) 110–125.

[20] Y. Sone, H. Sugimoto, Strong evaporation from a plane condensed phase, in: G.E.A. Meier, P.A. Thompson (Eds.), Adiabatic Waves in Liquid-Vapor Systems, Springer-Verlag, Berlin, 1990, pp. 293–304.

[21] K. Aoki, Y. Sone, K. Nishino, H. Sugimoto, Numerical analysis of unsteady motion of a rarefied gas caused by sudden changes of wall temperature with special interest in the propagation of a discontinuity in the velocity distribution function, in: A.E. Beylich (Ed.), VCH, Weinheim, 1991, pp. 222–231.

[22] S. Takata, M. Oishi, Numerical demonstration of the reciprocity among elemental relaxation and driven-flow problems for rarefied gas in a channel, Phys. Fluid 24 (2012) 012003.

[23] C.-W. Shu, Essentially non-oscillatory and weighted essentially non-oscillatory schemes for hyperbolic conservation laws, in: B. Cockburn, C. Johnson, C.-W. Shu, E. Tadmor (Editor-in-Chief: A. Quarteroni) (Eds.), Advanced Numerical Approximation of Nonlinear Hyperbolic Equations, Springer, Berlin, 1998, pp. 325–403.

[24] T. Tsuji, K. Aoki, Numerical analysis of nonlinear acoustic wave propagation in a rarefied gas, in: A. Santos, M. Mareschal (Eds.), Rarefied Gas Dynamics, AIP, Melville, 2013 (to appear).

[25] C. S. Wang Chang, G. E. Uhlenbeck, On the propagation of sound in monatomic gases, Report, University of Michigan (1952).

[26] L. Sirovich, J. K. Thurber, Propagation of forced sound waves in rarefied gasdynamics, J. Acoust. Soc. Am. 37 (1965) 329–339.

[27] D. Kahn, D. Mintzer Kinetic Theory of Sound Propagation in Rarefied Gases, Phys. Fluids 8, (1965) 1090–1102.

[28] J. R. Thomas, Jr., C. E. Siewert, Sound-wave propagation in a rarefied gas, Trans. Theory and Stat. Phys. 8 (1979) 219–240.

[29] S. K. Loyalka, T. C. Cheng, Sound-wave propagation in a rarefied gas, Phys. Fluids 22 (1979) 830–836.

[30] T. Yano, Y. Inoue, Quasisteady streaming with rarefaction effect induced by asymmetric sawtooth-like plane waves, Phys. Fluids 8 (1996) 2537–2551.

[31] S. Caprino, G. Cavallaro, C. Marchioro, On a microscopic model of viscous friction, Math. Models Methods Appl. Sci. 17 (2007), 1369–1403.

[32] G. Cavallaro, C. Marchioro, On the approach to equilibrium for a pendulum immersed in a stokes fluid, Math. Models Methods Appl. Sci. 20 (2010), 1999–2019.

[33] G. Cavallaro, C. Marchioro, T. Tsuji, Approach to equilibrium of a rotating sphere in a Stokes flow, Annali dell'Universita di Ferrara 57 (2011), 211–228.

Chapter 4

Part 2: Gas motion in a micro gap between longitudinally oscillating and stationary plates

Abstract Unsteady motion of a gas between two parallel plates is investigated in the case where one of the plates starts longitudinal (harmonic) oscillation. A kinetic-theoretic approach is employed under the condition that the distance between the two plates is comparable to the mean free path of the gas molecules and/or the frequency of oscillation of the plate is comparable to their mean collision frequency. More specifically, the Bhatnagar–Gross–Krook (BGK) model of the Boltzmann equation is solved numerically for wide ranges of parameters, such as the Knudsen number and the Mach number, with special interest in the fully nonlinear wave motion. As the result, the time evolution of the local flow field and the periodic state attained at later times are obtained accurately. It is shown that, in the periodic state, one-period average of the momentum (or energy) transferred from the oscillating to the stationary plate takes a non-zero value in contrast to the linear theory, and it becomes minimum at an intermediate Knudsen number (for a given oscillation of the plate and for a given distance between the center of the oscillating plate and the stationary plate).

1 Introduction

Gas motion caused by a micro-mechanical oscillator plays an important role in MEMS devices and has been investigated by many authors in connection with, for instance, the squeeze film damping [1, 2, 3, 4, 5]. A typical setting is an oscillator placed in the vicinity of another micro component. When the distance between the two components is comparable to the mean free path of gas molecules, the ordinary gas dynamics (or the Navier–Stokes and Euler equations) fails to describe the behavior of the gas. In this case, an approach based on kinetic theory (or the Boltzmann equation) [6] is required. In addition, if the oscillator undergoes an oscillation with very high frequency comparable to the mean collision frequency of gas molecules, the ordinary gas dynamics is not valid any more and should be replaced by kinetic theory.

In the present paper, we consider this problem restricting ourselves to a one-dimensional setting.

That is, we investigate, on the basis of kinetic theory, the transient and subsequent (almost) time-periodic behavior of a gas between two infinitely wide plates, parallel to each other, when one of the plates starts a longitudinal harmonic oscillation.

This problem and the case where the plate at rest is absent (i.e., the gas occupies a half space bounded by the oscillating plate) are classical problems in kinetic theory that have been investigated extensively in connection with sound-wave propagation (see, e.g., [7, 8, 9, 10, 11, 12, 13]). Most of the existing works are based on the linearized kinetic equations under the assumption that the speed of oscillation of the plate is much lower than the sonic speed. In addition, the oscillating plate is usually approximated by a stationary wall, the oscillation being produced by imposing an oscillating macroscopic velocity in the boundary condition.

In contrast, the present paper aims at analyzing the full nonlinear problem numerically. When the amplitude of oscillation is increased at a fixed frequency, or when the frequency is increased at a fixed amplitude, the speed of oscillation of the plate may become comparable to the sonic speed. We consider such cases where the nonlinearity cannot be neglected. For this purpose, we have to handle the problem with a real moving boundary. It is a challenging numerical analysis for kinetic equations. We carry out accurate numerical analysis using the Bhatnagar–Gross–Krook (BGK) model [14, 15] of the Boltzmann equation and give precise description of time-dependent macroscopic profiles, the periodic state established after several periods of oscillation, and the momentum and energy transfer from the oscillating to the stationary plate.

2 Formulation of the problem

2.1 Problem and Assumptions

We consider an ideal monatomic gas in a uniform equilibrium state at rest, with density ρ_{0*} and temperature T_{0*}, between two infinitely wide plates, parallel to each other and kept at uniform and constant temperature T_{0*}. One of the plates is placed at $X_1 = a_* (> 0)$ and the other at $X_1 = d_* (> a_*)$, where X_i $(i = 1, 2, 3)$ denotes the Cartesian coordinate system with the X_1 axis perpendicular to the plates. At time $t_* = 0$, the plate at $X_1 = a_*$ starts an oscillation around $X_1 = 0$ with angular frequency ω_* according to $X_1 = X_w(t_*)$ with $X_w(t_*) = a_* \cos \omega_* t_*$ (see Fig. 4.1). We investigate the subsequent unsteady motion of the gas, in particular, steady oscillatory motion established at later times, numerically on the basis of kinetic theory when the size of the gap between two plates is comparable to the mean free path of the gas molecules and the frequency of oscillation of the plate is comparable to their mean collision frequency.

The assumptions for our analysis are as follows:

1. The behavior of the gas is described by the BGK model of the Boltzmann equation ([14, 15]; see also [6]).
2. The gas molecules undergo diffuse reflection on the plates (see, e.g., [6]). More specifically, the molecules reflected on each plate are distributed according to the half-range Maxwellian distribution characterized by the velocity and temperature of the plate and with the density adjusted in such a way that there is no net mass flow across the boundary.
3. The gas motion is one dimensional, that is, the motion is only in the X_1 direction, and the physical quantities do not depend on X_2 and X_3.

Before formulating the problem, we summarize the notations used throughout the present paper. We first introduce (and repeat) basic dimensional quantities, that is, t_* is the time variable, X_i the Cartesian coordinate system in space, ξ_i the molecular velocity, X_w the position (X_1 coordinate)

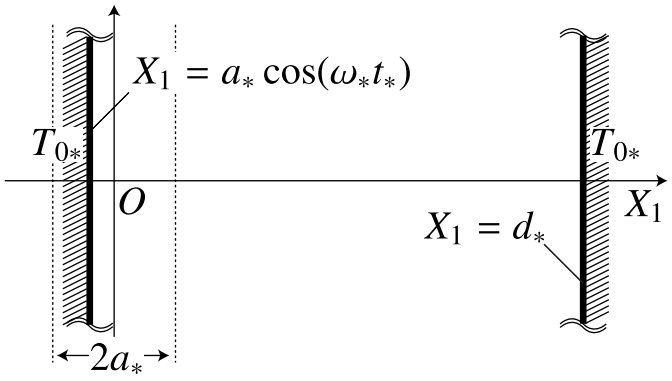

Fig. 4.1 A gas between an oscillating plate and a stationary plate.

of the plate, f_* the velocity distribution function of gas molecules, ρ_* the density, $(u_{1*},\, 0,\, 0)$ the flow velocity, T_* the temperature, p_{11*} the X_1-X_1 component of the stress tensor (normal stress), and $(q_{1*},\, 0,\, 0)$ the heat-flow vector. Then, adopting the time and length scales given respectively by

$$1/\omega_*, \qquad c_{0*}/\omega_*, \tag{4.1}$$

where $c_{0*} = (2RT_{0*})^{1/2}$ with R the gas constant per unit mass, we introduce the dimensionless counterparts, t, x_i, ζ_i, x_w, f, ρ, u_1, T, p_{11}, and q_1, as follows:

$$\begin{aligned} &t = t_*/(1/\omega_*), \quad x_i = X_i/(c_{0*}/\omega_*), \quad \zeta_i = \xi_i/c_{0*}, \quad x_w = X_w/(c_{0*}/\omega_*), \\ &f = f_*/(\rho_{0*}c_{0*}^3), \quad \rho = \rho_*/\rho_{0*}, \quad u_1 = u_{1*}/c_{0*}, \quad T = T_*/T_{0*}, \\ &p_{11} = p_{11*}/p_{0*}, \quad q_1 = q_{1*}/(p_{0*}c_{0*}), \end{aligned} \tag{4.2}$$

where $p_{0*} = R\rho_{0*}T_{0*}$. In addition, we define the Knudsen number Kn and the Mach number Ma as

$$\mathrm{Kn} = l_{0*}/(c_{0*}/\omega_*), \qquad \mathrm{Ma} = a_*\omega_*/(5RT_{0*}/3)^{1/2}, \tag{4.3}$$

where l_{0*} is the mean free path of the gas molecules at the reference equilibrium state at rest, $a_*\omega_*$ is the maximum speed of the oscillating plate, and $(5RT_{0*}/3)^{1/2}$ is the sonic speed at temperature T_{0*}; the l_{0*} is defined in terms of the collision frequency ν_{0*} of the gas molecules at the reference state as $l_{0*} = (2/\sqrt{\pi})(c_{0*}/\nu_{0*})$; for the BGK model, ν_{0*} is given as $\nu_{0*} = A_c\rho_{0*}$ with a constant A_c.

2.2 Basic Equations

The independent variables (i.e., the arguments of f) in the present spatially one-dimensional problem are x_1, ζ_1, ζ_2, ζ_3, and t. However, in the case of the BGK model, one can eliminate ζ_2 and ζ_3 (the molecular velocity components parallel to the plates) by introducing the following marginal velocity distribution functions g and h [16]:

$$\begin{bmatrix} g(x_1,\zeta_1,t) \\ h(x_1,\zeta_1,t) \end{bmatrix} = \int_{-\infty}^{\infty}\int_{-\infty}^{\infty} \begin{bmatrix} 1 \\ \zeta_2^2+\zeta_3^2 \end{bmatrix} f(x_1,\zeta_1,\zeta_2,\zeta_3,t)\,\mathrm{d}\zeta_2\mathrm{d}\zeta_3. \tag{4.4}$$

To be more specific, the BGK model equation for f is reduced to simultaneous integro-differential equations for g and h, which read as

$$\frac{\partial \Phi}{\partial t} + \zeta_1 \frac{\partial \Phi}{\partial x_1} = \frac{2}{\sqrt{\pi}} \frac{1}{\mathrm{Kn}} \rho \left(\lambda M - \Phi \right), \quad \left(\Phi = \begin{bmatrix} g \\ h \end{bmatrix}, \lambda = \begin{bmatrix} 1 \\ T \end{bmatrix} \right), \tag{4.5a}$$

$$M = \frac{\rho}{(\pi T)^{1/2}} \exp\left(- \frac{(\zeta_1 - u_1)^2}{T} \right), \tag{4.5b}$$

$$\rho = \int_{-\infty}^{\infty} g \mathrm{d}\zeta_1, \qquad u_1 = \frac{1}{\rho} \int_{-\infty}^{\infty} \zeta_1 g \mathrm{d}\zeta_1, \qquad T = \frac{2}{3\rho} \int_{-\infty}^{\infty} [(\zeta_1 - u_1)^2 g + h] \mathrm{d}\zeta_1. \tag{4.5c}$$

The initial condition for Eq. (4.5) is given by

$$g = h = M_0, \qquad M_0 = \pi^{-1/2} \exp(-\zeta_1^2), \qquad \text{at } \ t = 0. \tag{4.6}$$

The boundary condition on the oscillating plate is written as

$$g(x_1, \zeta_1, t) = h(x_1, \zeta_1, t) = M_w^{\mathrm{L}}(\zeta_1, t), \qquad \text{for } \ \zeta_1 - v_w(t) > 0, \ \text{ at } \ x_1 = x_w(t), \tag{4.7a}$$

$$M_w^{\mathrm{L}}(\zeta_1, t) = \pi^{-1/2} \sigma_w^{\mathrm{L}}(t) \exp\left(-[\zeta_1 - v_w(t)]^2 \right), \tag{4.7b}$$

$$\sigma_w^{\mathrm{L}}(t) = -2\sqrt{\pi} \int_{\zeta_1 - v_w(t) < 0} [\zeta_1 - v_w(t)] g(x_w(t), \zeta_1, t) \mathrm{d}\zeta_1, \tag{4.7c}$$

where

$$x_w(t) = \sqrt{5/6}\,\mathrm{Ma}\, \cos t, \qquad v_w(t) = \mathrm{d}x_w(t)/\mathrm{d}t = -\sqrt{5/6}\,\mathrm{Ma}\, \sin t, \tag{4.8}$$

that is, $c_{0*} v_w$ is the dimensional velocity of the plate. The boundary condition on the stationary plate is given by

$$g(x_1, \zeta_1, t) = h(x_1, \zeta_1, t) = M_w^{\mathrm{R}}(\zeta_1, t), \qquad \text{for } \ \zeta_1 < 0, \ \text{ at } \ x_1 = d, \tag{4.9a}$$

$$M_w^{\mathrm{R}}(\zeta_1, t) = \pi^{-1/2} \sigma_w^{\mathrm{R}}(t) \exp\left(-\zeta_1^2 \right), \tag{4.9b}$$

$$\sigma_w^{\mathrm{R}}(t) = 2\sqrt{\pi} \int_{\zeta_1 > 0} \zeta_1 g(d, \zeta_1, t) \mathrm{d}\zeta_1, \tag{4.9c}$$

where $x_1 = d$ indicates the dimensionless location of the stationary plate defined by

$$d = d_* / (c_{0*}/\omega_*). \tag{4.10}$$

Note that d depends not only on d_* but also on T_{0*} and ω_*.

As is seen from Eqs. (4.5)–(4.9), the present problem is characterized by the three parameters: Kn, Ma, and d. In place of these, we use

$$\mathsf{K} = (\sqrt{\pi}/2)\mathrm{Kn}, \qquad \mathsf{M} = \sqrt{5/6}\mathrm{Ma}, \qquad d, \tag{4.11}$$

in the following. Incidentally, another (and a more standard) way of non-dimensionalization is to use d_* as the length scale and $1/\nu_{0*}$ as the time scale. Then, one is led to the following three dimensionless parameters, rather than Kn, Ma, and d:

$$\widetilde{\mathrm{Kn}} = l_{0*}/d_*, \qquad \mathrm{Ma}, \qquad \tilde{\omega} = \omega_*/\nu_{0*}. \tag{4.12}$$

where Ma is the same, and $\widetilde{\mathrm{Kn}}$ is the standard Knudsen number. These are related to our parameters (4.11) as

$$\widetilde{\mathrm{Kn}} = (2/\sqrt{\pi})(\mathsf{K}/d), \qquad \mathrm{Ma} = \sqrt{6/5}\mathsf{M}, \qquad \tilde{\omega} = \mathsf{K}. \tag{4.13}$$

2.3 Additional Physical Quantities

The dimensionless normal stress p_{11} and heat flux q_1 are expressed in terms of the marginals g and h as

$$p_{11} = 2\int_{-\infty}^{\infty}(\zeta_1 - u_1)^2 g \mathrm{d}\zeta_1, \qquad q_1 = \int_{-\infty}^{\infty}(\zeta_1 - u_1)[(\zeta_1 - u_1)^2 g + h]\mathrm{d}\zeta_1. \tag{4.14}$$

We now denote, respectively, by $\mathcal{P}^\beta$ and $\mathcal{E}^\beta$ the X_1 component of the momentum and the energy, per unit area and time, transferred to the gas from the oscillating plate (when $\beta = \mathrm{L}$) or transferred to the stationary plate from the gas (when $\beta = \mathrm{R}$). Then, they are expressed as

$$\mathcal{P}^{\mathrm{L}} = p_{11}|_{x_1 = x_w(t)}, \qquad \mathcal{P}^{\mathrm{R}} = p_{11}|_{x_1 = d}, \tag{4.15a}$$

$$\mathcal{E}^{\mathrm{L}} = [q_1 + p_{11}v_w(t)]|_{x_1 = x_w(t)}, \qquad \mathcal{E}^{\mathrm{R}} = q_1|_{x_1 = d}. \tag{4.15b}$$

In addition, we introduce the time average $\bar{\phi}(\cdot, t)$ of a physical quantity ϕ, where $\phi = \rho$, u_1, T, $\mathcal{P}^\beta$, and $\mathcal{E}^\beta$, over a period 2π from $t - 2\pi$ to t, i.e.,

$$\bar{\phi}(\cdot, t) = \frac{1}{2\pi}\int_{t-2\pi}^{t}\phi(\cdot, t')\mathrm{d}t'. \tag{4.16}$$

2.4 Remarks on Numerical Method

Because of limited space, we only give very brief remarks on the present numerical method. As mentioned in Sec. 1, we investigate a strongly nonlinear problem with truly oscillating boundary, which continuously sends out discontinuities of the velocity distribution function in the gas. As can be seen from the results for free-molecular gas [17, 18], this makes the shape of the velocity distribution function highly oscillatory for large Knudsen numbers. We have developed a numerical method that can describe such a complex shape of the velocity distribution function accurately for a wide range of the Knudsen and Mach numbers. The details of the method will be explained in our forthcoming paper.

It should be mentioned that the nonlinear sound-wave propagation in a half space has been investigated using classical gas dynamics, e.g., [19], as well as kinetic theory [20]. In [20], the direct simulation Monte Carlo (DSMC) method was employed in contrast to the present deterministic method. The DSMC method is also used for one-dimensional slab problems, similar to the present problem, in [21, 22]. In [21], unsteady gas flows caused by a sudden start of longitudinal oscillation as well as transverse motion (with a constant speed) of one of the plates are investigated. This reference focuses on supersonic flows at small Knudsen numbers and the comparison between the DSMC results and the results based on the Navier–Stokes equations with slip boundary conditions. In [22], moving-boundary algorithms are applied to unsteady gas flows caused by oscillatory motion of a piston in micro-scales.

3 Numerical results

In the present paper, we restrict ourselves to the case of $d = 2(5/6)^{1/2}\pi$. This value corresponds to one wave length in the classical theory of sound wave propagation [23].

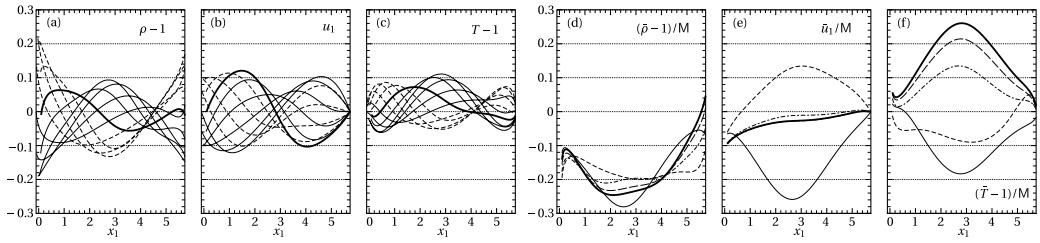

Fig. 4.2 Profiles of the macroscopic quantities for $(\mathsf{K},\ \mathsf{M}) = (0.2,\ 0.1)$. (a) ρ, (b) u_1, (c) T, (d) $\bar\rho$, (e) $\bar u_1$, and (f) $\bar T$. In panels (a)–(c), the profiles are shown at $t/2\pi = 29.1, \cdots, 29.5$ (solid line), $t/2\pi = 29.6, \cdots, 29.9$ (dashed line), and $t/2\pi = 30$ (bold line). In panels (d)–(f), the profiles are shown at $t/2\pi = 1$ (solid line), $t/2\pi = 2$ (dashed line), $t/2\pi = 6$ (dash-dotted line), $t/2\pi = 10$ (long-dashed line), and $t/2\pi = 30$ (bold line).

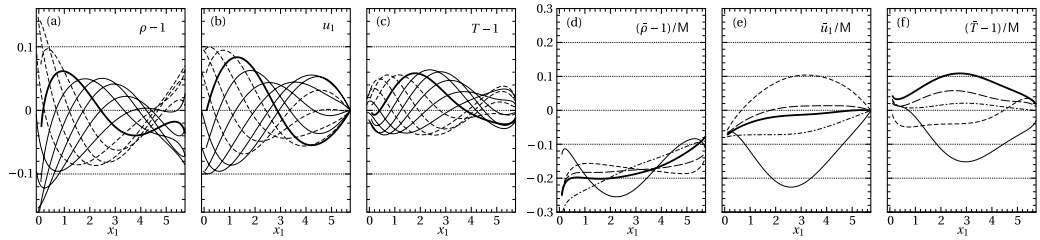

Fig. 4.3 Profiles of the macroscopic quantities for $(\mathsf{K},\ \mathsf{M}) = (0.5,\ 0.1)$. (a) ρ, (b) u_1, (c) T, (d) $\bar\rho$, (e) $\bar u_1$, and (f) $\bar T$. In panels (a)–(c), the profiles are shown at $t/2\pi = 19.1, \cdots, 19.5$ (solid line), $t/2\pi = 19.6, \cdots, 19.9$ (dashed line), and $t/2\pi = 20$ (bold line). In panels (d)–(f), the profiles are shown at $t/2\pi = 1$ (solid line), $t/2\pi = 2$ (dashed line), $t/2\pi = 3$ (dash-dotted line), $t/2\pi = 4$ (long-dashed line), and $t/2\pi = 20$ (bold line).

3.1 Profiles of Macroscopic Quantities

In this subsection, we show the profiles of ρ, u_1, and T. We first consider the case of relatively small Mach number, $\mathsf{M} = 0.1$. Figures 4.2(a)(b)(c), respectively, show the profiles of ρ, u_1, and T for $(\mathsf{K}, \mathsf{M}) = (0.2, 0.1)$ after the periodic state is judged to be established (see Sec. A). To be more specific, they are depicted at ten distinct times during one period ($t/2\pi = 29.1,\ 29.2,\ \cdots,\ 30$) . Since our parameter values, $(\mathsf{K}, \mathsf{M}) = (0.2, 0.1)$, are not very far from the case of classical theory of sound, the velocity profile is close to the sinusoidal shape. However, the density and temperature profiles deviate from it significantly. Figures 4.2(d)(e)(f), respectively, show the time development of the one-period averages, $\bar\rho - 1$, $\bar u_1$, and $\bar T - 1$ [cf. Eq. (4.16)], divided by M. The bold curves indicate these quantities at the periodic state, and the other curves those at the transient stage. Unlike the linearized problem, these quantities do not vanish even in the periodic state (nonlinear effect). Note that, in the panels (d)(e)(f), we show the result for the domain $x_1 \in [\mathsf{M}, d]$ because $\bar\phi$ cannot be defined inside the amplitude of the oscillation of the plate, i.e., $x_1 \in [-\mathsf{M}, \mathsf{M}]$. Therefore, $\int_{\mathsf{M}}^{d}(\bar\rho - 1)dx_1$ does not vanish. This is why the mass is seemingly not conserved in panel (d).

Figures 4.3, 4.4, and 4.5 are, respectively, the figures for $\mathsf{K} = 0.5$, $\mathsf{K} = 1$, and $\mathsf{K} = 10$ corresponding to Fig. 4.2 (i.e., $\mathsf{M} = 0.1$). It is seen from panel (b)'s that the shape of the wave for u_1 deviates more from the sinusoidal shape as K increases. As seen from panel (f)'s, $\bar T$ at the periodic stage becomes more uniform in space for larger values of K.

Next, we show the profiles for larger Mach numbers, $\mathsf{M} = 0.2,\ 0.5,\ 1$, at a fixed value of K, i.e., $\mathsf{K} = 1$. That is, Figs. 4.6 ($\mathsf{M} = 0.2$), 4.7 ($\mathsf{M} = 0.5$), and 4.8 ($\mathsf{M} = 1$) are the figures to be

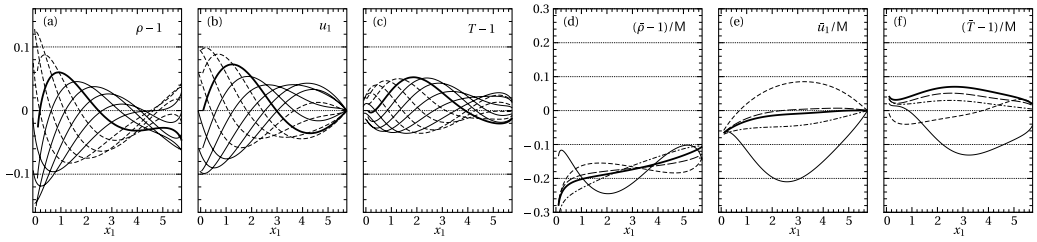

Fig. 4.4 Profiles of the macroscopic quantities for $(\mathsf{K},\ \mathsf{M}) = (1,\ 0.1)$. (a) ρ, (b) u_1, (c) T, (d) $\bar{\rho}$, (e) $\bar{u}_1$, and (f) $\bar{T}$. In panels (a)–(c), the profiles are shown at $t/2\pi = 19.1, \cdots, 19.5$ (solid line), $t/2\pi = 19.6, \cdots, 19.9$ (dashed line), and $t/2\pi = 20$ (bold line). In panels (d)–(f), the profiles are shown at $t/2\pi = 1$ (solid line), $t/2\pi = 2$ (dashed line), $t/2\pi = 3$ (dash-dotted line), $t/2\pi = 4$ (long-dashed line), and $t/2\pi = 20$ (bold line).

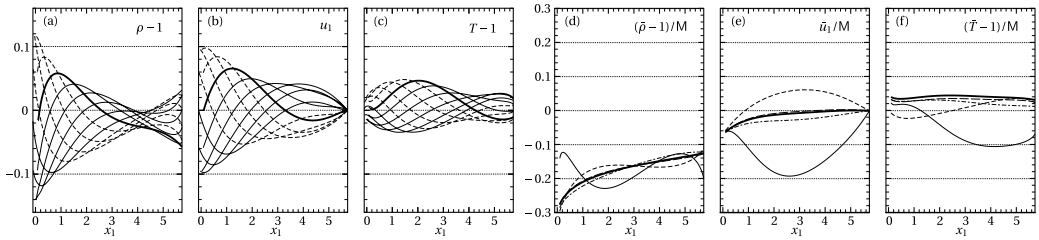

Fig. 4.5 Profiles of the macroscopic quantities for $(\mathsf{K},\ \mathsf{M}) = (10,\ 0.1)$. (a) ρ, (b) u_1, (c) T, (d) $\bar{\rho}$, (e) $\bar{u}_1$, and (f) $\bar{T}$. In panels (a)–(c), the profiles are shown at $t/2\pi = 19.1, \cdots, 19.5$ (solid line), $t/2\pi = 19.6, \cdots, 19.9$ (dashed line), and $t/2\pi = 20$ (bold line). In panels (d)–(f), the profiles are shown at $t/2\pi = 1$ (solid line), $t/2\pi = 2$ (dashed line), $t/2\pi = 3$ (dash-dotted line), $t/2\pi = 4$ (long-dashed line), and $t/2\pi = 20$ (bold line).

compared with Fig. 4.4. The profiles in Fig. 4.6, where M is still rather small, do not differ much from those in Fig. 4.4. However, as M increases, clear differences arise naturally. In particular, panel (c)'s and panel (f)'s show that there appears a significant temperature rise for larger M. More precisely, the temperature rise is in such a manner that the profile is lifted up more for larger M, with its wavy shape being kept almost the same.

3.2 Momentum and Energy Transfer

We next discuss the momentum transfer $\mathcal{P}^\beta$ [Eq. (4.15a)] and the energy transfer $\mathcal{E}^\beta$ [Eq. (4.15b)] after the periodic state is judged to be established (see Sec. A). Figures 4.9(a) and (b) show, respectively, $\mathcal{P}^{\rm L}$ and $\mathcal{P}^{\rm R}$ versus t for $\mathsf{M} = 0.1$ and for several K. Figures 4.9(c) and (d) are the corresponding figures for $\mathcal{E}^{\rm L}$ and $\mathcal{E}^{\rm R}$. We see from panels (a) and (c) that $\mathcal{P}^{\rm L}$ and $\mathcal{E}^{\rm L}$, the quantities on the oscillating plate, are weakly dependent on K. In contrast, $\mathcal{P}^{\rm R}$ [panel (b)] and $\mathcal{E}^{\rm R}$ [panel (d)] on the stationary plate vary significantly depending on K, since the manner of deformation of waves while propagating in the gas is different for different K. Figure 4.10 is the corresponding figure for $\mathsf{M} = 1$. As in the case of $\mathsf{M} = 0.1$, the quantities $\mathcal{P}^{\rm L}$ and $\mathcal{E}^{\rm L}$ on the oscillating plate depend weakly on K, but the curves deviate more significantly from sinusoidal-like shape compared with the former case.

In Fig. 4.11(a) and (b), we depict the one-period averages of the momentum and energy transfer from oscillating plate to the gas ($\bar{\mathcal{P}}^{\rm L}$ and $\bar{\mathcal{E}}^{\rm L}$), and from the gas to the stationary plate ($\bar{\mathcal{P}}^{\rm R}$ and $\bar{\mathcal{E}}^{\rm R}$) for various values of K and M in the periodic state. As one can see, $\bar{\mathcal{P}}^{\rm L}$ and $\bar{\mathcal{P}}^{\rm R}$ (or $\bar{\mathcal{E}}^{\rm L}$ and $\bar{\mathcal{E}}^{\rm R}$) coincide with each other in the periodic state (see Sec. A). Therefore, the values in the figure

indicate the one-period averages of the momentum (or energy) transferred from the oscillating plate to the stationary plate. One can see that these quantities take their minimum values with respect to K around $\mathsf{K} \approx 1$. Since the initial (dimensionless) distance $d - \mathsf{M}$ between the plates is smaller than the average distance d, it is natural to think that the stationary plate is pulled (relative to the pressure exerted on the plate in the initial equilibrium state) by the oscillating plate on the average. In fact, it is the case (i.e., $\bar{\mathcal{P}}^{\beta} - 1 < 0$) when the oscillation is weak ($\mathsf{M} = 0.1$). However, as M increases, it is pushed more strongly by the oscillating plate.

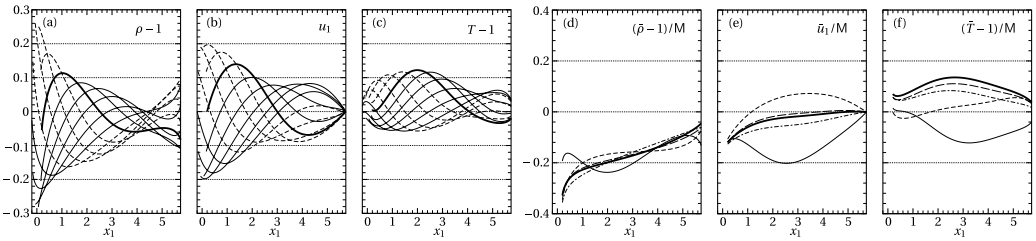

Fig. 4.6 Profiles of the macroscopic quantities for $(\mathsf{K},\ \mathsf{M}) = (1,\ 0.2)$. (a) ρ, (b) u_1, (c) T, (d) $\bar{\rho}$, (e) $\bar{u}_1$, and (f) $\bar{T}$. In panels (a)–(c), the profiles are shown at $t/2\pi = 19.1, \cdots, 19.5$ (solid line), $t/2\pi = 19.6, \cdots, 19.9$ (dashed line), and $t/2\pi = 20$ (bold line). In panels (d)–(f), the profiles are shown at $t/2\pi = 1$ (solid line), $t/2\pi = 2$ (dashed line), $t/2\pi = 3$ (dash-dotted line), $t/2\pi = 4$ (long-dashed line), and $t/2\pi = 20$ (bold line).

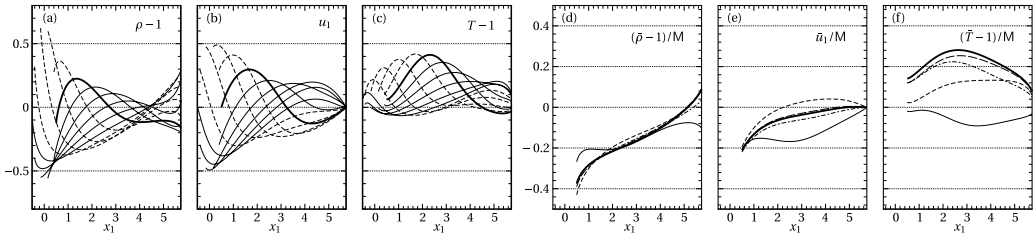

Fig. 4.7 Profiles of the macroscopic quantities for $(\mathsf{K},\ \mathsf{M}) = (1,\ 0.5)$. (a) ρ, (b) u_1, (c) T, (d) $\bar{\rho}$, (e) $\bar{u}_1$, and (f) $\bar{T}$. In panels (a)–(c), the profiles are shown at $t/2\pi = 19.1, \cdots, 19.5$ (solid line), $t/2\pi = 19.6, \cdots, 19.9$ (dashed line), and $t/2\pi = 20$ (bold line). In panels (d)–(f), the profiles are shown at $t/2\pi = 1$ (solid line), $t/2\pi = 2$ (dashed line), $t/2\pi = 3$ (dash-dotted line), $t/2\pi = 4$ (long-dashed line), and $t/2\pi = 20$ (bold line).

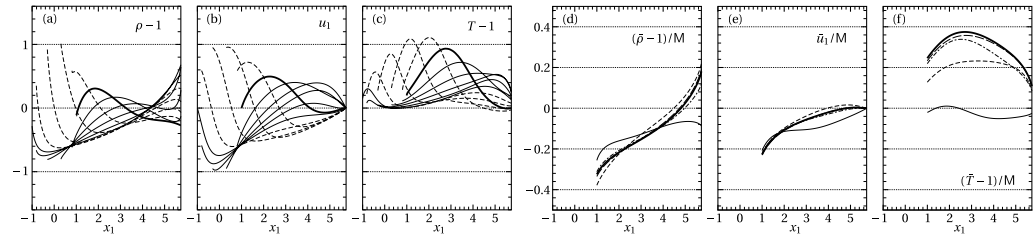

Fig. 4.8 Profiles of the macroscopic quantities for $(\mathsf{K},\ \mathsf{M}) = (1,\ 1.0)$. (a) ρ, (b) u_1, (c) T, (d) $\bar{\rho}$, (e) $\bar{u}_1$, and (f) $\bar{T}$. In panels (a)–(c), the profiles are shown at $t/2\pi = 19.1, \cdots, 19.5$ (solid line), $t/2\pi = 19.6, \cdots, 19.9$ (dashed line), and $t/2\pi = 20$ (bold line). In panels (d)–(f), the profiles are shown at $t/2\pi = 1$ (solid line), $t/2\pi = 2$ (dashed line), $t/2\pi = 3$ (dash-dotted line), $t/2\pi = 4$ (long-dashed line), and $t/2\pi = 20$ (bold line).

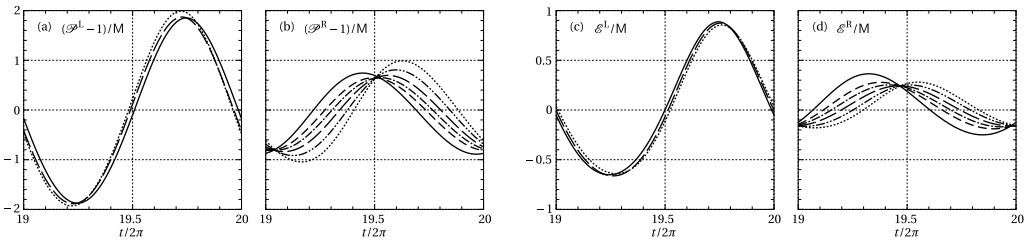

Fig. 4.9 Momentum transfer $\mathcal{P}^\beta$ and energy transfer $\mathcal{E}^\beta$ versus time ($19 \le t/2\pi \le 20$) for $\mathsf{M} = 0.1$. (a) $\mathcal{P}^{\rm L}$, (b) $\mathcal{P}^{\rm R}$, (c) $\mathcal{E}^{\rm L}$, and (d) $\mathcal{E}^{\rm R}$. The results for several different K are shown: $\mathsf{K} = 5$ (solid line), $\mathsf{K} = 2$ (dashed line), $\mathsf{K} = 1.4$ (dash-dotted line), $\mathsf{K} = 1$ (long-dashed line), $\mathsf{K} = 0.7$ (dash-double-dotted line), $\mathsf{K} = 0.5$ (dotted line). In panels (a) and (c), only the results for $\mathsf{K} = 0.5,\ 1,\ 5$ are shown.

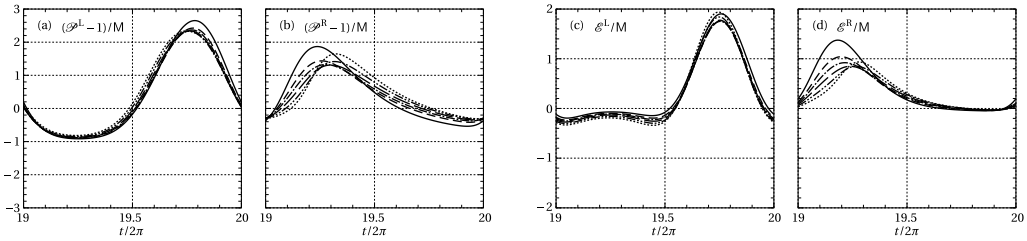

Fig. 4.10 Momentum transfer $\mathcal{P}^\beta$ and energy transfer $\mathcal{E}^\beta$ versus time ($19 \le t/2\pi \le 20$) for $\mathsf{M} = 1$. (a) $\mathcal{P}^{\rm L}$, (b) $\mathcal{P}^{\rm R}$, (c) $\mathcal{E}^{\rm L}$, and (d) $\mathcal{E}^{\rm R}$. The results for several different K are shown: $\mathsf{K} = 5$ (solid line), $\mathsf{K} = 2$ (dashed line), $\mathsf{K} = 1.4$ (dash-dotted line), $\mathsf{K} = 1$ (long-dashed line), $\mathsf{K} = 0.7$ (dash-double-dotted line), $\mathsf{K} = 0.5$ (dotted line).

3.3 Accuracy of Computations

The computations have been carried out carefully with appropriate accuracy checks. For instance, for some typical cases, we have performed computations with different grid systems and estimated the error in the obtained numerical solutions. Here, we omit the details because of the limited space, only mentioning an error estimate based on the mass conservation.

Because of the conservation of mass of the gas contained between the plates, the total mass per unit area of the plates, $\check{\rho}(t) = \int_{x_w(t)}^{d} \rho(x_1, t)\mathrm{d}x_1$, should be constant. In other words, we have the identity

$$\check{\rho}(t) = \check{\rho}(0) = \int_{x_w(0)}^{d} \rho(x_1, 0)\mathrm{d}x_1 = d - x_w(0) = d - \mathsf{M}, \qquad \text{for all } t. \tag{4.17}$$

However, $\check{\rho}(t)$ obtained in the actual numerical computation [say, $\check{\rho}_{\rm comp}(t)$] varies with time and thus does not satisfy Eq. (4.17), since the present numerical method is not conservative. We therefore modify the density by replacing $\rho(x_1, t)$ by $[(d-\mathsf{M})/\check{\rho}_{\rm comp}(t)]\rho(x_1, t)$ at the end of each time step. The quantity

$$\|\check{\rho}_{\rm comp}(t)\|_\infty \equiv \frac{1}{\mathsf{M}} \max_{t/2\pi\in[0,20]} |\check{\rho}_{\rm comp}(t) - \check{\rho}(0)| \tag{4.18}$$

gives a measure of the error contained in the numerical solutions. In fact, it decreases as we increase the accuracy of computation by using, e.g., a smaller time step and/or a finer grid system.

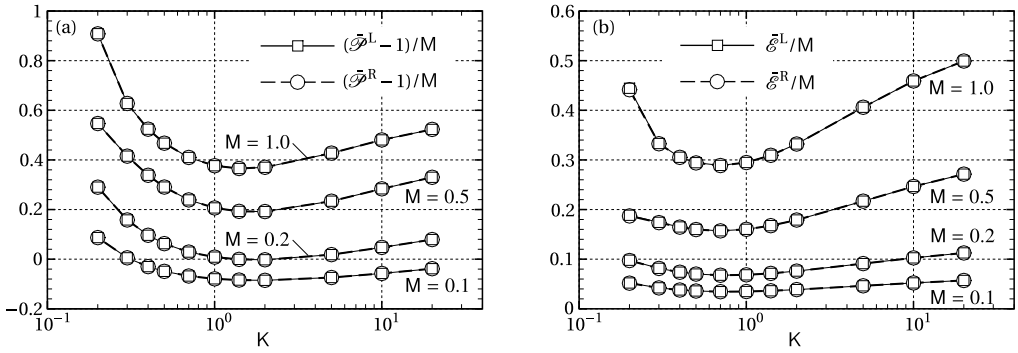

Fig. 4.11 Momentum transfer $\bar{\mathcal{P}}^{\beta}$ and energy transfer $\bar{\mathcal{E}}^{\beta}$ over a period versus K for $\mathsf{M} = 0.1,\ 0.2,\ 0.5$, and 1 at the periodic state. (a) $\bar{\mathcal{P}}^{\rm L}$ and $\bar{\mathcal{P}}^{\rm R}$, (b) $\bar{\mathcal{E}}^{\rm L}$ and $\bar{\mathcal{E}}^{\rm R}$. In panel (a), the solid line with □ indicates $(\bar{\mathcal{P}}^{\rm L}-1)/\mathsf{M}$, and the dashed line with ◯ indicates $(\bar{\mathcal{P}}^{\rm R}-1)/\mathsf{M}$. In panel (b), the solid-line with □ indicates $\bar{\mathcal{E}}^{\rm L}/\mathsf{M}$, and the dashed line with ◯ indicates $\bar{\mathcal{E}}^{\rm R}/\mathsf{M}$. The results at $t/2\pi = 30$ are shown for $(\mathsf{K},\ \mathsf{M}) = (0.2,\ 0.1)$ and $(0.2,\ 0.2)$, those at $t/2\pi = 15$ are shown for $(\mathsf{K},\ \mathsf{M}) = (0.2,\ 1)$, and those at $t/2\pi = 20$ are shown for other cases.

For the result presented in the present paper, we have confirmed that

$$\begin{array}{llllll} \|\check{\rho}_{\rm comp}(t)\|_\infty < 1.3\times10^{-3} & \text{for} & \mathsf{M}=0.1, & \|\check{\rho}_{\rm comp}(t)\|_\infty < 1.3\times10^{-3} & \text{for} & \mathsf{M}=0.2, \\ \|\check{\rho}_{\rm comp}(t)\|_\infty < 1.1\times10^{-3} & \text{for} & \mathsf{M}=0.5, & \|\check{\rho}_{\rm comp}(t)\|_\infty < 3.0\times10^{-3} & \text{for} & \mathsf{M}=1. \end{array} \tag{4.19}$$

for $\mathsf{K} = 0.2, \cdots, 20$.

4 Concluding remarks

In the present paper, we have investigated numerically the unsteady motion of a gas between two parallel plates, caused by a sudden start of longitudinal oscillation of one of the plates, on the basis of kinetic theory. We focus our attention on the nonlinear problem with high-speed oscillation of the plate. The BGK model of the Boltzmann equation has been analyzed, for various values of the Knudsen number (or K) and the Mach number (or M), using an accurate numerical method that is capable of describing the discontinuities of the molecular velocity distribution function in the gas generated continuously by the oscillating plate. The transient macroscopic profiles at earlier times as well as the (almost) periodic state at later times (after several periods of oscillation from the initial time) have been obtained accurately. In the linear setting used mostly in the literature, a one-period average of the deviation of any physical quantity from its equilibrium value vanishes in the periodic state. In contrast, it does not vanish even after a periodic state have been established in the present problem. We have shown that the one-period average of the momentum (or energy) transferred from the oscillating to the stationary plate $\bar{\mathcal{P}}^{\beta}$ (or $\bar{\mathcal{E}}^{\beta}$) takes its minimum with respect to K (for fixed M and d). Moreover, we have pointed out that, depending on the values of K and M, the difference $\bar{\mathcal{P}}^{\beta} - 1$ can be either positive or negative, which means that the stationary plate is either pushed or pulled (relative to the initial pressure) on the average by the oscillating plate.

A Approach to periodic state

In Secs. 3.1 and 3.2, we showed some results for the periodic state that seems to be almost established after several periods form the initial time. In this appendix, we give some additional

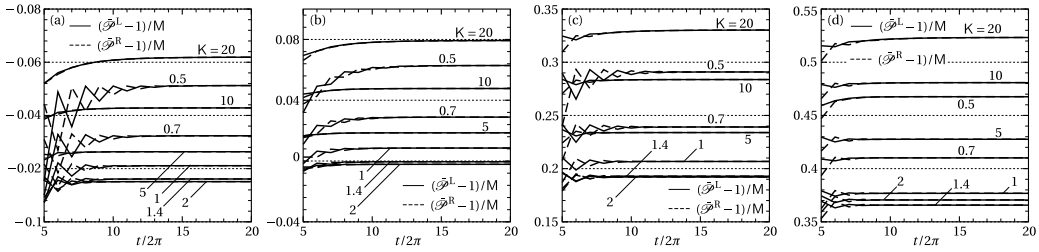

Fig. 4.12 Momentum transfer over a period $\bar{\mathcal{P}}^{\beta}$ versus time ($5 \leq t/2\pi \leq 20$) for different M and K. (a) $\mathsf{M} = 0.1$, (b) $\mathsf{M} = 0.2$, (c) $\mathsf{M} = 0.5$, and (d) $\mathsf{M} = 1$. The solid line indicates $(\bar{\mathcal{P}}^{\mathrm{L}} - 1)/\mathsf{M}$, and the dashed line $(\bar{\mathcal{P}}^{\mathrm{R}} - 1)/\mathsf{M}$.

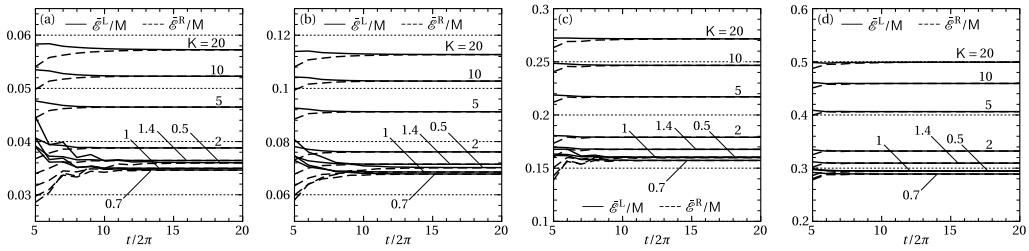

Fig. 4.13 Energy transfer over a period $\bar{\mathcal{E}}^{\beta}$ versus time ($5 \leq t/2\pi \leq 20$) for different M and K. (a) $\mathsf{M} = 0.1$, (b) $\mathsf{M} = 0.2$, (c) $\mathsf{M} = 0.5$, and (d) $\mathsf{M} = 1$. The solid line indicates $\bar{\mathcal{E}}^{\mathrm{L}}/\mathsf{M}$ and the dashed line $\bar{\mathcal{E}}^{\mathrm{R}}/\mathsf{M}$.

data that demonstrate the process of approach to the periodic state. We show in Figs. 4.12 and 4.13 the time evolution of $\bar{\mathcal{P}}^{\beta}$ and $\bar{\mathcal{E}}^{\beta}$ (solid line: $\beta = \mathrm{L}$, dashed line: $\beta = \mathrm{R}$) for $\mathsf{M} = 0.1$, 0.2, 0.5, and 1 and for $\mathsf{K} = 0.5, \cdots, 20$. If an exact periodic state is established, the averaged quantities over a period, $\bar{\mathcal{P}}^{\beta}$ and $\bar{\mathcal{E}}^{\beta}$, do not depend on time t, and furthermore, $\bar{\mathcal{P}}^{\mathrm{L}} = \bar{\mathcal{P}}^{\mathrm{R}}$ and $\bar{\mathcal{E}}^{\mathrm{L}} = \bar{\mathcal{E}}^{\mathrm{R}}$ hold because of the momentum and energy conservations. From these figures, the periodic state is seemingly established at the 20th period from the initial state. This observation is more or less confirmed by Tables 1 and 2. More specifically, Table 1 shows $\bar{\mathcal{P}}^{\beta}$ at later times, e.g., $t/2\pi = 16$, 17, 18, 19, and 20, for the cases of $\mathsf{M} = 0.1$ and 1 and $\mathsf{K} = 0.2$, 1, and 20. Table 2 is the corresponding table for $\bar{\mathcal{E}}^{\beta}$. These tables indicate that for $\mathsf{K} = 0.2$, the periodic state is obtained only approximately, and further computation until later times is required to obtain better approximation of the periodic state. It is seen from Fig. 4.12 that, for large K, $\bar{\mathcal{P}}^{\mathrm{L}}$ and $\bar{\mathcal{P}}^{\mathrm{R}}$ tend to approach each other first and then evolve to a constant value as time proceeds. This tendency is not seen clearly for $\bar{\mathcal{E}}^{\mathrm{L}}$ and $\bar{\mathcal{E}}^{\mathrm{R}}$ in Fig. 4.13.

Table 4.1 Momentum transfer $\bar{\mathcal{P}}^{\mathrm{L}}$ and $\bar{\mathcal{P}}^{\mathrm{R}}$ at later times for $\mathsf{K} = 0.2$, 1, and 20 and for $\mathsf{M} = 0.1$ and 1.

$(\bar{\mathcal{P}}^{\beta} - 1)/\mathsf{M}$								
$\mathsf{M} = 0.1, \mathsf{K} = 0.2$			$\mathsf{M} = 0.1, \mathsf{K} = 1$			$\mathsf{M} = 0.1, \mathsf{K} = 20$		
$t/2\pi$	$\beta = \mathrm{L}$	$\beta = \mathrm{R}$	$t/2\pi$	$\beta = \mathrm{L}$	$\beta = \mathrm{R}$	$t/2\pi$	$\beta = \mathrm{L}$	$\beta = \mathrm{R}$
26	$8.7043(-2)^{*}$	$8.6792(-2)$	16	$-7.8898(-2)$	$-7.8891(-2)$	16	$-3.8190(-2)$	$-3.8194(-2)$
27	$8.6983(-2)$	$8.7096(-2)$	17	$-7.8896(-2)$	$-7.8891(-2)$	17	$-3.8156(-2)$	$-3.8158(-2)$
28	$8.7212(-2)$	$8.7055(-2)$	18	$-7.8896(-2)$	$-7.8890(-2)$	18	$-3.8132(-2)$	$-3.8135(-2)$
29	$8.7186(-2)$	$8.7229(-2)$	19	$-7.8895(-2)$	$-7.8890(-2)$	19	$-3.8116(-2)$	$-3.8117(-2)$
30	$8.7317(-2)$	$8.7212(-2)$	20	$-7.8895(-2)$	$-7.8889(-2)$	20	$-3.8104(-2)$	$-3.8105(-2)$
$\mathsf{M} = 1, \mathsf{K} = 0.2$			$\mathsf{M} = 1, \mathsf{K} = 1$			$\mathsf{M} = 1, \mathsf{K} = 20$		
$t/2\pi$	$\beta = \mathrm{L}$	$\beta = \mathrm{R}$	$t/2\pi$	$\beta = \mathrm{L}$	$\beta = \mathrm{R}$	$t/2\pi$	$\beta = \mathrm{L}$	$\beta = \mathrm{R}$
11	$9.0137(-1)$	$8.9822(-1)$	16	$3.7675(-1)$	$3.7683(-1)$	16	$5.2312(-1)$	$5.2315(-1)$
12	$9.0460(-1)$	$9.0255(-1)$	17	$3.7675(-1)$	$3.7683(-1)$	17	$5.2317(-1)$	$5.2322(-1)$
13	$9.0667(-1)$	$9.0534(-1)$	18	$3.7675(-1)$	$3.7683(-1)$	18	$5.2321(-1)$	$5.2325(-1)$
14	$9.0800(-1)$	$9.0712(-1)$	19	$3.7675(-1)$	$3.7683(-1)$	19	$5.2322(-1)$	$5.2328(-1)$
15	$9.0885(-1)$	$9.0827(-1)$	20	$3.7675(-1)$	$3.7683(-1)$	20	$5.2325(-1)$	$5.2329(-1)$

* read as 8.7043×10^{-2}.

Table 4.2 Energy transfer $\bar{\mathcal{E}}^{\mathrm{L}}$ and $\bar{\mathcal{E}}^{\mathrm{R}}$ at later times for $\mathsf{K} = 0.2$, 1, and 20 and for $\mathsf{M} = 0.1$ and 1.

$\bar{\mathcal{E}}^{\beta}/\mathsf{M}$								
$\mathsf{M} = 0.1, \mathsf{K} = 0.2$			$\mathsf{M} = 0.1, \mathsf{K} = 1$			$\mathsf{M} = 0.1, \mathsf{K} = 20$		
$t/2\pi$	$\beta = \mathrm{L}$	$\beta = \mathrm{R}$	$t/2\pi$	$\beta = \mathrm{L}$	$\beta = \mathrm{R}$	$t/2\pi$	$\beta = \mathrm{L}$	$\beta = \mathrm{R}$
26	$5.1731(-2)^{*}$	$5.2191(-2)$	16	$3.4960(-2)$	$3.4973(-2)$	16	$5.7218(-2)$	$5.7274(-2)$
27	$5.1786(-2)$	$5.2196(-2)$	17	$3.4960(-2)$	$3.4972(-2)$	17	$5.7226(-2)$	$5.7267(-2)$
28	$5.1779(-2)$	$5.2161(-2)$	18	$3.4961(-2)$	$3.4972(-2)$	18	$5.7233(-2)$	$5.7262(-2)$
29	$5.1810(-2)$	$5.2162(-2)$	19	$3.4961(-2)$	$3.4972(-2)$	19	$5.7237(-2)$	$5.7258(-2)$
30	$5.1807(-2)$	$5.2142(-2)$	20	$3.4961(-2)$	$3.4972(-2)$	20	$5.7239(-2)$	$5.7256(-2)$
$\mathsf{M} = 1, \mathsf{K} = 0.2$			$\mathsf{M} = 1, \mathsf{K} = 1$			$\mathsf{M} = 1, \mathsf{K} = 20$		
$t/2\pi$	$\beta = \mathrm{L}$	$\beta = \mathrm{R}$	$t/2\pi$	$\beta = \mathrm{L}$	$\beta = \mathrm{R}$	$t/2\pi$	$\beta = \mathrm{L}$	$\beta = \mathrm{R}$
11	$4.3469(-1)$	$4.4249(-1)$	16	$2.9480(-1)$	$2.9498(-1)$	16	$4.9926(-1)$	$4.9927(-1)$
12	$4.3766(-1)$	$4.4337(-1)$	17	$2.9480(-1)$	$2.9498(-1)$	17	$4.9930(-1)$	$4.9928(-1)$
13	$4.3957(-1)$	$4.4393(-1)$	18	$2.9480(-1)$	$2.9498(-1)$	18	$4.9932(-1)$	$4.9928(-1)$
14	$4.4079(-1)$	$4.4429(-1)$	19	$2.9480(-1)$	$2.9498(-1)$	19	$4.9934(-1)$	$4.9928(-1)$
15	$4.4158(-1)$	$4.4453(-1)$	20	$2.9480(-1)$	$2.9498(-1)$	20	$4.9934(-1)$	$4.9929(-1)$

* read as 5.1731×10^{-2}.

References

[1] Karniadakis, G. E. & Beskok, A. (2002). Micro Flows: Fundamentals and Simulation, Chap. 7, Springer-Verlag.

[2] Hutcherson, S. & Ye, W. (2004). On the squeeze-film damping of micro-resonators in the free-molecule regime, J. Micromech. Microeng., 14, 1726–1733 .

[3] Bao, M. & Yang, H. (2007). Squeeze film air damping in MEMS. Sensor Actuat. A, 136, 3–27.

[4] Guo, X. & Alexeenko, A. (2009). Compact model of squeeze-film damping based on rarefied flow simulations. J. Micromech. Microeng., 19, 045026.

[5] Desvillettes, L. & Lorenzani, S. (2012). Analytical and numerical computations for resonances in microchannels. Rarefied Gas Dynamics, edited by A. Santos. AIP (to be published).

[6] Sone, Y. (2007). Molecular Gas Dynamics: Theory, Techniques, and Applications. Birkäuser.

[7] Sirovich, L. & Thurber, J. K. (1965). Propagation of forced sound waves in rarefied gasdynamics. J. Acoust. Soc. Am., 37, 329–339.

[8] Grad, H. (1966). High frequency sound according to the Boltzmann equation. J. SIAM Appl. Math., 14, 935–955.

[9] Thomas, Jr. J. R. & Siewert, C. E. (1979). Sound-wave propagation in a rarefied gas. Trans. Theory and Stat. Phys., 8, 219–240.

[10] Loyalka S. K. & Cheng, T. C. (1979). Sound-wave propagation in a rarefied gas. Phys. Fluids, 22, 830–836.

[11] Hadjiconstantinou N. G. & Garcia, A. L. (2001). Molecular simulations of sound wave propagation in simple gases. Phys. Fluids, 13, 1040–1046.

[12] Garcia, R. D. M. & Siewert, C. E. (2006). The linearized Boltzmann equation: Sound-wave propagation in a rarefied gas. Z. Angew. Math. Phys., 57, 94–122.

[13] Kalempa, D. & Sharipov, F. (2009). Sound propagation through a rarefied gas confined between source and receptor at arbitrary Knudsen number and sound frequency Phys. Fluids, 21, 103601.

[14] Bhatnagar, P. L., Gross, E. P., & Krook, M. (1954). A model for collision processes in gases. I. Small amplitude processes in charged and neutral one-component systems. Phys. Rev., 94, 511–525.

[15] Welander, P. (1954). On the temperature jump in a rarefied gas. Ark. Fys., 7, 507–553.

[16] Chu, C. K. (1965). Kinetic-theoretic description of the formation of a shock wave. Phys. Fluids, 8, 12–22.

[17] Tsuji, T. & Aoki, K. (2011). Decay of an oscillating plate in a free-molecular gas. Rarefied Gas Dynamics, edited by D. A. Levin, et. al., pp. 140–145. AIP.

[18] Tsuji, T. & Aoki, K. (2012). Decay of a linear pendulum in a free-molecular gas and in a special Lorentz gas. J. Stat. Phys., 146, 620–645.

[19] Inoue, Y. & Yano, T. (1993). Propagation of strongly nonlinear plane waves. J. Acoust. Soc. Am., 94, 1632–1642.

[20] Ohwada, T. & Kunihisa, M. (2003). Direct simulation of a flow produced by a plane wall oscillating in its normal direction. Rarefied Gas Dynamics, edited by A. D. Ketsdever & E. P. Muntz, pp. 202–209, AIP.

[21] Stefanov, S., Cospodinov P., & Cercignani, C. (1998). Monte Carlo simulation and Navier-Stokes finite difference calculation of unsteady-state rarefied gas flows. Phys. Fluids, 10, 289–300.

[22] Radar, D. J., Gallis, M. A., & Torczynski, J. R. (2011). DSMC moving-boundary algorithms for simulating MEMS geometries with opening and closing gaps. Rarefied Gas Dynamics, edited by D. A. Levin, et. al., pp. 760–765. AIP.

[23] Landau, L. D. and Lifshitz, E. M. (1959). Fluid Mechanics, Pergamon Press.

Conclusion

The present thesis consists of several numerical investigations of time-dependent problems in rarefied gas dynamics with a stationary or moving boundary. More specifically, in Chapters 1, 3, and 4, the moving boundary problems for the free-molecular gas (Chapters 1, 3, and 4), the special Lorentz gas (Chapter 3), and the gas described by the Bhatnagar-Gross-Krook (BGK) model (Chapter 4) are considered. In these chapters, the cases where the boundary motion is coupled with the gas behavior are mainly concerned, although the case with an assigned boundary motion is also treated in Chapter 4. The time-dependent problem with a stationary boundary for the free-molecular gas is considered in Chapter 2.

In the case of a free-molecular gas (i.e., the Knudsen number is infinite), because of the absence of inter-molecular collisions, a gas molecule transfers directly the information in the past to the future by its free flight until it hits a physical boundary. In other words, a gas molecule at a time may contain the long-memory from the far past (e.g., the initial condition). After being reflected on the boundary, the molecule obtains the new information, that is, the long-memory is destroyed by the collision with the boundary. Hence, if the long-time behavior of the solution in time-dependent problems of a free-molecular gas with a stationary or moving boundary is under concern, it is necessary to understand the long-memory of the problem and how it is destroyed. Since the destruction of the long-memory is caused only by the collision with the boundary in the case of the free-molecular gas, the geometrical shape of the boundary plays an important role in determining the long-time behavior. In Chapters 1 and 3, where the unsteady motion of a boundary in the infinite expanse of a free-molecular gas is considered, the long-memory manifests itself as the recollision of gas molecules with the boundary. In Chapter 2, where a free-molecular gas is contained in a fixed vessel, the slow molecules at the initial time contain the long-memory. Although the physical meanings of the long-memory are different depending on the problems, its role in determining the long-time behavior of the solution seems same: the long-memory makes the rate of approach to the time-asymptotic state be proportional to an inverse integer power of time (the algebraic approach).

On the other hand, when an interaction of gas molecules with a background (the special Lorentz gas, Chapter 3) or an inter-molecular collision (the BGK model, Chapter 4) is considered (i.e., the Knudsen number is finite), the destruction of the long-memory is enhanced, and thus the resulting long-time behavior of the solution is qualitatively different from that of the free-molecular gas. In particular, the analysis based on the special Lorentz gas in Chapter 3 clarifies that the rate of approach is exponentially fast in the case of the special Lorentz gas. This exponential approach should be contrasted with the algebraic approach for the free-molecular gas. In the case of the BGK model in Chapter 4, the rate of approach seems to be proportional to a half-integer power of time, however, more careful investigation is necessary in order to conclude this half-integer algebraic rate and clarify its underlying mechanism.

The long-memory appears in the velocity distribution functions as the localized structure, namely, the variation of them due to the boundary is confined in a small region in the molecular

velocity space. These localized structures include singularities such as discontinuities in the velocity distribution function. Moreover, they become more localized as time goes on. Accurate numerical analyses for the problems containing these singularities are difficult in general, since the ordinary higher-order schemes do not work due to the singularities. The numerical error induced by the singularities destroys the long-memory of the problem, and this unphysical disappearance of the long-memory leads to the wrong long-time behavior. Throughout the thesis, the method based on the characteristics, which is capable of capturing the singularities accurately, are mainly employed in order to catch the correct long-time behavior of the solution. In Chapter 4, the occurrence of the singular behavior of the velocity distribution function is closely discussed, and the proper treatment of it in the numerical analysis is introduced. It is shown that the careful treatment of the singular behavior is necessary under certain conditions.

The time-dependent problems with a stationary or moving boundary treated in this thesis are restricted to some simple cases, such as the case of a free-molecular gas (Chapters 1, 2, and 3) or the case of a spatially one-dimensional problem (Chapter 4). Owing to the simplicity of the problems, it is able to obtain the details of the long-time behavior of the solution, and the correct shape of the velocity distribution function including the singularities. The present results can be extended in the following directions. First of all, it is of great interest to develop an easily-implemented and efficient numerical method to simulate time-dependent problems of rarefied gas flows with a stationary or moving boundary in practical applications, since the present method is too complicated to apply to spatially two- or three-dimensional problems that one often faces in micro engineering. The knowledge about the velocity distribution function established in the thesis will be helpful for this purpose, and the numerical solutions obtained in the present simple settings will serve as the reference solutions to be compared with the newly-developed methods in the future. Another extension is to investigate some fundamental problems in physics involving a moving boundary in the framework of kinetic theory, such as a linear pendulum treated in Chapter 3. The piston problem, for instance, is the one which has been under concern in statistical physics for a couple of decades. The effect of the boundary condition, as well as the shape of the boundary, is also to be studied more carefully. It should be mentioned that, in the present thesis, only the convex boundary (convex toward the gas side) has been considered for the cases with the moving boundary. The long-memory for the case with the a concave moving boundary is expected to have different features, since the gas molecules can be trapped in the concaved part of the boundary.

List of publications

Chapter 1

K. Aoki, T. Tsuji, and G. Cavallaro, "Approach to steady motion of a plate moving in a free-molecular gas under a constant external force," *Phys. Rev. E* **80**(1), 016309 [13 pages] (2009).

Chapter 2

T. Tsuji, K. Aoki, and F. Golse, "Relaxation of a free-molecular gas to equilibrium caused by interaction with vessel wall," *J. Stat. Phys.* **140**(3), pp. 518–543 (2010).

Chapter 3

T. Tsuji and K. Aoki, "Decay of a linear pendulum in a free-molecular gas and a special Lorentz gas," *J. Stat. Phys.* **146**(3), pp. 620–645 (2012).

Chapter 4

T. Tsuji and K. Aoki, "Moving boundary problems in a rarefied gas," in preparation

T. Tsuji and K. Aoki, "Gas motion in a micro gap between longitudinally oscillating and stationary plates," in *the Proceedings of 3rd European Conference on Microfluidics* [12 pages], to be published.

Other publications

T. Tsuji and K. Aoki, "Decay of an oscillating plate in a free-molecular gas," in *the Proceedings of 27th International Symposium on Rarefied Gas Dynamics*, AIP Conference Proceedings 1333, edited by D. A. Levin, I. Wysong, A. Garcia, and L. A. Gochberg, (AIP, Melville), pp. 140–145 (2011).

G. Cavallaro, C. Marchioro, and T. Tsuji, "Approach to equilibrium of a rotating sphere in a Stokes flow," *Ann. Univ. Ferrara* **57**(2), pp. 211–228 (2011).

T. Tsuji and K. Aoki, "Numerical analysis of nonlinear acoustic wave propagation in a rarefied gas," in *the Proceedings of 28th International Symposium on Rarefied Gas Dynamics*, [8 pages], to be published.